Mass Transfer to/from Distributed Sinks/Sources in Porous Media

by

Weishu Zhao

A thesis

presented to the University of Waterloo

in fulfillment of the

thesis requirement for the degree of

Doctor of Philosophy

in

Chemical Engineering

Waterloo, Ontario, Canada, 2006

I hereby declare that I am the sole author of this thesis. This is a true copy of the thesis, including any required final revisions, as accepted by my examiners.

I understand that my thesis may be made electronically available to the public.

Abstract

This research addresses a number of fundamental issues concerning convective mass transfer across fluid-fluid interfaces in porous media. Mass transfer to/from distributed sinks/sources is considered for i) the slow dissolution of liquid filaments of a wetting non-aqueous phase liquid (NAPL) held in the corners of angular pores or throats and ii) the fate of gas bubbles generated during the flow of a supersaturated aqueous phase in porous media.

1.   Effects of the stability of NAPL films on wetting NAPL dissolution

Wettability profoundly affects the distribution of residual NAPL contaminants in natural soils. Under conditions of preferential NAPL wettability, NAPL is retained within small pores and in the form of thick films (liquid filaments) along the corners and crevices of the pore walls. NAPL films in pore corners provide capillary continuity between NAPL-filled pores, dramatically influencing the behaviour of NAPL dissolution to the flowing aqueous phase by convection and diffusion. A pore network model is developed to explore the dissolution behaviour of wetting NAPL in porous media. The effects of initial NAPL distribution and NAPL film stability on dissolution behaviour are studied using the simulator. NAPL phase loses continuity and splits into disconnected clusters of NAPL-filled pores due to rupture of NAPL films. Quasi-state drainage and fingering of the aqueous phase into NAPL-filled pores is treated as an invasion percolation process and a stepwise procedure is adopted for the solution of flow and solute concentration fields. NAPL film stability is shown to critically affect the rate of mass transfer as such that stable NAPL films provide for more rapid dissolution. The network simulator reproduces the essential physics of wetting NAPL dissolution in porous media and explains the concentration-tailing behaviour observed in experiments, suggesting also new possibilities for experimental investigation.

2.   Convective Mass Transfer across Fluid Interfaces in Straight Angular Pores

Steady convective mass transfer to or from fluid interfaces in pores of angular cross-section is theoretically investigated. The model incorporates the essential physics of capillarity and solute mass transfer by convection and diffusion in corner fluid

filaments. The geometry of the corner filaments, characterized by the fluid-fluid contact angle, the corner half-angle and the interface meniscus curvature, is accounted for. Boundary conditions of zero surface shear ('perfect-slip') and infinite surface shear ('no-slip') at the fluid-fluid interface are considered. The governing equations for laminar flow within the corner filament and convective diffusion to or from the fluid-fluid interface are solved using finite-element methods. Flow computations are verified by comparing the dimensionless resistance factor and hydraulic conductance of corner filaments against recent numerical solutions by Patzek and Kristensen [2001]. Novel results are obtained for the average effluent concentration as a function of flow geometry and pore-scale Peclet number. These results are correlated to a characteristic corner length and local pore-scale Peclet number using empirical equations appropriate for implementation in pore network models. Finally, a previously published "2D-slit" approximation to the problem at hand is checked and found to be in considerable error.

3. Bubble evolution driven by solute diffusion during the process of supersaturated carbonated water flooding

In situ bubble growth in porous media is simulated using a pore network model that idealizes the pore space as a lattice of cubic chambers connected by square tubes. Evolution of the gas phase from nucleation sites is driven by the solute mass transfer from the flowing supersaturated water solution to the bubble clusters. Effects of viscous aqueous phase flow and convective diffusion in pore corners are explicitly accounted for. Growth of bubble clusters is characterised by a pattern of quasi-static drainage and fingering in the gas phase, an invasion percolation process controlled by capillary and gravitational forces. A stepwise solution procedure is followed to determine the aqueous flow field and the solute concentration field in the model by solving the conservation equations. Mobilization of bubbles driven by buoyancy forces is also studied. Results of bubble growth pattern, relative permeability and macroscopic mass transfer coefficient are obtained under different gas saturations and aqueous flow conditions.

Acknowledgements

To my parents, my wife and my son

TABLE OF CONTENTS

List of Figures

List of Tables

Nomenclature

a_i specific interfacial area

A cross-sectional area

b meniscus-apex distance

Bo Bond number

C concentration

Ca Capillary number

C_s equilibrium solubility

D dispersion coefficient, m^2/s

d_{50} median grain size, m

D_m molecular diffusion coefficient, m^2/s

d_p characteristic length

dt time interval in simulations with film disconnection

E_d normalized effluent concentration

f_q nucleation fraction

F   flux

g hydraulic conductance

                 gravitational constant

h height

                 film thickness

H Henry's constant

J interface curvature

K permeability

                 mass transfer rate coefficient

K_{diss} dissolution coefficient

K_r relative permeability

L length

n	mole mass
	node identification number
N	number of nucleation sites
P	pressure
P_C	capillary pressure
$P_C^{sanp-off}$	snap-off capillary pressure
P_C^{piston}	piston-type drainage capillary pressure
Pe	Peclet number
P_i	partial pressure
PV	pore volume
ΔP	pressure drop
Q	flow rate
r	radius
r^2	coefficient of linear regression
R	ideal gas constant
	radius
Re	Reynolds number
R_V	equivalent volumetric radius of tube
S	saturation
Sc	Schmidt number
S_f	supersaturation coefficient
S_{gc}	critical gas saturation
Sh	Sherwood number
Sh'	modified Sherwood number
t	time
t_d	dimensionless time
t_{step}	time interval for each simulation step
u	liquid velocity

U	Darcy velocity
V	velocity
	volume
W	width of crevice on pore wall
x_i	mole fraction of dissolved gas in aqueous phase
z	coordination number of pore network

Greek symbols

β	filament half angle
σ	interfacial tension
	standard deviation of pore size distribution
μ	population mean of pore distribution
	water viscosity
ρ	density
λ	pore size distribution index
	eigen value
Π	disjoining pressure
δ	tube diameter
θ	contact angle
ϕ	porosity
	dimensionless concentration
ζ, ξ	dimensionless distance
χ	hydraulic resistance factor

Subscripts and superscripts

*	dimensionless
	critical
$< >$	average
A	advancing
$diff$	diffusive
e	equilibrium
eff	effective
g	gas
i, j	coordinates
l	liquid
min	minimum
max	maximum
N	NAPL
o	oil
p	pore
R	receding
s	solid
S	surface
t	tube
w	water
x, y, z	coordinates

Chapter 1

Introduction and Objective

Mass transfer between two fluid phases simultaneously present within a porous medium is frequently encountered in engineering practice. For example, during the dissolution of residual nonqueous phase liquids (NAPL) for soil remediation, convective diffusion transfers an organic solute from the NAPL into a flowing aqueous phase. [e.g., Powers et al., 1991; Dillard and Blunt, 2000; Bradford et al., 1999; Sahloul et al., 2002]. In cases of supersaturated water injection (SWI) for NAPL recovery [Li, 2004] or solution gas drive for oil recovery [Sheng et al., 1999a; b; Bora et al., 2000], gas bubbles nucleate in a supersaturated liquid phase and grow as a result of solute mass transfer from the liquid phase. A similar situation is found within the porous gas diffusion layer at the anode of a direct methanol fuel cell (DMFC). In that instance, product CO_2 in excess of the solubility concentration results in the formation of gas bubbles near the anode catalyst surface layer, limiting methanol transport to the reaction sites [e.g., Argyropoulos et al., 1999ab; Yang et al., 2005]. In other instances, mass transport of oxygen or other reactive gases from gas bubbles in soil or rock directly influences the process of bioremediation of organic contaminants [e.g., Wilson et al., 1994; Borden et al., 1997; Deeb et al., 2000], or gas bubbles are generated as a result of biological activity (biogenic methane generation)

[e.g., Reynolds et al., 1992; Beckwith and Baird, 2001; Kellner et al., 2004]. What is common in all of these situations is the need to describe the physics of mass transfer to (from) sinks (sources) in porous media (gas bubbles or liquid ganglia). Not only are these sinks (sources) distributed in a complex fashion, presenting interfacial areas for mass transfer that depend on the mass transfer process itself, but they can be mobile, as is the case with growing bubbles in porous media. In this research, mass transfer across fluid-fluid interfaces to (from) distributed sinks (sources) is considered with an aim to improve the understanding of two processes of importance to environmental engineering. These are (i) dissolution of wetting NAPL sources in soil and (ii) *in situ* growth of gas bubbles (sinks) in porous media by convective diffusion from an injected supersaturated liquid phase.

1.1   NAPL dissolution

Hazardous non-aqueous phase liquids (NAPL), such as gasoline, halogenated solvents and other petroleum products enter the subsurface through leakage from storage tanks, improper disposal of wastes or accidental spillage. Non-aqueous phase liquids that are lighter than water (LNAPL) and non-aqueous phase liquids that are heavier than water (DNAPL) are generally immiscible with water and have very low aqueous solubility. Once such contaminants enter the subsurface, they are entrapped in the pore space of soil, posing a serious threat to groundwater resources and an unprecedented challenge to remediation efforts.

NAPL dissolution to the mobile aqueous phase has been found to be a mass transfer limited process [Miller et al., 1990; Powers et al., 1991; Powers et al., 1992; Sahloul et al., 2002]. Pore-scale studies [Dillard and Blunt, 2000; Zhou et al., 2000; Sahloul et al., 2002] suggested that the rate of NAPL dissolution is determined by corner film flow and diffusion. Factors that control the mass transfer of NAPL dissolution should include the hydrodynamic properties of the aqueous phase and the configuration and distribution of the NAPL sources, which largely depend on the wettability and microstructure of the porous medium.

Numerous experimental and theoretical researches on NAPL dissolution have been focused on water wet systems [e.g., Powers et al., 1992; Jia et al., 1999; Dillard et al., 2001; Held and Celia, 2001]. However, although water has a natural tendency to wet the surfaces of soil grains, some NAPLs can alter the wettability of soil grains, rendering them oil-wet [Dwarakanath et al., 2002]. If soil is preferentially wetted by water, residual non-wetting NAPL forms discrete ganglia in pores of high aspect ratio. Under oil-wet conditions, however, the NAPL is likely to be entrapped within the smaller pores and in the form of filaments along the corners of pores invaded by the non-wetting phase (water). Changes in the pore-scale configuration of residual NAPL due to wettability variation can dramatically influence the aqueous phase flow field [Wang, 1988] and NAPL-water interfacial area [Bradford and Leij, 1997]. Since the processes of inter-phase mass transfer are sensitive to system hydrodynamics and interfacial area, mass transfer during residual NAPL dissolution is obviously different between water-wet and NAPL-wet systems, and an understanding of the differences is essential in designing effective remedial strategies for NAPL-contaminated sites. Glass micromodel

experiments on wetting NAPL dissolution by Sahloul et al. [2002] showed that slow dissolution of residual NAPL residing in the corners of water-invaded pores is accompanied by quasi-static drainage of water in NAPL-filled pores. The "capillary pumping" of NAPL from NAPL-filled pores to dissolving thick NAPL films creates new paths for water flow and increases the interfacial area for mass transfer. Based on the mechanism of wetting NAPL dissolution revealed by micro-model experiments [Sahloul et al., 2002], Zhao and Ioannidis [2003] developed a pore network model to simulate wetting NAPL dissolution and suggested that the tailing behavior could be attributed to NAPL film disconnection. Their model suggested that the rupture and concomitant loss of hydraulic continuity of thick NAPL films critically affects the NAPL dissolution behavior. However, the role of NAPL film stability on NAPL dissolution was not accounted for.

1.2 NAPL remediation technologies

Remediation of NAPL-contaminated sites has traditionally involved pumping as much of the free organic phase from the aquifer as possible, followed by *in situ* water flushing, a technique known as pump-and-treat remediation, to dissolve NAPL ganglia or "blobs" retained within the porous medium and to remove the dissolved organic from the aquifer [Testa and Wiengardner, 1991]. Although the pump-and-treat technique (Figure 1.1) is the most commonly used approach to subsurface cleanup, it is usually quite ineffective due to rate-limited interphase mass transfer.

Air sparging is a remediation method for NAPLs with relatively high volatilities. In this approach, air is injected into the subsurface saturated zone, enabling the transfer of volatile contaminants into the gas phase, which is then vented through the unsaturated zone. The most serious problem confronting air sparging is the buoyancy-driven capillary fingering of injected air through the high permeability paths around the injection point [e.g., Ji et al., 1993; Tomlinson et al., 2003]. The lack of direct contact between residual NAPL and air, which results from air by-passing contaminated zones of relatively lower permeability, often severely undermines the effectiveness of the technology. A schematic of this phenomenon is shown in Figure 1.2.

Other NAPL remediation technologies include soil excavation, surfactant flooding, *in situ* chemical oxidation, and bioremediation. All of the aforementioned technologies encounter various technical difficulties and there is a pressing need for developing novel technologies for NAPL remediation and particularly for the efficient removal of free-phase residual NAPL. The research presented here aims to support on-going efforts at University of Waterloo to develop such a novel NAPL remediation technology, namely supersaturated water injection or SWI. The SWI method involves flushing with water supersaturated with carbon-dioxide (or other gases) beneath or into the NAPL source zone. This technology has the potential to overcome the serious problems with air sparging, namely that the injected air tends to by-pass the low permeability zones through high permeability zones near the injection point. Experimental studies of SWI [Li, 2004] have shown that the injected supersaturated water can deliver dissolved gas phase to low permeability zones, where gas bubbles nucleate and subsequently grow to contact, volatilize and mobilize NAPL ganglia. In

order to design remediation strategies using this promising new technology, theoretical investigations of the *in situ* evolution of gas bubbles from supersaturated aqueous solutions within porous media are required to better understand the relevant mass transfer issues.
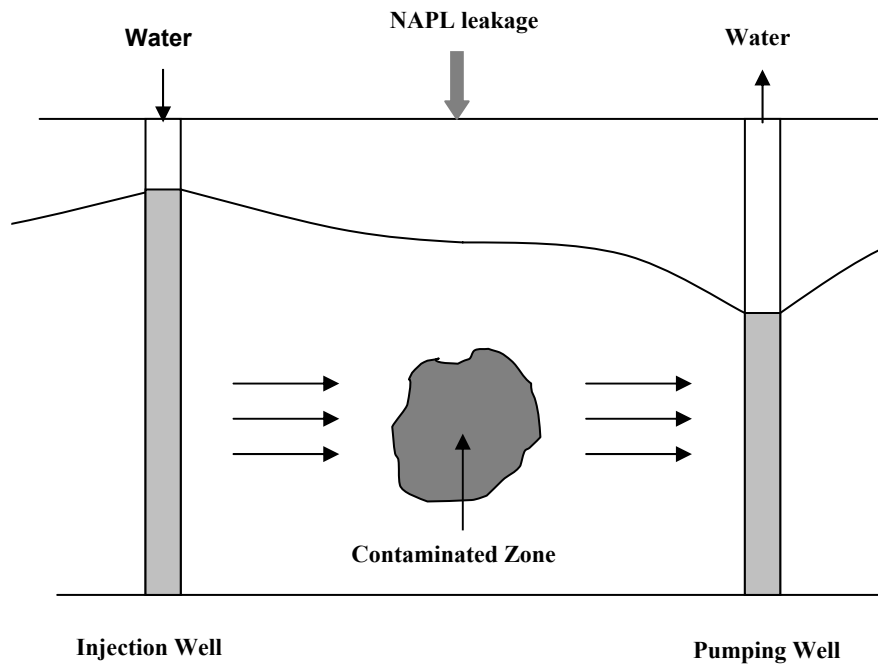
Figure 1.1 Schematic of pump-and-treat technology.
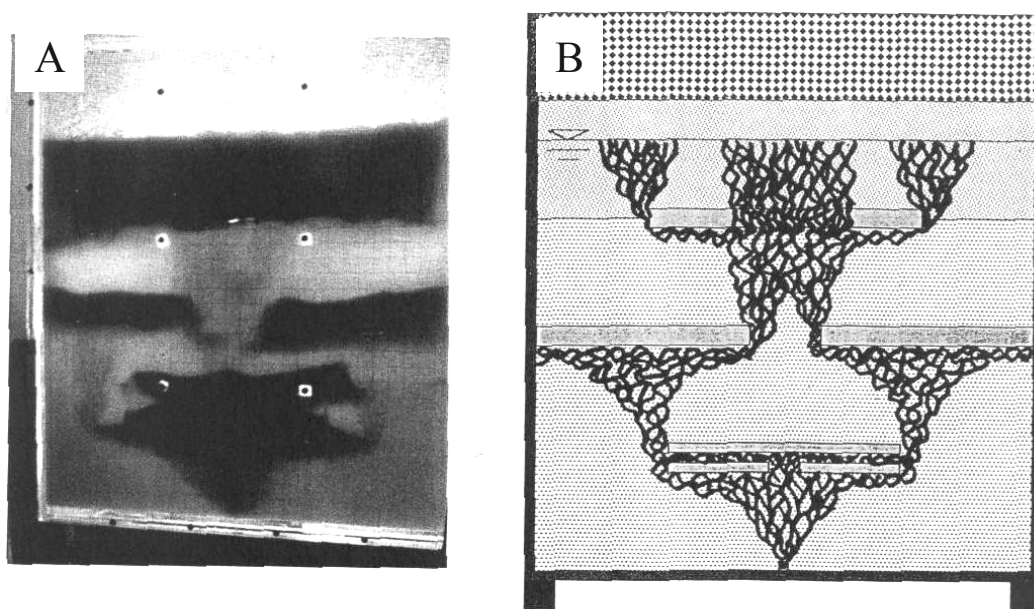
Figure 1.2 Schematic of air pathways during air sparging by-passing zones of low permeability [from Ji et al., 1993]

.

1.3   *In-situ* gas evolution in porous media

Formation of gas bubbles may have significant effects on geochemical and hydraulic properties of groundwater environment [Donaldson et al., 1997]. Dissolved gas transport in porous media involves a diffusion-controlled gas partitioning process when mass transfer takes place between the mobile aqueous phase and the trapped gas phase. The presence of a discontinuous gas phase in natural aquifers may be the result of bubble entrapment due to water table fluctuations or biogenic gas production [e.g., Reynolds et al., 1992; Beckwith and Baird, 2001; Kellner et al., 2004]. Some groundwater remediation technologies also introduce gas phase to the subsurface. For example, air is injected below the water table during *in situ* air sparging in order to recover volatile

organic contaminants and during *in situ* chemical oxidation processes and CO_2 is generated when chlorinated solvents are oxidized by introduced oxidants, such as $KMnO_4$. Higher gas saturation in subsurface can be achieved by supersaturated water injection (18-27% compared to 14-17% by *in situ* air sparging) [Fry et al., 1997]. Experiments on SWI [Li, 2004] showed that relatively homogeneous gas distributions could be obtained even in heterogeneous porous media. These phenomena could benefit the remediation of volatile NAPLs (as already mentioned) and the bioremediation process, where delivery of reactive gases to assist the microbial degradation of the organic contaminants is required [e.g., Wilson et al., 1994; Borden et al., 1997; Deeb et al., 2000]. The related process of solution gas drive (SGD) in oil reservoirs has been studied extensively [e.g., Li and Yortsos, 1995a; El Yousfi, et al., 1997; Dominguez et al., 2000]. In SGD, the supersaturation leading to bubble nucleation and growth is usually the result of pressure depletion, which is essentially different from the SWI, where the aqueous phase is mobile and the gas partition process is mainly controlled by convective mass transfer.

1.4   Pore network modeling

Application of network models is an effective way to investigate the capillary, flow and transport properties of porous media. A network model is a detailed model of a porous medium, generally incorporating pore-scale descriptions of the medium and of the physical pore-scale events. To model porous media, the disordered and geometrically complex void space is typically represented as a network of lager spaces (pores)

connected by narrow constrictions (throats). The assumption that the pore space can be conceptually simplified as pore bodies and throats and mapped onto a regular or irregular lattice of sites and bonds is well justified for consolidated porous rocks and random packing of particles and is probably applicable to most geologic materials [e.g., Imdakm and Sahimi, 1991; Dullien 1992; Reeves and Celia, 1996; Thompson and Fogler, 1997]. A different size is assigned to each pore body and throat from a representative pore size distribution. Regular geometries are usually assumed to simplify the pore elements (e.g., spherical pores and cylindrical throats) and analytical equations are used to compute fluid volumes and interfacial shapes and areas. By reasonably specifying size, shape, connectivity and spatial arrangement of pores and throats, researchers can use network models to simulate a broad range of transport and capillary phenomena in porous media [Ioannidis and Chatzis, 1993; Sahimi, 1993; Yiotis et al., 2001; 2005; Blunt et al., 2002]. Because network models enable the prediction of macroscopic transport properties of porous media from the microstructure, they can be used to explain the experimental results and relate the macroscopic properties to pore-scale physics.

Pore network models have been extensively used to simulate mass transfer processes in porous media, for example, non-wetting NAPL dissolution [Zhou et al., 2000; Dillard and Blunt, 2000; Dillard et al., 2001; Held and Celia, 2001]; wetting NAPL dissolution [Zhou et al., 2000; Zhao and Ioannidis, 2003]; drying of porous media [Yiotis et al., 2001; 2005; Freitas and Prat, 2000] and solution gas drive [Li and Yortsos, 1995a; Dominguez et al., 2000; Tsimpanogiannis and Yortsos, 2002; 2004]. Pore network modeling is the main method used in this research to study convective mass transfer in porous media.

1.5 Research scope and objectives

1.5.1 Dissolution of residual NAPL that preferentially wets the solid surface

A 2D pore network model is developed to explore the effects of stability of wetting NAPL films on NAPL dissolution. Effects of initial NAPL distribution, pore structure and disjoining pressure on NAPL dissolution dynamics are studied. Results of simulations show that thick NAPL films in pore corners provide capillary continuity between NAPL-filled pores, dramatically influencing the dynamics of NAPL dissolution to a flowing aqueous phase by convection and diffusion. Physicochemical and pore structure parameters affecting the stability of thick NAPL films are thus expected to affect the dissolution behaviour. NAPL film stability critically affects the rate of mass transfer, such that stable NAPL films provide for more rapid dissolution. The network simulator reproduces the essential physics of wetting NAPL dissolution in porous media and explains the concentration-tailing behaviour observed in experiments, suggesting also new possibilities for experimental investigation.

1.5.2 Bubble evolution driven by solute diffusion during the process of supersaturated carbonated water flooding

In situ bubble growth in porous media is simulated using a 2D pore network model that idealizes the pore space as a lattice of cubic chambers connected by square tubes. Evolution of the gas phase from nucleation sites is driven by the solute mass transfer from the flowing supersaturated water solution to the bubble clusters. Effects of viscous aqueous phase flow and convective diffusion in pore corners are explicitly

accounted for. Growth of bubble clusters is characterised by a pattern of quasi-static drainage and fingering in the gas phase, an invasion percolation process controlled by capillary and gravitational forces. A stepwise solution procedure is followed to determine the aqueous flow field and the solute concentration field in the model by solving the conservation equations. Mobilization of bubbles driven by buoyancy forces is also studied. Results of bubble growth pattern, relative permeability and macroscopic mass transfer coefficient are obtained under different gas saturations and aqueous flow conditions.

Chapter 2

Background

Environmental research since the late 1980s has succeeded in elucidating many aspects of the behavior of non-aqueous phase liquids (NAPL) in subsurface formations. NAPLs entering the subsurface penetrate through the soil vertically and displace the previously existing pore water under the action of viscous, gravitational and capillary forces. Once they reach the water table, NAPLs lighter than water (LNAPL) depress the water table slightly and spread laterally along the water table. Due to fluctuations of the water table, LNAPL may be trapped below the water table. NAPLs denser than water (DNAPL) may move downward continuously until they encounter a capillary barrier. During the migration, NAPL ganglia are formed from residual segments of NAPL breaking off from the main body of the liquid and are held in aquifer pore spaces by capillary forces [Geller and Hunt, 1993]. The mechanism and degree of entrapment of NAPL in soil depends on physical and chemical characteristics of both the NAPL and the porous medium.

2.1 Pore-level events and multiphase flow in porous media

2.1.1 Pore Structure

A porous medium generally consists of solid matrix and pore space. It is rather difficult to describe the microscopic structure of pore space in an exact manner because of its geometrical complexity. The pore space of geologic media, such as soil and reservoir rock, consists of a network of large pores (pore bodies) communicating through relatively narrow constrictions (pore throats). Figure 2.1 is the schematic of a part of a 2D network of pore space. Since the shape of an actual pore is quite irregular, approximations of pore shape with regular geometries, such as cube, sphere, etc, are commonly made in theoretical studies of the effects of pore structure. A geometrically specified pore structure model enables the computation of volumes and surface areas of the pores.
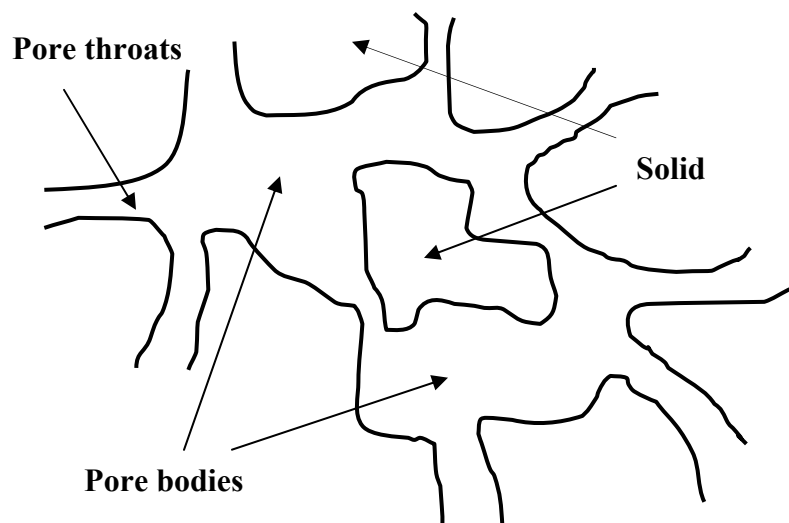
Figure 2.1 Part of a 2D network of pore space.

With the exception of geometric characterization of 3D microtomographic images of the pore space [e.g., Auzerais et al., 1996], pore structure characterization is accomplished by indirect experimental methods. Such methods include 2-D image analysis, mercury porosimetry and nitrogen adsorption methods, all of which have been reviewed by Dullien [1992]. It should be noted that indirect methods of pore structure characterization do not provide identical results because of the different assumptions made to interpret the experimental data [Dullien 1992]. For the case of unconsolidated media, such as soil, the effects of pore structure are often correlated with the particle or grain size distribution. Median grain size d_{50}, which is the grain diameter greater than that of 50% of the particles by weight, is an important parameter used by many researchers instead of the average pore size.

2.1.2   Wettability and spreading coefficient

Wettability is a fluid-solid property that characterizes solid surfaces and is determined by solid-liquid interactions. Wettability critically affects the spreading of a liquid over a solid surface, the penetration of a liquid into a porous medium or the displacement of one liquid by another [Berg, 1993].

Wettability can be described by the contact angle (θ) between the solid surface and the interface between two fluids. A low contact angle measured through the fluid phase of interest corresponds with preferential wetting of the solid by that phase. Figure 2.2 shows two sessile liquid drops (fluid A) immersed in another liquid phase (fluid B) over a solid surface with different contact angles.

Fluid B

θ Fluid A θ Fluid A

(a)   (b)
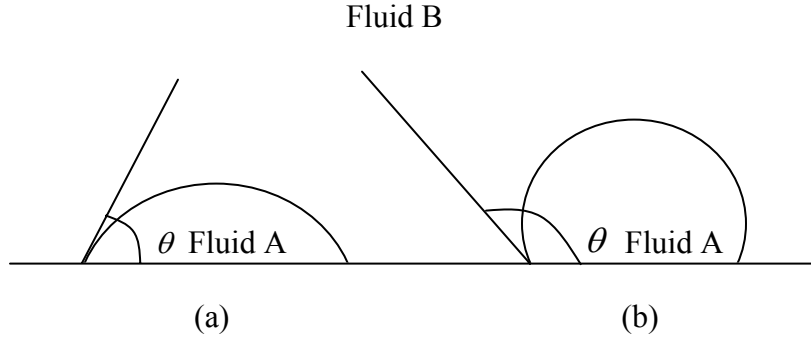
Figure 2.2 Schematic of contact angle between resting drops and solid surface, preferential wetting of the solid by (a) fluid A (b) fluid B.

The form of entrapped NAPL within the pore space is determined by the physicochemical properties of the fluid and the physical characteristics of soil. Soil wettability is one of the important factors that can influence the distribution of residual NAPL as well as the rate of NAPL dissolution into the water phase. In a NAPL-water-solid system, NAPL with a contact angle less than 90^0 is considered the wetting phase and the solid surface is called NAPL-wet, otherwise NAPL with a contact angle larger than 90^0 is the non-wetting phase and the solid surface is called water-wet. Contact angle can be related to interfacial tensions through Young's equation,

$$\cos\theta = \frac{\sigma_{NS} - \sigma_{WS}}{\sigma_{NW}}$$

(2.1)

where σ_{NS} is the interfacial tension between NAPL and solid, σ_{WS} is the interfacial tension between water and solid, σ_{NW} is the interfacial tension between NAPL and water.

In water-wet porous media, water occupies the smaller pores and the pore space immediately adjacent to the solid in the larger pores, while residual NAPL is entrapped in

15

the form of ganglia occupying one or more pores. In NAPL-wet porous media, NAPL is entrapped in smaller pores and spreads over the solid surface of larger pores leaving water between the NAPL films along the pore corners. Figure 2.3 shows the distribution of NAPL in water-wet and NAPL-wet porous media. In many situations, porous media have both NAPL-wet and water-wet solid surfaces. Such a condition is termed fractional wettability. Residual NAPL in a porous medium with fractional wettability can be entrapped as singlets or multi-pore ganglia in the pores with water-wet solid surfaces and as NAPL films coating the NAPL-wet solid surfaces.
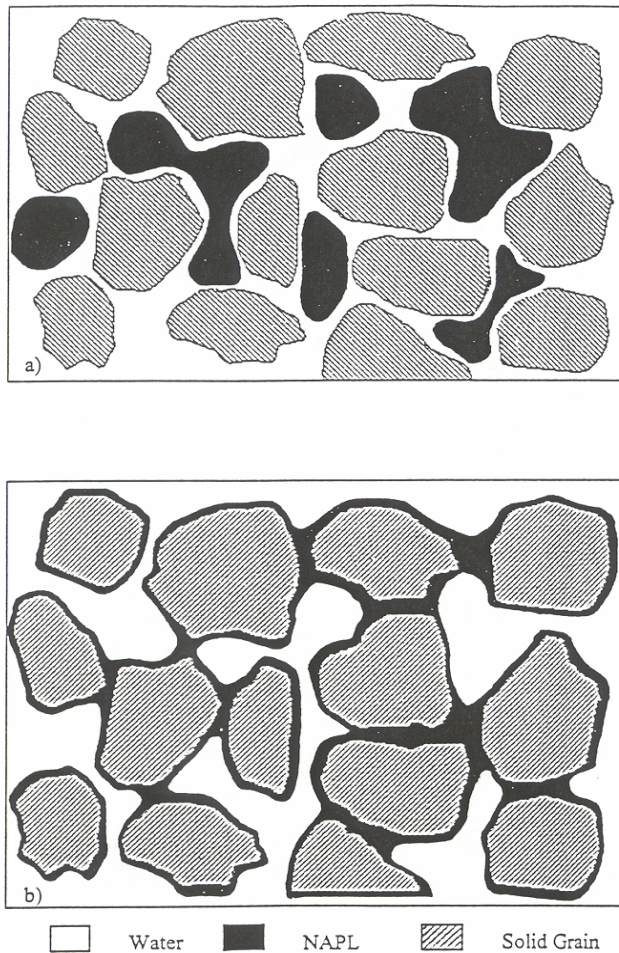
Figure 2.3 Schematic of NAPL distribution in porous media (a) Water-wet system (b) NAPL-wet system [from Sahloul et al., 2002].

The distribution of fluids in porous media also depends on fluid-fluid interaction. In a NAPL-water-gas system, for example, upon contact with a gas phase, NAPL spontaneously spreads over water and a NAPL film is formed between gas and water (see Figure 2.4) if the three-phase system has a positive spreading coefficient. The spreading coefficient, S, is defined as

$$S = \gamma_{gw} - \gamma_{go} - \gamma_{ow} \qquad (2.2)$$

where γ is the interfacial tension and the subscripts g, w and o denote gas, water and oil (NAPL) respectively. In systems with negative spreading coefficient, non-zero contact angles will be formed among the three phases along the contact line [Chatzis et al., 1988; Vizika and Lombard, 1996; Grattoni and Dawe, 2003]. Hawes et al. [1996, 1997] indicated that the spreading coefficient can substantially influence the growth pattern of gas bubbles and the value of the critical gas saturation. The visualization experiments conducted by Grattoni et al. [2001] show that as oil is spreading, it will redistribute in the pore space in the form of films around gas bubbles and can be mobilized along with the bubbles, as they move upwards due to buoyancy. Such observations have also been made by Li [2004] in experimental studies of the SWI process for NAPL recovery (see Figure 2.5). A schematic of the mechanism of this behaviour is shown in Figure 2.6. Even a non-spreading oil can be mobilized when gas expansion displaces water or oil and push the oil slugs through pore throats [Grattoni and Dawe, 2003].

17
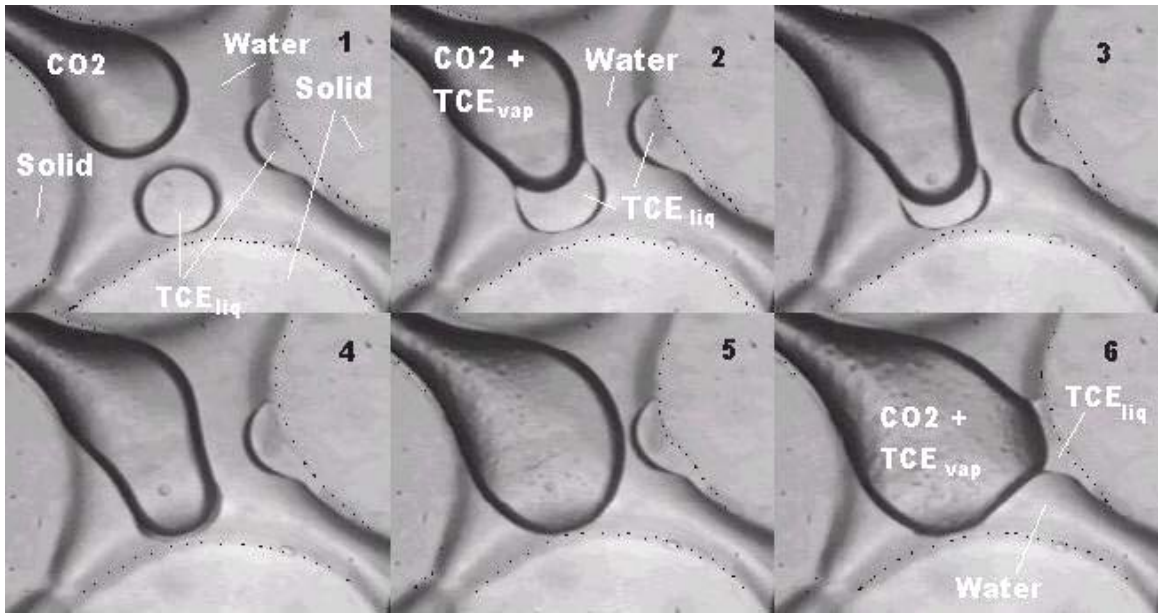
Figure 2.4 NAPL (TCE) spreads around a CO_2 bubble [from Li, 2004].
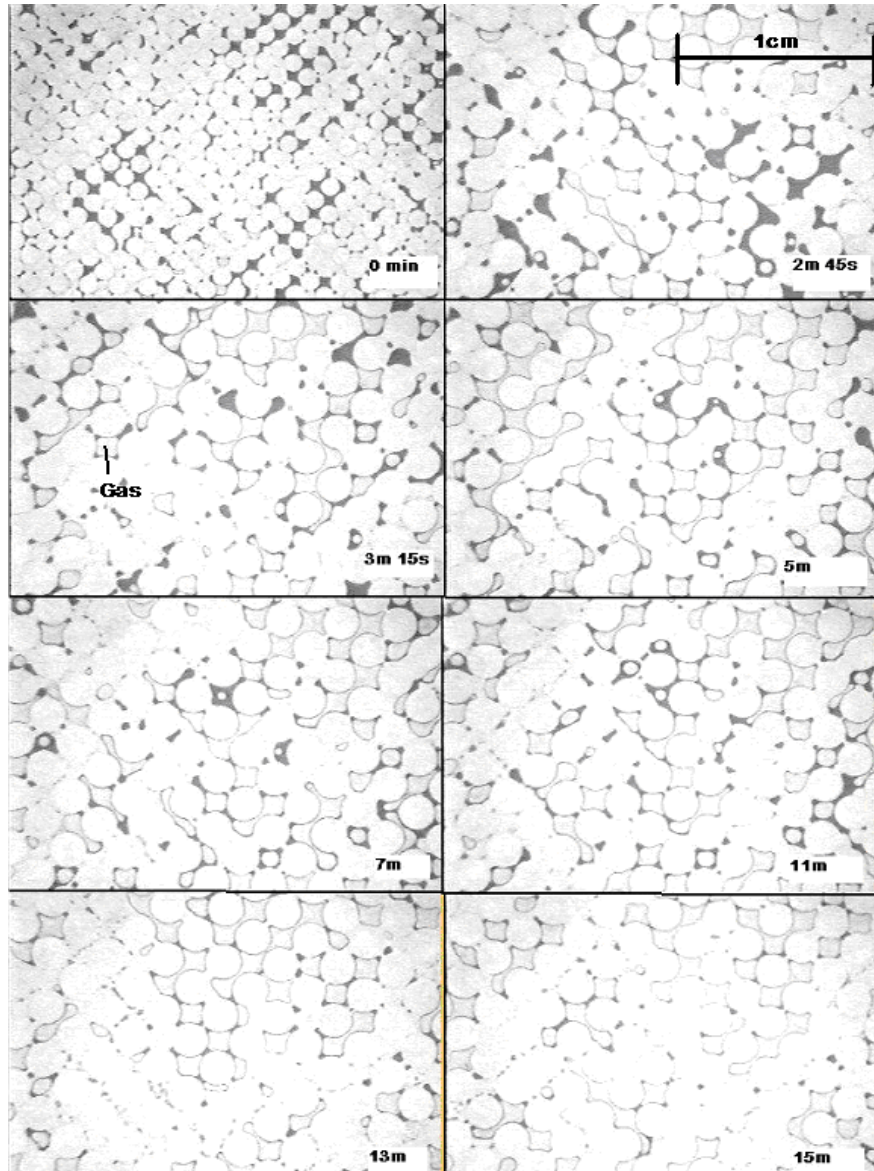
Figure 2.5 Recovery of nonvolatile NAPL by SWI [from Li, 2004].
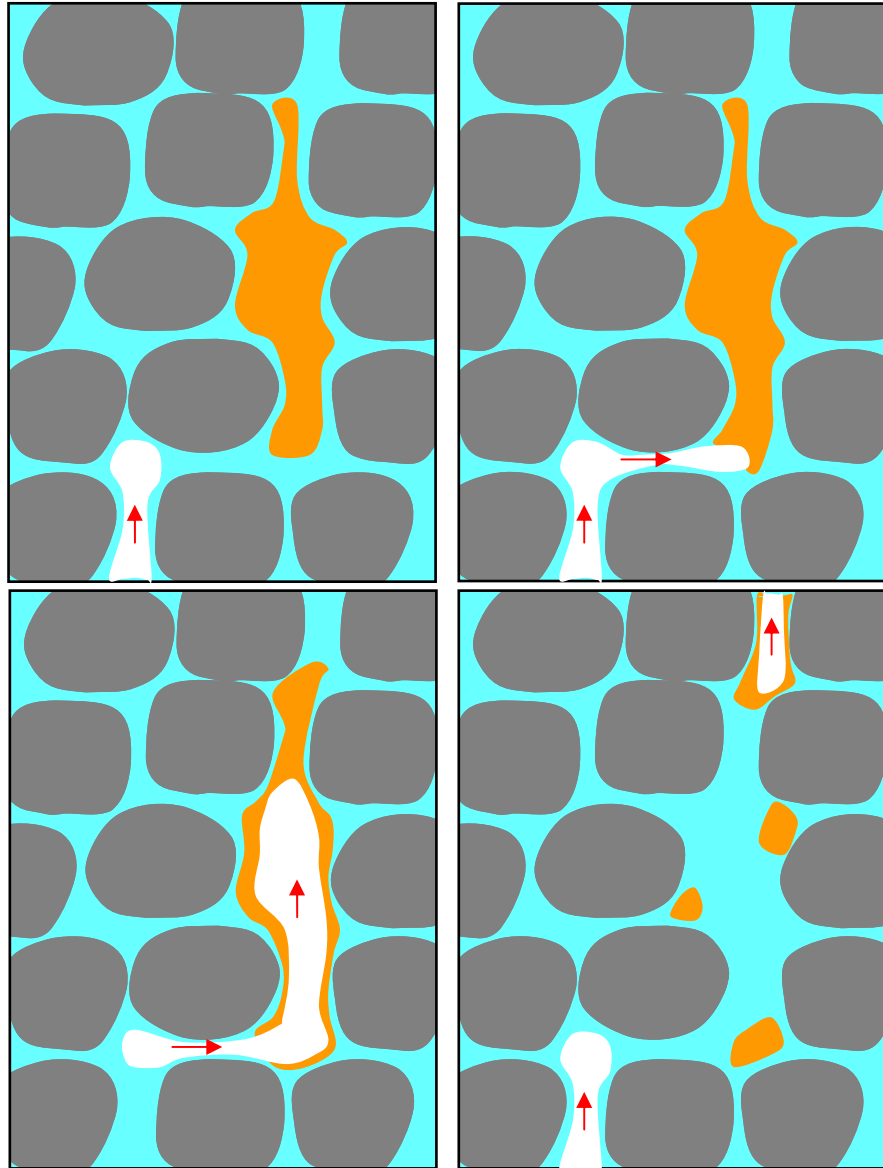
Figure 2.6 Mechanism of NAPL mobilization by moving bubbles.

2.1.3 Capillarity

Capillary phenomena play an important role in NAPL entrapment in porous media. Capillary pressure P_C is defined as the pressure difference between two immiscible fluids at equilibrium within the pore space and is expressed as

$$P_C = P_{nw} - P_w \qquad (2.3)$$

where P_{nw} is the pressure of the non-wetting phase and P_w is the pressure of the wetting phase. Capillary pressure involves the interfacial tension and the interfacial curvature in Laplace's equation:

$$P_C = \sigma J = \sigma(\frac{1}{r_1} \pm \frac{1}{r_2}) \qquad (2.4)$$

where σ is the interfacial tension and J is the curvature of the interface, which is characterized by two principal radii of the curved surface r_1 and r_2. The principal curvature radii at a point on the interface lie on two planes perpendicular to each other and intersect at the point, as shown in Figure 2.7.

(a) $P_C = \sigma(\frac{1}{r_1} - \frac{1}{r_2})$ (b) $P_C = \sigma(\frac{1}{r_1} + \frac{1}{r_2})$
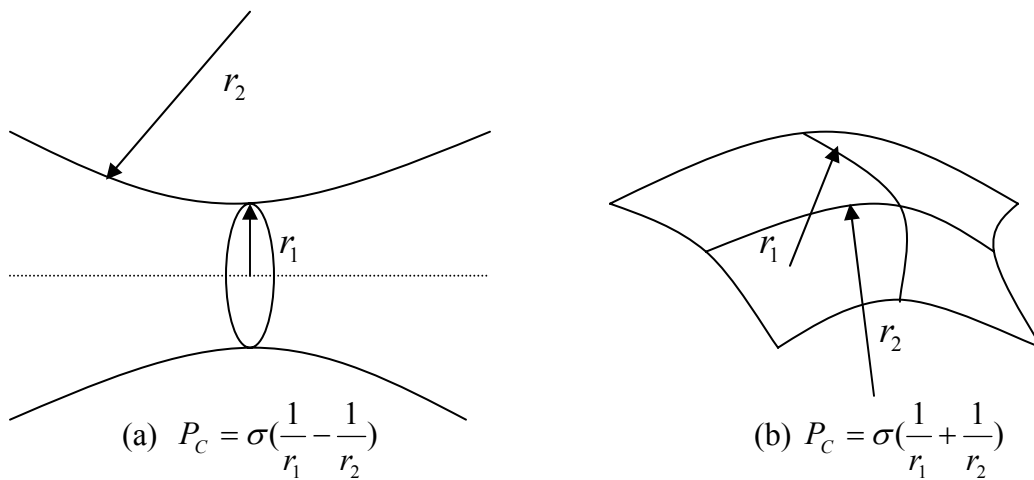
Figure 2.7 Schematic of the curvature of interface (a) concave interface (b) convex interface.

In a cylindrical capillary tube, capillary pressure is given by

$$P_C = \sigma J = \frac{2\sigma \cos\theta}{r} \qquad (2.5)$$

where r is the radius of the tube and θ is the contact angle. However, the geometry of pores in porous media is more complex and conduits with angular cross-section are often used to represent the channels in porous media. An expression of capillary pressure for an interface in a tube with rectangular cross-section was given by Legait [1983]:

$$P_C = \sigma J = \frac{\sigma}{R_t}\left(\frac{\theta + \cos^2\theta - \frac{\pi}{4} - \sin\theta\cos\theta}{\cos\theta - \sqrt{\frac{\pi}{4} - \theta + \sin\theta\cos\theta}} \right) \qquad (2.6)$$

where R_t is the characteristic size of the tube and θ is the contact angle.

2.1.4 Drainage and imbibition

Understanding of the pore scale events during immiscible displacement is necessary in modeling the macroscopic behavior of fluids in porous media. Drainage and imbibition are fundamental processes of immiscible displacement. The former is the process of displacement of the wetting phase by the non-wetting phase, whereas the latter is the process of displacement of non-wetting phase by the wetting phase. In both cases contact angle hysteresis exists. Namely, the observed receding contact angle θ_R during drainage is smaller than the equilibrium or static contact angle θ_E, while the advancing contact angle θ_A is larger than θ_E [Dullien, 1992]. The contact angle hysteresis phenomena are depicted in Figure 2.8.
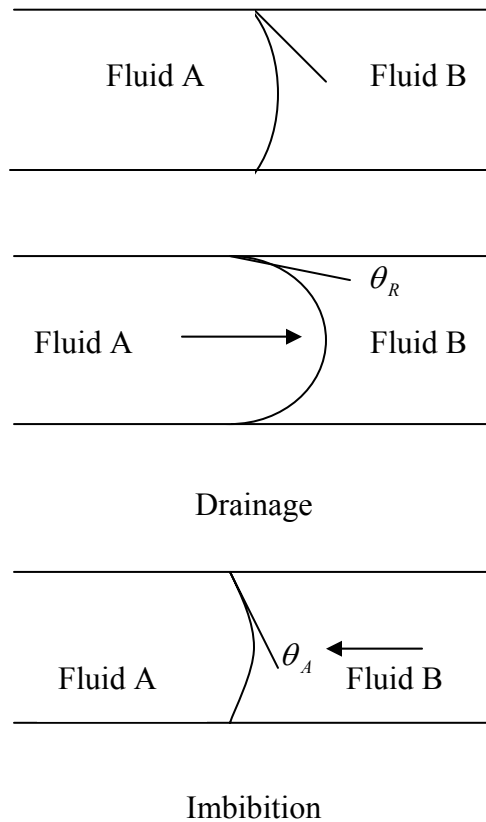
Figure 2.8 Schematic of drainage and imbition and effects of contact angle hysteresis.

Understanding of the pore-scale mechanisms of drainage- and imbibition-type displacement is necessary in order to understand NAPL entrapment. This understanding has been provided by Chatzis and Dullien [1983], who used pore doublet models to visualize drainage and imbibition displacements. Figure 2.9 and Figure 2.10 depict the displacement processes in doublet models. When the fluid flow rate is low, the process is controlled by capillary forces. During an imbition displacement, the advancing wetting phase enters the narrower pore first because of the capillary pressure difference between the pores. If the aspect ratio of the pore (i.e. the ratio of pore body size to pore throat size) is low, non-wetting phase in the pore will totally recede from the pore (Figure 2.9 a).

Otherwise, a singlet blob will be entrapped in the pore. Once the wetting phase reaches the downstream node, a similar imbibition process takes place in the larger pore or a snap-off phenomenon happens at the downstream node causing non-wetting phase entrapment in the larger pore (Figure 2.9b). Conversely, in a drainage process, the non-wetting phase displaces the wetting phase in the larger pore first and the wetting phase in smaller pore is entrapped when the non-wetting phase bypasses it (Figure 2.10). The fundamental difference of pore scale fluid displacement between imbibition and drainage is attributed to the fact that imbibition is controlled by the pore body radii whereas drainage is controlled by the throat radii [Chatzis and Dullien, 1983].

(a) imbibition process in pore doublet with low aspect ratio

(b) imbibition process in pore doublet with high aspect ratio
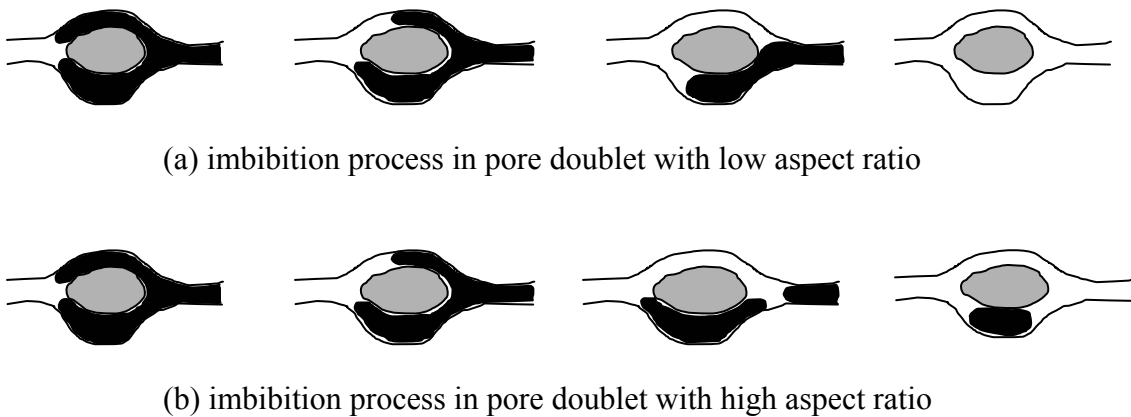
Figure 2.9 Imbibition displacement mechanism in pore doublet [after Chatzis et. al., 1983].

Figure 2.10 Drainage displacement mechanism in pore doublet [after Chatzis et. al. 1983].

Quasi-static drainage experiments in porous media show that the capillary pressure increases with increasing saturation of the non-wetting phase. The relationship between capillary pressure and non-wetting phase saturation is called the drainage capillary pressure curve. On the contrary, an imbibition process is characterized by decreasing values of capillary pressure as the non-wetting phase saturation decreases. A set of capillary curves is shown in Figure 2.11.
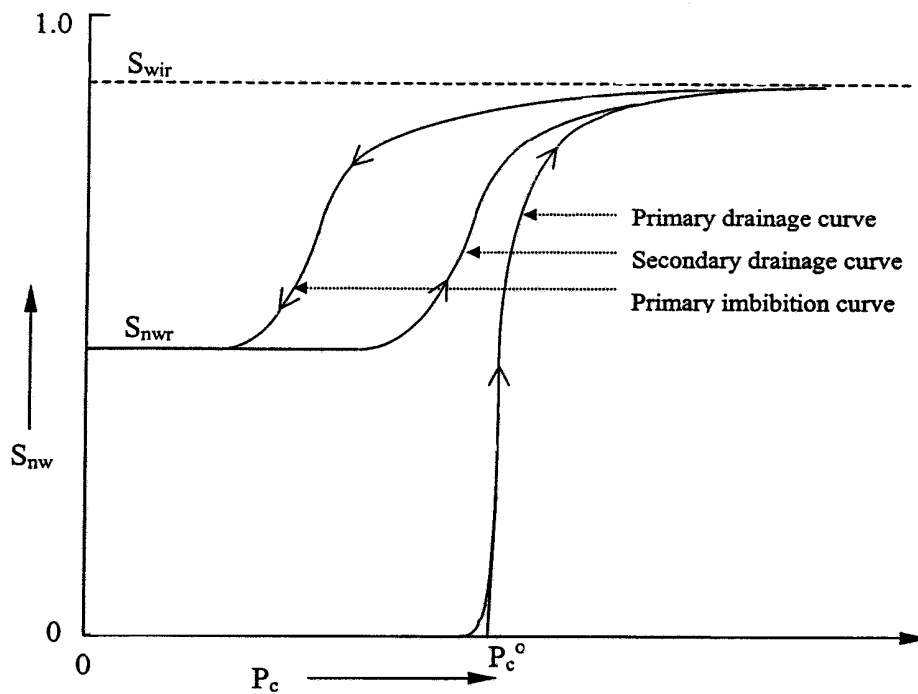
Figure 2.11 Typical capillary pressure curves [after Chatzis, 1980].

It can be seen that a minimum capillary pressure (entry pressure) must be reached before drainage begins. When the capillary pressure reaches a value P_C^0 commonly referred to as the breakthrough capillary pressure, a steep increase in non-wetting phase saturation is observed. At this pressure, a percolation threshold is reached and the non-wetting phase can form a sample-spanning cluster. A residual (or sometimes called irreducible) saturation of the wetting phase S_{wir} is gradually approached as capillary pressure is further increased – a situation connected to the gradual loss of bulk connectivity of the wetting phase (which nevertheless remains connected through wetting films and wetting fluid filaments in pore corners). The imbibition curve does not retrace the drainage curve, but instead hysteresis is observed. A minimum non-wetting phase saturation S_{nwr} is reached at low values of capillary pressure. The reason that the non-wetting phase cannot be completely displaced is permanent entrapment of the non-wetting phase due to the snap-off and bypassing mechanisms during the imbibition process, as shown in Figure 2.9b [e.g., Chatzis and Dullien, 1983; Ioannidis et al., 1991].

2.1.5 Permeability

Under creeping flow conditions, single-phase flow of incompressible fluids in porous media is governed by Darcy's law:

$$\vec{v} = -\frac{K}{\mu}(\nabla P - \rho \vec{g}) \tag{2.7}$$

where $\vec{v}$ is the Darcy velocity, K is the absolute permeability, μ is the dynamic viscosity of the fluid, ∇P is the pressure gradient and ρ is the fluid density.

For a porous medium with multiphase flow, the relative permeability of fluid i, K_{ri}, is defined as

$$K_{ri} = \frac{K_i}{K} \tag{2.8}$$

where K_i is the effective permeability of fluid i and Equation (2.7) can be written as

$$\vec{v}_i = -\frac{K_{ri}K}{\mu_i}(\nabla P_i - \rho_i g) \tag{2.9}$$

where the subscript i denotes fluid i.

Relative permeability is often correlated to phase pressures and saturations. Pressure-saturation-permeability or *P-S-K* relations are of critical importance for multiphase flow modeling. Numerous empirical correlations of *P-S-K* relations have been proposed using pressure-saturation (*P-S)*, saturation-permeability (*S-K)* and hysteretic models for two- or three-phase systems [Miller et al., 1998]. An example of such correlation is the Brooks-Corey model, which is frequently used in reservoir engineering and groundwater modeling:

$$K_{rw} = S_{eff}^{(2+3\lambda)/\lambda} \tag{2.10}$$

$$K_{rnw} = (1 - S_{eff})^2 (1 - S_{eff})^{(2+\lambda)/\lambda} \tag{2.11}$$

$$S_{eff} = \frac{S_w - S_{iw}}{1 - S_{iw}} \tag{2.12}$$

where K_{rw} and K_{rnw} are the drainage relative permeabilities of the wetting and non-wetting phase respectively, λ is the experimentally determined pore size distribution index, S_{eff} is the effective saturation, S_w is the wetting phase saturation and S_{iw} is the

irreducible wetting phase saturation. A more thorough review of correlations of relative permeability is given by Miller et al. [1998].

2.2   NAPL dissolution

2.2.1   Mass transfer during NAPL dissolution

Correlations in forms of dimensionless numbers are often developed to express the effects of fluid flow on mass transfer. The Reynolds number quantifies the relative magnitude of inertial force and viscous forces:

$$\text{Re} = \frac{\rho_w U d_p}{\mu_w} \tag{2.13}$$

The Schmidt number is used to relate viscous momentum transfer to diffusive mass transfer:

$$Sc = \frac{\mu_w}{D_m \rho_w} \tag{2.14}$$

where μ_w is the aqueous phase viscosity, ρ_w is the aqueous phase density, U is the Darcy velocity, d_p is the characteristic length, and D_m is the molecular diffusion coefficient of NAPL in water. The Peclet number is defined as the product of Reynolds number and Schmidt number and measures the relative significance of convective to diffusive mass transfer,

$$Pe = \text{Re} \, Sc = \frac{U d_p}{D_m} \tag{2.15}$$

The Sherwood number is used to correlate the dissolution rate coefficient,

$$Sh = \frac{k_{diss} d_p}{D_m} \qquad (2.16)$$

Much of the early theoretical and experimental work pertaining to mass transfer during NAPL dissolution in porous media concentrated on ideal systems, that is, either perfect spheres packed in columns or theoretical investigations assuming an ideal geometry of pore structure. The theoretical studies dealt with mass transfer into fluids flowing around single cylinders [Dobry and Finn, 1956] or spheres [Ranz and Marshall, 1952]. The theoretical work also involved the mass transfer behavior in packed beds, which is significantly different from the ideal systems. Correlations based on the packed bed experiments were developed to study mass transfer coefficients [Williamson et al., 1963; Wilson et al., 1966; Dwivedi and Updhyay, 1977; Wakao et al., 1978]. Table 2.1 lists some theoretical and experimental correlations reported in the chemical engineering literature.

With reference to column (1D) experiments, convection, dispersion and interphase mass transfer for a single component, slowly-dissolving NAPL are described by the following system of equations [*e.g.*, Baldwin and Gladden, 1996; Johns and Gladden, 1999]:

$$\frac{\partial}{\partial t}[(1 - S_o)C] = D\left[(1 - S_o)\frac{\partial^2 C}{\partial x^2} - \frac{\partial S_o}{\partial x}\frac{\partial C}{\partial x}\right] - \frac{U}{\phi}\frac{\partial C}{\partial x} + K_{diss}a_i(C_s - C) \quad (2.17)$$

$$\frac{\partial S_o}{\partial t} = -K_{diss}a_i(C_s - C)/\rho_o \qquad (2.18)$$

in which ϕ is the porosity, S_o is the NAPL saturation, C is the organic solute concentration in aqueous phase, C_s and ρ_o are the equilibrium solubility and density of the NAPL, U is the Darcy velocity, D is the hydrodynamic dispersion coefficient, K_{diss}

is the mass transfer coefficient and a_i is the NAPL-water specific interfacial area. With few exceptions, only the lumped parameter $K_{diss}a_i$ is determined experimentally and a phenomenological approach is adopted to correlate $K_{diss}a_i$ with the volumetric NAPL content, the aqueous phase Darcy velocity and system properties, such as the median grain size and molecular diffusivity [Imhoff et al., 1998].

Table 2.1 Theoretical and experimental mass transfer correlations.

System	Correlation		Ref
Theoretical			
Single sphere	$Sh = 0.89 Pe^{1/3}$	$Pe \gg 1$	1
	$Sh = \dfrac{4}{Pe} \ln(\dfrac{1}{1 - Pe/2})$	$Pe \ll 1$	1
	$Sh = 2 + 1.24 Pe^{1/3}$	$0 < Pe \ll 1000$	2
	$Sh = (4 + 1.21 Pe^{2/3})^{1/2}$	$0 < Pe \ll 10000$	3
Multi-particle	$Sh \rightarrow 2.0(2Pe/\lambda)^{1/3}$ $\lambda -$ dimensionless length	$Pe \rightarrow \infty$ creeping flow	4
	$Sh = 1.26 \left[\dfrac{1 - (1-n)^{5/3}}{W} \right]^{1/3} Pe^{1/3}$ $W = 2 - 3(1-n)^{1/3} + 3(1-n)^{5/3} - 2(1-n)^2$	$1 \ll Pe < 1000$	5
Experimental			
Benzoic acid-water	$Sh = \dfrac{1.09}{n} Pe^{1/3}$	$0.0016 < Re < 55$ $0.35 < n < 0.75$	6
	$Sh = 2 + 1.1 Sc^{1/3} Re^{0.6}$	$3 < Re < 2000$	7
	$Sh = \left[\dfrac{0.765}{Re^{0.82}} + \dfrac{0.365}{Re^{0.386}} \right] \dfrac{u}{nSc^{0.58}}$	$0.01 < Re < 15000$	8
	$Sh = \dfrac{1.17u}{Re^{0.415} Sc^{2/3}}$	$10 < Re < 2500$	3

References: 1. Friedlander, 1957   2. Levich, 1962

   3. Sherwood et al., 1975   4. Sorensen and Stewart, 1974

   5. Pfeffer, 1964   6. Wilson and Geankoplis, 1966

   7. Wakao and Funazkri, 1978   8. Dwivedi and Updhyay, 1977

The last term of the Equation (2.17) represents the mass transfer flux due to a linear driving force:

$$J = K_{diss} a_i (C_S - C) \qquad (2.19)$$

If steady state is assumed and the dispersion term is neglected, Equation (2.13) can be rewritten as follows:

$$U \frac{\partial C}{\partial x} = K_{diss} a_i (C_S - C) \qquad (2.20)$$

The solution of Equation (2.20) for a zero inlet concentration is

$$K_{diss} a_i = -\frac{U}{L} \ln(C_S - C) \qquad (2.21)$$

where C is the NAPL concentration at the column outlet ($x = L$). Equation (2.21) shows that the mass transfer rate coefficient $K_{diss} a_i$ can be determined by measuring the effluent concentration, column length and Darcy velocity. Equation (2.21) is applied when non-equilibrium conditions prevail, that is when $C < C_S$. Effluent concentration curves have been measured experimentally [Miller et al., 1990; Powers et al., 1992; 1994a; Imhoff et al., 1994; Guo and Thompson, 2001]. Figure 2.12 shows normalized effluent concentration (the ratio of effluent concentration to NAPL solubility) as a function of the number of pore volumes of water pumped through the column.

To obtain a predictive expression for the dissolution rate coefficient, the estimates of lumped parameter $K_{diss} a_i$ obtained from experimental data are used to develop empirical relations in terms of dimensionless numbers. Although the specific NAPL-water interfacial area a_i is difficult to obtain, $K_{diss} a_i$ can be easily calculated using Equation (2.21). A modified Sherwood number, Sh' was defined by Miller et al. [1990] as an alternative to Equation (2.16):

31

$$Sh' = \frac{k_{diss} a_i d_p^2}{D_m} \qquad (2.22)$$

Mass transfer correlations developed in the environmental engineering literature are summarized in Table 2.2.
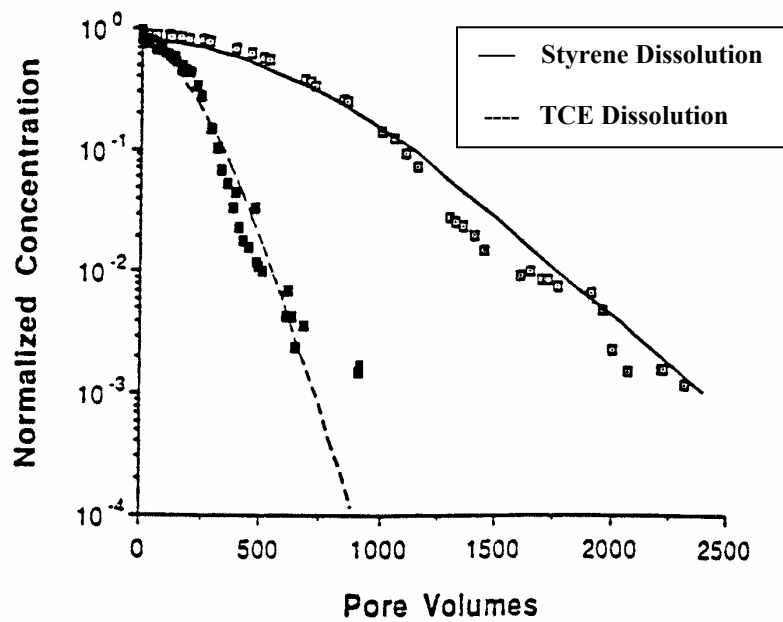
Figure 2.12 Normalized effluent concentration curves for styrene and TCE dissolution [Powers et al., 1994a].

Table 2.2 Correlations obtained from experimental work in the environmental engineering literature.

NAPL	Correlation		Ref
TCE Styrene	$Sh' = 57.7 \, \text{Re}^{0.61} \, d_{50}^{0.64} U_i^{0.41}$	$10 < Pe < 250$	1
TCE Styrene	$Sh' = 4.13 \, \text{Re}^{0.598} \, \delta^{0.673} U_i^{0.369} (\dfrac{\theta_n}{\theta_{n_0}})^{\beta_4}$ $\beta_4 = 0.518 + 0.114\delta + 0.1U_i$	$10 < Pe < 170$	2
Naphthalene	$Sh = 77.6 \, \text{Re}^{0.654}$	$1 < Pe < 200$	3
TCE	$Sh' = 340 \theta_n^{0.87} (\text{Re}')^{0.71} (d_{50}/x)^{0.31}$	$1 < Pe < 25$ $0 < \theta_n < 0.04$ $1.4 \leq x/d_{50} \leq 180$	4
TCE	$Sh' = 1.34 \theta_n^{0.9} \, \text{Re}^{0.75} \, Sc^{0..486}$		5

$U_i = d_{60}/d_{10}$ - uniformity index, θ_n - volumetric NAPL fraction

θ_{n0} - initial volumetric NAPL fraction, δ - normalized grain size

References: 1. Powers et al., 1992   2. Powers et al., 1994a   3. Powers et al., 1994b
         4. Imhoff et al., 1994   5. Imhoff et al., 1997

All of the correlations listed in Table 2.2 have been developed from data obtained from experiments with water-wet systems. However, none of them can provide an accurate description of dissolution data obtained from systems with fractional wettability [Bradford et al., 1999]. In order to describe the fractional wettability dissolution datasets, Bradford et al. [2000] developed a two-parameter power function correlation for the modified Sherwood number:

$$Sh' = \alpha \, \text{Re}^{0.645} \, Sc^{0..486} \left(\frac{\theta_n}{\theta_{n0}} \right)^{\beta} \tag{2.23}$$

where α and β are parameters that are adjusted to explain the dissolution data using a

non-linear least squares fitting method:

$$\alpha = 0.254 \delta^{0.475} U_i^{-1.187}, \qquad r^2 = 0.999 \qquad (2.24)$$

$$\beta = 0.959(1.0 - F_o)^{\frac{6.265}{U_i}}, \qquad r^2 = 0.879 \qquad (2.25)$$

where F_o is the mass fraction of NAPL-wet sand and r^2 is the coefficient of linear regression. This empirical correlation yielded good predictions for the dissolution behavior of the higher NAPL-wet fraction systems. However, predictions for the lower NAPL-wet fraction systems were unsuccessful.

Although the previously developed correlations can be used to explain the data from certain experiments, they have considerable limitations [Khachikian and Harmon, 2000]. The dissolution rate coefficient is a parameter that is influenced by many dynamic effects, such as changes of local hydrodynamic conditions, NAPL blob size, NAPL saturation and NAPL-water interfacial area during the dissolution process. The empirical correlations cannot properly account for the dissolution rate at the pore level. In addition, they are not applicable to the data obtained from other experiments under different conditions and generally they are not applicable to field settings. Pore network modeling based on the basic physics of the process can provide insight into the NAPL dissolution mechanisms and assist in overcoming these limitations [Dillard et al., 2001].

2.2.2 Wetting-NAPL dissolution in column experiments

Most of NAPL dissolution investigations have been conducted in water-wet porous media. However, fractional wettability, that is the condition for which water-wet and NAPL-wet solid surfaces are present in a porous medium, is recognized as a

ubiquitous condition in real soil formations [Brown et al., 1956; Salathiel, 1973]. There are much fewer experiments reported in the literature for NAPL-wet systems than for water-west systems. Parker et al. [1991] studied multi-component NAPL dissolution in NAPL-wet porous media. In their experiments, sand grains in a column were coated with NAPL before the column was saturated with water, making the sand NAPL-wet. Water was flushed through the column at constant Darcy velocity and concentration data versus time were obtained. Bradford et al. [1999] reported on the dissolution behavior of tetrachloroethylene (PCE) in porous media with fractional wettability. The experimental porous media consisted of various sieve sizes of Ottawa sands, some of which were treated with a 3-5% solution (by volume) of octadecyltrichlorosilane (OTS) in ethanol to render them hydrophobic. Fractional wettability media were obtained by mixing various mass fractions of untreated and OTS-treated Ottawa sands. Dissolution experiments were conducted after PCE entrapment in the column. Effluent data from a representative PCE dissolution experiment with 100% fraction of NAPL-wet sands are plotted in Figure 2.13. A series of effluent curves obtained from the experiments with different fractions of NAPL-wet sands are shown in Figure 2.14. Their research revealed that an increase in the NAPL-wet soil fraction tends to result in a longer period of high effluent concentrations, followed by a rapid reduction of concentration until a low concentration level is attained (tailing). A concentration rebound was also observed in the tailing region after a long-term interruption of water flow (Figure 2.13). Effluent concentration was at a high value when the water flow resumed and decreased rapidly to the level reached before the interruption began. The concentration rebound was used as evidence of the presence of limited amounts of separate phase NAPL ganglia or less accessible NAPL films in the

medium. The concentration curves were interpreted by assuming that residual NAPL is entrapped both as films covering NAPL-wet solids and as ganglia near water-wet solids. The distribution of NAPL depends on the extent of fractional wettability and the pore structure of the medium. Because the ratio of NAPL-water interfacial area to the medium volume is much higher when NAPL is present as films than as ganglia, a larger interfacial area is obtained as the fraction of NAPL-wet sands is increased. The existence of the NAPL films is responsible for the longer period of high effluent concentrations in systems with a higher fraction of NAPL-wet sand. The ganglia in contact with NAPL films provide a supply of NAPL to the films, which promotes the dissolution of the ganglia and facilitates the maintenance of high interfacial area and high effluent concentration. As dissolution proceeds, the NAPL films are dissolved, the interfacial area decreases dramatically, and so does the effluent concentration. The low concentration tailing behavior observed was attributed to three possible effects: (1) desorption of NAPL from the sands, (2) presence of persistent NAPL ganglia that dissolve much slower by comparison to the NAPL films and/or (3) NAPL films not easily accessible to flowing water [Bradford, 1999]. The explanation of the tailing behavior is still controversial, even in water-wet media. Miller et al. [1998] suggested that the tailing could be due to dissolution fingering. Imhoff et al. [1998] reported that rate-limited desorption of NAPL may account for the concentration tailing. A continuum numerical model of porous media with fractional wettability was developed by Bradford et al. [2000] to explain the tailing phenomenon from the desorption point of view.

36
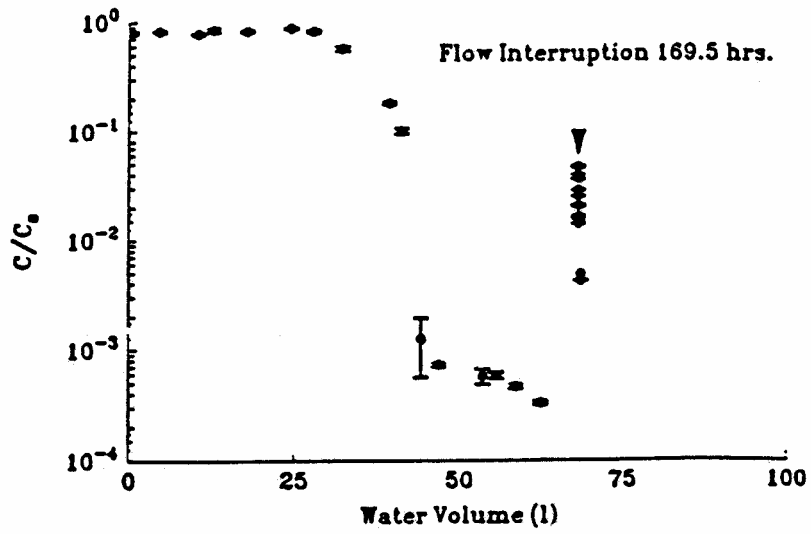
Figure 2.13 Effluent concentration curve for 100% NAPL-wet system [from Bradford et al., 1999].
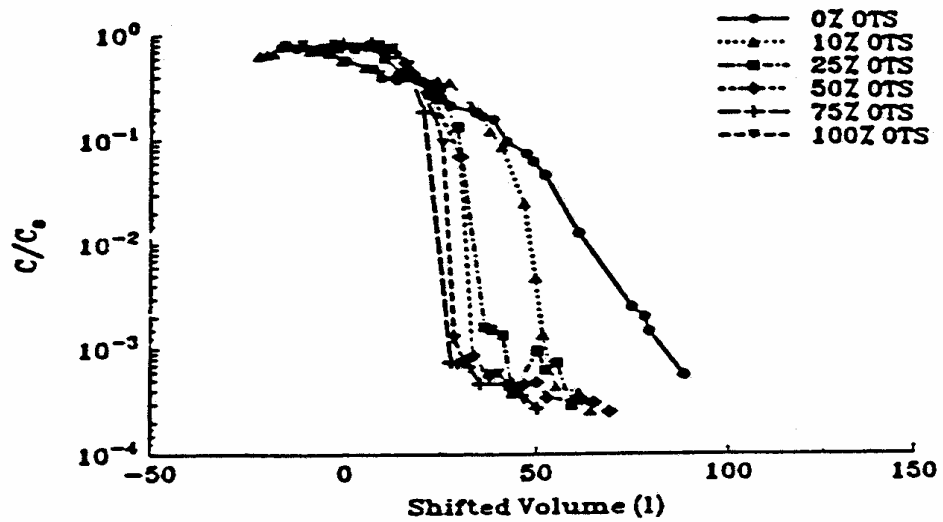
Figure 2.14 Effluent concentration curves for different fractions of NAPL-wet sands [from Bradford et al., 1999].

2.2.3 Observations in micro-model experiments

Sahloul et al. [2002] studied NAPL dissolution behavior in transparent glass micro-model experiments. Since a thorough understanding of NAPL dissolution behavior at the pore level is crucial to prediction of NAPL dissolution rate and network modeling, it is worth to examine their observations in more detail.

Figure 2.15 shows the pore network patterns used to make 2-D transparent glass micro-models with different wettability. In the water-wet model (Figure 2.15a), NAPL doublet ganglia are entrapped and water is injected with very low flow rate through the flow bypass channels open to the pore doublet containing entrapped NAPL. Due to the difference in water pressure along the pore doublet, water can flow along the corners of irregular pore walls and around the trapped NAPL ganglia and mass transfer by convection and diffusion takes place in the space between the NAPL-water interface and the pore wall. The evolution of the size and shape of the dissolving NAPL ganglia was visualized over time with image analysis techniques. Figure 2.16 is a set of pictures showing the dissolution history of non-wetting NAPL ganglia in the model. It is observed that, as the ganglia shrink in size, a progressively thicker collar of the water phase forms in the pore throat and a snap-off event occurs in the pore throat. The newly formed NAPL-water interfaces spontaneously retreat towards the pore bodies forming two singlet ganglia. The singlet ganglia dissolve sequentially and not simultaneously: the ganglion upstream will dissolve first because the driving force for dissolution $(C_s - C_{water})$ is greater upstream.

In a NAPL-wet model (Figure 2.15b), NAPL coats the solid walls in the form of films along the corners of the water flowing channel and entrapped NAPL completely

occupies the pore doublet. The NAPL films present in the inner and outer corners of the water bypassing channels are gradually dissolved. As dissolution proceeds, the outer film, which in the micro-model is actually disconnected from the rest of NAPL, dissolves completely. However, the inner NAPL film dissolves to a certain thickness only. Driven by capillary pressure gradients, continuous supply of NAPL from the trapped ganglia to the dissolving films by film flow along pore corners makes the dissolving film thickness remain constant. At this stage, water displaces NAPL and gradually invades the throat followed by a sequence of snap-off events that increase the interfacial area for mass transfer until the throat and the adjacent pore are completely drained. The sequence of phenomena is shown in Figure 2.17. This phenomenon takes place again when water penetrates the other throat and pore until an additional open channel for water flow becomes available [Sahloul et al, 2002]. The pore network modeling of NAPL dissolution in this work is based on the dissolution mechanism of wetting NAPL briefly reviewed above and will be discussed in detail in Chapter 3.

(a)   (b)
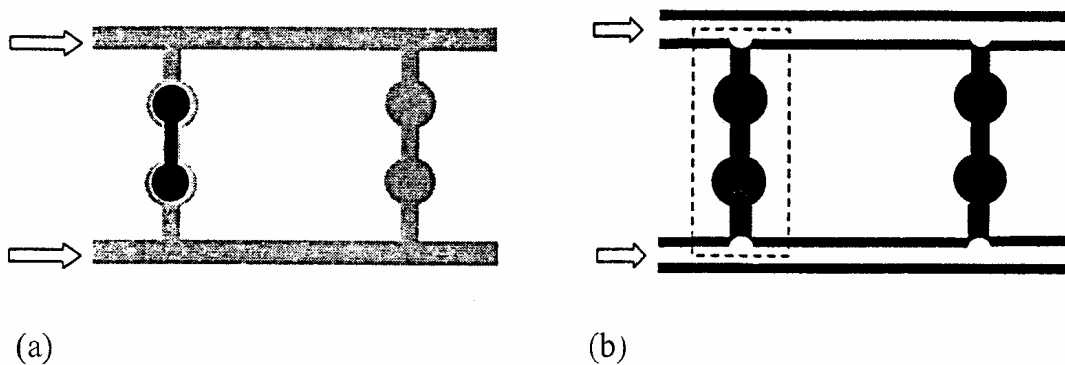
Figure 2.15 Schematic description of the glass models (a) water-wet (b) NAPL-wet Residual NAPL shown in black [Sahloul et al. 2002].
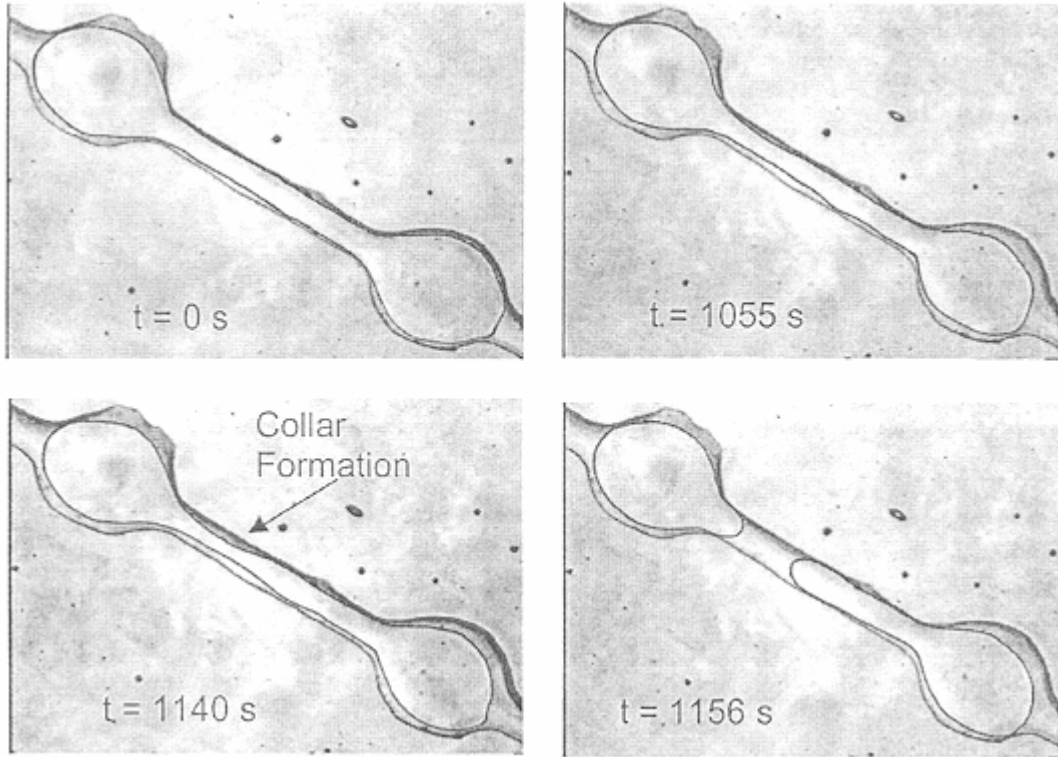
Figure 2.16 Non-wetting NAPL dissolution in micro-model [Sahloul et al. 2002].
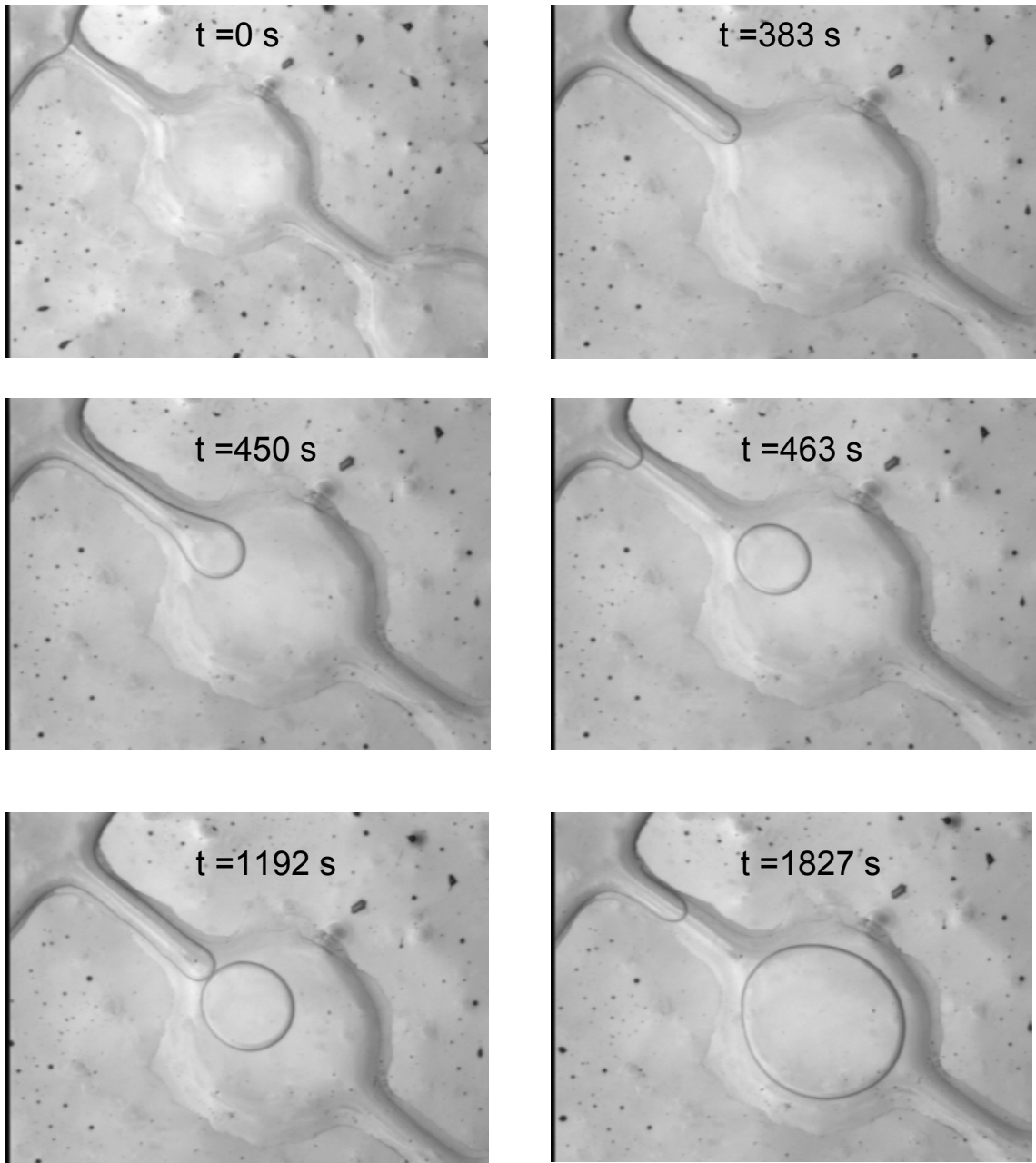
Figure 2.17 Wetting NAPL dissolution in micro-model [Sahloul et al. 2002].

2.3   Remediation of subsurface NAPL sources

Remediation of NAPL contaminated sites involves control of the dissolved NAPL plume in groundwater and removal of the NAPL sources. This research will focus on the latter issue. Technologies for NAPL source-zone remediation are of two types, mass-removal technologies that bring NAPL to the surface for disposal and treatment (e.g., pump-and-treat, steam flushing, air sparging, surfactant flushing, co-solvent flushing) and mass-destruction technologies that destroy NAPL *in situ* (e.g., chemical oxidation, chemical reductive dehalogenation, biodegradation) [Cherry et al., 1996].

Pump-and-treat is the most commonly used method, and is a dissolution treatment whereby large amounts of water are flushed through the contaminated area and water with dissolved NAPL is collected downstream and treated at the surface. This technology has been in practice since the 1980s, but proven ineffective. Decades are required to achieve total source zone restoration. The failure of pump-and-treat promoted the development of new *in situ* technologies. Steam injection combined with soil vacuum extraction (SVE) is used to vaporize and remove NAPL. Chemicals such as surfactants and co-solvents are added to the flushing water to increase the effective solubility of NAPL. Although these methods are much more effective in NAPL removal than the conventional pump-and-treat technology, there are still many technical difficulties. Heterogeneities of permeability and NAPL distribution in the soil often impede the contact of the flushing fluids with NAPL, which is critical in the restoration of the source zone using these technologies. New contaminations may be caused by downward

mobilization of NAPL with decreased interfacial tension or by the injected chemicals themselves [Cherry et al., 1996].

Another method for restoring NAPL sources is air sparging. Air or other gases are injected below or within the source zone of volatile contaminants, which are volatilized into the air phase and transported upward to the vadose zone, where they are collected in vacuum extraction wells. Air sparging also benefits the bioremediation process by introducing oxygen to the source zone. Laboratory and site investigations show that air migrates upward in air channels or stream tubes instead of rising bubbles and forms parabolic or V-shaped air plumes that are centered around the injection well during the process [e.g., Ji, et al., 1993; Lundegard and LaBrecque, 1995; Elder and Benson, 1999]. Contaminated soil inside the channels would be aerated. However, regions outside the air channels are much less affected by the air flow [Hinchee, 1994]. Since the air phase tends to migrate through preferential pathways (high permeability portions of the medium), it bypasses the NAPL in zones of lower permeability (see Figure 1.2), which tremendously reduces the effectiveness of the technology.

Research on a novel technology of NAPL remediation, based on introducing supersaturated carbonated water (SWI) to the source zone, is on-going at the University of Waterloo. To overcome the problems of residual NAPL inaccessibility during air sparging, water highly supersaturated with carbon dioxide is injected beneath the NAPL sources. A patented technology, Gas inFusion^{TM}, which has the ability to efficiently dissolve large amounts of gas into water makes SWI possible. A conceptual design of the SWI technology for NAPL remediation is shown in Figure 2.18 [Li, 2004].

Column experiments using SWI [Li, 2004] show that NAPL ganglia can be recovered by volatilization and mobilization. 2D experiments (Figure 2.19) conducted by Li [2004] also reveal that SWI is a significant improvement on direct gas injection in a porous medium. Gas channelling phenomena observed in air sparging process [e.g. Ji et al., 1993; Tomlinson et al., 2003] can be avoided and dissolved gas can be delivered to zones of low permeability. Bubbles are nucleated and subsequently grow to make direct contact with NAPL ganglia, making recovery of NAPL, especially volatile ones, much more effective than air sparging.
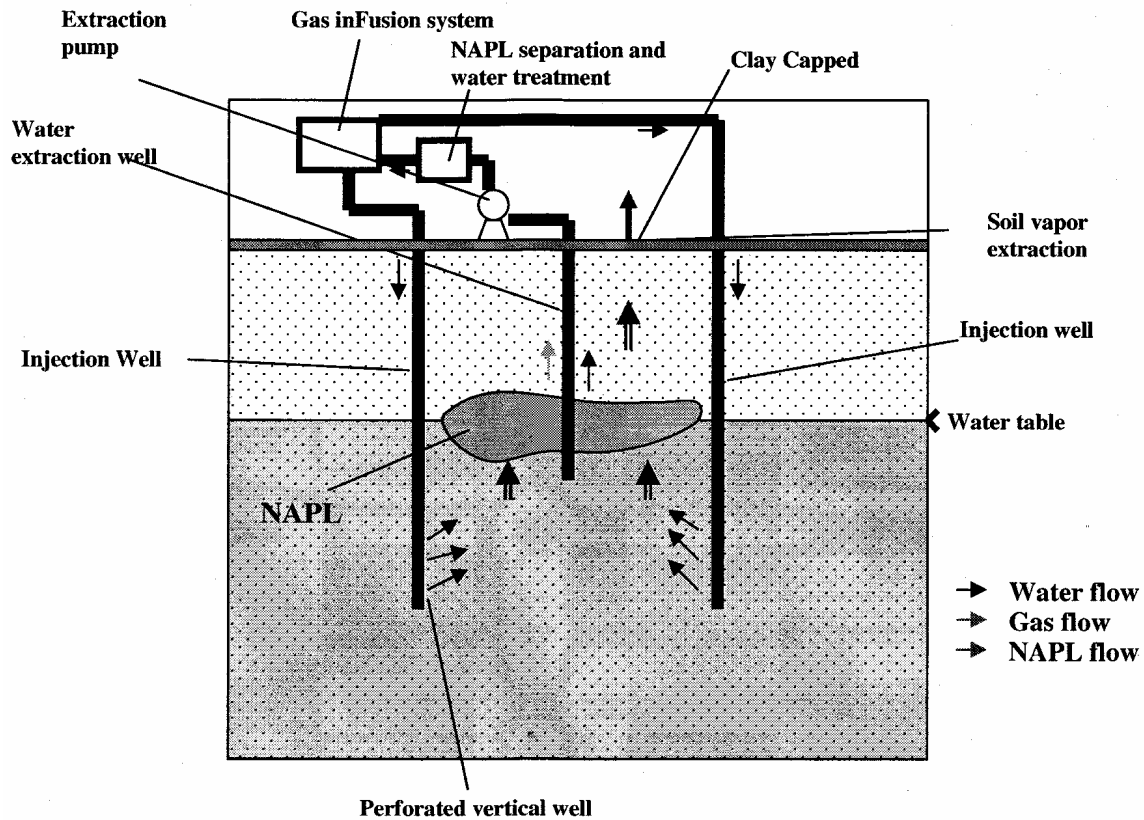
Figure 2.18 Conceptual design of supersaturated water injection (SWI) for NAP remediation [Li, 2004].
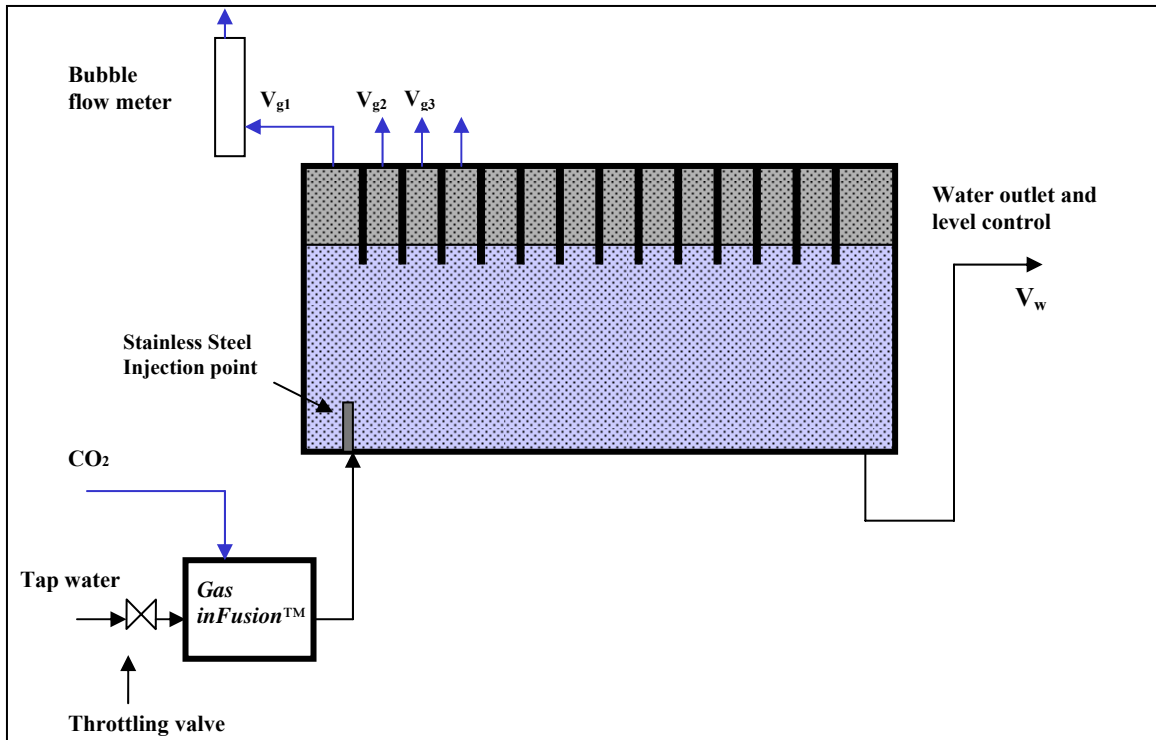
Figure 2.19 Flow diagram of the gas evolution experiment by Li [2004].

In summary, the following advantages of this method are apparent and make the SWI technology promising:

1. High degree of supersaturation of the injected water allows *in-situ* gas bubble nucleation in the porous medium, even in zones with low permeability, where capillary forces prevent direct NAPL-gas contact during air sparging.

2. The gas distribution in the medium is more homogeneous by comparison to air sparging, during which gas flows in high permeability channels.

3. Higher gas saturation can be obtained when surpersaturated water is injected to restore the DNAPL contaminated zone under the water table.

4. A larger zone of influence might be obtained. Preliminary experiments show that bubbles appear far away from the water injection point.

5. Upon contact with bubbles, NAPL (with positive spreading coefficient) will spontaneously spread around the bubbles and be vaporized into the gas phase if the NAPL is volatile. Multiple bubbles in NAPL phase lead to large interfacial area and thus effective mass transfer.

6. Lower interfacial tension between NAPL and gas (compared with the water-gas IFT) makes gas flow easier in the pore network due to smaller capillary resistance.

7. NAPL in the form of spreading films could be mobilized by the growth and upward migration of bubbles due to solution gas drive and buoyancy.

8. In the bioremediation processes where oxygen presence is critical for biodegradation [e.g., Wilson et al., 1994a; Borden et al., 1997a; Deeb et al., 2000], O_2 could be introduced to the source zone more effectively when water with supersaturated O_2 is injected.

9. Other options of treatments could be available such as combining soil vacuum extraction and follow-up air injection to mobilize the bubbles trapped in the media.

To design the NAPL remediation strategy using SWI, theoretical studies on behaviours of bubble growth and mass transfer during gas evolution in porous media are required. Mass transfer of gas evolution by solute diffusion and mechanisms of bubble nucleation, expansion, coalescence and fragmentation will be discussed in Chapter 5.

2.4   Pore network modeling

2.4.1   General

Network models are used to investigate the macroscopic properties of porous media on the basis of pore-scale descriptions of the pore structure and multiphase flow phenomena. Due to the geological complexity and topological randomness of the pore space, it is practically impossible to reproduce the structure of real porous media in an exact manner. Simple geometry is often applied to idealize the pore space and a lattice with sites (pore bodies) and bonds (throats) is constructed to represent the topology of the medium [Dullien, 1992]. Figure 2.20 shows some examples of lattices of pore space with circles representing sites and lines denoting bonds, where z is the coordination number describing the number of neighboring pores that each pore connected to.

Using pore network models can be traced to the pioneering work of Fatt [1956]. Pore network models overcome the limitations of early conceptualizations of pore space that involved bundles of parallel capillary tubes of varying radii (Figure 2.21a). Early pore network models were based on the assumption that the pore intersections do not have volume of their own [Berkowitz and Ewing, 1998]. However, since pore bodies contribute to the majority of the pore volume, most researchers nowadays use models that have pore bodies with size and volume [e.g., Chatzis and Dullien, 1985; Ferrand and Celia, 1990a; Bryant et al., 1993b; Ioannidis and Chatzis, 1993; Jia and Yortsos, 1999; Dillard and Blunt, 2000;]. It is noted that there exist no dead-end capillaries in these networks. Experiments have indicated that the volume fraction of blind pores is quite small (about 1%) in sandstone or sintered glass beads [Mysels and Stigter, 1953].

47
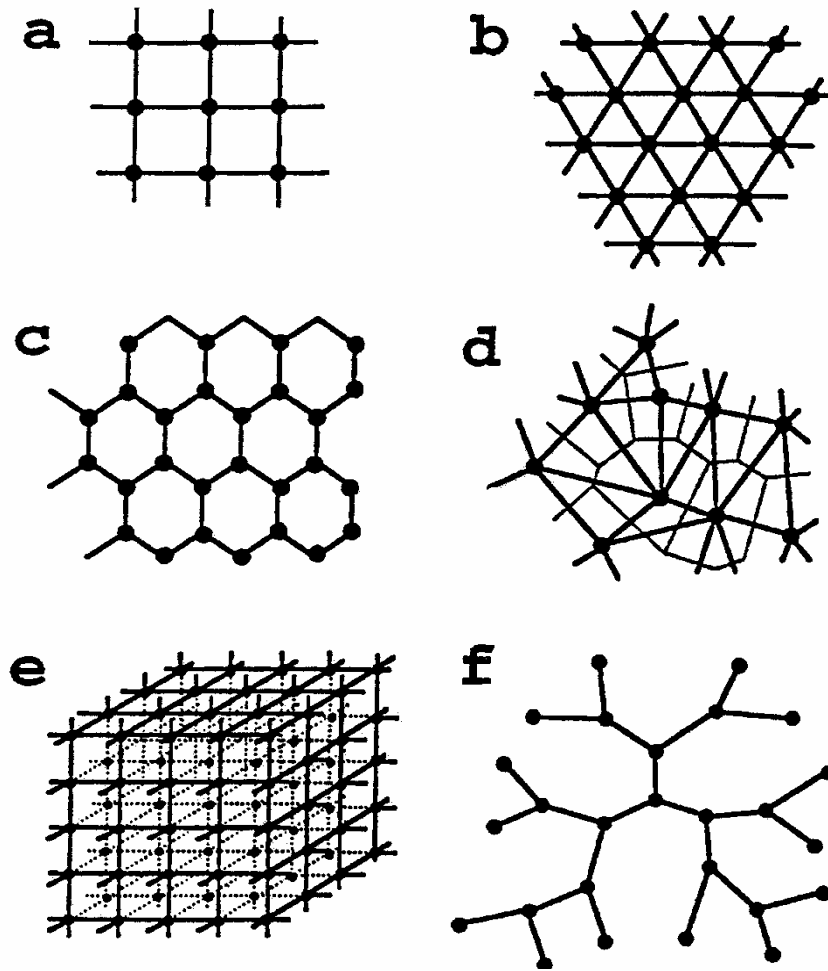
Figure 2.20 Typical lattices used in network modeling [from Berkowitz and Ewing, 1998]

(a) square $z = 4$ (b) triangle $z = 6$ (c) honey comb $z = 3$ (d) voronoi $\bar{z} = 6$ (e) cubic $z = 6$

(f) Cayley tree $z = 3$.
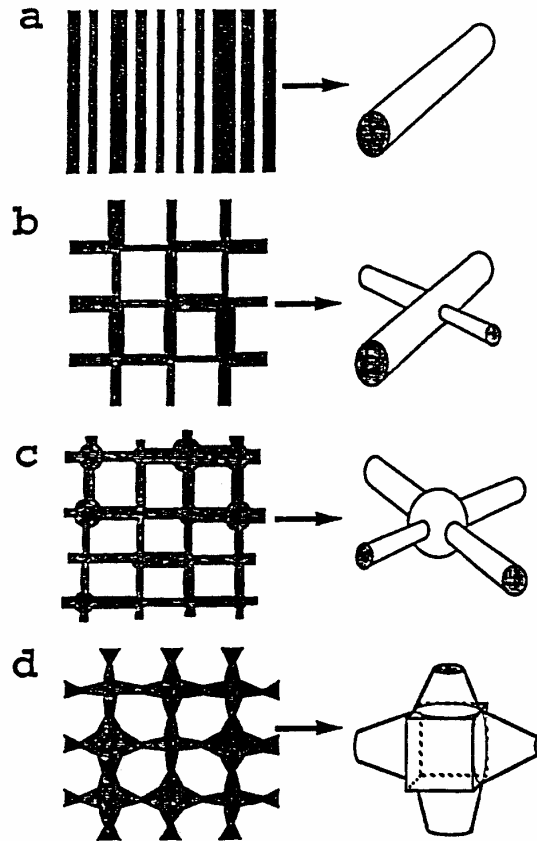
Figure 2.21 Evolution of pore space models [from Berkowitz and Ewing, 1998]

(a) parallel tubes (b) tube network (c) ball-and-stick (d) biconical.

Chatzis and Dullien [1977] first studied the differences between 2D and 3D networks and pointed out that since two continuous phases cannot exist in two-dimensional networks, 3D networks and not 2D ones must be used to model immiscible displacement. They also demonstrated that the minimum size of a network, 40 by 40 for 2D and 20 by 20 by 20 for 3D, is necessary to approximate an infinite lattice [Chatzis and Dullien, 1977]. Nowadays, much modeling work is still done on 2D lattices with actually 3D network elements (pore bodies and throats), allowing for the existence of bicontinua (e.g., continuous NAPL phase and water phase) in the models. For our purposes, network

dimensionality is not crucial since water and NAPL can co-exist within angular pores.

In many cases, independent distributions of pore and throat sizes are assumed, e.g. normal, lognormal, Weibull etc. However, studies of the pore structure indicate that a correlation exists between the size of a pore body and the adjacent throat size. The radius of a throat must be smaller than the smaller of the two adjacent pores [Wardlaw et al., 1987]. Normally, the throat size is a function of the pore size given a certain aspect ratio and most of the resistance to fluid flow is in the narrow bonds [Koplik, 1982].

Network modeling has developed enormously as percolation theory was used to describe multiphase flow properties in porous media. Percolation theory is a branch of probability theory dealing with properties of random media [Sahimi, 1993; Berkowitz and Ewing, 1998]. The application of percolation theory to this work involves the breakthrough phenomenon for quasi-static drainage displacement. Figure 2.22 shows a network at the point of breakthrough [Chatzis and Dullien, 1977]. Nodes of different size are distributed randomly over the network and whenever a bond is "open" both the neighboring nodes connected with the bond are also assumed to be "open". The bonds in the network are labeled with consecutive numbers representing the pore sizes. Stepwise penetration of the non-wetting phase into the network takes place through the inlet face. The largest pore (index $= 1$) accessible from the inlet face is penetrated first. The second largest pore is open at the next step, and so forth. When at a particular step the non-wetting phase reaches the outlet face of the network, a cluster of bonds and sites filled with non-wetting phase spans the entire network and the condition is termed "breakthrough" [Dullien, 1992].
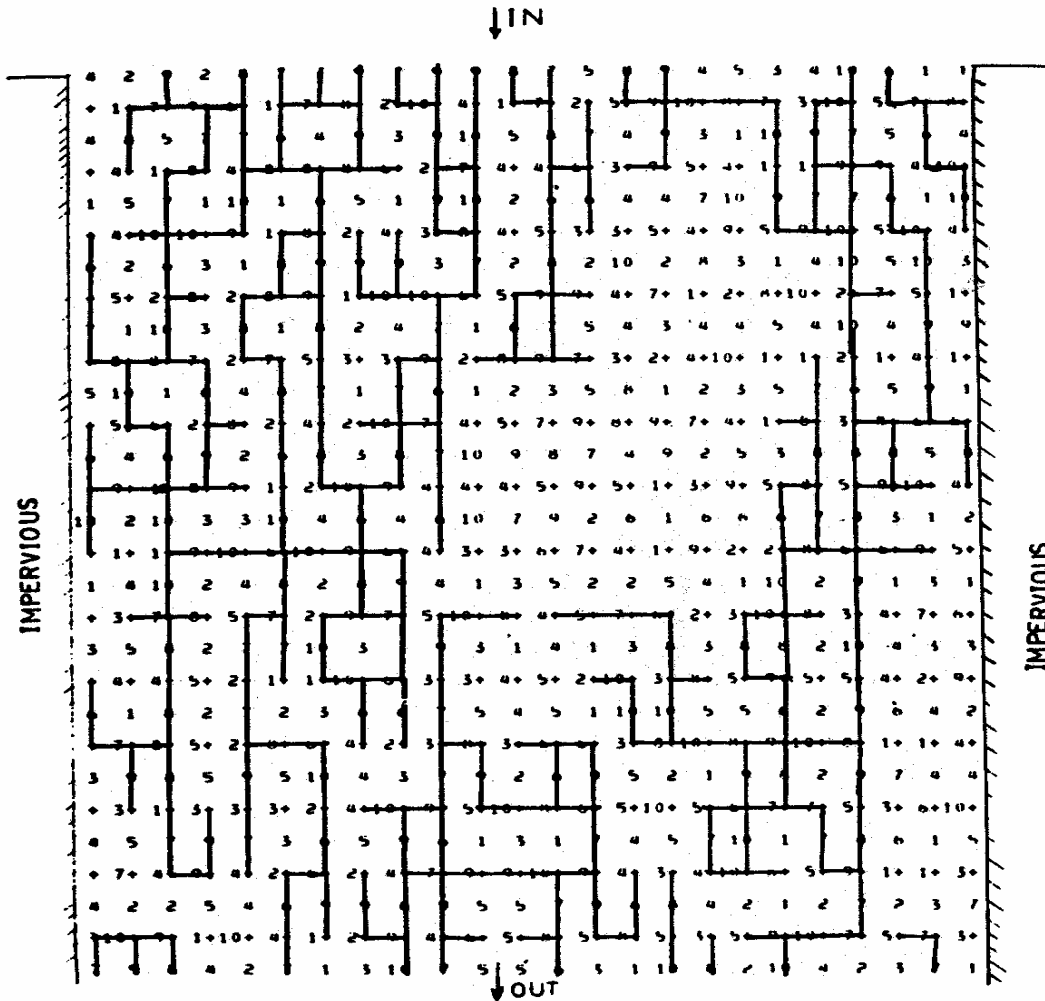
Figure 2.22 Square lattice at breakthrough [Chatzis and Dullien, 1977].

In principle, local capillary equilibrium is assumed during pore-scale simulations and the configurations of fluids in pores of different shape are determined by Young-Laplace equation. The flow of each phase is determined by the hydraulic conductance of each phase in each pore and throat and the pressure difference between the neighbouring pores. Mass conservation equations are used to compute the pressure field throughout the

51

network when all of the interfaces are assumed to be locked in place for a certain simulation step. From the calculated fluid flow field, macroscopic properties such as absolute and relative permeability can be obtained. This approach is valid when displacement takes place at sufficiently low values of the capillary number (so-called quasi-static displacement).

Although pore network models based on regular lattices are extensively used to represent pore spaces, recently developed pore-scale modelling techniques focus on deriving geologically realistic networks. In order to capture properties of a porous medium (in terms of topology, pore size distribution, spatial correlation of the pore space, etc.), pore network models are constructed from 3D voxel-based images that may be generated by X-ray microtomography [e.g., Biswal et al. 1999; Oren and Bakke, 2002] or by 3D reconstruction (stochastic or process-based) informed by 2D thin sections [e.g., Quiblier, 1984; Adler and Thovert, 1998; Liang et al., 2000; Oren and Bakke, 2003]. Such models are often used to predict multiphase flow and transport properties in porous media. In the current study, pore network models with simple geometric elements (cubic pores and square throats) on regular lattices are used for the purpose of qualitatively investigating mass transfer in porous media and providing new insights into the simulated processes by incorporating the basic physics behind the phenomena of interest.

2.4.2 Pore network modeling of NAPL dissolution

Pore network modeling proved effective in investigations of the properties of fluid flow in porous media and thus is a powerful tool of the investigation of NAPL dissolution. Numerical pore networks have been developed recently to study several aspects of the dissolution problem. Jia and Yortsos [1999] studied mass transfer in flow with varying Peclet number over various macroscopic- and microscopic-scale source geometries. They adjusted the local mass transfer rate to explain the dissolution at the interface and conducted network model simulations to test their theoretical analysis and compare the results to etched glass micro-model experiments. Zhou et al. [2000] used a conceptual model, which was constructed with bundles of parallel tubes, to predict NAPL dissolution rate. A mechanism of corner flow of water between the NAPL-water interface and pore walls was proposed. Three different diffusion mechanisms of non-wetting NAPL were taken into account and each of them was shown to control dissolution in a different range of Peclet numbers. They also studied a NAPL-wet system and argued that wetting NAPL dissolution is governed exclusively by corner diffusion, a mechanism whereby wetting NAPL phase in the corners of the pores diffuses into the water phase in the center of the pores. Based on the model of Zhou et al. [2000], Dillard and Blunt [2000] developed a network model to investigate the fundamental physics of non-equilibrium NAPL dissolution in water-wet systems. Relative permeability curves were obtained and the observed hydraulic conductivity was reproduced. The results of NAPL volume effluent concentration and modified Sherwood number versus Peclet number were compared with the data obtained from the experiments conducted by Powers et al. [1992] for water-wet system. Dillard et al. [2001] estimated dissolution rate coefficient and

NAPL-water specific interfacial area in subsequent work and attempted to develop a methodology for incorporating pore-scale processes into field-scale prediction of NAPL dissolution. Held and Celia [2001] developed a 3D pore network model to predict the evolution of interfacial front in column experiments of porous media initially at residual non-aqueous phase saturation. Comparisons were made between their results and the experimental data of Mayer and Miller [1992] and Imhoff et al. [1994] for water-wet systems.

It should be noted that all of the aforementioned network models were developed to simulate NAPL dissolution for water-wet systems. Effects of soil wettability on NAPL dissolution have been investigated by some researchers using various methods, namely column experiments [Parker et al., 1991; Mayer and Miller, 1992; Imhoff et al., 1994; Bradford et al., 1999], micro-model experiments [Sahloul et al., 2002] and conceptual or continuum models [Zhou et al., 2000; Bradford et al., 2000]. A 2D network model was developed by Yiotis et al. [2001] to investigate drying of porous solids, a process involving vaporization of a wetting phase (e.g. water, hexane, etc) to the gas phase in porous materials. This is a drainage process and is similar to wetting-NAPL dissolution. However, their model does not take into consideration the effects of wetting films, and is essentially different from the mechanism underpinning the model developed in this work.

The experiments of Sahloul et al. [2002] have demonstrated the qualitative features of residual NAPL dissolution in NAPL-wet systems. The pore-scale mechanisms were shown to involve "capillary pumping" of NAPL from NAPL-filled pores to dissolving thick NAPL films residing in the corners of water-invaded pores. Capillary pumping is driven by and tends to balance capillary pressure increases in areas of active

54

dissolution, where NAPL-water menisci recede further into the crevices and corners of pore walls. This mechanism results in piston-type drainage of NAPL-filled pores by water, creating new paths for water flow. Based on this mechanism, Zhao and Ioannidis [2003] developed a pore network model to simulate wetting NAPL dissolution. Figure 2.23 is the simulation result of NAPL effluent concentration as a function of volume of water injected. The tailing behaviour of the effluent NAPL concentration, as observed in column experiments, is attributed to the rupture and concomitant loss of hydraulic continuity of thick NAPL films [Zhao and Ioannidis, 2003]. The simulations indicated that the distribution and stability of NAPL films critically affect the dissolution behaviour of wetting NAPL and deserve further investigation.
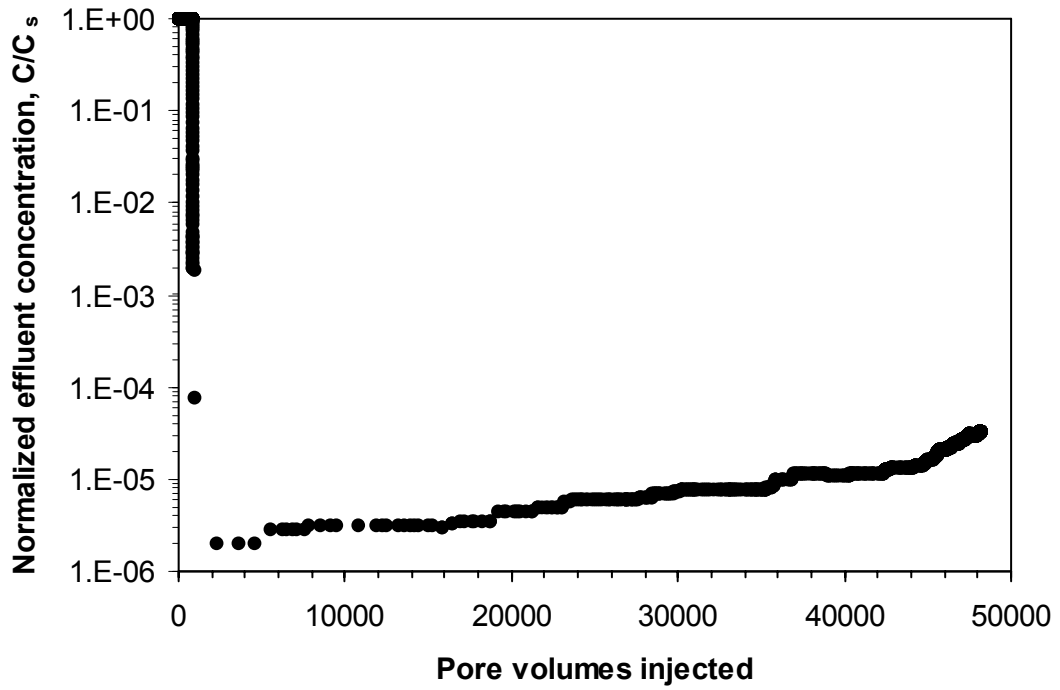
Figure 2.23 Normalized effluent solute concentration as a function of pore volume of water injected. Low-concentration tailing is due to significant bypassing of the contaminated zone by the flowing aqueous phase, after NAPL film disconnection [Zhao and Ioannidis, 2003].

2.4.3 Pore network modeling of multiphase flow and mass transfer

The approach used in two phase flow modeling has been extended to three-phase (oil/NAPL, water, gas) flow by many researchers [e.g. Mani and Mohanty, 1998, Hui and Blunt, 2000, van Dijk et al., 2001; a recent bibliography can be found in Blunt, 2001]. The purpose of these models is to predict phase displacement events and macroscopic properties of three phase flow in porous media by incorporating physically-based pore-scale mechanisms.

To model three phase flow in porous media, a common method is to construct three-phase relative permeabilities from two-phase data using empirical models that have little or no physical basis [Blunt, 2001]. Many efforts are made to predict three-phase relative permeability using pore network models [e.g., Fenwick and Blunt, 1998 a b, Blunt et al., 2002, Held and Celia, 2001 a]. Three-phase permeabilities in porous media are significantly influenced by the configurations of fluids, which strongly depend on the wettability of the media [Blunt, 2001]. Using a three phase network model, Mani and Mohanty [1998] showed that gas and oil relative permeabilities are functions of spreading coefficient. Kovscek et al. [1993] investigated the fluid configuration in a star-shaped pore and stated that the solid surfaces in a single pore can have different wettability. Experiments and free energy calculations conducted by Dong and Chatzis [1995] and Dong et al. [1995] showed that NAPL layers may form between water and gas when NAPL imbibes into pore crevices. Hui and Blunt [2000] studied three-phase configurations in triangular tubes and suggested that different configurations of NAPL layers between water and gas may arise in water-wet or mixed-wet pores with different distributions of contact angles. These spreading layers provide the connectivity of NAPL

phase for NAPL flow and the large interfacial area for mass transfer.

A number of network models have been developed to model gas evolution in porous media due to solute diffusion [Li and Yortsos, 1995 a, b, Hawes et al., 1996, Carmeliet, et al., 1999, Du and Yortsos, 1999, McDougall and Sorbie, 1999, Dominguez et al., 2000, Pérez-Aguilar et al., 2002, Tsimpanogiannis and Yortsos, 2002, 2004]. These models involve simulations of nucleation and subsequent growth of bubbles in porous media. Attention is given to the effects of depressurization rate, capillarity, wettability, viscosity and gravity on the rate and pattern of bubble nucleation and gas cluster growth, bubble mobilization and critical gas saturation.

Chapter 3

Effect of NAPL film stability on the dissolution of residual wetting NAPL in porous media

3.1   Summary

Wettability profoundly affects not only the initial distribution of residual NAPL contaminants in natural soils, but also their subsequent dissolution into a flowing aqueous phase. Under conditions of preferential NAPL wettability, the residual NAPL phase is found within the smaller pores and in the form of continuous thick films along the corners and crevices of the pore walls. Such films expose a much greater interfacial area for mass transfer than would be exposed by the same amount of non-wetting NAPL. Importantly, capillary and hydraulic continuity of thick NAPL films is essential for sustaining NAPL-water counterflow during the course of NAPL dissolution in flowing groundwater - a mechanism which maintains and even increases the interfacial area for mass transfer. Continued dissolution results in gradual thinning of the NAPL films, which may become unstable and rupture causing disconnection of the residual NAPL in the form of clusters. A pore network simulator is developed to demonstrate that NAPL film instability drastically modifies the microscopic configuration of residual NAPL, and

hence the local hydrodynamic conditions and interfacial area for mass transfer, with concomitant effects on macroscopically observable quantities, such as the aqueous effluent concentration and the fractional NAPL recovery with time. These results strongly suggest that the disjoining pressure of NAPL films may exert an important, and hitherto unaccounted, control on the dissolution behaviour of a residual NAPL phase in oil wet systems.

3.2 Background

The potential of environmentally significant non-aqueous phase liquids (NAPL), such as chlorinated degreasing or dry-cleaning solvents, creosote and weathered fuel hydrocarbons, to change the wettability of natural mineral surfaces upon introduction into the subsurface has been recently recognized. For example, coal tar and creosote can wet quartz media at acidic or neutral pH conditions [Powers et al., 1996; Barranco and Dawson, 1999; Zheng and Powers, 1999; Zheng et al., 2001; Zheng et al., 2001]. Changes of wettability in NAPL-water-solid systems might occur in the presence of organic additives and greases [Jackson and Dwarakanath, 1999]. Contaminant aging has also been found to have an impact on wettability alteration [Powers and Tamblin, 1995; Harrold et al., 2001].

Wettability plays a key role in multiphase flow, affecting the efficiency of immiscible displacement [Dwarakanath et al., 2002] by dictating the pore-scale configuration of NAPL and water [Hui and Blunt, 2000]. Following immiscible displacement by water, a NAPL that does not wet the mineral surface is retained by

capillary forces in the form of discrete blobs or ganglia within larger pores of high aspect ratio, whereas a wetting NAPL is trapped within smaller pores and in the form of thick films along the corners and crevices of the pore walls. For the same volumetric NAPL content, both the interfacial area available for mass transfer and the hydrodynamic conditions for water flow at the pore scale are markedly different depending on wettability. These differences have a significant effect on the dynamics of residual NAPL dissolution into a flowing aqueous phase - an effect that only recently has come under investigation. For example, column dissolution experiments with porous media containing both water-wet and oil-wet surfaces have revealed that increasing the NAPL-wet fraction results in rather long periods of high (near-equilibrium) effluent concentrations, followed by a rapid rate of concentration reduction and significant concentration tailing at low levels [Bradford et al., 1999]. Such observations are in contrast to the macroscopic behaviour seen in similar water-wet systems [Powers et al., 1994; Imhoff et al., 1994] and reflect the effect of wettability on the initial NAPL distribution and subsequent dissolution behaviour at the pore scale.

The wetting of mineral surfaces by water or oil is controlled by surface forces (electrostatic, van der Waals and structural) that become important when two interfaces (fluid-fluid and fluid-solid) approach each other [Hirasaki, 1991; Drummond and Israelachvili, 2002]. At equilibrium, the pressure difference across the fluid-fluid interface (the capillary pressure), P_c, is given by the augmented Young-Laplace equation:

$$P_c = 2\sigma H + \Pi(h) \qquad (3.1)$$

where σ is the interfacial tension, H is the mean curvature of the fluid-fluid interface and

$\Pi(h)$ is the disjoining pressure, which depends on the distance h between the fluid-fluid and fluid-solid interfaces and measures the net surface force tending to attract or repel them. A thick wetting water film between the NAPL and the mineral surface must become unstable and collapse to a thin layer of hydration water of thickness δ before NAPL can adhere to the solid, usually by means of adsorption of NAPL-soluble, high-molecular-weight polar compounds with surface active characteristics [Buckley et al., 1989; Kovscek et al., 1993; Barranco and Dawson, 1999; Zheng and Powers, 1999]. It is generally accepted that wetting water film instability and collapse occurs at a critical film thickness h_w^{crit}, corresponding to a local maximum Π^{max} in the disjoining pressure isotherm (Figure 3.1) [Hirasaki, 1991; Kovscek et al., 1993]. The corresponding critical capillary pressure is thus given by:

$$P_c^{crit} = 2\sigma H^{crit} + \Pi^{max} \qquad (3.2)$$
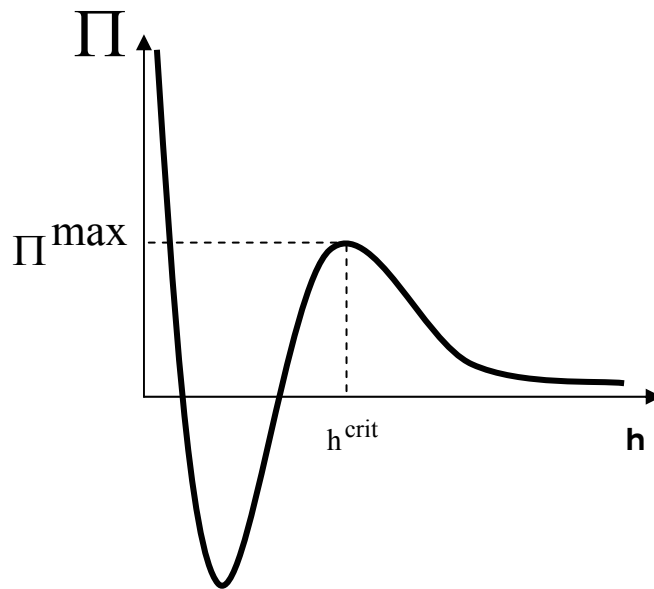
Figure 3.1 Schematic of disjoining pressure isotherm for wetting films on solids.

Following immiscible displacement of the NAPL by water, mineral surfaces of altered wettability retain thick NAPL films within water-invaded pores. The stability of these NAPL films is expected to depend on the thickness δ of the hydration water layer covering the solid surface [Hirasaki, 1991]. Specifically, for an NAPL film over hydration water on a silica substrate, it is theoretically predicted that the disjoining pressure is repulsive if $\delta = 0$ (no hydration water) and, consequently, the NAPL film is stable for any value of its thickness h_{NAPL}. On the other hand, if $\delta >> h_{NAPL}$, the disjoining pressure is attractive and the NAPL film is unstable for any value of its thickness h_{NAPL}. At intermediate values of δ, the disjoining pressure exhibits a maximum Π^{max} at a critical NAPL-film thickness h_{NAPL}^{crit} [Hirasaki, 1991; Kovscek et al., 1993] and a NAPL film is expected to become unstable at a critical capillary pressure which is given by Equation (3.2).

To the best of the author's knowledge, no direct measurements of the disjoining pressure of NAPL films in environmentally significant systems are available in the literature. Yet, reversal of wettability from oil-wet to water-wet conditions has been documented, mainly in relation to oil recovery from oil-wet reservoir rocks by imbibition of aqueous surfactant solutions [Austad et al., 1998; Standnes and Austad, 2000; 2003a; 2003b]. It has also been shown that quartz sand surfaces, which at low pH become oil-wet after being exposure to coal tar [Powers et al., 1996; Barranco and Dawson, 1999; Zheng and Powers, 1999; Zheng et al., 2001], may become water-wet again in the presence of surfactants at concentrations below the critical micelle concentration [Dong

et al., 2004]. These findings suggest that NAPL films over hydration water can be destabilized, as expected from theoretical considerations [Hirasaki, 1991].

This research seeks not to examine the physicochemical parameters and mechanisms (surfactant-related or not) governing the stability of NAPL films, but instead to demonstrate that conditional stability of NAPL films can profoundly affect the dissolution of residual wetting NAPL in a flowing aqueous phase. Experiments of NAPL dissolution in oil-wet transparent glass micromodels provide the motivation [Sahloul et al., 2002]. These experiments, which have been carried out under conditions of $\delta = 0$ (unconditionally stable NAPL films), have shown that slow dissolution of residual NAPL residing in the corners of water-invaded pores is accompanied by quasi-static piston-type invasion of water (drainage) in NAPL-filled pores. This mass-transfer-driven drainage was explained as corresponding to NAPL-water counterflow driven by the increase in capillary pressure in areas of active dissolution, where NAPL-water menisci tend to recede farther into the crevices and corners of pore walls. This mechanism creates new paths for water flow and increases the interfacial area for mass transfer.

A pore network simulator that captures the aforementioned mechanism was developed by Zhao and Ioannidis [2003] to study the dissolution of a wetting NAPL. Simulations have suggested that the sharp reduction of effluent concentration from near-equilibrium values and the significant concentration tailing observed in column experiments [Bradford et al., 1999] may be explained by a rapid reduction of the interfacial area for mass transfer that takes place if capillary and hydraulic continuity is lost between NAPL-filled pores and NAPL filaments in water-invaded pores. It was hypothesized that this happens when NAPL films covering the mineral surface become

unstable, but NAPL film stability was not explicitly accounted for in the simulations.

Rupture of initially stable NAPL films over hydration water ($h_{NAPL} \gg \delta$) on silica substrates seems inevitable, because the NAPL film thickness continuously decreases during the dissolution process. NAPL film rupture may therefore be an important factor affecting the dissolution of residual wetting NAPL in porous media. In this research a previously developed pore network simulator [Zhao and Ioannidis, 2003] is extended and used to explore the effects of initial NAPL distribution and NAPL film stability on NAPL phase continuity, evolution of NAPL-water interfacial area, NAPL recovery rate and aqueous phase effluent concentration. NAPL dissolution is considered in oil-wet pore networks after water flooding to NAPL saturations corresponding to water breakthrough or lower. The results obtained provide new insights on the dissolution dynamics of a residual wetting NAPL in porous media.

3.3   Pore network model

3.3.1   Model construction

The void space in real porous media is a network of irregularly shaped pores communicating with each other through constrictions in the pore space continuum (pore throats). The complexity of actual pore space geometry precludes a precise description of the shape of fluid-fluid interfaces and compels us to introduce several assumptions and simplifications, which should nevertheless preserve the essential physics of the process under consideration.

The pore space is modeled as an irregular network of pores, each connected to four nearest neighbors. For computational convenience, each pore is represented by a

cubic chamber (pore body) and parts of four tubes of square cross section (pore throats). The pore body radius, R_p, is randomly distributed over the nodes of a square lattice from a log-normal distribution:

$$y = f(x \mid \mu, \sigma) = \frac{1}{x\sigma\sqrt{2\pi}} \exp\left[-\frac{(\ln x - \mu)^2}{2\sigma^2} \right] \qquad (3.3)$$

where μ is the population mean and σ is the standard deviation. In this work, only pore-throat correlations are accounted for. The tube radius, R_t, and the tube length, L_t, are correlated to the radii of adjoining pores i and j as follows:

$$R_t(i, j) = \frac{1}{2}\min[R_p(i), R_p(j)] \qquad (3.4)$$

$$L_t(i, j) = R_p(i) + R_p(j) \qquad (3.5)$$

The square tubes serve a dual purpose. They model the presence of local constrictions (pore throats) in terms of the variable R_t, and account for the length of wetting fluid filament in the corners and crevices of pores in terms of the variable L_t. The pore network is assumed to have two open and two impermeable boundaries.

Neither the emplacement of NAPL into an initially water-saturated pore network, nor the subsequent development of NAPL-wetness the NAPL-invaded pores is modeled here, although this is certainly possible [Dixit et al., 1999]. Instead, a pore network in which NAPL has displaced water from all pores is used, causing a uniform change in wettability from water-wet to oil-wet. The pore walls are thus assumed to be covered by hydration water of thickness δ (neglected in volumetric calculations). The simulation begins with quasi-static drainage of the NAPL by water. This establishes initial

conditions of residual NAPL saturation corresponding to breakthrough of the aqueous phase (or lower, *e.g.* Runs 7 and 8, Table 3.2), as shown in Figure 3.2(a). Each water invaded pore is assumed to contain NAPL filaments held in the corners of a square tube of radius R_t and length L_t, as shown in Figure 3.2 (b). Subsequently, water begins to flow through the open paths from left to right at constant volumetric flow rate. Organic solute is removed by diffusion and convection as NAPL dissolution takes place at the NAPL-water interfaces. It is important to emphasize that, unless NAPL filaments become disconnected, the NAPL phase is continuous at all NAPL saturations. It should also be clear that connectivity of corner filaments is assumed rather than obtained from explicit geometric considerations. Figure 3.2 (c) shows a specific pore geometry for which corner filaments would be explicitly continuous in a 2D network.
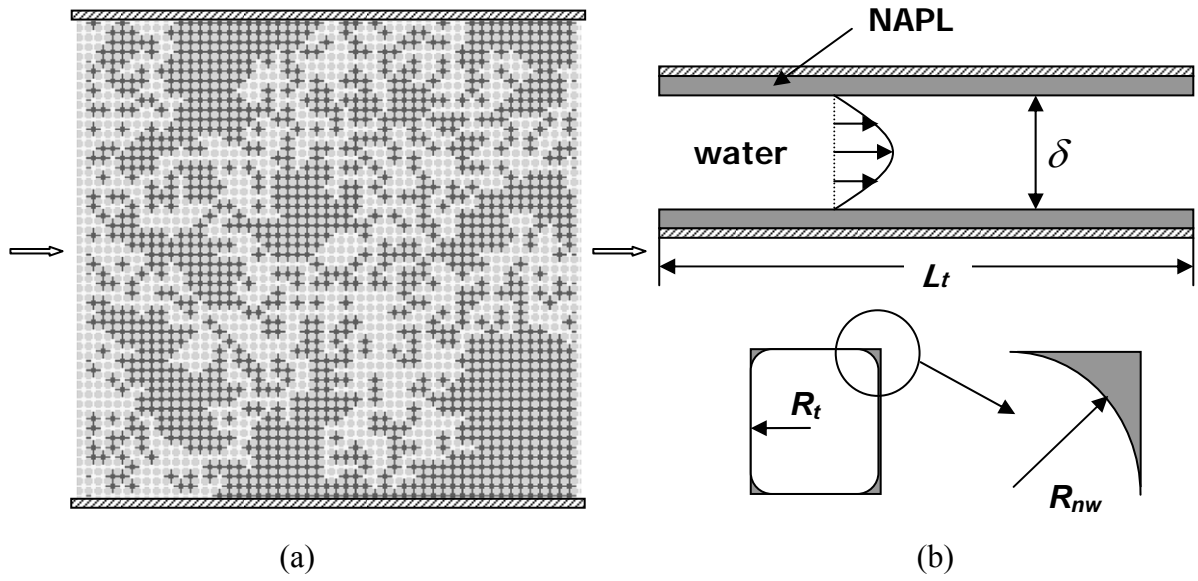
Figure 3.2 (a) Schematic of pore network model. White and black elements represent water-invaded and NAPL-filled chambers and tubes respectively (b) Schematic of a water invaded tube. (c) Schematic of corner filaments in a pore and a throat.

3.3.2   Aqueous phase flow

NAPL-water interfaces held in the corners of water-invaded tubes have the shape of circular arcs of radius R_{nw}. The radius of curvature of a newly formed arc meniscus in a water-invaded pore is related to the entry capillary pressure P_c^o, interfacial tension σ, contact angle θ and pore throat radius R_t as follows [Legait, 1983]:

$$P_c^o = \frac{\sigma}{R_t}\left(\frac{\theta + \cos^2\theta - \dfrac{\pi}{4} - \sin\theta\cos\theta}{\cos\theta - \sqrt{\dfrac{\pi}{4} - \theta + \sin\theta\cos\theta}}\right) = \frac{\sigma}{R_{nw}^o} \tag{3.6}$$

For $P_c > P_c^o$, the radius of curvature of such NAPL-water interfaces is determined by interfacial tension and capillary pressure:

$$R_{nw} = \frac{\sigma}{P_c} \tag{3.7}$$

Furthermore, the cross-sectional area available for flow of water in a water-invaded tube is estimated as:

$$A_w = 4R_t^2 - (4 - \pi)R_{nw}^2 \tag{3.8}$$

Dissolution at a NAPL-water interface results in a tendency of the interface to recede farther into the corner, causing an increase in interfacial curvature and generating a gradient in capillary pressure. This tendency is balanced by flow of NAPL out of a NAPL-filled pore which is simultaneously invaded by water. Experiments in glass micromodels have quantitatively confirmed that the rate of advancement of a water-NAPL interface into a previously NAPL-filled pore is controlled by the rate of NAPL

dissolution at NAPL-water interfaces in the corners of previously water-invaded pores [Sahloul et al., 2002]. Water invasion into NAPL-filled pores is assumed to follow an invasion percolation pattern [Zhao and Ioannidis, 2003] – an assumption tantamount to neglecting viscous resistance in the NAPL phase.

Assuming capillary equilibrium and slow dissolution, NAPL from the largest accessible pore supplies the dissolving corner menisci in water-invaded tubes, giving rise to an invasion percolation pattern. Water flow in water-invaded tubes is assumed to follow Poiseuille's law:

$$Q_{ij} = g_{ij}(P_i - P_j)$$

(3.9)

where Q is the water flow rate between two adjacent nodes in the network, g is the hydraulic conductance of the connecting channel and P is the water pressure at a node. For a tube with square cross section, the hydraulic conductance may be expressed as:

$$g = \frac{\pi R_{eff}^4}{8\mu L_t}$$

(3.10)

where μ is the water viscosity and R_{eff} is an effective radius defined as follows [Dillard and Blunt, 2000]:

$$R_{eff} = \frac{1}{2}\left(\sqrt{\frac{A_w}{\pi}} + R_t\right)$$

(3.11)

The pressure field in the network is determined from the solution of a system of algebraic equations, obtained by applying mass conservation at the nodes of the network:

$$\sum_j Q_{ij} = 0$$

(3.12)

3.3.3 Convective mass transfer in pore throats

Within a water-invaded tube, dissolved NAPL is transported by diffusion and convection away from the NAPL-water interface. For slow NAPL dissolution, quasi-steady-state conditions may be assumed. Following previous studies [Dillard and Blunt, 2000; Zhou et al., 2000; Sahloul et al., 2002; Zhao and Ioannidis, 2003] the 2-D slit model (see Figure 3.2 (b)) is adopted here as an approximation of solute transport in the 3D pore channels of the pore network.

The aqueous phase velocity is a function of y-direction only and the NAPL concentration is a function of both x-direction and y-direction. Gravitational effects are neglected and the density and diffusivity are assumed constant. With reference to Figure 3.2(b), the velocity distribution may be obtained from the equations of continuity and motion:

$$\frac{d^2 V_x}{dy^2} = -\frac{\Delta P}{\mu L_t} \tag{3.13}$$

where V_x is water velocity, ΔP is the pressure drop across the tube, μ is the water viscosity and L_t is the length of the tube. Boundary conditions applied to the O.D.E are

$$\text{B.C.1: } V_x = 0 : y = 0 \tag{3.14}$$

$$\text{B.C.2: } V_x = 0 : y = \delta \tag{3.15}$$

and the water velocity is evaluated by solving Equation (3.13):

$$V_x(y) = -\frac{\Delta P}{\mu L_t}(y^2 - \delta \cdot y) \tag{3.16}$$

Accordingly, the maximum velocity and the average velocity of water in a tube are

$$V_{max} = V_x(\frac{\delta}{2}) = \frac{\Delta P}{4\mu L_t}\delta^2 \qquad (3.17)$$

$$V_{av} = \frac{\int_0^\delta V_x dy}{\delta} = \frac{\Delta P}{6\mu L_t}\delta^2 = \frac{2}{3}V_{max} \qquad (3.18)$$

The NAPL concentration profile in a tube is determined from the steady-state transport equation representing convection and diffusion:

$$V \cdot \nabla C - D_m \nabla^2 C = 0$$

(3.19)

where C is the NAPL concentration, a function of both x and y, and D_m is the binary diffusion coefficient of NAPL in water. The term $V \cdot \nabla C$ represents convection whereas the term $D_m \nabla^2 C$ represents diffusion. Assuming that convection is dominant by comparison to diffusion in x-direction, Equation (3.19) becomes:

$$V_x \frac{\partial C}{\partial x} = D_m \frac{\partial^2 C}{\partial y^2} \qquad (3.20)$$

Substituting the velocity distribution in Equation (3.16) and solving Equation (3.20), the NAPL concentration profile $C(x, y)$ can be determined. Equation (3.20) is rewritten in dimensionless form:

$$\frac{\partial \phi}{\partial \xi} = \frac{1}{2\zeta - \zeta^2}\frac{1}{Pe}\frac{\partial^2 \phi}{\partial \zeta^2} \qquad (3.21)$$

where $\phi \equiv \dfrac{C - C_{in}}{C_S - C_{in}}$ is the dimensionless concentration, C_S is the NAPL solubility,

$\zeta \equiv y/\delta$ and $\xi \equiv x/\delta$ are the dimensionless distances and Pe is the pore-scale Peclet number,

$$Pe \equiv \frac{V_{\max} \delta}{D_m} \tag{3.22}$$

A numerical approach (method of lines) is employed to solve the above P.D.E. using a non-stiff O.D.E solver. The boundary conditions imposed to the problem are:

$$\text{B.C.1:} \quad C = C_S : \ y = 0 \tag{3.23}$$

$$\text{B.C.2:} \quad \frac{\partial C}{\partial y} = 0 : \ y = \delta \tag{3.24}$$

$$\text{B.C.3:} \quad C = 0 : x = 0 \tag{3.25}$$

The dimensionless distance in y-direction, ζ, is divided into n segments by defining $(n+1)$ nodes. The second derivative term is approximated as:

$$\frac{\partial^2 \phi_i}{\partial \zeta^2} = \frac{\phi_{i+1} - 2\phi_i + \phi_{i-1}}{(\Delta \zeta)^2} \qquad i = 2, 3, 4, \ldots\ldots, n \tag{3.26}$$

where $\Delta \zeta = \dfrac{1}{n}$ and the range of ζ is from 0 to 1. Accordingly,

$$\zeta_i = (i-1)\Delta \zeta \qquad i = 1, 2, 3, \ldots\ldots, n+1 \tag{3.27}$$

For the terminal node (i = n+1), $\dfrac{\partial \phi}{\partial \zeta} = 0$ (B.C.2) and the three-point backward approximation is applied:

$$\frac{\partial \phi_{n+1}}{\partial \zeta} = \frac{3\phi_{n+1} - 4\phi_n + \phi_{n-1}}{(\Delta \zeta)^2} = 0 \tag{3.28}$$

From Equation (3.28),

$$\phi_{n+1} = \frac{4}{3}\phi_n - \frac{1}{3}\phi_{n-1} \tag{3.29}$$

Differentiating Equation (3.29) with respect to ξ,

$$\frac{d\phi_{n+1}}{d\xi} = \frac{4}{3}\frac{d\phi_n}{d\xi} - \frac{1}{3}\frac{d\phi_{n-1}}{d\xi} \qquad (3.30)$$

From Equation (3.26) and Equation (3.30), a system of simultaneous O.D.E is obtained to solve for the concentration at each ζ-node as a function of ξ:

$$\frac{d\phi_i}{d\xi} = \frac{1}{2\zeta - \zeta^2}\frac{1}{Pe}\frac{\phi_{i+1} - 2\phi_i + \phi_{i-1}}{(\Delta\zeta)^2} \qquad i = 2, 3, 4, \ldots\ldots, n \qquad (3.31)$$

$$\frac{d\phi_i}{d\xi} = \frac{4}{3}\frac{d\phi_{i-1}}{d\xi} - \frac{1}{3}\frac{d\phi_{i-2}}{d\xi} \qquad i = n+1 \qquad (3.32)$$

The mathematical model enables one to obtain the normalized average dissolved NAPL concentration, E_d, at the exit end of the tube. E_d is a function of dimensionless residence time t_d and is an important parameter in the solution of the concentration field in the network. The normalized average dissolved NAPL concentration, E_d, at the exit end of the tube is given by

$$E_d = \frac{1}{C_s - C_{in}}\int_0^{\delta}[C(L_t/\delta, y) - C_{in}]dy \qquad (3.33)$$

or:

$$E_d = \int_0^1 \phi(\frac{L_t}{\delta}, \zeta)d\zeta \qquad (3.34)$$

E_d is a function of dimensionless residence time t_d,

$$t_d = \frac{1}{Pe}\frac{L_t}{\delta} \qquad (3.35)$$

Solving the O.D.E. (3.31) and (3.32), a correlation between E_d and t_d can be obtained. Figure 3.3 shows a plot of E_d versus t_d curve. The Matlab programs developed to solve this problem are given in Appendix A.
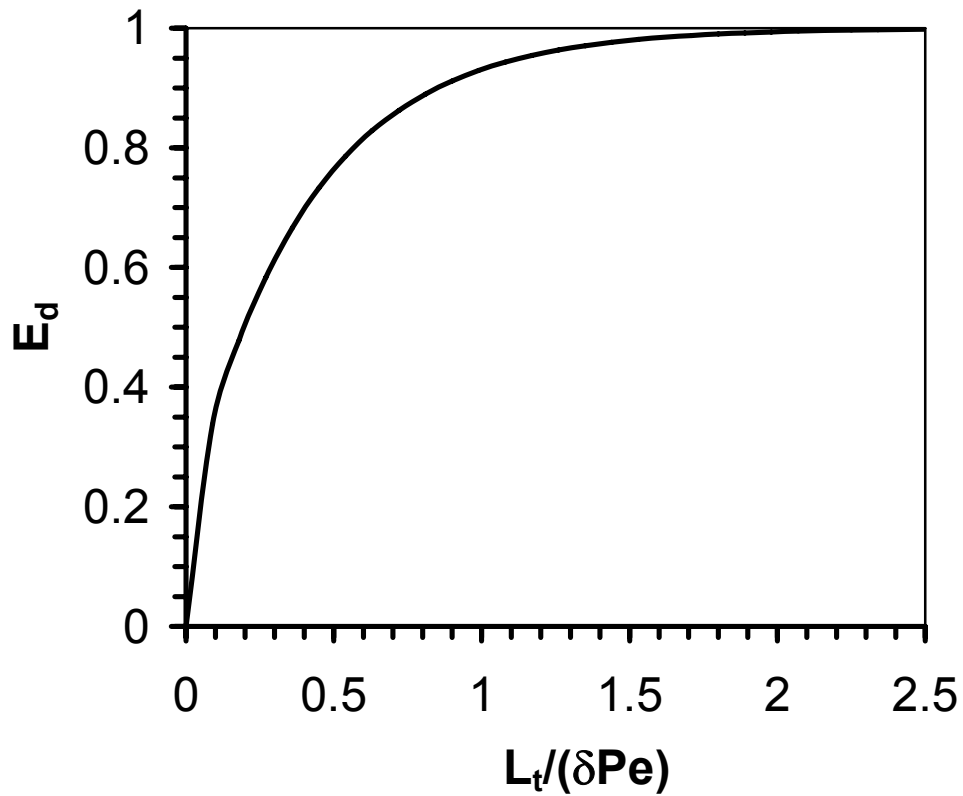
Figure 3.3 Normalized average solute concentration, E_d, vs. $L_t/(\delta Pe)$, where the pore-scale Peclet number is defined as $Pe \equiv \dfrac{3\overline{V}\delta}{2D_m}$ and $\overline{V}$ is the average water velocity in the tube.

The 2-D slit model used here is an approximation of convective mass transfer occurring in the 3-D pore throat. The approximation, however, is considered adequate for the purposes of the present investigation, which is primarily focused on qualitative trends. A more accurate solution of the problem of convective mass transfer to/from wetting fluid filaments along corners of angular pores is obtained in Chapter 4.

3.3.4 Mass balance of dissolved NAPL

With the flow field known, the concentration field is obtained by imposing mass conservation of the solute at network nodes corresponding to water-invaded pores,

$$\sum_j F_{ij} = 0 \qquad (3.36)$$

where F_{ij} is the solute flow from node j to node i. The effect of interfacial curvature on the solubility of NAPL is neglected and C_s is assumed to be constant. With reference to Figure 3.4, the following possible solute flows into and out of node a are take into account:

(i)   Solute mass transfer by aqueous phase advection from node 1. In this case, the solute concentration C_{in} entering node a, and the solute mass transfer rate $F_{1,a}$ are written as follows:

$$C_{in} = C_1 + E_d(C_S - C_1) \qquad (3.37)$$

$$F_{1,a} = Q_{1,a}C_{in} = Q_{1,a}\left[C_1 + E_d(C_s - C_1)\right] \qquad (3.38)$$

(ii)   The solute mass transfer rate by aqueous phase advection out of node a is written as:

$$F_{a,2} = Q_{a,2}C_a \qquad (3.39)$$

(iii)   Solute mass transfer by diffusion from a NAPL-filled pore (node 3 in Figure 3.4). The solute mass transfer rate by diffusion into node a is written as:

$$F_{3,a} = D_m A_t \frac{(C_s - C_a)}{R_p} \qquad (3.40)$$

where A_t is the cross sectional area of the pore throat and R_p is the radius of pore a.

(iv)   Finally, the rate of solute mass transfer by diffusion from a water-invaded pore with no advection ($P_4 = P_a$) is written as:

$$F_{4,a} = D_m A_w \frac{(C_4 - C_a)}{L_t} \qquad (3.41)$$

where A_w is the cross-sectional area of aqueous phase in the tube.

Given the pressure field in the network worked out, the water flow rate in each water-invaded tube is computed from Poiseuille's law. Imposing mass conservation of dissolved NAPL to every water-invaded chamber, a system of linear algebraic equations for the NAPL concentrations in the water-invaded chambers is obtained. The concentration field of the network is then obtained by solving the linear system.
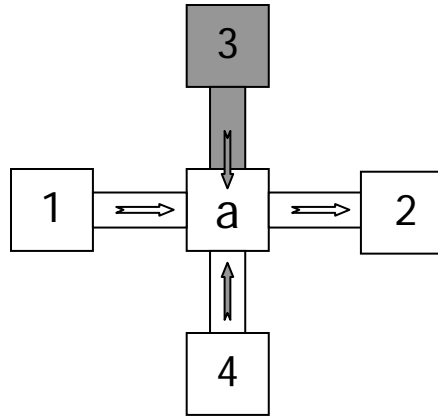
Figure 3.4 Schematic depicting dissolved organic flows into and out of a chamber. (Shaded arrows represent flows by diffusion only).

3.3.5 NAPL displacement

During the simulation, the chambers serve as containers for the NAPL and water phases and it is assumed that they have no capillary or flow resistance. The tubes serve as conductors for water flow and mass transfer and act as capillary barriers. When water phase flows through the open channels of the network, NAPL diffuses from the NAPL-water interface and pore drainage events take place in the NAPL-filled tubes and chambers. In this work, the mechanism of wetting NAPL dissolution observed by Sahloul et al. [2002] in glass micro-models is applied to simulate the pore drainage process.

The interfacial meniscus remains stationary at the inlet of a NAPL-filled tube until the interfacial pressure difference exceeds the threshold capillary pressure of the tube. As water invades a NAPL-filled tube, a piston-type displacement of NAPL occurs in the tube as NAPL in the bulk phase continuously supplies NAPL to the dissolving NAPL films by corner film flow. This process may be followed by several snap-off events after the meniscus enters the neighboring chamber until both the tube and the chamber contain only NAPL films coating the solid walls. At this point, a new channel is available to the water flow [Sahloul, et al., 2002].

For each simulation time step, a NAPL-filled tube is emptied, as shown in Figure 3.5. If the tube lies between a water-invaded chamber and a NAPL-filled chamber, both the tube and the adjacent NAPL-filled chamber are emptied (Figure 3.5a). In the case that a NAPL-filled tube lies between two water-invaded chambers, only the tube is emptied at this step (Figure 3.5 b). It is assumed that the thickness of NAPL films remains uniform throughout the network at each step, as NAPL from a water-invaded tube and/or chamber is assumed to supply the dissolving films.
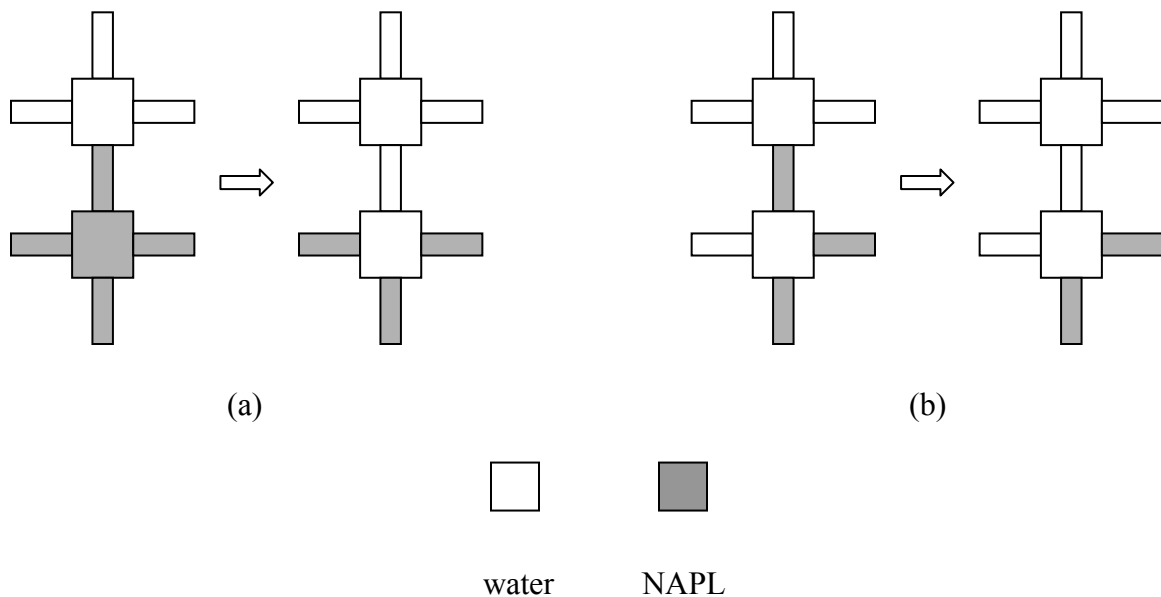
Figure 3.5 The evolution of pore drainage for a simulation time step (a) NAPL-filled tube and chamber are invaded (b) NAPL-filled tube between two water-invaded chamber is invaded.

As shown in Figure 3.2 (a), the network is initially saturated with NAPL except for open boundary channels for water flow. Water flows from the left face to the right face. At each time step, aqueous phase invades the NAPL-filled tube with the biggest radius available and displaces the NAPL in the tube and neighbouring NAPL-filled chamber (if available). The pressure field and concentration field are computed and several parameters, such as NAPL saturation, interfacial area, capillary pressure and effluent concentration, are calculated accordingly. In the next time step, simulation continues with a drainage event taking place in the next biggest tube accessible.

3.3.6 Disconnection of NAPL films

When the capillary pressure in a water-invaded tube reaches a critical value, NAPL films coating the pore walls are assumed to become unstable, causing disconnection of corner NAPL filaments at both ends of the tube. Pore wall curvature has an effect on the film stability condition [Kovscek et al., 1993]. For the situation depicted in Figure 3.6 (a), where the curvature of the film away from the sphere contact is approximately that of the sphere, the critical capillary pressure for film rupture is

$P_c^{crit} = \Pi^{max} - 2\sigma/r_i$, where r_i is the sphere radius [Kovscek et al., 1993].

Consequently, the wetting film on the smallest sphere ruptures at a lower value of capillary pressure. In the pore network geometry depicted in Figure 3.6 (b), flat NAPL films lie between the water and the solid walls, whereas the configuration of the NAPL-filled corners is that of constant curvature circular arcs. Here, the critical capillary pressure for rupture of the flat wetting films is simply $P_c^{crit} = \Pi^{max}$. To account for pore wall curvature on the critical capillary pressure for film rupture, Equation (3.2) is expressed as follows:

$$P_c^{crit} = \Pi^{max} - x\sigma/R_t \tag{3.42}$$

where R_t is the pore throat radius and x is a geometric parameter related to pore wall curvature that is positive for convex (*e.g.*, "star-shaped") pores. In this research it is assumed that $x = 1$. Equation (3.42) is motivated by the fact that small pores and throats are found between small grains, where the film curvature is larger.

The simulations begin with a continuous NAPL phase, as shown in Figure 3.2 (a). As dissolution proceeds, the capillary pressure reaches the critical value for NAPL film

rupture so that NAPL corner filaments in some of the water-invaded tubes become

disconnected.

(a)   **(b)**
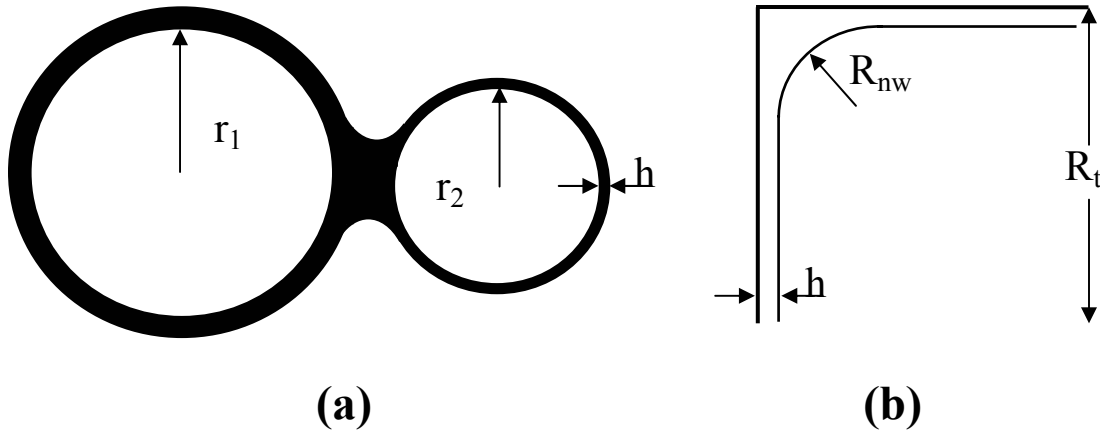
Figure 3.6 Schematics of wetting films (a) over spherical grains and (b) on the surface of

rectangular pores.

To account for the dissolution of disconnected corner filaments, the volume of

NAPL held in the corners is calculated:

$$V_{film} = A_{nw} L_t = (4 - \pi) R_{nw}^2 L_t \qquad (3.43)$$

where A_{nw} is the cross-sectional area of NAPL phase in the tube. Because of NAPL

disconnection, the capillary pressure is no longer uniform in the network. Instead, R_{nw}

varies among corner menisci belonging to different NAPL clusters and must be

calculated separately. Over a small time interval Δt, the loss of NAPL volume from the

corner filaments in a tube is given by

$$\Delta V_{film} = \frac{Q_{ij}\Delta t(C_{ij}^{out} - C_{ij}^{in})}{\rho_o}$$

(3.44)

where Q_{ij} is the water flow rate between nodes i and j, ρ_o is the NAPL density, C_{ij}^{in}

and C_{ij}^{out} are the organic solute concentrations at the inlet and outlet of the tube and

$C_{ij}^{out} = C_{ij}^{in} + E_d(C_S - C_{ij}^{in})$. Furthermore, $C_{ij}^{in} = C_i$, where C_i is the organic solute

concentration in node i. Accordingly, Equation (3.44) becomes:

$$\Delta V_{film} = \frac{Q_{ij}\Delta t E_d(C_S - C_i)}{\rho_o}$$

(3.45)

V_{film} is updated for each simulation step and when $V_{film} \leq 0$ the film in the tube disappears

and mass transfer ceases ($E_d = 0$).

3.3.7 Labelling of NAPL clusters

As mentioned before, the rupture of NAPL films causes disconnection of the

NAPL phase into a number of clusters. The cluster multiple labeling algorithm by

Hoshen and Kopelman [1976] is modified for application to the bonds of the network.

Instead of clustering the NAPL-filled pores, the modified algorithm focuses on the tubes

with NAPL or NAPL corner filaments. Each tube is a bond with six neighbors in the

network (Figure 3.7 a) and is assigned a binary index as follows. NAPL-filled bonds and

water-invaded bonds in which the capillary pressure is below the critical value for film

rupture are assigned an index of unity. Water-invaded bonds in which the critical

capillary pressure has been reached (*i.e.*, tubes with disconnected corner filaments) and

bonds without corner filaments are assigned an index of zero. Those tubes marked with unity indices are clustered to determine the continuity of NAPL. At each simulation step, the lattice is scanned to update the status of the bonds and all distinct clusters of bonds with index equal to unity are found (see Figure 3.7 b). Two types of NAPL clusters are identified. Type-F clusters are clusters with NAPL filaments, whereas Type-NF are clusters without NAPL filaments. Absence of NAPL filaments in Type-NF clusters means that NAPL in this form exposes a much smaller interfacial area for mass transfer, admits no water flow through it, and thus dissolves at a much slower rate than NAPL in the form of Type-F clusters.

3.3.8   Summary of simulation procedure

Fortran program developed to carry out the simulations is given in Appendices. Figure 3.8 is a brief flow chart of the program. Capillary pressure is uniform within each NAPL cluster, but different among different clusters. For each cluster present in the network, the mass loss of NAPL is computed and accumulated at each time step. When it becomes equal to the mass of NAPL in the largest accessible NAPL-filled pore in the cluster, that pore and its entry tube are considered invaded by water. The pressure and concentration fields in the network are computed anew and several parameters, such as the NAPL saturation and cluster distribution, the NAPL-water interfacial area and the average effluent concentration, are computed.

(a)

(b)
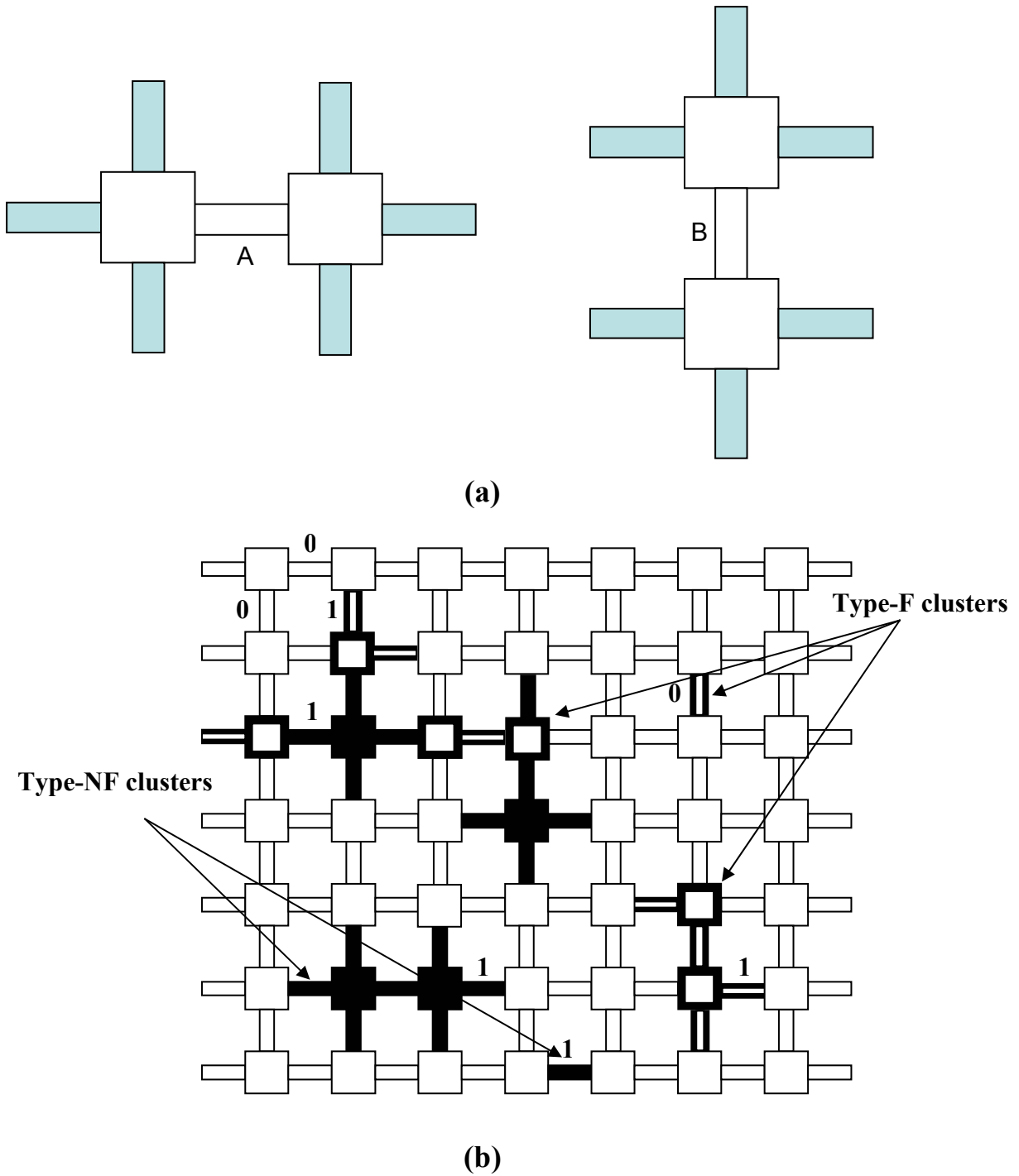
Figure 3.7 (a) Schematic of typical bonds (A and B) with 6 neighbor bonds (shaded)

(b) Schematic of NAPL clusters in the network. White represents water phase and black

represents NAPL. Statuses 0 or 1 are shown for some typical bonds.
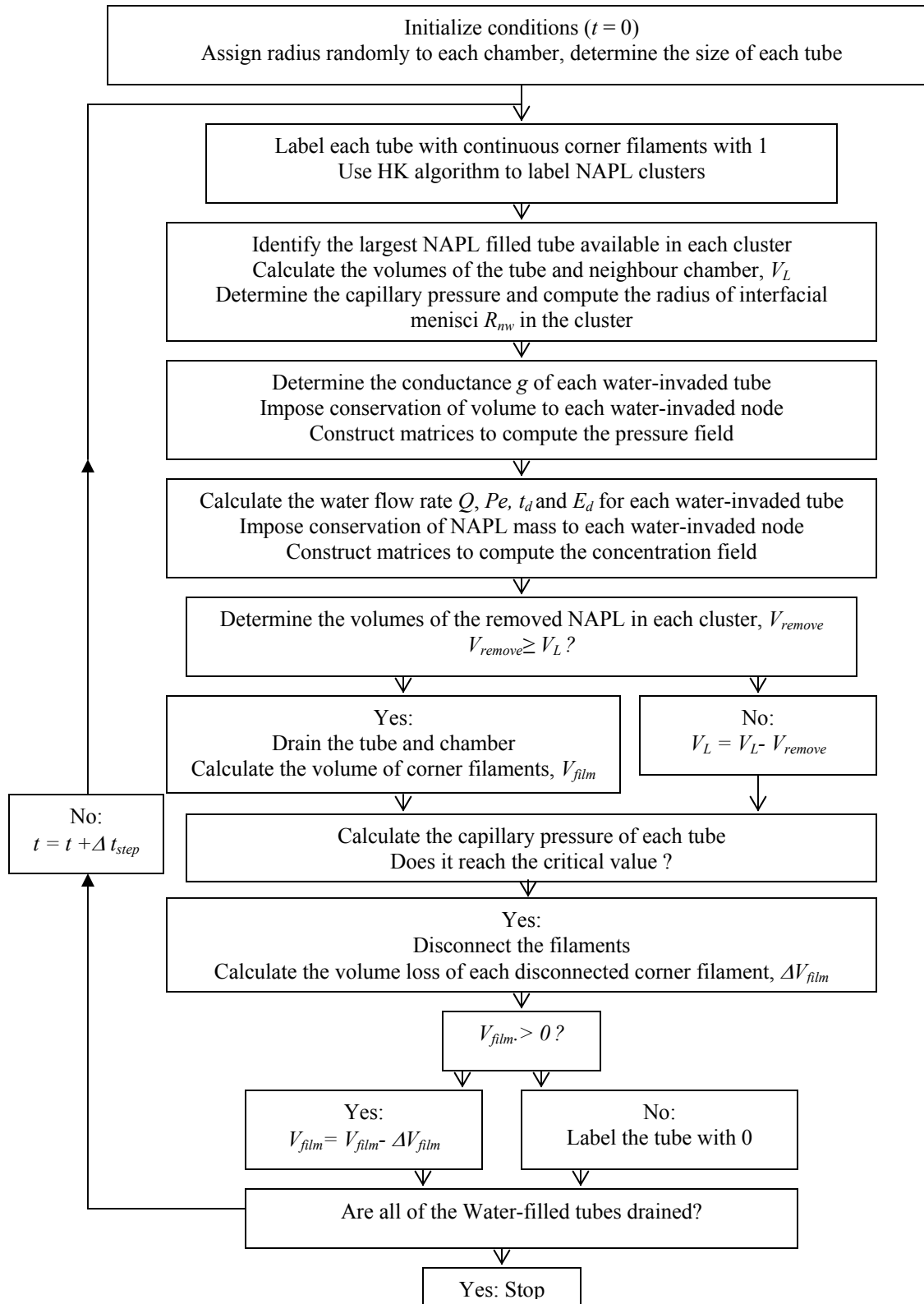
Figure 3.8 Flow chart of simulation without NAPL film disconnection.

3.4 Results and discussion

A network of 50×50 chambers, as shown in Figure (3.2 a), was used to obtain simulation results. Parameter values chosen in the simulation such as physical properties of NAPL and constant water injection rate are listed in Table 3.1. A set of runs are conducted under the conditions of different pore size distributions, initial NAPL saturations and NAPL disjoining pressures, as summarized in Table 3.2.

Table 3.1 Parameters used in the simulations.

Parameter	Value
Interfacial tension, σ [N/m]	2.7×10^{-2}
Contact angle, θ	20°
Diffusion coefficient, D_m [m^2/s]	8.8×10^{-10}
NAPL density, ρ_o [kg/m^3]	1.463×10^3
Water viscosity, μ [Pa-s]	8.9×10^{-4}
NAPL solubility, C_S [kg/m^3]	1.277
Water flow rate, Q [m^3/s]	1×10^{-7}

Table 3.2 Set of simulation runs.

Run No.	Average pore radius, $\langle R_p \rangle$ [μm]	Standard deviation [μm]	Disjoining pressure [Pa]	Initial NAPL saturation
1	552	174	280	0.36
2	552	174	320	0.36
3	552	174	280	0.36
4	552	174	320	0.36
5	552	174	280	0.36
6	552	174	320	0.36
7	552	174	320	0.13
8	552	174	280	0.13
9	55	174	1400	0.36
10	55	174	1600	0.36

3.4.1 NAPL cluster development

As already mentioned, the aqueous phase invades the largest accessible NAPL-filled tube and adjacent chamber, while NAPL is dissolved at NAPL-water interfaces and is removed by diffusion and advection in the aqueous phase. As dissolution proceeds, the capillary pressure increases and the condition $P_c = P_c^{crit}$ is satisfied for some of the water-invaded tubes. The NAPL film in these tubes becomes unstable and the corner filaments are disconnected at the tube junctions. In this manner the NAPL phase breaks up into separate clusters. During a single time step in the simulation, the capillary pressure is uniform within each cluster, but generally different between clusters.

Representative results, obtained from the same realization of the pore network (Runs 1 and 2, Table 3.2), are shown in Figure 3.9 (Π^{max} = 280 Pa) and Figure 3.10 (Π^{max} = 320 Pa), where a higher value of Π^{max} corresponds to more stable NAPL films. In these figures, the biggest and the second biggest cluster are shown in red and blue, respectively. For these two clusters only, water-invaded tubes and chambers containing connected NAPL films and corner filaments are shown in orange.

It is clear by comparing Figure 3.9 and Figure 3.10 that the microscopic configuration of residual NAPL during dissolution in a flowing aqueous phase is dramatically affected by the stability of NAPL films. Relatively larger clusters of residual NAPL remain in the network when NAPL films are less stable (Π^{max} = 280 Pa). On the contrary, when Π^{max} = 320 Pa, the same total amount of residual NAPL is found in the form of numerous small clusters. These differences are explained by considering
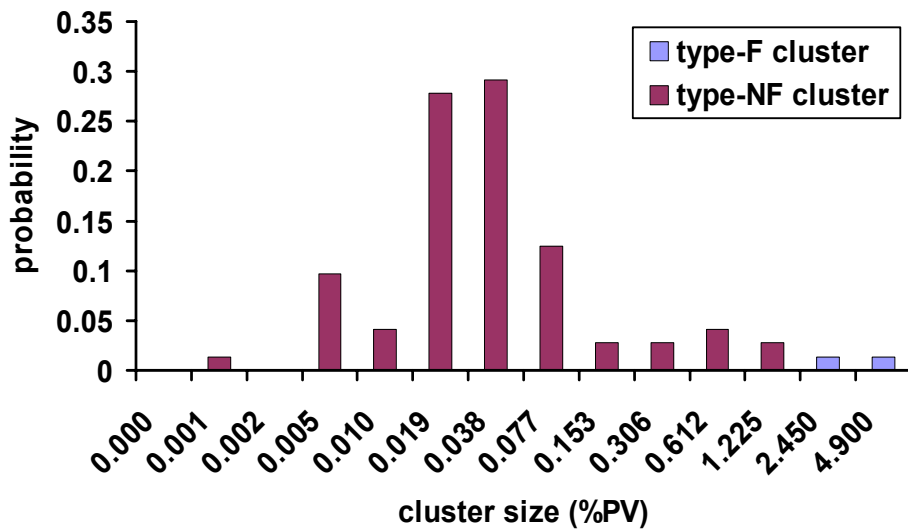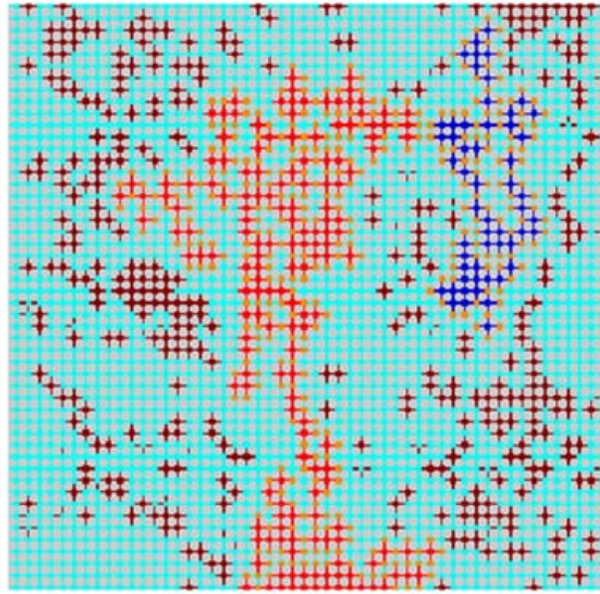
(a)   PV = 6511 S_n= 8.01%

Figure 3.9 (a). Visualization of dissolution of NAPL clusters and corresponding cluster size distributions for run 1 ($\Pi^{max} = 280 Pa$).
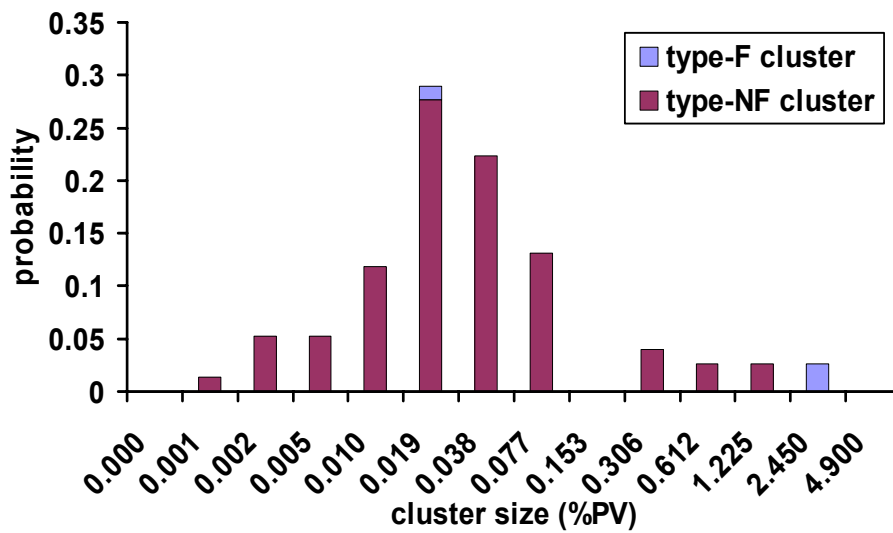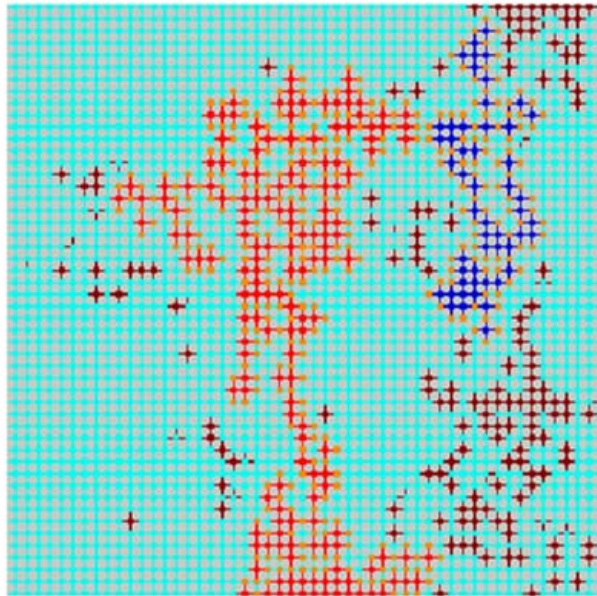
(b) $PV = 6673$ $S_n = 6.84\%$

Figure 3.9 (b) Visualization of dissolution of NAPL clusters and corresponding cluster size distributions for run 1 ($\Pi^{max} = 280Pa$).
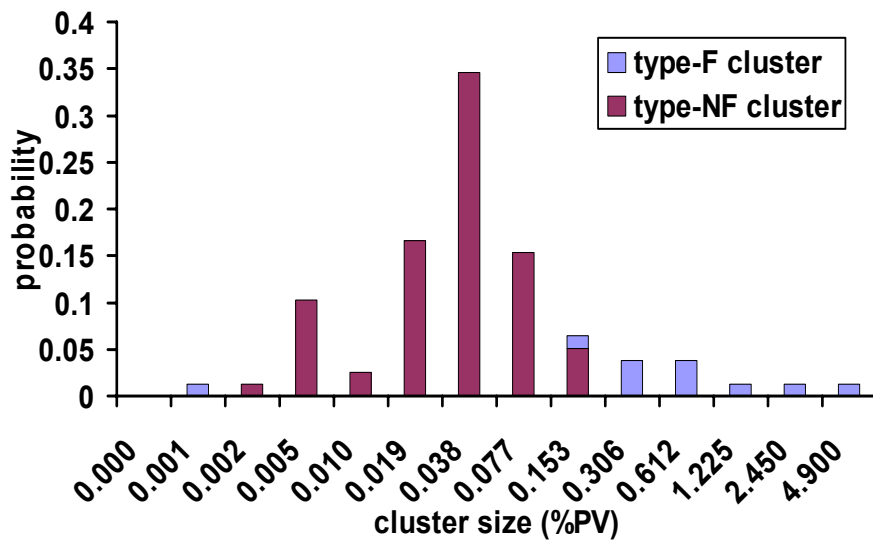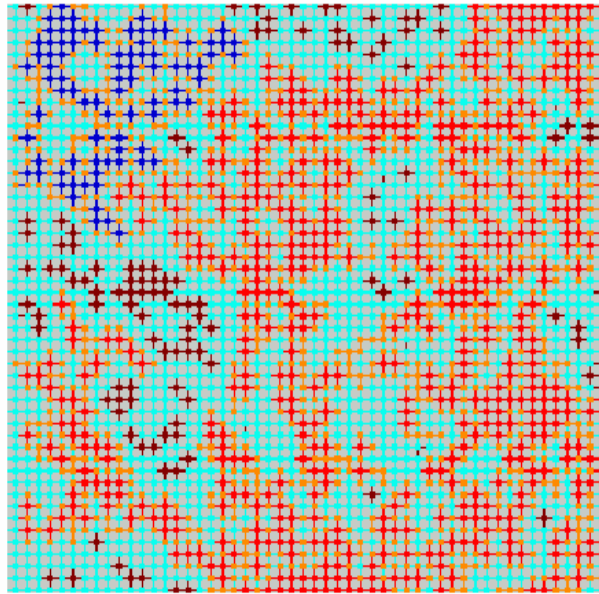
(a)   PV = 1255 S_n=11.11%

Figure 3.10 (a). Visualization of dissolution of NAPL clusters and corresponding cluster size distributions for run 2 ($\Pi^{max} = 320 Pa$).
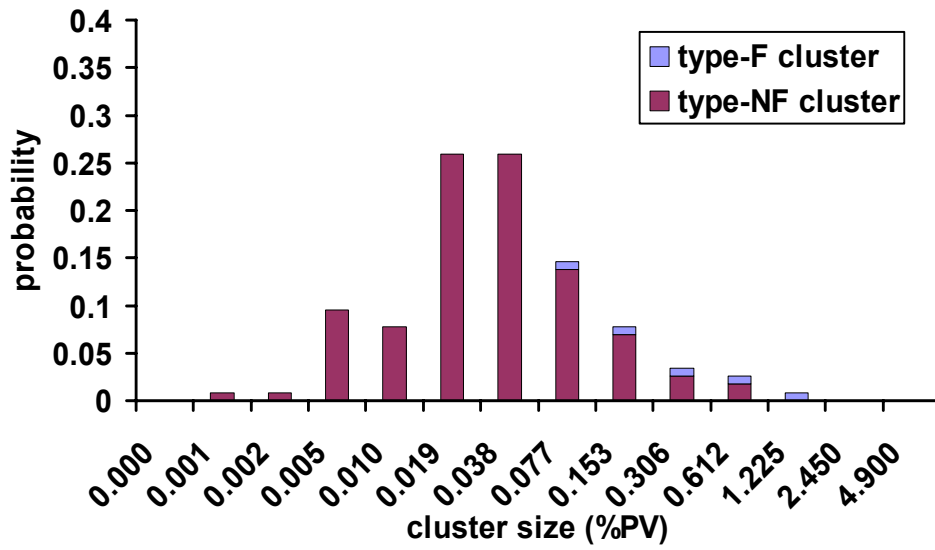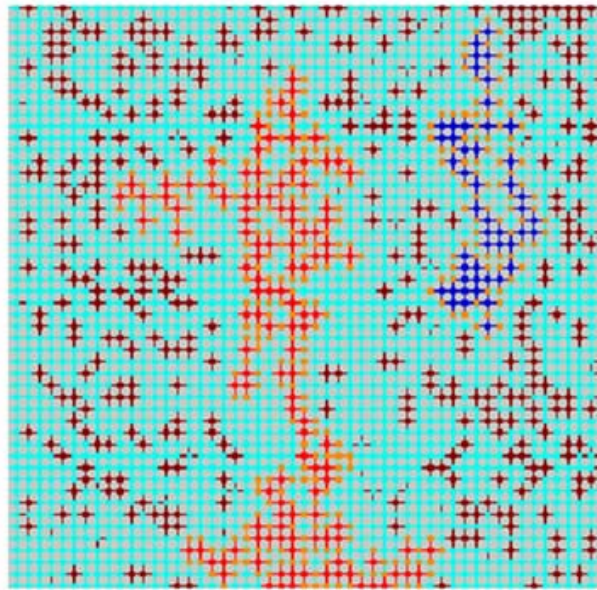
(b)   PV = 1640 S_n=7.72%

Figure 3.10 (b). Visualization of dissolution of NAPL clusters and corresponding cluster

size distributions for run 2 ($\Pi^{max} = 320Pa$).
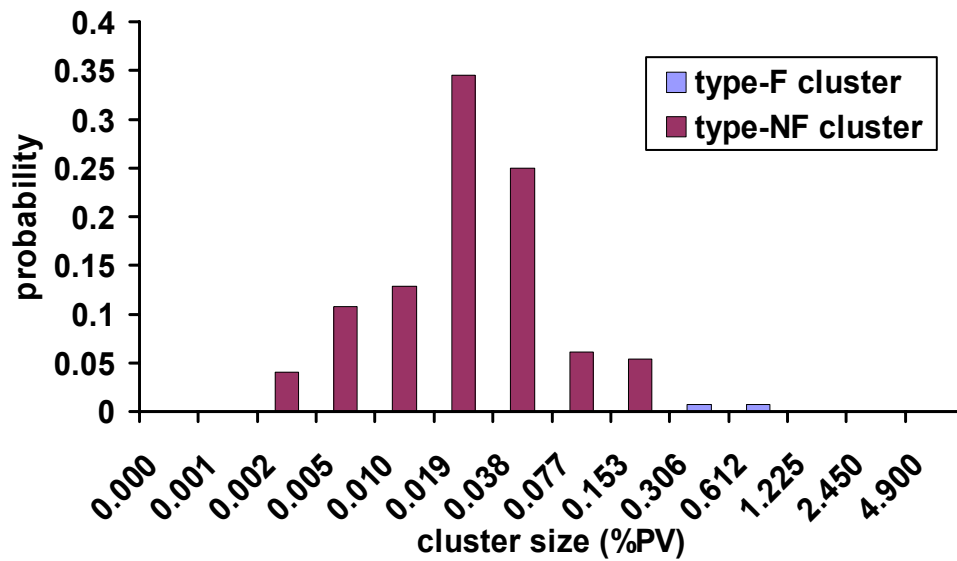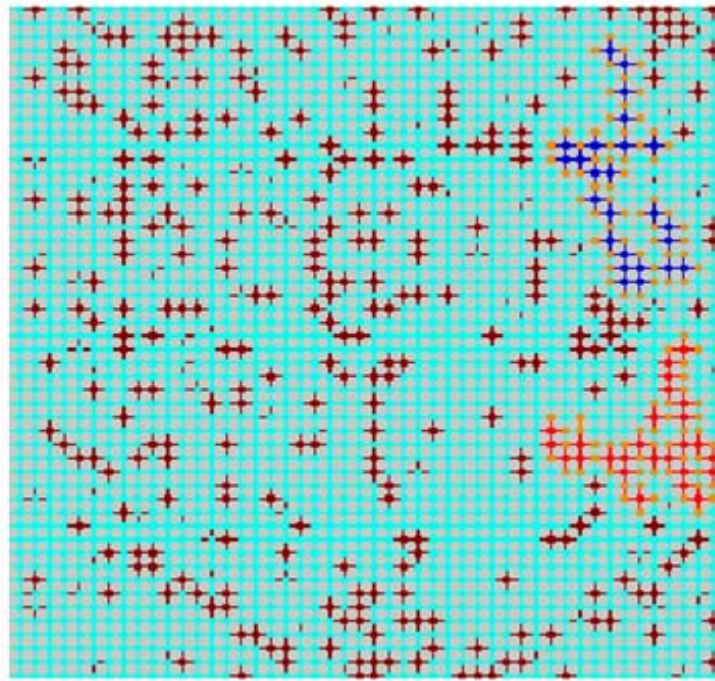
(c)   PV = 2050 S_n= 6.41%

Figure 3.10 (c). Visualization of dissolution of NAPL clusters and corresponding cluster

size distributions for run 2 ($\Pi^{max} = 320Pa$).

that when NAPL films are weaker, fragmentation of the NAPL phase takes place at an earlier stage in the dissolution process, thus creating larger clusters. Of these clusters, the most persistent ones are those exposing the least interfacial area for mass transfer, in particular type-NF clusters. When NAPL films are stronger, however, fragmentation of the NAPL phase takes place when a much larger fraction of originally NAPL-filled pores have been invaded by water, leading to the formation of smaller clusters.

The evolution of NAPL-water interfacial area, shown in Figure 3.11, further illustrates the significance of NAPL film stability. Starting from the same initial condition (point A), a system with weak NAPL films experiences a rapid reduction in total interfacial area at a relatively high volumetric NAPL content, as the NAPL phase is disconnected and isolated NAPL filaments quickly dissolve in the flowing aqueous phase (point B). On the contrary, a system with strong NAPL films is able to maintain and, in fact, increase its NAPL-water interfacial area for mass transfer as dissolution proceeds. In a system with strong NAPL films, it is type-F NAPL clusters that contribute almost exclusively to the mass transfer area (see Figure 3.11). On the contrary, in a system with weak NAPL films, there exist few type-F clusters and their contribution to the total interfacial area for mass transfer is relatively small. As the volumetric NAPL content decreases during dissolution, the interfacial area contributed by type-F clusters diminishes. The key effect of increased NAPL film stability is to prolong the presence of type-F clusters. For the simulation results shown in Figure 3.11, the contribution of type-F clusters to the total interfacial area for mass transfer becomes negligible when $S_n <$ 0.05 and $S_n < 0.15$ for systems with strong and weak NAPL films, respectively. For S_n < 0.05, there is no difference on the dependence of mass transfer area on NAPL

saturation between the two systems and one expects the corresponding NAPL residual to be removed by dissolution in exactly the same number of pore volumes of the injected aqueous phase. Reduction of residual NAPL saturation from the initial value of $S_n^o =$ 0.36 to $S_n = 0.05$, however, is expected to require a much smaller number of pore volumes of the injected aqueous phase when $\Pi^{max} = 320$ Pa than when $\Pi^{max} = 280$ Pa. This is an immediate consequence of the smaller mass transfer area in the latter case.
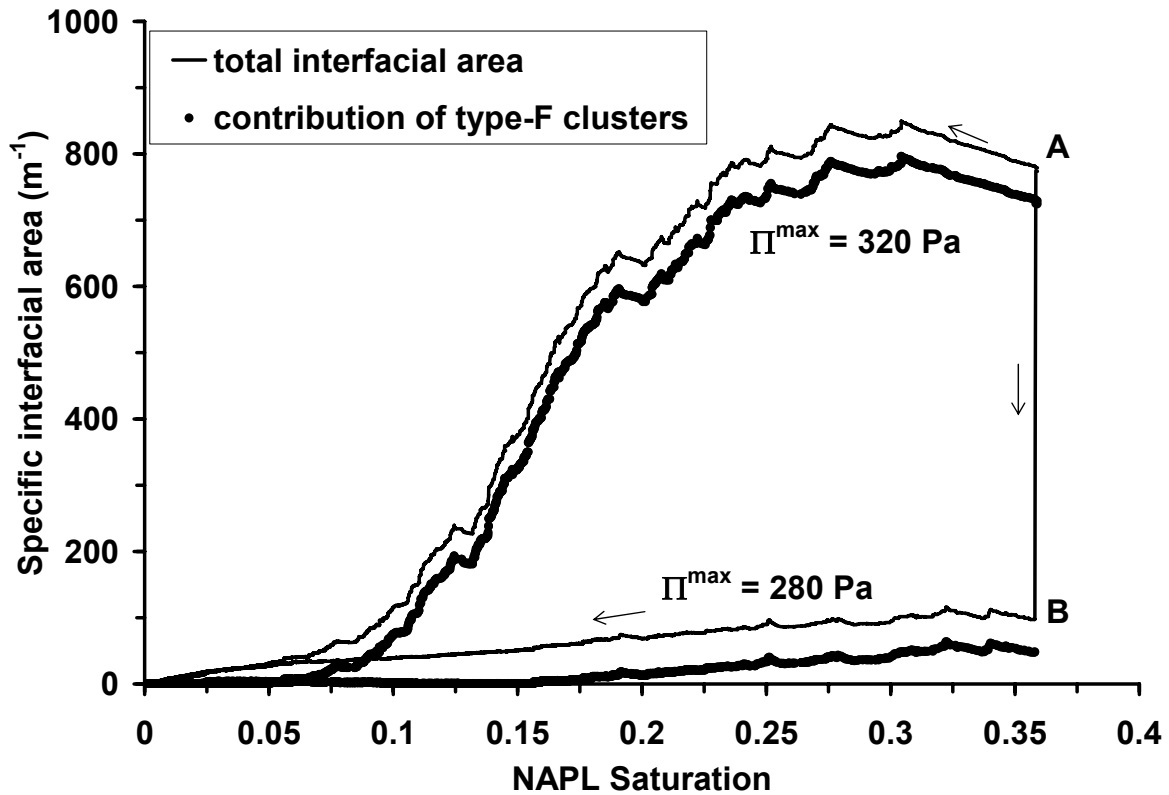
Figure 3.11 Specific interfacial area vs. NAPL saturation for run 1 and 2.

3.4.2 Effluent concentration and NAPL recovery

Normalized effluent concentration is plotted against the number of pore volumes of water injected in Figure 3.12 (Π^{max} = 320 Pa) and Figure 3.13 (Π^{max} = 280 Pa). Results from three different realizations of the pore network are shown in each figure (see Table 3.2). The following comments are in order. Firstly, increasing the stability of NAPL films results in a longer period of high effluent concentration (near NAPL solubility), which is followed by a rapid reduction of concentration and tailing at low concentration levels. When NAPL films are weak, fragmentation of the NAPL phase takes place early on in the dissolution process, creating large clusters with few or no films in the network. In this case, the lower interfacial area available for mass transfer results in effluent concentration that rapidly drops to a lower level (around 10% of NAPL solubility). Secondly, greater film instability increases the sensitivity of effluent concentration to the initial NAPL distribution. This is evident by comparing Figure 3.12, in which little difference is seen between the results from three different realizations of the pore network, and Figure 3.13. Less stable NAPL films increase the variability in the distribution of disconnected NAPL films, influencing the NAPL concentration field in the relatively small pore networks considered in this work.
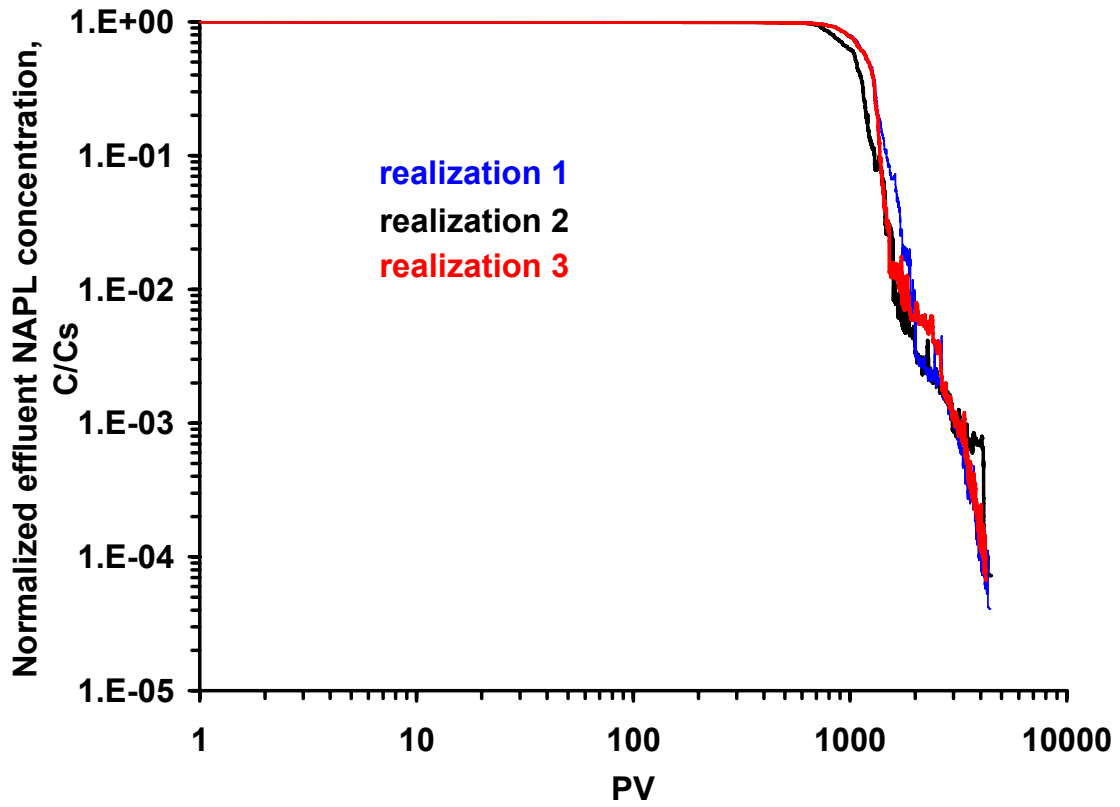
Figure 3.12 Normalized effluent concentration vs. pore volume of water injected for run

2, 4, 6 ($\overline{Rp}$ = 0.552mm, S_n^o = 0.36, $\Pi^{max} = 320Pa$).
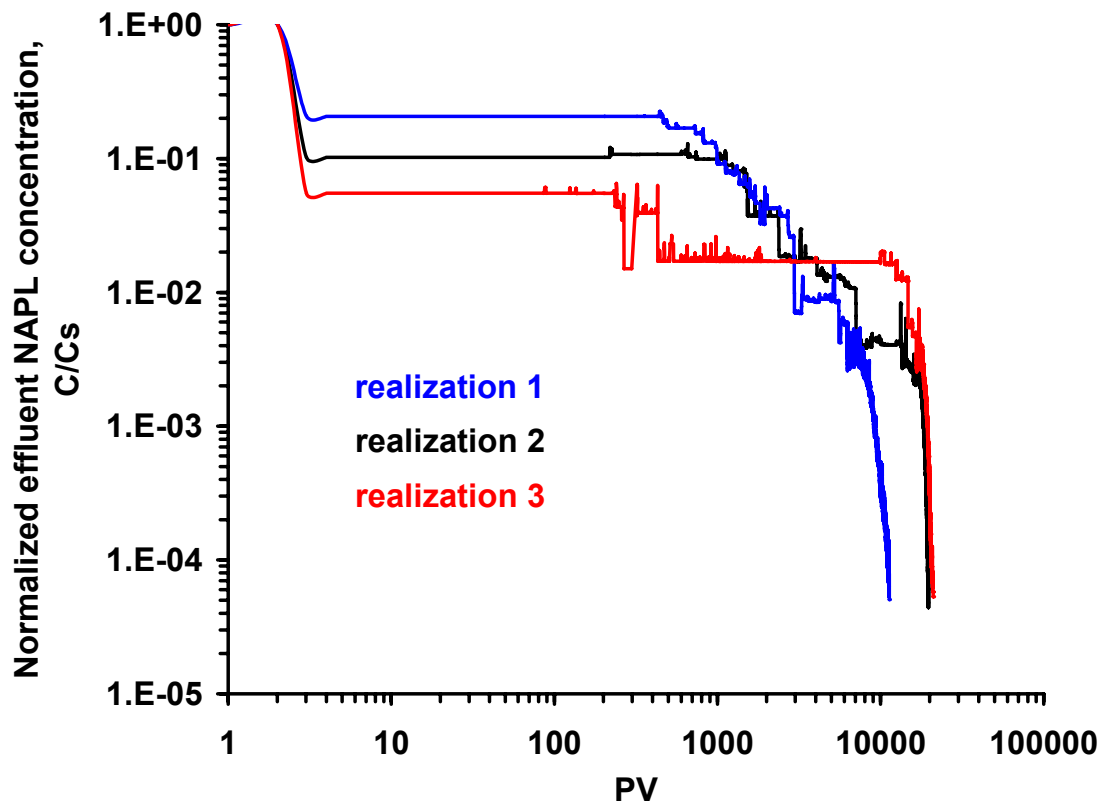
Figure 3.13 Normalized effluent concentration vs. pore volume of water injected for run

1, 3, 5 ($\overline{Rp} = 0.552$mm, $S_n^o = 0.36$, $\Pi^{max} = 280Pa$).

The effect of initial NAPL saturation on effluent concentration is shown in Figure 3.14 (Π^{max} = 320 Pa, Run 7, Table 3.2) and Figure 3.15 (Π^{max} = 280 Pa, Run 8, Table 3.2). A lower value of S_n^o corresponds to a higher initial value of capillary pressure, for which a larger number of NAPL film disconnection events take place. As a result, the initial interfacial area for mass transfer is lower and the effluent concentration drops to lower values. The observed fluctuations of the effluent concentration seen in Figure 3.14 and Figure 3.15, which are also seen in Figure 3.13, can be explained as follows. At late stages in the dissolution process or when the NAPL saturation is low, mostly type-NF clusters are present (see Figure 3.11). Drainage events create type-F clusters which are short-lived, particularly when NAPL films are weak (see Figure 3.15). Spikes in effluent concentration correspond with the appearance and disappearance of such clusters as a consequence of determining the effluent concentration from steady-state solute balances.

The fractional NAPL recovery history is plotted in Figure 3.16 (Π^{max} = 320 Pa) and Figure 3.17 (Π^{max} = 280 Pa). As expected, the same amount of NAPL takes a much longer time to be removed when NAPL films are weak (~10000 PV vs. ~4000 PV for 99% recovery). The abrupt increase in NAPL recovery history for systems with weak NAPL films (see Figure 3.17) corresponds with S_n = 0.15, the saturation at which type-F clusters effectively cease to contribute to the interfacial area for mass transfer. Under such conditions, the disappearance of NAPL from a few pores in the network can dramatically affect the concentration field, as illustrated in Figure 3.18. It deserves to be mentioned that the pore network model used in this work does not attempt to account quantitatively for NAPL-water interfacial areas in real porous media, but rather to

illustrate key qualitative features of the dissolution of a wetting NAPL. Thus, the number of pore volumes required to remove the NAPL from the pore network model is likely to be considerably overestimated.
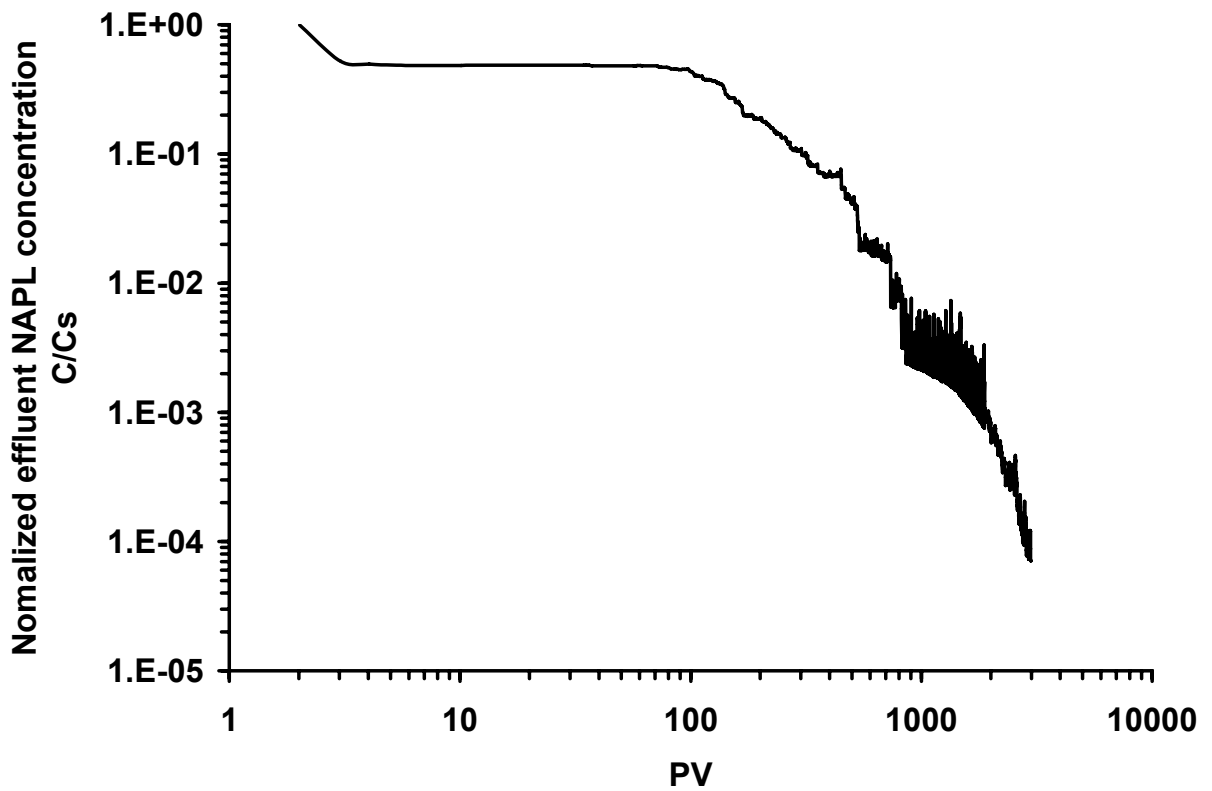
Figure 3.14 Normalized effluent concentration vs. pore volume of water injected for run 7

($\overline{Rp}$ = 0.552mm, S_n^o = 0.13, Π^{max} = 320Pa).
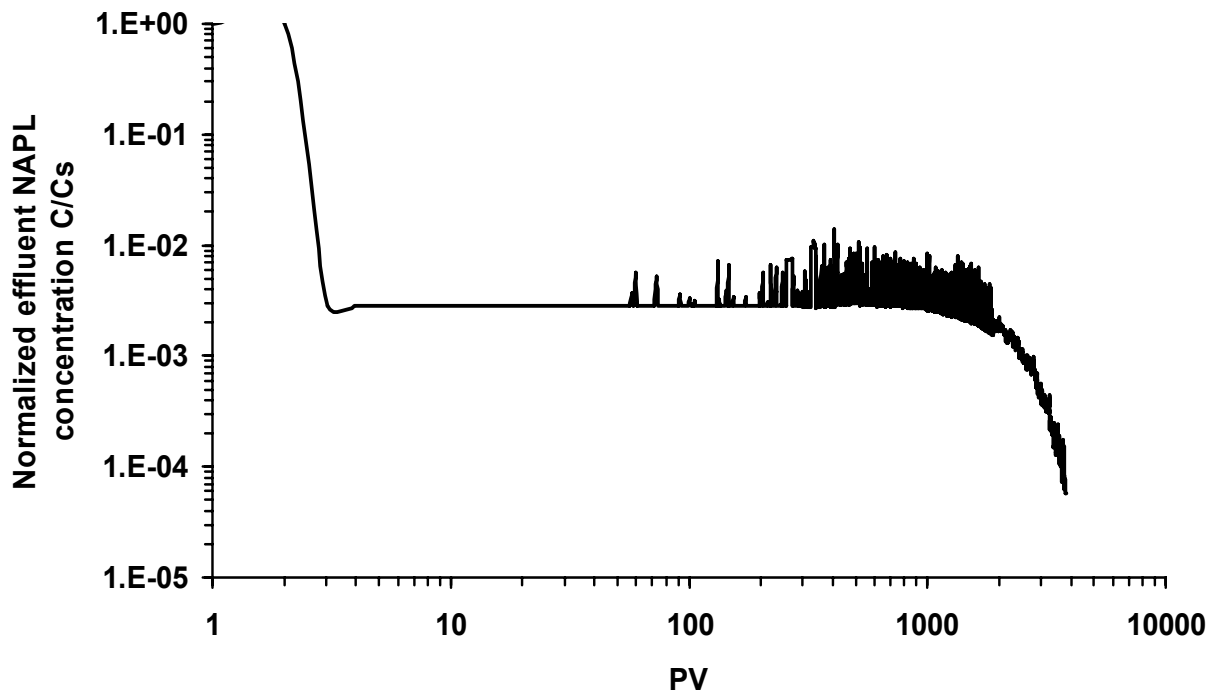
Figure 3.15 Normalized effluent concentration vs. pore volume of water injected for run

8

$(\overline{Rp} = 0.552\text{mm}, S_n^o = 0.13, \Pi^{\max} = 280Pa)$.
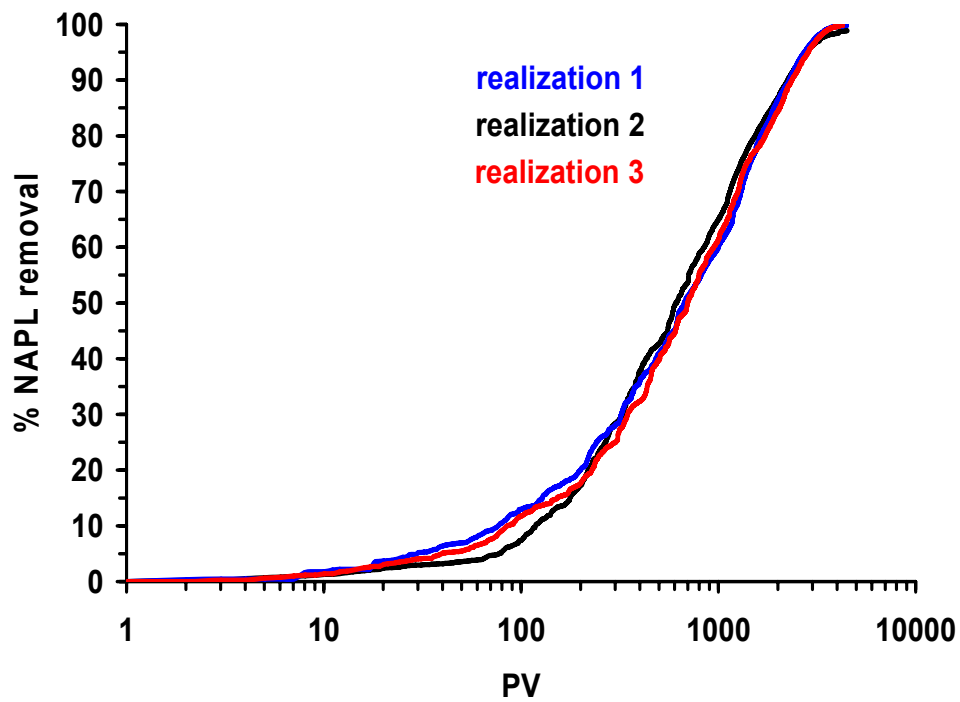
Figure 3.16 Percentage of NAPL removal vs. pore volume of water injected for run 2, 4,

6

$(\overline{Rp} = 0.552\text{mm}, \ S_n^o = 0.36, \ \Pi^{\max} = 320Pa)$.
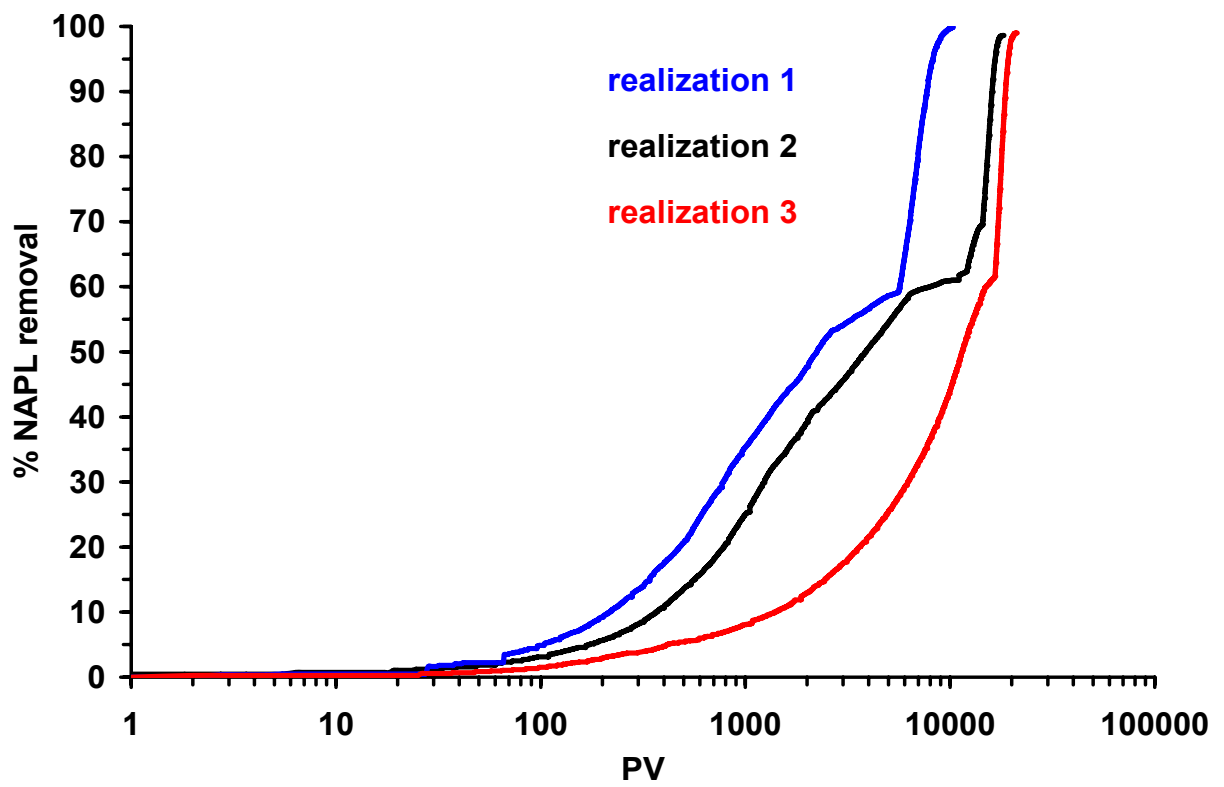
Figure 3.17 Percentage of NAPL removal vs. pore volume of water injected for run 1, 3,

5

($\overline{Rp}$ = 0.552mm, S_n^o = 0.36, $\Pi^{\max}$ = 280Pa).
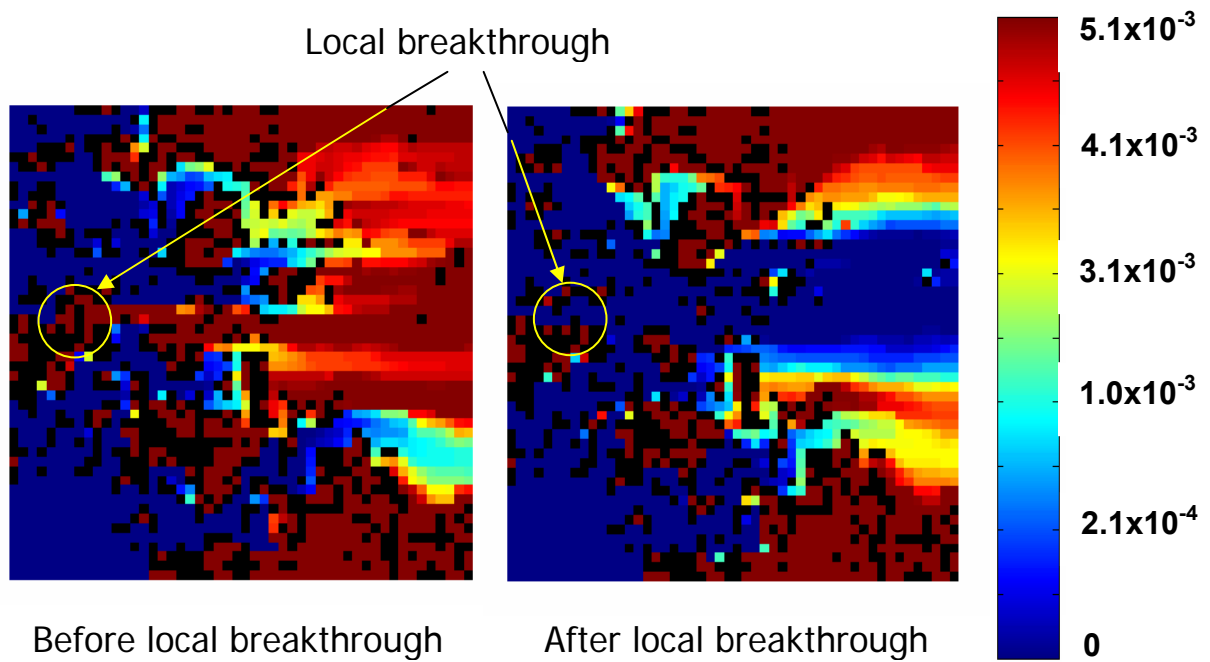
Figure 3.18 Visualizations of NAPL concentration fields before and after a local breakthrough (run 1).

3.4.3 Effect of pore size distribution

The condition of NAPL film instability, Equation (3.42), provides the connection between the disjoining pressure and the pore size distribution and explains the choice of Π^{max} values used in the simulations presented here. Critical capillary pressures at which significant changes in behaviour are seen, are related to the typical capillary pressures for displacement. Corner NAPL filaments first appear when a tube is invaded, at $P_c = P_c^o$, and become disconnected when $P_c = P_c^{crit}$. Therefore the range of capillary pressures over which corner filaments in a tube remain connected is $P_c^o < P_c < P_c^{crit}$ and it is convenient to define a critical pressure ratio P_c^{crit}/P_c^o which depends on pore size and Π^{max}. Corner filaments in tubes for which $P_c^{crit}/P_c^o \leq 1$ become immediately disconnected. The pattern of residual NAPL fragmentation during dissolution in a flowing aqueous phase is controlled by S_n^o and the distribution of critical pressure ratio. Such distributions are shown in Figure 3.19 for different choices of Π^{max} and pore size distribution (see Table 3.2). Run 1 and Run 9, as well as Run 2 and Run 10, are characterized by identical S_n^o and critical pressure ratio distribution. Their effluent concentration curves are compared in Figure 3.20. These curves are in essential agreement. The small difference is due to the effect of pore size on *Pe*. That is, for a given volumetric flow rate of the aqueous phase, pore-scale mass transfer rates are higher in a network of smaller pores and thus the drop in effluent concentration takes place at an earlier stage in the dissolution process. Finally, the effect of increasing Π^{max} for a given pore size distribution is to shift the curves of Figure 3.19 to the right. This

corresponds to NAPL films that remain stable at high values of capillary pressure. Under such conditions, most of the NAPL can be drained out of the pore network, few or no isolated clusters of NAPL-filled pores are created during dissolution, and the interfacial area for mass transfer remains high at very low values of the NAPL saturation [Zhao and Ioannidis, 2003].
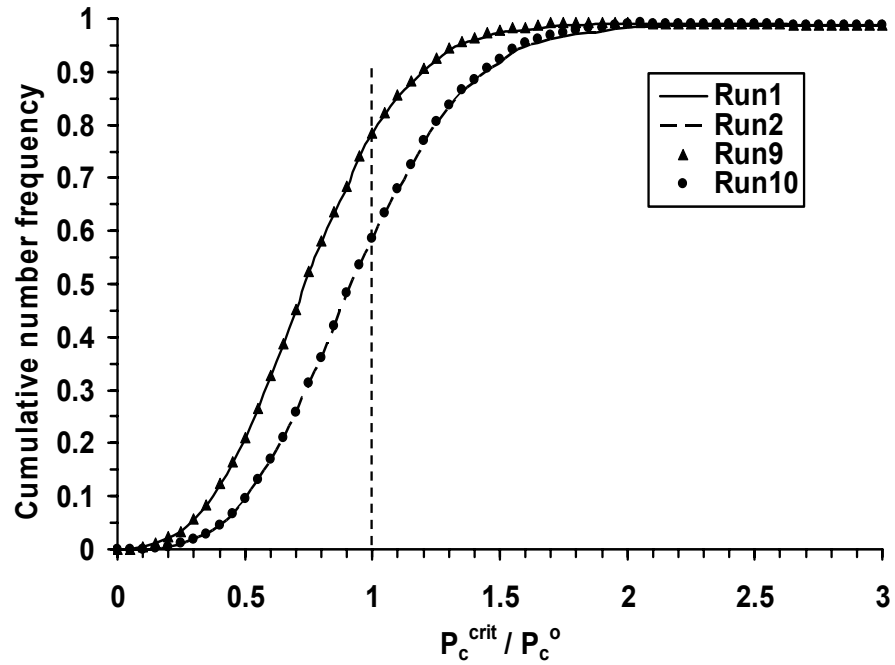
Figure 3.19 Distributions of critical pressure ratio for run 1, 2, 9 and 10.
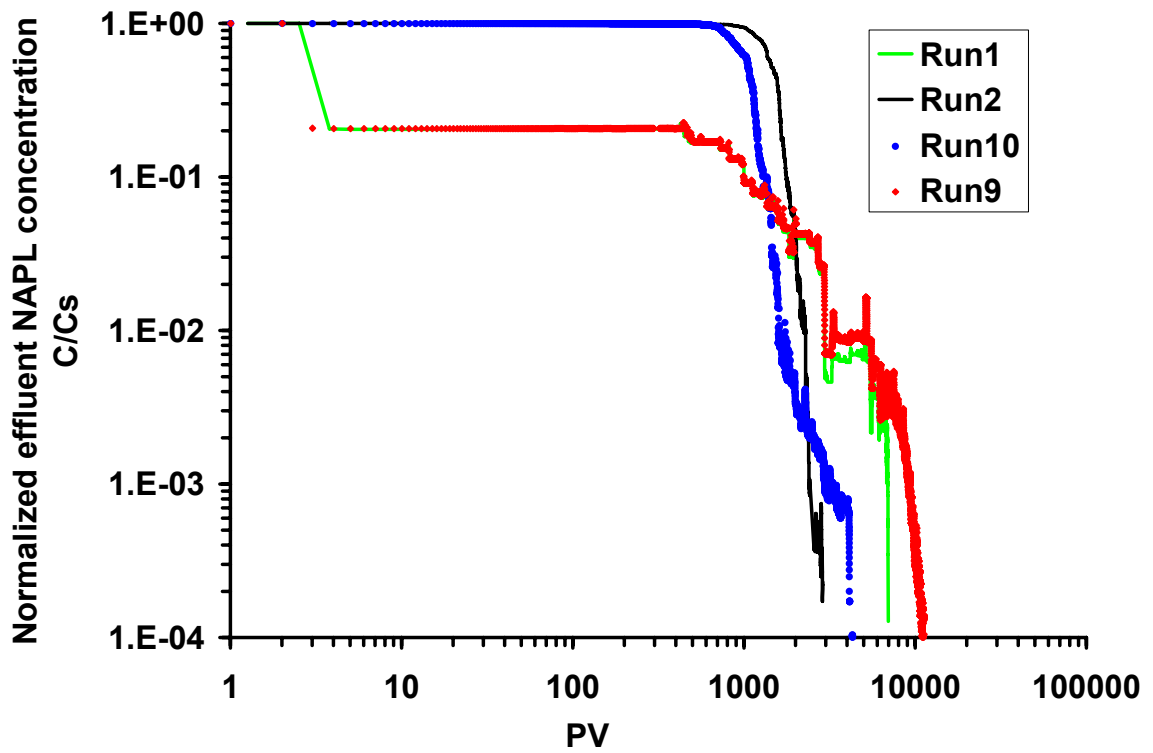
Figure 3.20 Normalized effluent concentration vs. pore volume of water injected for run

9 and 10 ($\overline{Rp}$ = 0.055mm, S_n^o = 0.36).

3.5   Conclusions

A pore network model is developed to explore the qualitative effects of NAPL film stability on the dissolution behavior of residual wetting NAPL in porous media. The simulation was based on the mechanism of mass-transfer-driven drainage observed in experiments using transparent glass micromodels [Sahloul et al., 2002]. Advection and diffusion of organic solute from NAPL-water interfaces were accounted for. A stepwise solution procedure was used to obtain the flow and solute concentration fields in the network as the aqueous phase gradually invades NAPL-filled throats and pores and a quasi-state drainage pattern develops. Wetting NAPL films held in the corners of throats were assumed responsible for the hydraulic continuity of the NAPL phase and the large interfacial area for mass transfer during dissolution in a flowing aqueous phase. Film rupture was related to disjoining pressure and film curvature and the fragmentation of residual NAPL into distinct clusters during dissolution was followed. The results indicate that the dissolution behavior is very sensitive to the stability and distribution of thick NAPL films along pore corners. Rupture of NAPL films results in severe loss of NAPL-water interfacial area and a large reduction in the rate of mass transfer. On the contrary, long-term high effluent NAPL concentrations (near NAPL solubility) are observed when NAPL films are stable. The simulations strongly suggest that factors affecting NAPL film stability may play an important role in residual NAPL dissolution in oil wet systems.

Chapter 4

Convective Mass Transfer across Fluid Interfaces

in Straight Angular Pores

4.1   Summary

Steady convective mass transfer to or from fluid interfaces in pores of angular cross-section is theoretically investigated. This situation is relevant to a variety of mass transport process in porous media, including the fate of residual non-aqueous phase liquid ganglia and gas bubbles. The model incorporates the essential physics of capillarity and solute mass transfer by convection and diffusion in corner fluid filaments. The geometry of the corner filaments, characterized by the fluid-fluid contact angle, the corner half-angle and the interface meniscus curvature, is accounted for. Boundary conditions of zero surface shear ('perfect-slip') and infinite surface shear ('no-slip') at the fluid-fluid interface are considered. The governing equations for laminar flow within the corner filament and convective diffusion to or from the fluid-fluid interface are solved using finite-element methods. Flow computations are verified by comparing the dimensionless resistance factor and hydraulic conductance of corner filaments against recent numerical solutions by Patzek and Kristensen [2001]. Novel results are obtained for the average

effluent concentration as a function of flow geometry and pore-scale Peclet number. These results are correlated to a characteristic corner length and local pore-scale Peclet number using empirical equations appropriate for implementation in pore network models. Finally, a previously published "2D-slit" approximation to the problem at hand is checked and found to be in considerable error.

4.2   Background

Mass transfer across fluid-fluid interfaces in geologic porous media arises in a variety of circumstances of importance to environmental engineering. An important example concerns the dissolution into a flowing aqueous phase of residual non-aqueous phase liquids (NAPL) trapped in the form of ganglia [Dillard and Blunt, 2000; Zhou et al., 2000; Dillard et al., 2001; Sahloul et al., 2002]. This situation is encountered in the so-called pump-and-treat method for soil remediation [Khachikian and Harmon, 2000].

Another important example concerns the transport of dissolved gases in the presence of trapped gas bubbles [Donaldson et al., 1997; Williams and Oostrom, 2000; Holocher et al., 2003]. Bubble-mediated mass transfer can affect significantly the interpretation of atmospheric gas concentration in groundwater, as well as intrinsic and enhanced bioremediation processes dependent on the actual dissolved gas content of gases such as oxygen and nitrogen. In both cases, flow of the aqueous phase along the nooks and crannies of pores containing trapped NAPL ganglia or gas bubbles imparts a significant convective component to solute mass transfer [Dillard and Blunt, 2000; Zhou et al., 2000; Sahloul et al., 2002]. The fact that more than one fluid phase can be present

within the same pore is well recognized in the literature on pore network modeling, where straight pore channels of angular cross-section are most often used to represent the pore space [*e.g.*, Ioannidis and Chatzis, 1993; Hui and Blunt, 2000]. When two fluids are present in an angular pore, the non-wetting phase fills the central part of the pore, whilst the wetting phase occupies the pore corners as corner films or filaments. Solute mass transfer takes place across the fluid-fluid interface during, for instance, dissolution of NAPL ganglia, when organic solute diffuses into and is carried away by the flowing aqueous phase. Pore-scale studies of NAPL dissolution [Dillard and Blunt, 2000; Zhou et al., 2000; Sahloul et al., 2002] show that the rate of dissolution is largely determined by corner film flow and diffusion. In these studies, convective mass transfer from a fluid-fluid interface in the 3D conduit formed by the pore walls and the arc meniscus has been approximated by the analogous 2D problem in a slit [Dillard and Blunt, 2000; Zhou et al., 2000; Sahloul et al., 2002]. This approximation captures qualitatively the physics of mass transfer in a corner filament, but its quantitative accuracy is uncertain. A solution, however, to the problem of convective diffusion to or from fluid interfaces in pores of angular cross-section, does not exist in the literature. The related problem of mass transfer from planar films to simple shear flows has been solved [Stone, 1989], but this solution is not applicable to the problem at hand.

4.3 Corner flow

Straight pores of triangular or rectangular cross-sections are commonly used in pore network models to approximate the complex and largely unknown pore geometry [*e.g.*, Ioannidis and Chatzis, 1993; Hui and Blunt, 2000; Zhao and Ioannidis, 2003; Piri and Blunt, 2005]. A pore corner filled by a wetting fluid filament, confined between the pore walls and an arc meniscus (interface separating the wetting fluid filament from the non-wetting phase filling the center of the pore) is depicted in Figure 4.1. The shape of the filament cross section is determined by the corner half angle, β, the contact angle, θ, and the radius of curvature of the interface, R_{nw}.

Under conditions of steady laminar flow, the hydrodynamic problem may be stated as follows:

$$\nabla^2 V_z = -\frac{\Delta P}{\mu L} \tag{4.1}$$

where $V_z = V_z(x, y)$ is the fluid velocity, ΔP is the pressure drop across a length L of the corner and μ is the fluid viscosity. Spatial coordinates are scaled using the meniscus-apex distance, b, defined as follows:

$$b = R_{nw} \frac{\cos\theta - \sin\beta}{\sin\beta} \tag{4.2}$$

In this manner, Equation (4.1) is written in dimensionless form as:

$$\frac{1}{\text{Re}}\nabla^2 V_z^* - \nabla P^* = 0 \tag{4.3}$$

111
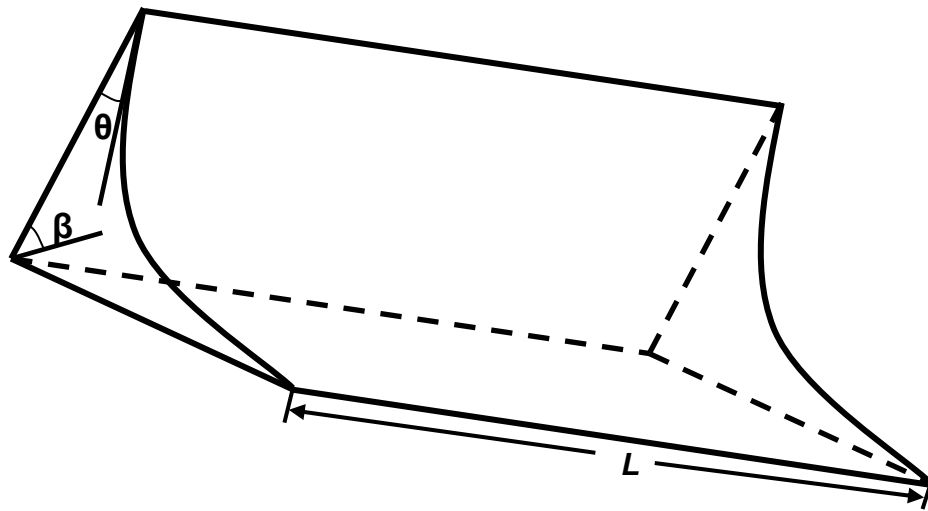
(a)
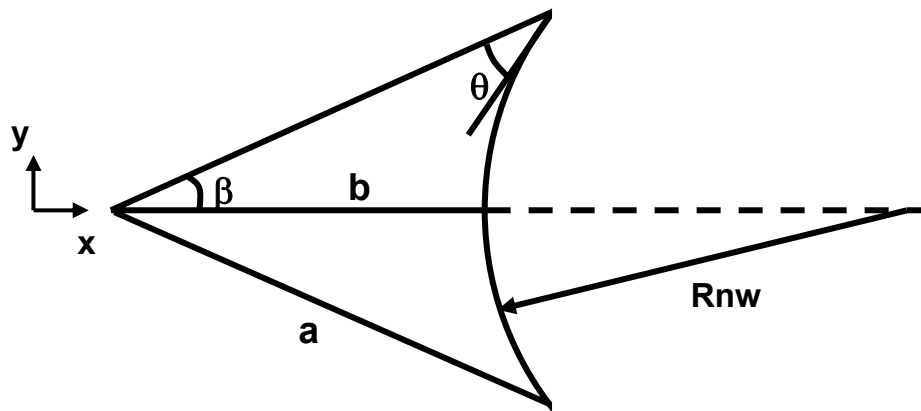
(b)

Figure 4.1 Corner fluid filament (a) and cross-section (b). Flow is perpendicular to the cross-section.

where $\mathrm{Re} \equiv (\rho V_0 b)/\mu$ is the Reynolds number, ρ is the density of the wetting fluid, $V_0 \equiv (b^2 \Delta P)/(\mu L)$ is a characteristic fluid velocity, $V_z^* \equiv V_z/V_0$ is the dimensionless fluid velocity and $P^* \equiv \Delta P/(\rho V_0^2) = L/(b\,\mathrm{Re})$ is the dimensionless fluid pressure. Due to the symmetry of the corner geometry, only half of the flow domain needs to be considered. A no-slip boundary condition is imposed along the pore walls, whereas at the fluid-fluid interface both the perfect-slip and the no-slip conditions are considered. These conditions are given by Equation (4.4) and Equation (4.5), respectively:

$$\frac{\partial V_z^*}{\partial x^*} = \frac{\partial V_z^*}{\partial y^*} = 0 \tag{4.4}$$

$$V_z^* = 0 \tag{4.5}$$

A hydraulic resistance factor may be defined as follows:

$$\chi \equiv \frac{\Delta P}{\mu L \langle V_z \rangle} b^2 = \frac{V_0}{\langle V_z \rangle} = \frac{1}{\langle V_z^* \rangle} \tag{4.6}$$

where $\langle V_z \rangle$ is the average fluid velocity and $\langle V_z^* \rangle \equiv \langle V_z \rangle / V_0$ is the dimensionless average fluid velocity. The volumetric flow rate of the wetting phase is given by

$$Q = \int_S V_z \, dS = g \frac{\Delta P}{L} \tag{4.7}$$

In Equation (4.7), S is the cross-sectional area of the half-domain,

$$S = \frac{b^2}{2} \left[\frac{\sin\beta}{\cos\theta - \sin\beta} \right]^2 \left[\frac{\cos\theta \cos(\theta + \beta)}{\sin\beta} + \beta + \theta - \frac{\pi}{2} \right] \tag{4.8}$$

and g is the hydraulic conductance,

$$g = \frac{b^4}{\mu} \int_S V_z^* dS^* = \frac{b^4}{\mu} g^* \qquad (4.9)$$

where $S^* \equiv S/b^2$ is the dimensionless cross-sectional area and g^* is the dimensionless hydraulic conductance.

Equation (4.3) is solved by a finite-element method implemented in the FEMLAB® 3.0 environment and employing the linear solver UMFPACK [Van Schijndel, 2003; COSMOL, 2003]. The PDE (incompressible Navier-Stokes equation) is predefined in the software package and the GUI for entering the input parameters is shown in Figure 4.2. Up to 14,000 triangular elements were used to discretize the 3D half-domain (see Figure 4.3) and convergence of the solutions was established by refining the meshes. Other information about boundary and sub-domain settings on FemLab® platform is given in Appendix A.
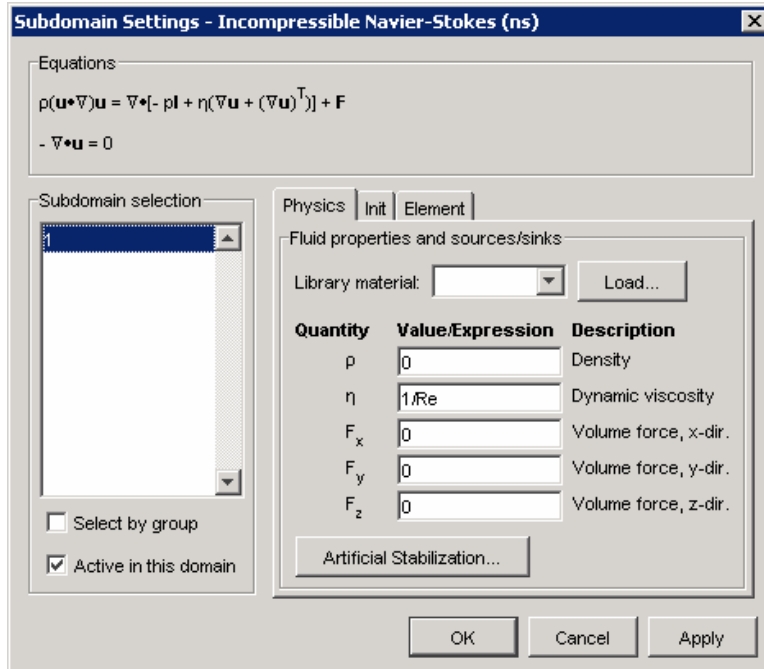
Figure 4.2 FEMLAB graphic user interface of entering sub-domain input parameters for impressible Navier-Stokes Equation.
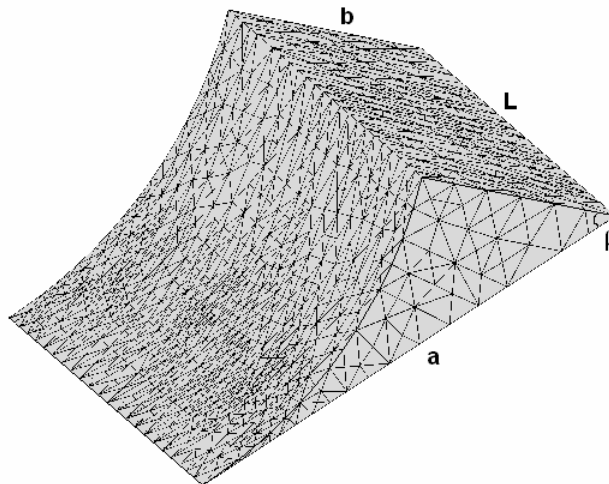
Figure 4.3 Finite element mesh for the half domain of the wetting filament.

115

4.4 Convective mass transfer in a corner filament

Equation (4.10) is the governing equation for steady transfer of a solute within the flowing corner filament to or from the fluid-fluid interface (Figure 4.1):

$$D_m \nabla^2 C = V_z \frac{\partial C}{\partial z}$$

(4.10)

where D_m is the molecular diffusion coefficient, $C = C(x, y, z)$ is the solute concentration and V_z is the fluid velocity. In dimensionless form, Equation (4.10) is written as

$$\nabla^2 C^* = Pe V_z^* \frac{\partial C^*}{\partial z^*}$$

(4.11)

where $P_e \equiv (V_0 b)/D_m$ is a pore-scale Peclet number, V_z^* is the dimensionless fluid velocity and $z^* \equiv z/b$. The dimensionless concentration is defined as

$$C^* = \frac{C - C_i}{C_0 - C_i}$$

(4.12)

where C_0 is the inlet concentration and C_i is the concentration at the fluid-fluid boundary. Both C_0 and C_i are assumed constant. The no-flux boundary condition, $\vec{n} \cdot \nabla C^* = 0$, is imposed on the pore wall.

Coupled with Equation (4.3), Equation (4.11) is solved using the same finite-element method described in Section 4.3. Predefined PDE for convection and diffusion is

solved to obtain the concentration distribution in the sub-domain. Figure 4.4 is the GUI for entering the input parameters. Boundary and sub-domain settings are given in Appendices.
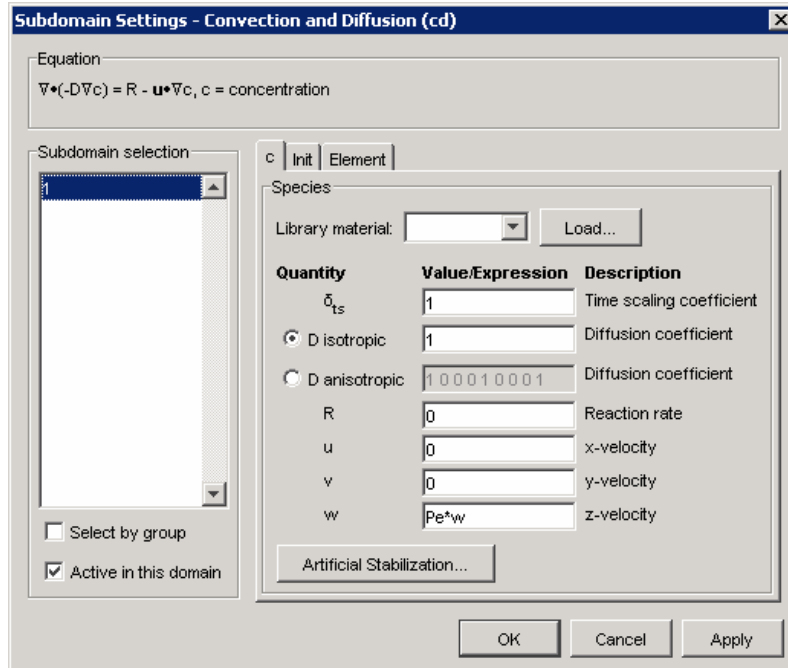
Figure 4.4 FEMLAB graphic user interface of entering sub-domain input parameters for convection and diffusion equation.

From the obtained concentration profile, the average ("mixing-cup") solute concentration, E_d, at the exit end of the corner filament is computed:

$$E_d = \frac{\int_S V^* C^* dS^*}{\int_S V^* dS^*}$$ (4.13)

For a given flow geometry (*i.e.*, fixed β and θ) and if diffusion along the *z*-direction can be neglected (*i.e.*, for sufficiently high values of *Pe*), E_d is expected to depend only on the dimensionless residence time [Dillard and Blunt, 2000; Zhou et al., 2000; Sahloul et al., 2002].

$$t_d = \frac{z D_m}{V_0 b^2} = \frac{1}{Pe} z^*$$ (4.14)

As discussed in Chapter 3, the parameter E_d is important in calculations of the concentration field in pore network models via the solution of solute mass balance equations at the network nodes.

4.5 Results and discussion

4.5.1 Hydraulic resistance factors and hydraulic conductances

Representative visualization of the velocity fields in the wetting filament is shown in Figure 4.5. Calculated dimensionless hydraulic resistance factors and hydraulic conductances for flow domains corresponding to different values of the half-angle β (30° and 45°) and contact angle θ (0°, 10°, 20°, 30° and 40°) are listed in Table 1 and Table 2, respectively. The results are compared to the numerical solutions reported by Patzek and Kristensen [2001], whose work refined results first published by Ransohoff and Radke

[1988]. The difference is less than 2%. Note that in the work of Patzek and Kristensen, the spatial coordinates are scaled with the distance a (see Figure 4.1), which is different from the meniscus-apex distance b (see Figure 4.1) used in this study.

It is important to note that the pore geometry considered here possesses translational invariance and therefore flow is characterized by one velocity component only. Stated differently, only two-dimensional arc menisci are considered. This is clearly a simplification motivated by the need for consistency with existing pore network simulators of flow and transport, which presently neglect the negative curvature of pore channels in real porous media [*e.g.*, Ransohoff and Radke, 1988; Man and Jing, 2000; Piri and Blunt, 2005]. The development of transverse velocities in a convergent-divergent pore channel geometry and their potential interaction with arc menisci in pore corners is not explored here.
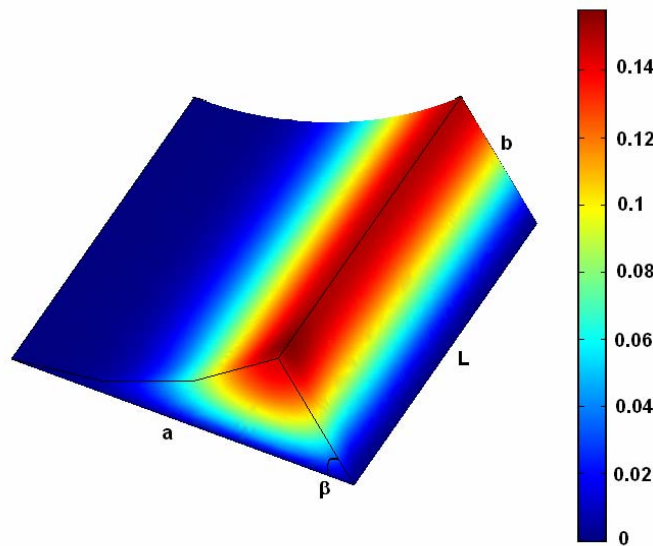
Figure 4.5 Fluid velocity distribution of wetting filament (perfect-slip condition at the fluid-fluid interface, $\beta = 45°$, $\theta = 0°$, $Pe = 50$).

Table 4.1 Hydraulic resistance factors for wetting fluid filament under conditions of perfect-slip and no slip at the fluid-fluid interface. Values in brackets are the resistance factors reported by Patzek and Kristensen [2001], but scaled with b (meniscus-apex distance defined in this work).

	$\theta \rightarrow$	0°	0°	10°	20°	30°	40°
$\beta = 30°$	perfect-slip	29.83	[30.10]	29.55	29.09	28.66	28.21
	no-slip	63.98		63.36	62.34	61.38	60.60
$\beta = 45°$	perfect-slip	15.45	[15.68]	15.17	14.78	14.42	14.08
	no-slip	42.00		41.25	40.07	39.05	38.28

Table 4.2 Hydraulic conductance of wetting fluid filament. Values in brackets are the conductance values reported by Patzek and Kristensen [2001], but scaled with b (meniscus-apex distance defined in this work).

β	$\theta \rightarrow$	0°	10°	20°	30°	40°
30°	perfect-slip	0.011481	0.011448	0.011333	0.011148	0.010951
		[0.011378]	[0.011332]	[0.011208]	[0.011032]	[0.010831]
	no-slip	0.005352	0.005340	0.005289	0.005205	0.005098
		[0.005304]	[0.005304]	[0.005250]	[0.005167]	[0.005063]
45°	perfect-slip	0.040491	0.040158	0.039169	0.037894	0.036563
		[0.03988]	[0.039512]	[0.038547]	[0.037253]	[0.035840]
	no-slip	0.014891	0.014774	0.014450	0.013991	0.013448
		[0.014764]	[0.014645]	[0.014324]	[0.013866]	[0.013324]

4.5.2   Effects of Peclet number and interface boundary condition on E_d

Representative visualization of the concentration fields in the wetting filament is shown in Figure 4.6. The normalized average effluent concentration, E_d, is plotted against the dimensionless corner length, L/b, in Figure 4.7. This figure reveals the effects of Peclet number and interface boundary condition. As expected, solute concentration reaches equilibrium ($E_d = 0$) over shorter distances along the corner for smaller values of the Peclet number, that is as diffusion becomes increasingly dominant over convection. The choice of interface boundary condition has a discernible effect on E_d, which is more pronounced at higher values of Pe (see Figure 4.7).
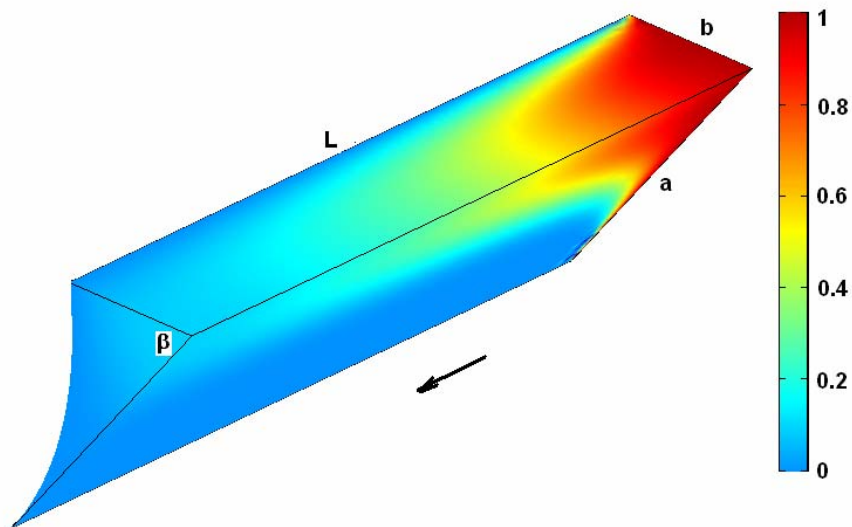
Figure 4.6 Solute concentration distribution in the wetting filament (perfect-slip condition at the fluid-fluid interface, $\beta = 45°$, $\theta = 0°$, $Pe = 150$).
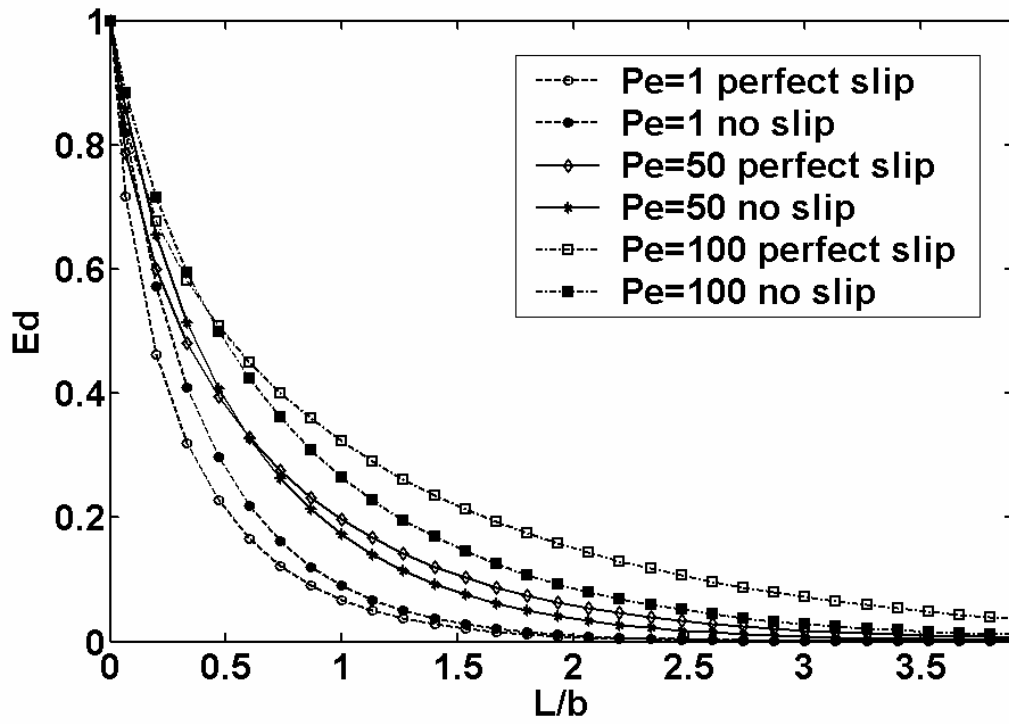
Figure 4.7 Effects of Peclet number and boundary condition at the interface ($\beta = 45°$, $\theta = 0°$).

4.5.3 Empirical correlations for E_d

For any fixed value of P_e and half-angle β, the value of contact angle θ has a negligible effect on computed values of E_d (see Figure 4.8). It is also found that E_d is independent of Pe for $Pe \leq 1$ (see Figure 4.9), and that it depends only on the dimensionless residence time, t_d (cf. Equation 4.14), for sufficiently high values of Pe (see Figure 4.10), as expected.
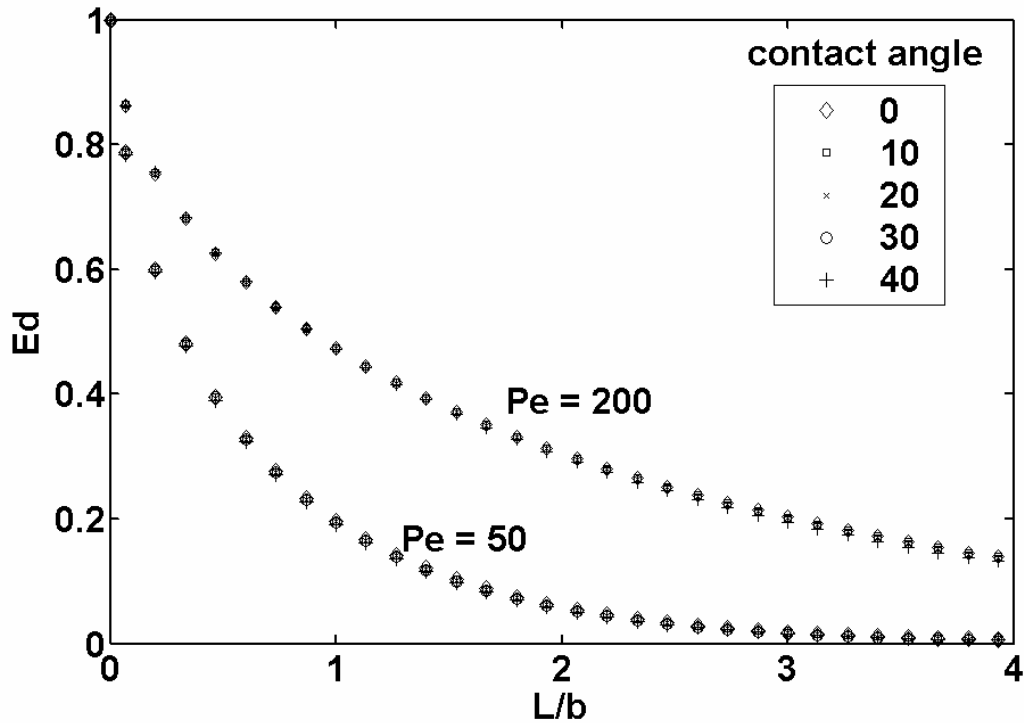
Figure 4.8 Effect of contact angle ($\beta = 45°$, perfect slip at the interface).

On the basis of these observations, the results of all computations are correlated in terms of a parameter ψ that smoothly interpolates between the behavior for low and high *Pe* values and is defined as follows:

$$\psi = \begin{cases} \dfrac{L}{b} & Pe \leq 1 \\[3em] \dfrac{1+\alpha Pe + \eta \ln Pe}{1 + \alpha Pe^2 + \eta (\ln Pe)^2}\left(\dfrac{L}{b}\right) & \begin{array}{l} 1 < Pe \leq 100 \ (\text{perfect slip}) \\[0.5em] 1 < Pe \leq 150 \ (\text{no slip}) \end{array} \\[3em] \dfrac{1}{Pe}\left(\dfrac{L}{b}\right) & \begin{array}{l} Pe > 100 \ (\text{perfect slip}) \\[0.5em] Pe > 150 \ (\text{no slip}) \end{array} \end{cases} \tag{4.15}$$

where α and η are empirical coefficients, the values of which depend on the half-angle, β, and the interface boundary condition. As shown in Figure 4.11, E_d curves for intermediate *Pe* values collapse into a single curve when ψ is defined according to Equation (4.15). A different master curve is obtained for each value of half-angle β and each choice of interface boundary condition. These master curves can be fitted by the following function:

$$E_d = \gamma \exp[-\lambda \psi^w] + (1-\gamma)\exp[-\sigma \psi] \tag{4.16}$$

in terms of the adjustable parameters γ, λ, w, and σ. This fitting function is shown as a solid line in Figure 4.9 - 4.11, whereas best-fit values of the parameters are listed in Table 4.3. Typical absolute and relative errors of the correlation, Equation (4.16), with respect to the numerical solution are shown in Figure 4.12 and 4.13. Relative errors are less than $\pm 10\%$, except at the exit end of the pore where E_d values are close to zero. Correlation of

the E_d data in terms of Equation (4.15) and Equation (4.16) facilitates the incorporation

of the results of this study in pore network models and should lead to more accurate

computations of mass transfer to or from trapped fluid phases in porous media [Dillard

and Blunt, 2000].
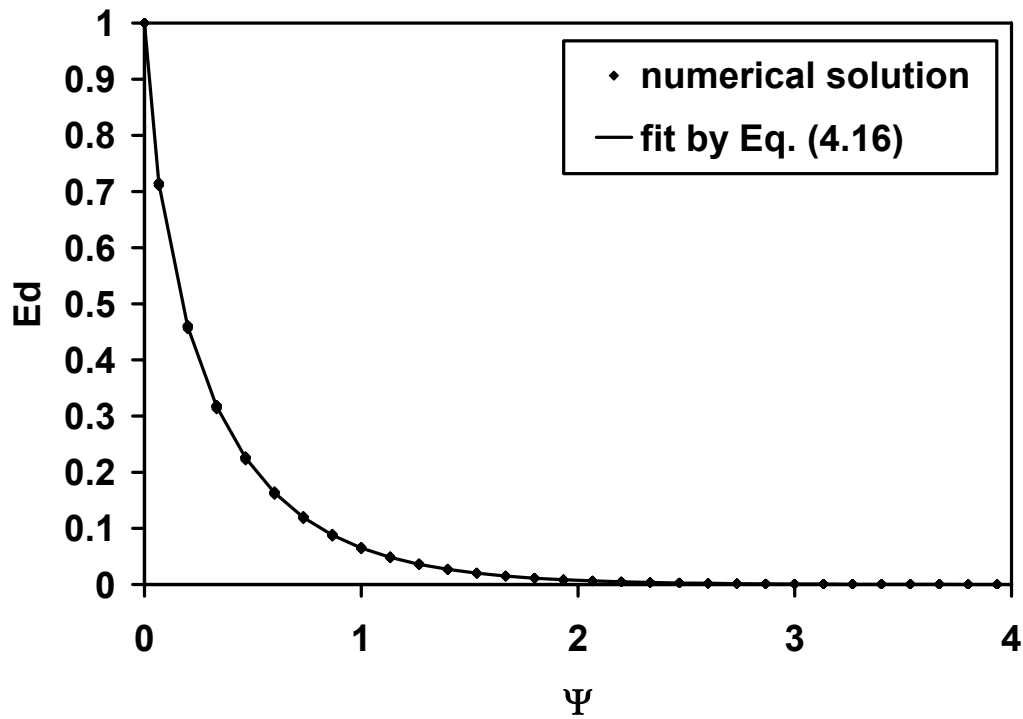
Figure 4.9 Dimensionless average exit concentration E_d as a function of the parameter ψ

for $P_e \leq 1$ ($\beta = 45°$, perfect slip at the interface, $\theta = 0°$, 10°, 20°, 30°, 40°).
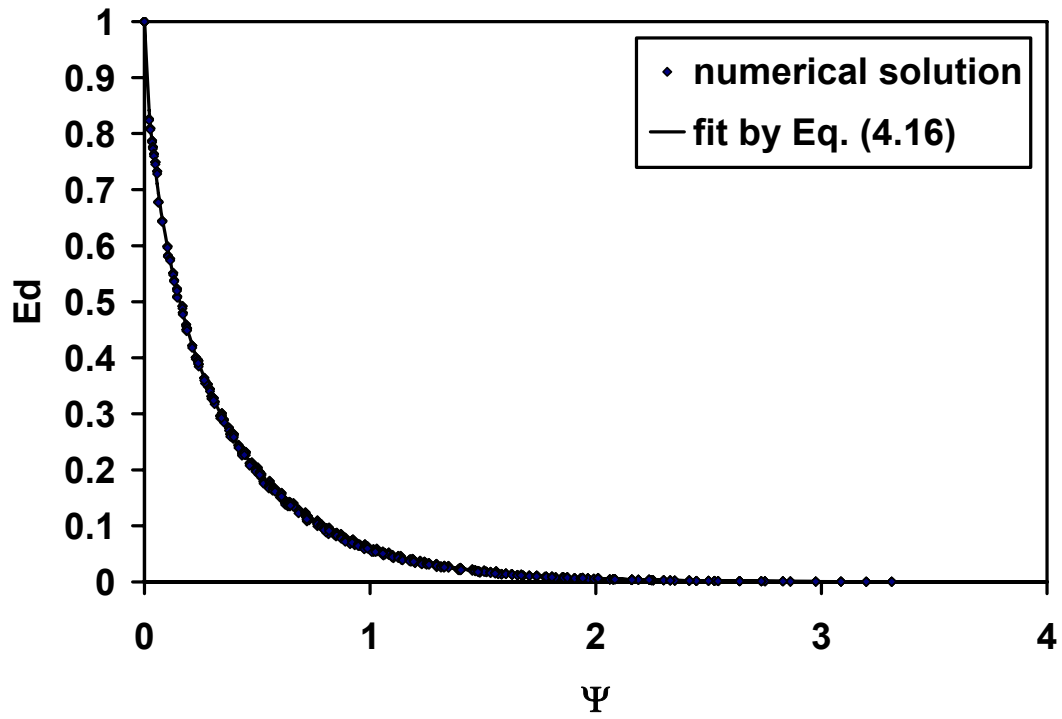
Figure 4.10 Dimensionless average exit concentration E_d as a function of the parameter

ψ for $1 \le P_e \le 100$ ($\beta = 45°$, perfect slip at the interface, $\theta = 0°$, $10°$, $20°$, $30°$, $40°$).
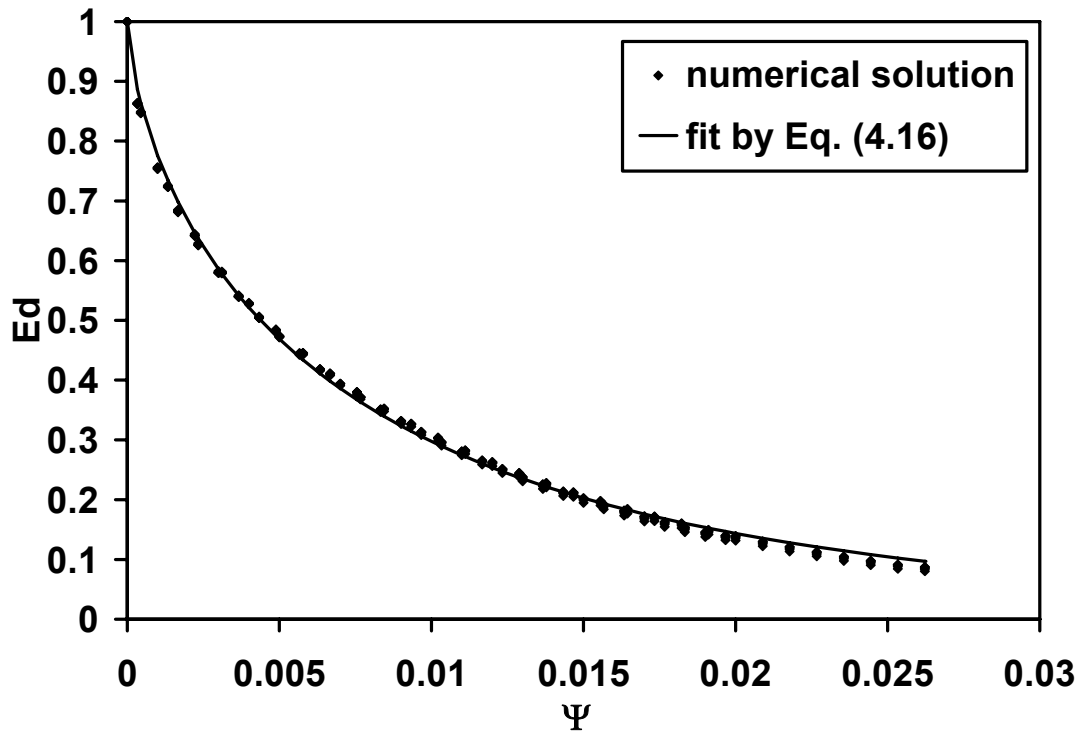
Figure 4.11 Dimensionless average exit concentration E_d as a function of the parameter ψ for $P_e > 100$ ($\beta = 45°$, perfect slip at the interface, $\theta = 0°$, $10°$, $20°$, $30°$, $40°$).

Table 4.3. Correlation parameters for Equation (4.16)

β	B.C.		α	η	γ	λ	w	σ
45°	Perfect-slip	Pe≤1			0.502429	4.45084	0.754991	2.1272
		1<Pe≤100	0.00018526	0.066813	0.441819	4.836317	0.672339	2.302964
		Pe>100			1	27.65009	0.679092	
45°	No-slip	Pe≤1			0.232082	5.286217	0.943766	2.180605
		1<Pe≤150	5.4122E-05	0.036969	0.207129	6.930067	0.911547	2.279209
		Pe>150			1	75.93903	0.837611	
30°	Perfect-slip	Pe≤1			0.566622	4.266318	0.750798	2.18938
		1<Pe≤150	5.0522E-05	0.019809	0.542916	3.980639	0.688368	2.28511
		Pe>150			1	61.91404	0.729914	
30°	No-slip	Pe≤1			0.249056	6.023966	1.001145	2.287237
		1<Pe≤150	2.2207E-05	0.01823	0.220152	7.112064	0.990951	2.363122
		Pe>150			1	142.1271	0.879357	
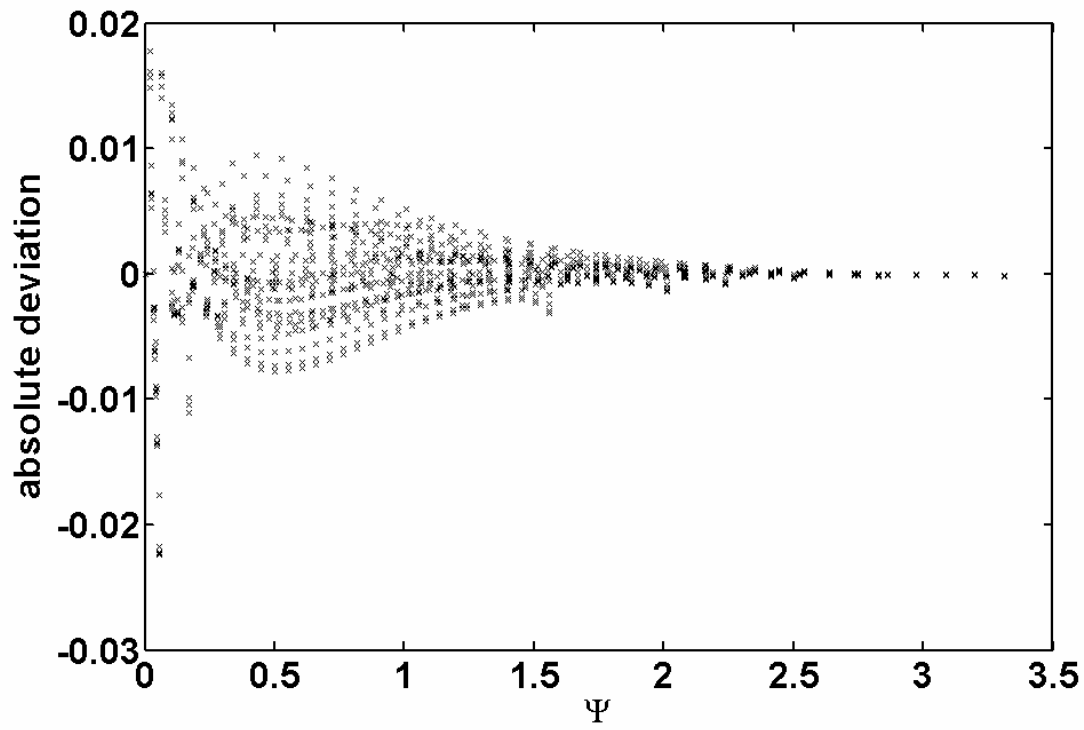
Figure 4.12 Absolute deviation of correlation, Equation (4.16), from simulation data for

$1 \leq P_e \leq 100$ (β = 45°, perfect slip at the interface, θ = 0°, 10°, 20°, 30°, 40°).
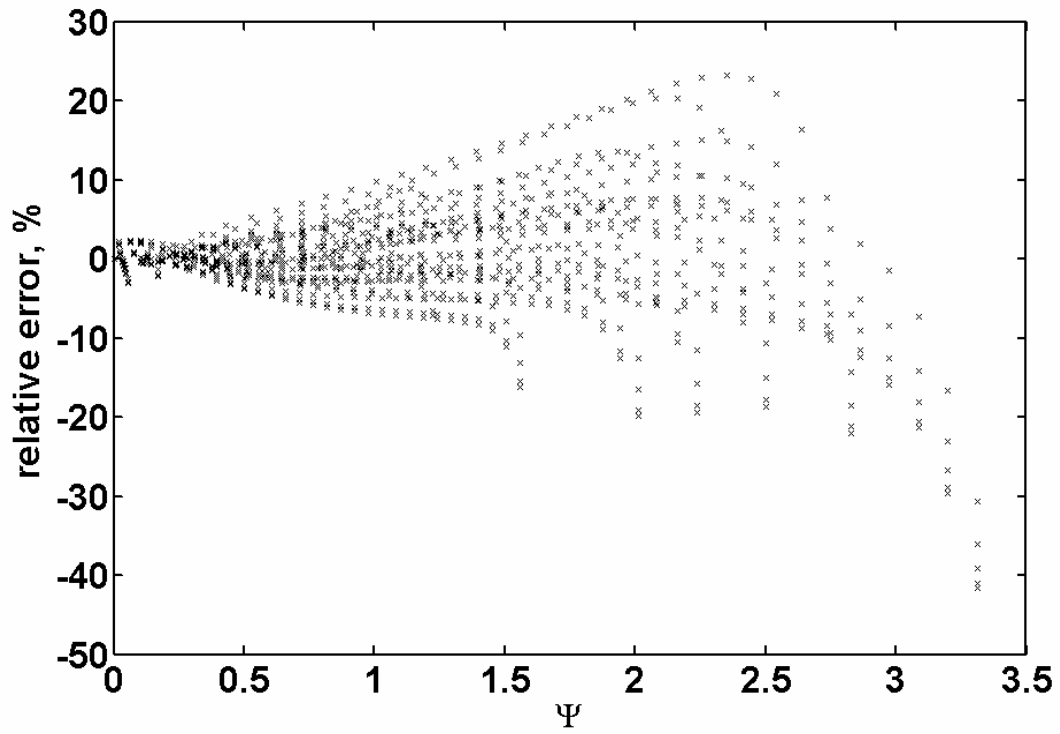
Figure 4.13. Relative error of correlation, Eq. [16], with respect to numerical solution for $1 \le P_e \le 100$ ($\beta = 45°$, perfect slip at the interface, $\theta = 0°, 10°, 20°, 30°, 40°$).

4.5.4 Comparison to the 2D slit model

In previous studies, convective mass transfer within a 3D corner fluid filament has been approximately analyzed in terms of convective mass transfer in a 2D slit [Dillard and Blunt, 2000; Zhou et al., 2000; Sahloul et al., 2002]. As shown in Figure 4.14, the pore corner is approximated by a slit formed between two parallel flat surfaces, the pore wall and the fluid-fluid interface. Both no-slip and perfect-slip interface boundary conditions are considered in the calculation of the flow field.
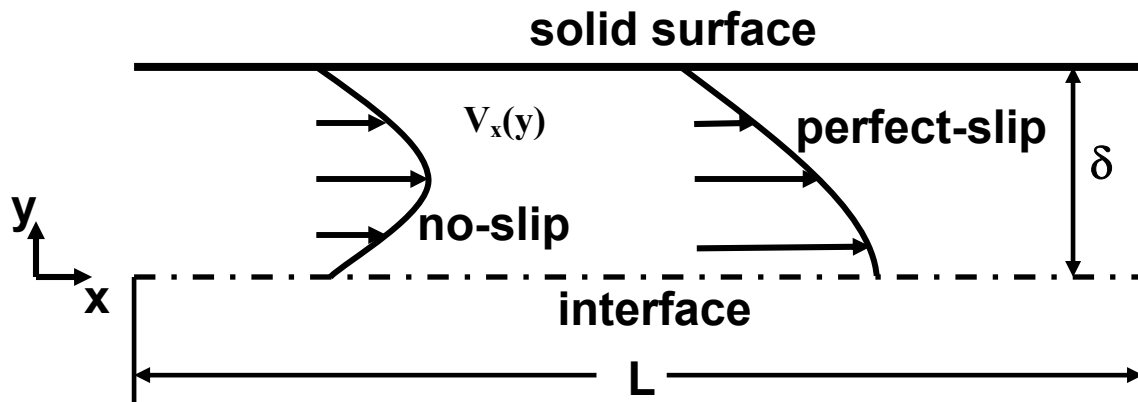
Figure 4.14 Schematic of slit model with velocity profiles under no-slip and perfect-slip conditions at the interface.

Referring to Figure 4.14, the boundary conditions for solute transport in the slit model may be expressed as:

$$V_x(\delta) = 0 \tag{4.17}$$

$$V_x(0) = 0 \qquad \text{no-slip at the interface} \tag{4.18}$$

$$\left. \frac{dV_x}{dy} \right|_{y=0} = 0 \qquad \text{perfect-slip at the interface} \tag{4.19}$$

The flow velocity profiles can be obtained by solving the motion equation with the following elementary results:

No-slip at the interface:
$$V_x(y) = \frac{\Delta P}{2\mu L}(\delta y - y^2) \tag{4.20}$$

$$\left\langle V_{slit} \right\rangle = \frac{\Delta P}{12\mu L}\delta^2 \tag{4.21}$$

Perfect-slip at the interface:
$$V_x(y) = \frac{\Delta P}{2\mu L}(\delta^2 - y^2) \tag{4.22}$$

$$\left\langle V_{slit} \right\rangle = \frac{\Delta P}{3\mu L}\delta^2 \tag{4.23}$$

where V is the fluid velocity, ΔP is the pressure drop across the corner length, μ is the fluid viscosity and $\left\langle V_{slit} \right\rangle$ is the average velocity.

Assuming that convection dominates diffusion along the x-direction, steady state solute transport is governed by the following equation:

$$V_x(y)\frac{\partial C}{\partial x} = D_m \frac{\partial^2 C}{\partial y^2} \tag{4.24}$$

133

where D_m is the molecular diffusion coefficient and C is the solute concentration. Similar with Equation (4.10-4.11), Equation (4.24) can be written in dimensionless form:

$$\frac{\partial^2 C^*}{\partial y^{*2}} = Pe V^* \frac{\partial C^*}{\partial x^*}$$

(4.25)

where $V^* \equiv \dfrac{V_x}{V_0}$, $x^* \equiv \dfrac{x}{\delta}$, $y^* = \dfrac{y}{\delta}$, $V_0 \equiv \dfrac{\Delta P}{\mu L}\delta^2$, $C^* = \dfrac{C - C_{int}}{C_0 - C_{int}}$, $P_e \equiv \dfrac{V_0 \delta}{D_m}$, C_0 is the inlet concentration and C_{int} is the interfacial concentration. Accordingly, the average ("mixing cup") exit concentration, E_d, and the dimensionless residence time, t_d, are defined as

$$E_d = \frac{\displaystyle\int_0^1 V^* C^* dy^*}{\displaystyle\int_0^1 V^* dy^*}$$

(4.26)

$$t_d = \frac{LD_m}{V_0 \delta^2} = \frac{1}{Pe}\frac{L}{\delta}$$

(4.27)

Equation (4.25) is solved numerically using the method of lines (described in Chapter 3).

It is interesting to ask if transport in the 3D filaments considered in this work can be quantitatively modeled as transport in a 2D slit. In view of the definition of Pe, setting $\delta = b$ results in the same value of Pe in a 2D slit as in a 3D filament. The E_d vs. t_d curves from the 2D slit model are compared to those from the 3D filament model in Figure 4.15 for perfect slip at the interface, and in Figure 4.16 for no slip at the interface.

These comparisons make it clear that convective transport to/from fluid-fluid interfaces in rectangular or triangular pores cannot be quantitatively modeled as convective transport in a 2D slit, as previously assumed [Dillard and Blunt, 2000; Zhou et al., 2000].
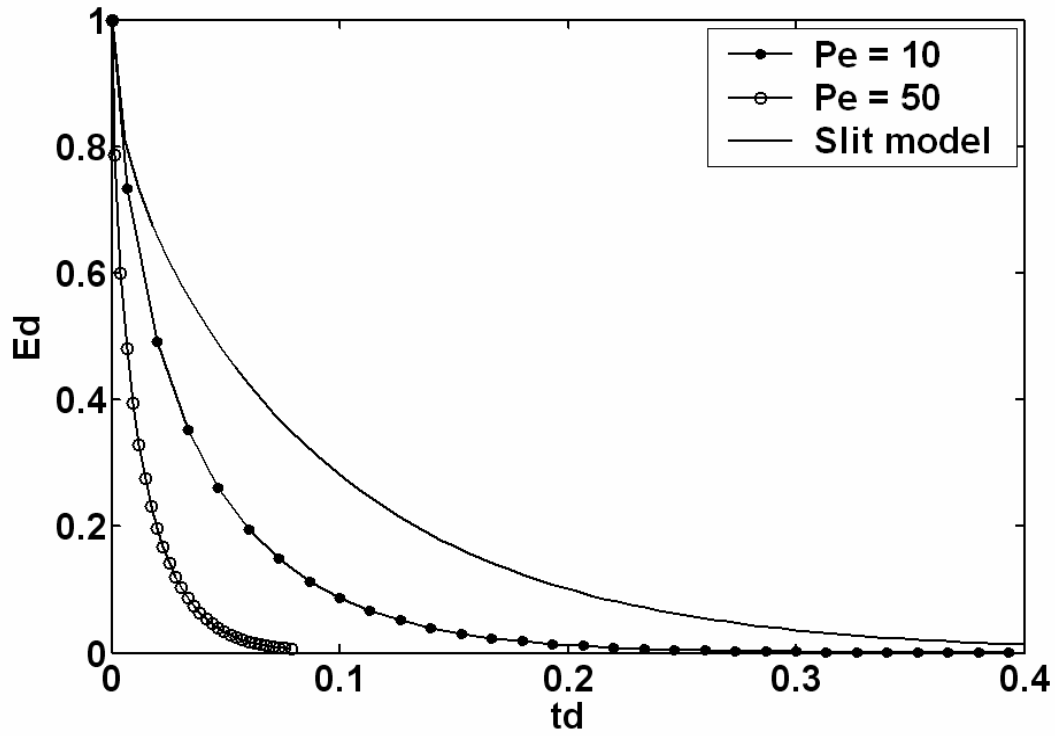
Figure 4.15 E_d vs. t_d curves for convective transport in 3D corner filament (markers) and 2D slit (solid line) ($\beta = 45°$, $\theta = 0°$, perfect-slip condition at the interface).
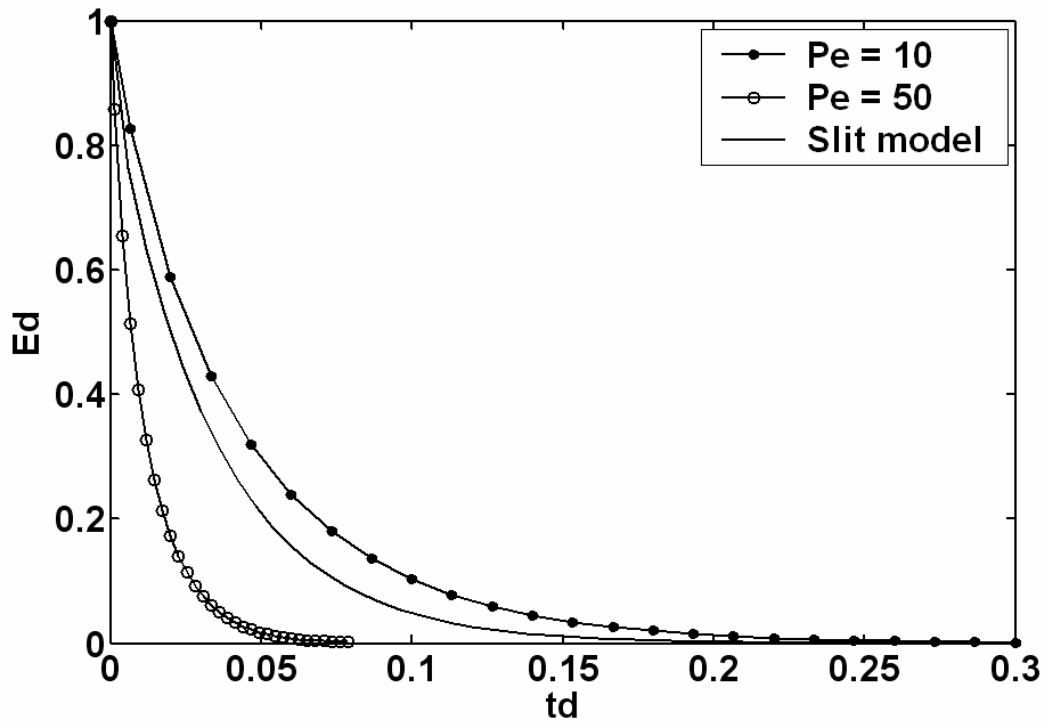
Figure 4.16 E_d vs. t_d curves for convective transport in 3D corner filament (markers) and

2D slit (solid line) ($\beta = 45°$, $\theta = 0°$, no-slip condition at the interface).

4.5.5   Verification and discussion on solution of convective mass transfer equations

The FEMLAB environment has been successfully used by others to solve complex problems involving coupled PDEs [e.g., van Schijndel, 2003]. In FEMLAB the finite element mesh is automatically generated by triangulation of the domain (see Figure 4.3). This mesh is used for discretization of the PDE problem and can be modified to improve accuracy. The linear solver is UMFPACK and a reference to the FEMLAB manual is made where further information on this solver may be found. For the flow problem, Equation (4.3), obtained numerical solutions of hydraulic resistance factors and hydraulic conductances (see section 4.5.2) are in very good agreement with the results of Patzek and Kristensen [2001]. For the coupled flow and transport problem, Equation (4.3) and Equation (4.11), finite element solutions are obtained for the case of 2D slit geometry (Figure 4.14). Figure 4.17 is the discretization and solute concentration profile of the slit domain. The results are in good agreement with the analytical solution of Equation (4.25) by the method of lines (valid for Pe sufficiently high to neglect axial diffusion), as shown in Figure 4.18.

If solute diffusion in the direction of liquid flow can be ignored (high Peclect number situations) then Equation (4.11) becomes:

$$\frac{\partial^2 C^*}{\partial x^2} + \frac{\partial^2 C^*}{\partial y^2} = Pe V_z^* \frac{\partial C^*}{\partial z^*}$$
(4.28)

Using the method of separation of variables, Equation (4.28) has a solution in the form:

$$C^*(x, y, z) = \exp(-\lambda z) C_\lambda^*(x, y)$$
(4.29)

where the eigenfunctions $C_\lambda^*(x, y)$ are solutions of the equation

$$\nabla^2 C_\lambda^* + \lambda Pe V_z^* C_\lambda^* = 0 \qquad (4.30)$$

A general solution of Equation (4.28) may then be expressed as the sum or integral in λ of the solutions of Equation (4.30), which leads to the following general expression for the average solute concentration, E_d:

$$E_d = \sum_\lambda \beta_\lambda \exp(-\lambda z) \frac{\int_S V_z^* C_\lambda^* dS}{\int_S V_z^* dS} \qquad (4.31)$$

where β_λ are coefficients selected to fit the boundary conditions.

Equation (4.31) shows that E_d is expected to be given in terms of a sum of exponentials. This provides justification for the empirical correlation (Equation 4.16), since it is well known that a stretched-exponential function can be used to approximate a sum of exponentials [Peyron et al., 1996].
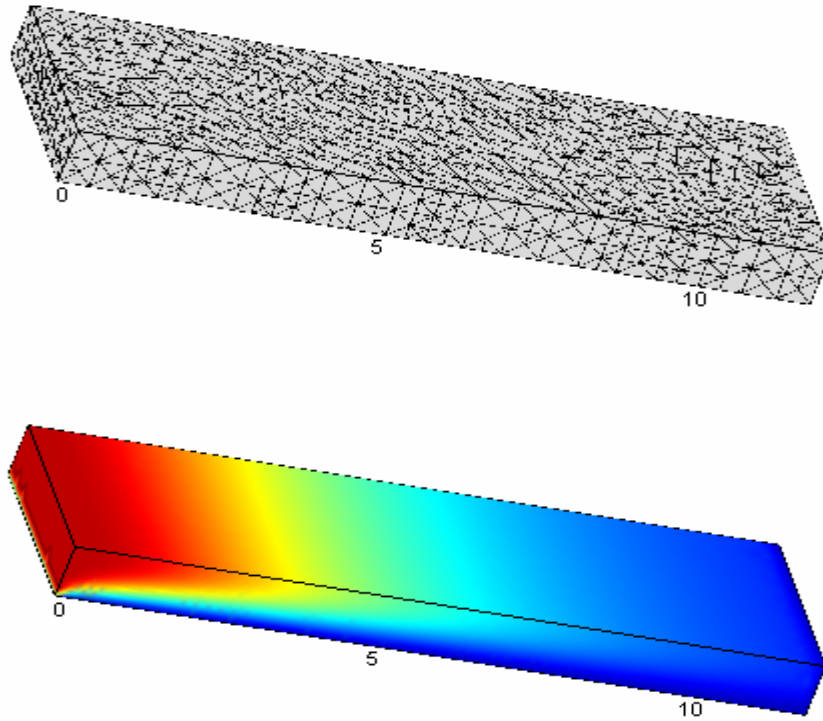
Figure 4.17 Mesh and concentration profile of a slit. x = 4, y = 1, z = 12, 16504 elements,

Pe = 150. Same colormap as in Figure 4.6.
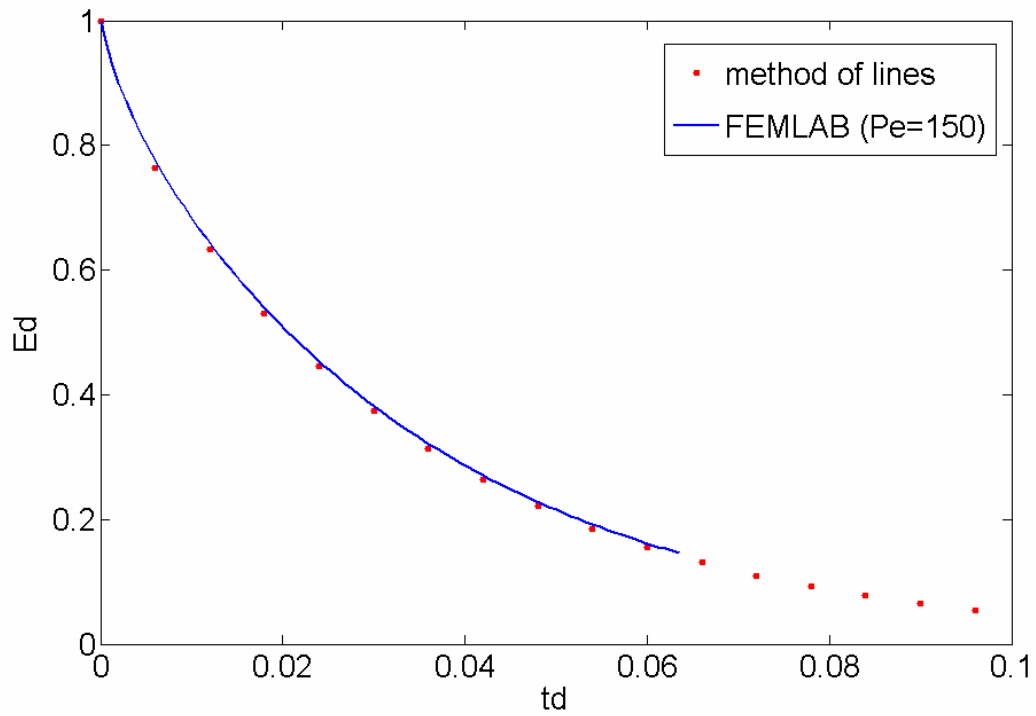
Figure 4.18 Comparison of E_d-t_d results between method of lines and FEMLAB.

4.6   Conclusions

With an aim to improve pore network computations of mass transfer to/from trapped non-aqueous phase ganglia or bubbles in porous media, we used finite element methods to study convective mass transfer in wetting fluid filaments along corners of angular pores. The flow and transport domain was described in terms of the corner half-angle, contact angle and interfacial meniscus curvature, thus accounting for the exact geometry of the fluid filament confined within the pore walls and an arc meniscus. Both perfect-slip and no-slip interfaces were considered. Solution of the flow problem yielded hydraulic resistance factors and hydraulic conductance of the corner filaments in agreement with the numerical results reported by Patzek and Kristensen [2001]. Novel results were obtained for the normalized average exit concentration in corner filaments. These results were correlated with the pore-scale Peclet number and the characteristic dimensions of the corner geometry, facilitating their use with pore network simulators in which pores and throats are modeled as straight tubes of rectangular or equilateral triangular cross-sections.

Chapter 5

Pore Network Simulation of Gas Evolution during Supersaturated Water Injection

5.1   Summary

In situ bubble growth in porous media is simulated using a 2D pore network model that idealizes the pore space as a lattice of cubic chambers connected by square tubes. Evolution of the gas phase from nucleation sites is driven by solute mass transfer from the flowing supersaturated water solution to the bubble clusters. Effects of viscous aqueous phase flow and convective diffusion in pore corners are explicitly accounted for. Growth of bubble clusters is characterised by a pattern of quasi-static drainage and fingering in the gas phase, an invasion percolation process controlled by capillary and gravitational forces. A stepwise solution procedure is followed to determine the aqueous flow field and the solute concentration field in the model by solving the conservation equations. Mobilization of bubbles driven by buoyancy forces and bubble fragmentation and coalescence are also modeled. Results of bubble growth pattern, relative permeability and macroscopic mass transfer rate coefficient are obtained under different gas saturations and aqueous flow conditions.

5.2 Background

In situ development of gas saturation within initially fluid-saturated porous media is encountered in a variety of processes of technological significance (for example the solution gas-drive (SGD) process for oil recovery [Sheng et al., 1999a; b; Bora et al., 2000], the CO_2 evolution process in gas diffusion layer inside direct methanol fuel cells (DMFC) [e.g., Argyropoulos et al., 1999 a; b; Yang et al., 2005], the CO_2 leakage from CO_2 storage reservoir [e.g., Pruess, 2005], accumulation of biogenic bubbles in peat [e.g., Reynolds et al., 1992; Beckwith and Baird, 2001; Kellner et al., 2004], the oxygen delivery during bioremediation [e.g., Wilson et al., 1994; Borden et al., 1997; Deeb et al., 2000], the supersaturated water injection (SWI) for NAPL recovery [Li, 2004]). The growth of gas phase in porous media involves the interplay of many factors, such as bubble nucleation, capillarity, diffusion and advection, all of which should be accounted for in studying multi-phase flow and mass transfer issues in porous media.

5.2.1 Bubble Nucleation

Nucleation is the process of formation of bubbles in a pure homogeneous liquid or a solution containing dissolved gas at supersaturation. The saturation or equilibrium concentration of a dissolved gas in the aqueous phase at a certain temperature can be determined by Henry's law:

$$x_i = \frac{P_i}{H} \qquad (5.1)$$

where x_i is the mole fraction of dissolved gas in the aqueous phase, P_i is the partial

pressure of the gas and H is Henry's constant. Supersaturation is the condition for which the dissolved gas concentration exceeds the equilibrium value at the system temperature and pressure. In most studies devoted to the problem of gas evolution in porous media due to solute diffusion, supersaturation is achieved by depressurizing the system [e.g., Li and Yortsos, 1995a; El Yousfi, et al., 1997; Dominguez et al., 2000].

A supersaturated solution is thermodynamically unstable such that bubbles will nucleate and subsequently grow by solute mass transfer. Pre-existing nuclei or cavities with trapped micro-bubbles are usually considered responsible for bubble generation at low levels of supersaturation [e.g., Dean, 1944; Jones et al., 1998; Li and Yortsos, 1995a, b; Bora et al., 2000], otherwise high levels of supersaturation are required [Kamath and Boyer, 1995; Jones et al., 1999a, b]. The mechanism of bubble production in the former case is referred to as heterogeneous nucleation, whereas the latter is termed homogeneous nucleation.

The most plausible bubble nucleation mechanism in porous media is heterogeneous nucleation [Yortsos and Parlar, 1989; Kamath and Boyer, 1995; Dominguez et al. 2000], in which case a nucleation site (crevice) on the pore wall containing pre-existent or nucleated gas is activated when the local supersaturation exceeds the capillary barrier of the site. Figure 5.1 shows the mechanism of heterogeneous nucleation in a pore with a pre-existing micro-bubble trapped in wall crevice. The necessary condition is expressed by the following equation

$$HC - P_l \geq \frac{2\gamma}{W}$$
(5.2)

where H is the Henry constant, C and P_l are local solute concentration and pressure in the liquid respectively, γ is the interfacial tension and W is the radius of the crevice mouth.
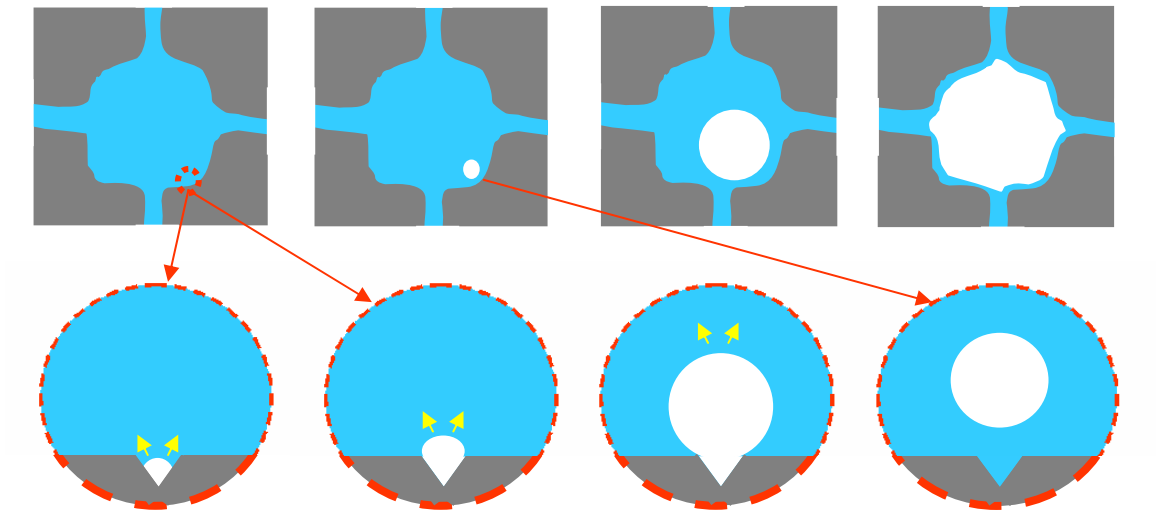
Figure 5.1 Schematic of bubble nucleation from a crevice with a pre-existing nucleus.

Kashchiev and Firoozabadi [1993], Firoozabadi and Kashchiev [1996] and Firoozabadi [1997] suggested that a number of bubbles can nucleate at the same time on randomly distributed sites and are not generated from pre-existing microbubbles. However, this instantaneous nucleation (homogeneous) mechanism, which does not take the surface heterogeneity into consideration, could be valid only when a sudden increase in supersaturation occurs. With a gradual supersaturation change, for example during slow pressure depletion, the heterogeneous or progressive nucleation would be the mechanism at play [Li and Yortsos, 1995a; b]. Experiments using micromodels [El Yousfi, et al., 1997] show that bubbles of the order of 1 µm appear progressively in supersaturated carbonated water before they are released from the pore walls and continue to grow. Their observations are in agreement with the heterogeneous nucleation model. However, the period of bubble nucleation is short (about 15% of the time

required in pressure depletion) and the instantaneous mechanism could be applied to approximate the nucleation process in exploring bubble evolution over a long period [Arora and Kovscek, 2003].

5.2.2 Bubble growth

Once nucleated, gas bubbles begin to grow as a result of mass transfer driven by the solute concentration difference between the supersaturated bulk liquid phase and the solute concentration at the gas-liquid interface. Transparent micromodel observations show that initial bubble nucleation is followed by rapid detachment of the bubble from the pore wall and migration towards the center of the pore [e.g., El Yousfi et al., 1991; Dominguez et al., 2000], where it continues to grow until it fills the pore body (see Figure 5.1). SGD experiments in transparent micromodels by George et al. [2005] also show that nucleated bubbles grow to fill pores before they are mobilized.

The difference between SGD and SWI is that in the former process, mass transfer is controlled by solute diffusion, while the latter process is controlled by convective mass transfer. Growth of gas bubbles involves two periods of the process: increase of gas volume as a result of solute mass transfer, corresponding to the growth of unconfined bubbles and increase of gas pressure, corresponding to the growth of single bubbles or gas clusters confined by capillary forces within pore bodies.

The general convection-diffusion equation for solute mass transfer in a bulk fluid phase can be written as [Li and Yortsos, 1995a]:

$$\frac{\partial C}{\partial t} + \vec{u} \bullet \nabla C = D \nabla^2 C \qquad (5.3)$$

146

where C is the volatile component concentration at the interface, D is the molecular diffusivity and $\bar{u}$ is the liquid velocity. For creeping flow and in the absence of gravity, the liquid velocity $\bar{u}$ obeys Stoke's equation:

$$\nabla P_l = \mu \nabla^2 \bar{u} \tag{5.4}$$

where P_l is the liquid pressure and μ is the liquid viscosity.

Contrary to the gas growth pattern in bulk phase, the bubble growth pattern in porous media is disordered and non-symmetric, reflecting the pore structure of the medium. Visualization experiments using micro-models show that invasion percolation (IP) is the growth mechanism whereby a locally spherical interface advances in the perimeter pore throat with the smallest capillary resistance ($P_g - P_l \geq P_c$) and subsequently occupies the adjacent pore, developing a ramified cluster [e.g., Li and Yortsos, 1995a; Dominguez et al., 2000]. However, for sufficiently large clusters, pressure drops in the liquid phase may be comparable to capillary forces and viscous effects must be considered [Satik, et al. 1995; Li and Yortsos, 1995 b]. This is also true when gravitational effects are considered [Hawes et al., 1996; Dominguez et al., 2000; Tsimpanogiannis and Yortsos, 2004]. The "one-at-a-time" IP pattern of bubble cluster growth can thus be violated such that gas phase may invade more than one perimeter pore throats at the same time as long as the capillary forces are overcome. The corresponding pattern is of the viscous fingering type and similar to DLA (diffusion-limited aggregation). Satik et al. [1995] studied growth patterns of a single bubble cluster and defined two critical radii of the bubble (R^P and R^{vf}) to determine the growth patterns (IP or DLA). When the characteristic cluster radius R is smaller than R^P, the growth is capillary-controlled and the percolation pattern is followed. When R is larger than R^{vf}, the

growth is viscous controlled and the DLA pattern is followed. A combined mechanism (percolation-modified DLA) was adopted when R is between the two critical values. The analyses of patterns and rates of bubble growth show that for a fixed supersaturation value, R^P and R^{vf} are a function of the capillary number

$$Ca = \frac{u\mu}{\sigma}$$
(5.5)

where u is the bubble velocity, μ is the liquid viscosity and σ is the interfacial tension. Both critical values tend to decrease with an increase of Ca, while higher supersaturation with the same capillary number leads to smaller critical radii.

Two bubbles may coalesce when they come close to each other as a result of migration or growth. This process involves drainage of the liquid film between two approaching menisci. In the absence of surfactants, critical thinning of the liquid film is likely to occur, leading to coalescence of the bubbles.

Bubble snap-off may take place in the pore throat when the interface moves through an invaded throat to a sufficiently large pore. A conceptual model of the snap-off process is shown in Figure 5.2. The liquid distribution in a noncircular capillary becomes unstable to snap-off as the interfacial curvature J decreases to a critical value, corresponding to the curvature of the inscribed circle [Ransohoff et al., 1987]. When the critical curvature is reached, the instability results in an essentially instantaneous snap-off process [Roof, 1970; Ransohoff et al., 1987]. Ransohoff et al.'s [1987] study of moving bubble behavior in smoothly constricted noncircular capillaries sets the criterion of bubble snap-off, which can be expressed as

$$R_p \geq J^* R_t$$
(5.6)

where R_p and R_t are the radii of the invaded pore and throat, respectively, and J^* is the critical interfacial curvature.

During imbibition displacement, snap-off can also take place. Snap-off capillary pressure during imbibition in pore throats could be computed as [Li and Wardlaw, 1986]

$$P_c^{snap-off} = \frac{P_c^{piston}}{\xi} \tag{5.7}$$

where P_c^{piston} is the drainage capillary pressure for piston-type invasion of the non-wetting phase into a pore or throat and ξ is the critical pressure ratio, the value of which depends on the local pore geometry [Tsakiroglou and Payatakes, 1991; Ioannidis and Chatzis, 1993]. In the absence of surfactant to stabilize the liquid film between bubbles, the new bubble formed by snap-off will likely recombine with the parent bubble if the latter continues to expand [Kam et al., 2001].
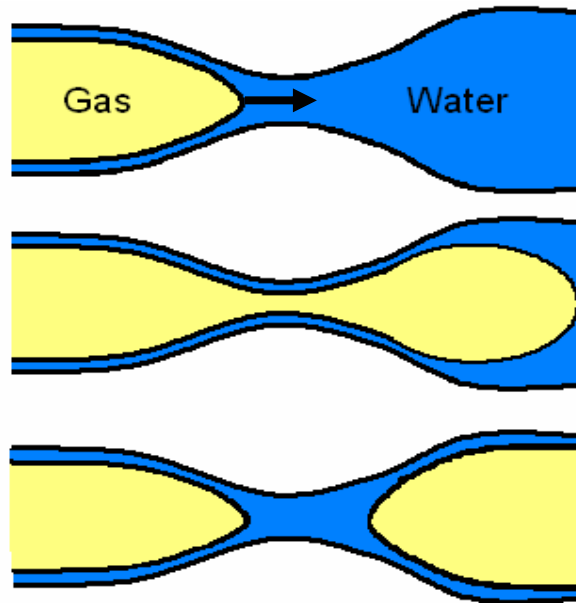
Figure 5.2 Schematic of bubble snap-off during gas expansion.

5.2.3 Bubble mobility

Multiple clusters can arise from various nucleation sites and each of them will grow provided that appropriate conditions for mass transfer into the cluster are met. Due to the growth and coalescence of clusters, the gas phase may become free to flow when a sample-spanning cluster is formed. This corresponds to the so-called critical gas saturation S_{gc} [e.g. Li and Yortsos, 1995b; Hawes et al. 1996] (foamy oil flow is an exception, where the gas released into oil flows in the form of small dispersed bubbles under conditions of solution gas drive [Sheng et al., 1999a]). Measured values of the critical gas saturation in the literature range from 0.5% to 38% PV [Sheng et al. 1999a]. The variation depends on experimental conditions. Many factors can affect the critical gas saturation. As supersaturation increases, the critical gas saturation also increases [Firoozabadi et al., 1992]. The pore structure seems to influence the critical gas saturation more than does the permeability of the medium [Kortekaas and van Poelgeest, 1991; Firoozabadi et al., 1992]. The nucleation fraction, which is defined as the number fraction of nucleated sites in the medium, determines the number of evolving clusters around the sites. Assuming low supersaturation or slow pressure depletion rate and fast mass transfer, Du and Yortsos [1999] simulated the critical gas saturation using a pore network model in the absence of viscous and gravity forces and obtained correlations between S_{gc} and the final nucleation fraction f_q: $S_{gc} = f_q^{0.16}$ in 3D and $S_{gc} = f_q^{0.09}$ in 2D. The validity of these results, however, is uncertain in the presence of gravity and viscous forces.

When a gas cluster is large enough so that the gravity effect cannot be neglected, buoyancy may mobilize the cluster upward. A cluster migration mechanism should be adopted in the model to incorporate buoyancy effects, such that when gas penetrates a

throat (drainage) due to the combined effect of capillarity and buoyancy of the cluster, withdrawal of the gas cluster (imbibition) should take place from another pore with lower location [Wagner et al., 1997]. Tsimpanogiannis and Yortsos [2004] studied the critical gas saturation in the presence of gravity and modified the definition of S_{gc} so that it corresponds to the gas saturation at which the gas phase first becomes mobile (onset of mobilization). S_{gc} was correlated with the Bond number, which is the ratio of gravitational forces to capillary forces:

$$Bo = \frac{\Delta \rho g k}{\sigma} \tag{5.8}$$

where $\Delta \rho$ is the density difference between liquid and gas, k is the permeability and σ is the interfacial tension. Their correlation reads $S_{gc} = Bo^{-0.91}$ in 2D lattices. Figure 5.3 shows the critical gas saturation vs. Bo for different nucleation fractions in a 40 by 40 network. Bond numbers on the order 10^{-3} or larger tend to result in bubble mobilization by buoyancy, whereas for low Bond number conditions ($Bo \leq 10^{-4}$), bubbles are unlikely to be mobilized before a sample-spanning cluster formed.

The definition of S_{gc} is based on the assumption that once the gas is mobilized, it will be free to flow. However, this is not necessarily true because the mobilized gas could be trapped again by capillary forces. Birovljev et al. [1995] studied the migration and fragmentation of a buoyant non-wetting phase cluster. The 2D IP cluster was formed not by nucleation and mass transfer from the liquid, but by slowly injecting gas into a horizontal liquid-saturated porous medium. The medium was tilted at a very slow rate and the cluster was mobilized and fragmented when upward migration took place through a sequence of steps involving drainage events at the leading front and imbibition events at

the trailing front, resulting in the formation of an elongated branch-like structure. At a greater angle of inclination, this structure fragmented and became trapped, only to be mobilized again and fragment into smaller fragments at even higher inclination angles.
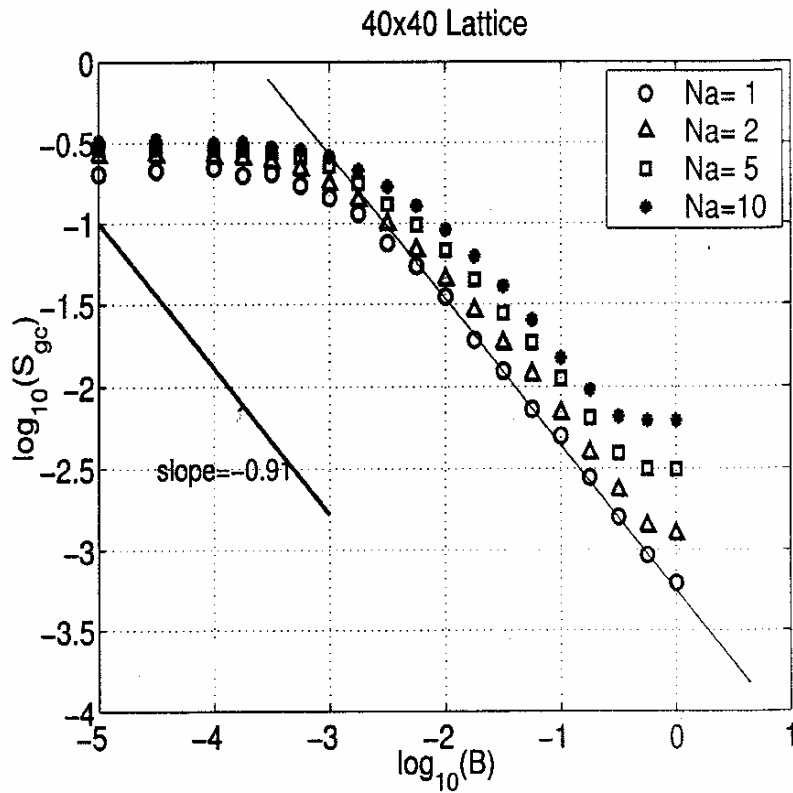
Figure 5.3 Critical Gas Saturation as a function of Bond number for different nucleation fraction [Tsimpanogiannis and Yortsos, 2004].

For gas and water in porous media with permeability lower than 10^{-10} m^2 (i.e., 100 Darcy), Bond numbers are on the order of 10^{-5} or smaller in the absence of surfactants. Studies by Tsimpanogiannis and Yortsos [2004], Birovljev et al. [1995] and Wagner et al. [1997] suggest that gas clusters grown by convective diffusion from supersaturated aqueous solutions would begin to migrate once they become large enough (of the order of tens of pores), but would fragment and become trapped, only to migrate again as a result of subsequent growth or coalescence with other growing or migrating clusters. Complex interactions between heterogeneous nucleation, convective mass transfer, capillarity and buoyancy govern the growth, coalescence, migration and fragmentation of gas clusters. Results of the simulations conducted by Tsimpanogiannis and Yortsos [2004] could be used to study the gas evolution *until* the onset of gas mobilization, after which the behavior of the mobilized gas remains unclear and is worth investigating.

5.2.4 Gas evolution in SWI experiments

In situ development of gas saturation in porous media during SWI was experimentally studied by Li [2004]. Supersaturated carbonated water was injected into a box (125 cm long by 70 cm high by 2.5 cm wide) that was filled with glass beads and initially saturated with water (see Fig. 2.19). Figure 5.4 are photographs showing gas evolution over time during SWI experiment. Gas was observed to evolve over the entire length of the box uniformly as a front advancing from the injection to the extraction end. Higher gas saturation is observed closer to the injection well than farther away.
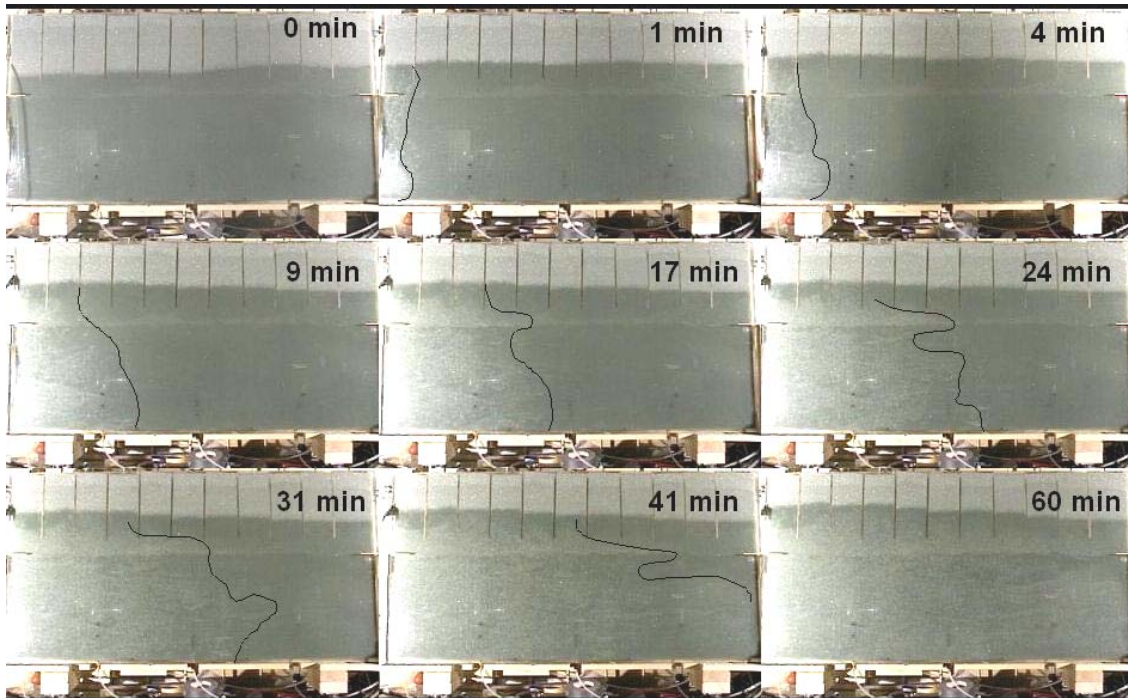
Figure 5.4 Photographs showing gas evolution in porous media over time during SWI Experiment [Li, 2004].

Gas flow rates were measurable only in the first 35 cm of distance from the injection point. Increasing the injection flow rate and injection pressure of carbonated water did not increase the distance beyond which gas production was undetectable. The rate of gas ebullition in the vicinity of the injection well, however, increased with increasing injection pressure and flow rate. Intermittent mobilization of gas, in the form of large bubbles migrating upwards, was observed at distances greater than 40 cm from the injection well. Figure 5.5 shows gas production rates as a function of distance from the injection end for various injection pressure conditions. Gas saturation development was observed to develop in the whole medium.
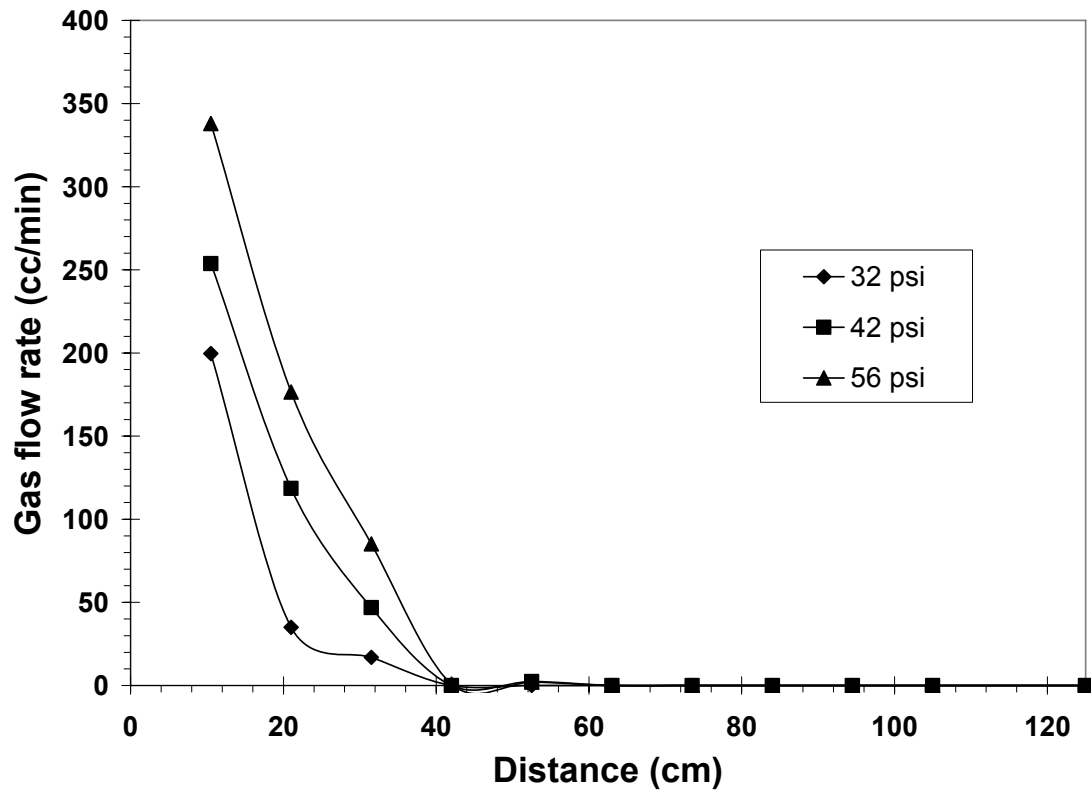
Figure 5.5 Gas evolution rates as a function of distance from the injection end for various

injection pressure conditions [Li, 2004].

5.3   Model development

5.3.1   Model description

A pore network model, similar to the one used in Chapter 3, is developed to represent the pore space. The model is a 2D lattice of cubic chambers connected by square tubes as shown in Figure 5.6 a. To incorporate the effects of liquid corner flow, an adjustment of pore-throat arrangement is made, as shown in Figure 5.6.b. The model is initially saturated with pure water and supersaturated water is injected at the left boundary and flows through tubes (bonds) and chambers (nodes) from the left to the right between the two impermeable boundaries. As bubbles emerge in the medium, non-wetting gas phase resides in centers of tubes and chambers while water flows around the bubbles through corner filaments. Each corner of chambers containing gas (pore A in Figure 5.6) and each water-filled chamber itself (pore B in Figure 5.6) serves as a node, where the aqueous phase is well mixed and the site is considered possessing uniform liquid pressure and solute concentration.

a

b   nodes
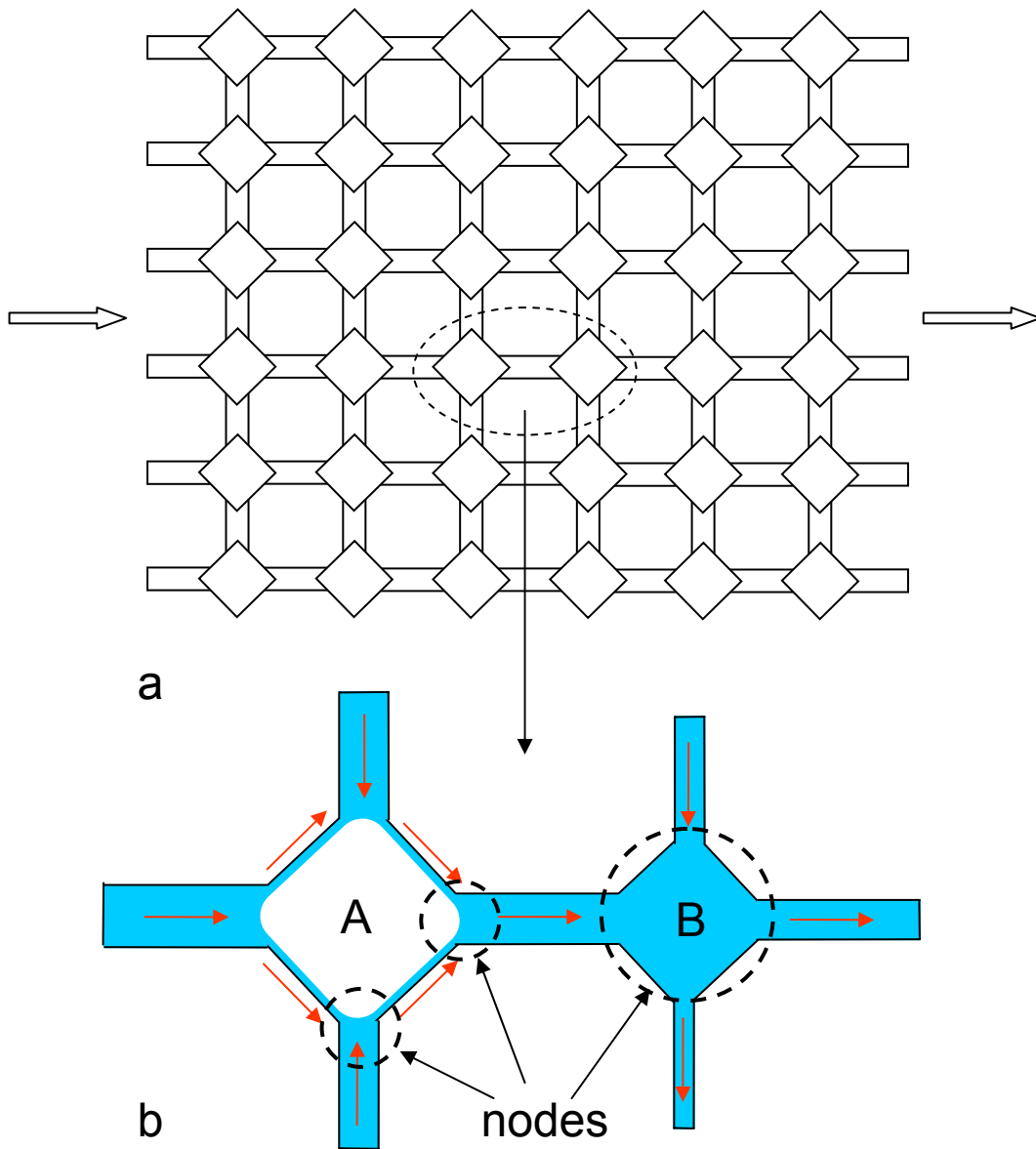
Figure 5.6 Schematic of pore network model with water flowing around a bubble. Arrows represent the water flow directions.

Under creeping flow conditions, the hydraulic conductance in a rectangular duct is a function of the shape factor of the cross section and is given by Patzek and Silin [2001] as:

$$g = g^* A^2 / \mu L_t \qquad (5.9)$$

where A is the cross sectional area of the tube, μ is the water viscosity, L_t is the tube length and g^* is the dimensionless hydraulic conductance. For a square duct, $g^* = 0.0351$. The corresponding liquid flow rate is $Q = g\Delta P$, where ΔP is the pressure drop in the tube.

The liquid flow and convective mass transfer problems have been solved in Chapter 4. The hydraulic conductance in a liquid filament, g_p can be calculated from meniscus-apex distance of the filament, b (see Figure 4.1), and the dimensionless hydraulic conductance, g^*, ($g_p = g^* b^4 / \mu$, Equation 4.9). The meniscus-apex distance b can be calculated using Equation (4.2) and g^* values are given in Table 4.2. The corresponding flow rate in the filament is $Q = g_p \Delta P / L$, where is ΔP is the pressure drop along the filament and L is the corner length. The field of liquid pressure or potential (if gravity is considered) can be obtained by imposing mass conservation equations at network nodes, $\sum Q = 0$.

Similarly, solute mass balances are considered. Figure 5.7 shows situations of solute flows into and out of the typical network nodes:

liquid filaments

(a)　　　　　　　(b)　　　　　　　(c)
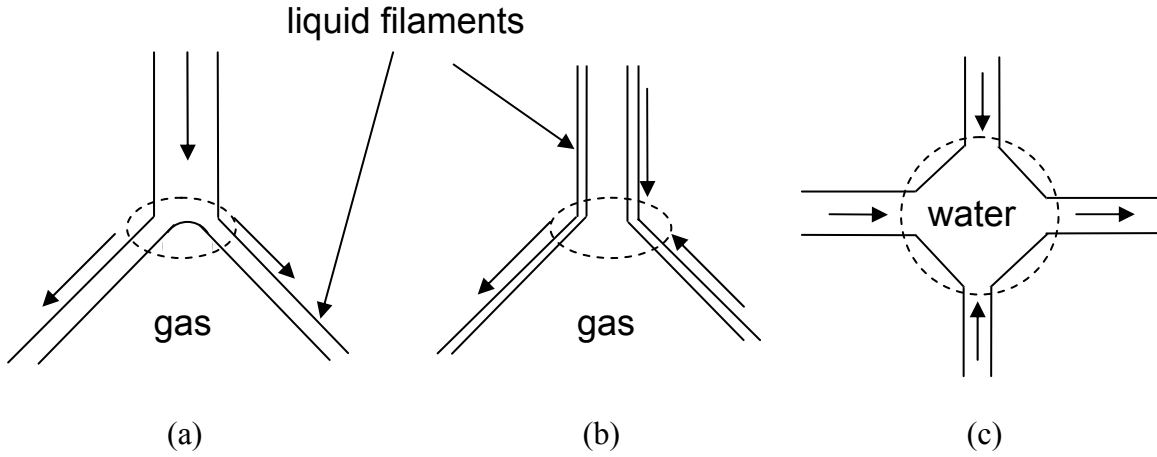
Figure 5.7 Schematic of solute flows into and out of network nodes (a) corner node connected to a liquid-filled bond (b) corner node connected to a gas-invaded bond (c) pore node.

(i)   Rate of solute transport by aqueous phase advection through tubes without gas-water interface into a node (Figure 5.7 a, c) is

$$F_{in} = Q_{in} C_{neighbor} \qquad (5.10)$$

where Q_{in} is the liquid flow rate into the node and $C_{neighbor}$ is the solute concentration in the neighbor node.

(ii)   Rate of solute transport by convective mass transfer through corner filaments into a node (Figure 5.7 b) is

$$F_{in} = Q_{in}\left[C_{int} + E_d (C_{neighbor} - C_{int}) \right] \qquad (5.11)$$

where E_d is the average effluent concentration, which has been obtained in Chapter 4, C_{int} is the equilibrium concentration at the interface given by Henry's Law, $C_{int} = P_g / H$, P_g is the gas pressure and H is the Henry's constant.

(iii)   The rate of solute transport by aqueous phase advection out of a node is simply

$$F_{out} = Q_{out} C_{node} \tag{5.12}$$

where Q_{out} is the liquid flow rate out of the node and C_{node} is the solute concentration in the node.

(iv)   The transport rates by diffusion of the solute into and out of a node are

$$F_{diff} = \pm D_m A_t \frac{C_{node} - C_{neighbor}}{L_t} \tag{5.13}$$

where D_m is the solute diffusivity, A_t is the cross-sectional area of the tube without gas-water interface, L_t is the tube length and the sign denotes direction of mass transfer. Note that Equation (5.13) is only used for tubes without a gas-water interface because in corner filaments diffusive mass transfer has been incorporated in Equation (5.11).

Solute mass balances are formulated by imposing solute mass conservation to each node:

$$\sum F = \frac{V_{node}(C_{node}^{n+1} - C_{node}^n)}{\Delta t} \tag{5.14}$$

where V_{node} is the node volume, C_{node}^{n+1} and C_{node}^n are the node concentrations at the current and previous simulation step, respectively, and Δt is the simulation time step. The term at the right hand side of Equation (5.14) is the mass accumulation term. The solute concentration field of the network is obtained by solving the system of linear algebraic equations generated by application of the Equation (5.14) to each node.

5.3.2 Bubble growth

The simulation of bubble growth involves three steps:

(i)   Nucleation

The mechanism of heterogeneous nucleation is adopted and nucleation sites are randomly assigned throughout the network except for the boundary pores, i.e., all nucleation sites are at least several pores away from the boundaries in order to avoid boundary effects. The number of nucleation sites is determined by a pre-selected nucleation fraction defined as

$$f_q = \frac{N}{N_t}$$ (5.10)

where N is the number of nucleation sites and N_t is the total number of pores in the network. A threshold solute concentration is set so that when the concentration in a nucleation site exceeds the threshold concentration, inequality (5.2) is assumed satisfied and the site is activated. Subsequent to nucleation, the host site is assumed immediately occupied by the nucleated gas bubble surrounded by water. The bubble pressure is

$$P_g = P_l + P_c$$ (5.10)

where P_l is the liquid pressure in the pore and P_c is the capillary pressure in the pore, calculated using Equation (3.6). The radius of curvature of the gas-water interface, $R_{nw} = \gamma/P_c$, and pore radius, R_p, are used to calculate the bubble volume, V_g. The ideal gas law

$$P_g V_g = nRT$$ (5.11)

is used to determine the bubble mass, n.

(ii)   Pressurization

A bubble or cluster is pressurized by convective mass transfer. The gas volume is assumed to be constant during this step until the perimeter throat with the smallest capillary pressure is invaded when

$$P_g - P_l \geq P_c \tag{5.12}$$

From the ideal gas law:

$$V_g \frac{dP_g}{dt} = RT \frac{dn}{dt} \tag{5.13}$$

The mass transfer rate from a corner filament to the bubble is determined by the water flow rate in the corner and the concentration difference between the two corner ends. The total flux is

$$N_A = \frac{dn}{dt} = \sum Q \Delta C \tag{5.14}$$

The updated mass and pressure of the bubble are determined using Equation (5.13) and Equation (5.14).

(iii)   Penetration

The pressurized bubble will invade the perimeter throat with the smallest capillary pressure and occupy the adjacent pore immediately when inequality (5.12) is satisfied. Mass transfer is neglected in this step. Both pressure and volume of the cluster change when the cluster displaces water in the newly invaded pore so that:

$$P_g V_g = V_g^0 P_g^0 = nRT \tag{5.15}$$

The updated cluster volume V_g is determined by local pore geometry by assuming a value of the curvature J_o of the interface. From Equation (5.15), the gas pressure P_g is

calculated to obtain the capillary pressure ($P_c = P_g - P_l$) and the interfacial curvature

($J = P_c / \gamma$). Based on the difference of J_o and J, additional iterations are taken on the

assumed J_o until convergence is reached. V_g, P_g and P_c are then updated.

As two clusters coalesce, the sums of masses and volumes of the merging clusters

are initially assigned to the new cluster and the cluster pressure is calculated accordingly.

The same iterative procedure is adopted to determine the equilibrium volume and

pressure of the new cluster.

5.3.3 Bubble mobilization and fragmentation

When a gas cluster is large enough so that the gravity effect cannot be neglected,

buoyancy may mobilize the cluster upward and the mobilization tendency increases with

increasing Bond number. A cluster migration mechanism should be adopted in the model

to incorporate gravity so that when gas penetrates a throat (tube j in Figure 5.8) due to the

buoyancy of the cluster, withdrawal of the gas cluster (imbibition) should take place from

another pore at a lower location (site i in Figure 5.8) [Wagner et al., 1997]. The threshold

for cluster mobilization can be expressed by the following inequality:

$$P_c^i - P_c^j + \Delta \rho g h_{ji} \geq 0 \tag{5.18}$$

where P_c is the capillary pressure of throat j and pore i, $\Delta\rho$ is the density difference

between liquid and gas, and $h_{ji} = z_j - z_i$ denotes the distance between pore j and pore i.

Note that $z_j > z_i$.

During the simulation, each cluster is scanned to find the migration pair of

invading throat and withdrawing pore. When a bubble is mobilized, imbibition takes

163

place in every perimeter throat of the withdrawing pore, i.e., the gas-water interfaces retreat from the pore to neighbors through connecting tubes. A cluster can be fragmented during mobilization depending on the nature of imbibition events (site i in Figure 5.9). Snap-off may take place at pore throats when Equation (5.7) is satisfied. The value $\xi = 6$ is chosen as representative of the critical pressure ratio in granular media [Chang and Ioannidis, 2003].
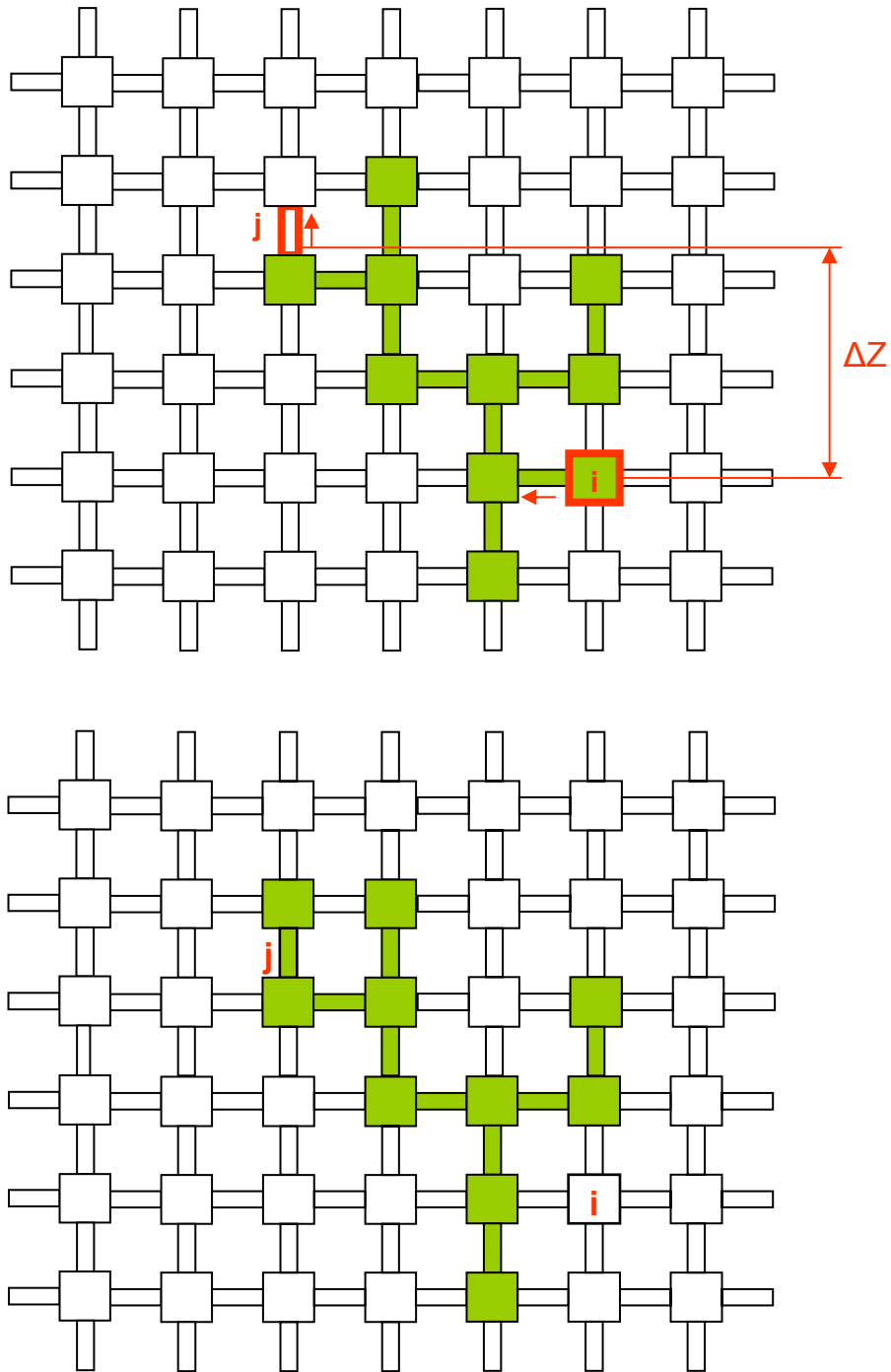
Figure 5.8 Schematic of gas cluster mobilization due to buoyancy. The cluster invades throat *j* as it withdraws from pore *i*.
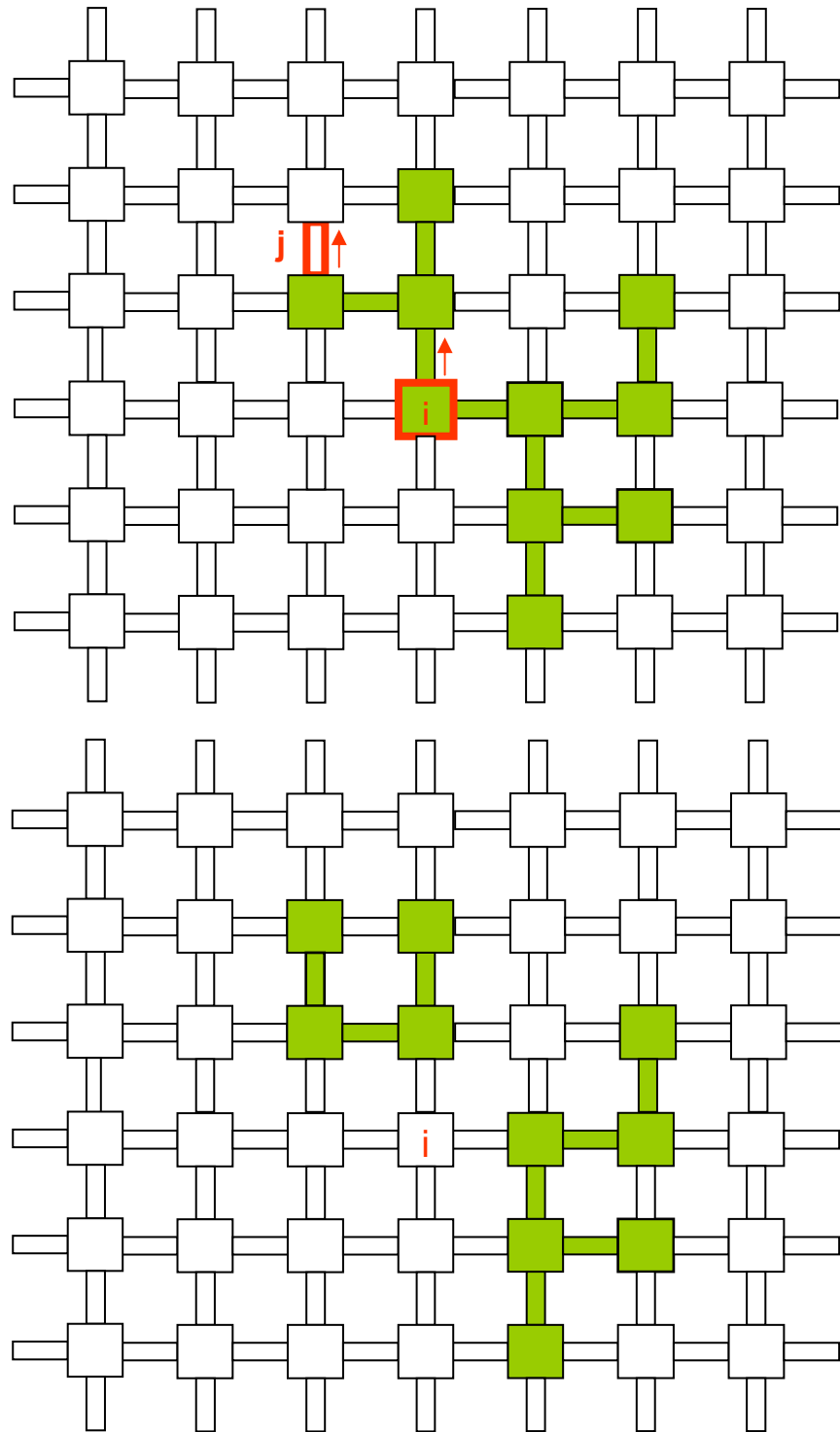
Figure 5.9 Schematic of gas cluster fragmentation during mobilization. The cluster is divided into two clusters as interfaces withdraw from pore *i* to neighboring pores.

5.4   Algorithmic issues

The Hoshen-Kopelman algorithm is used to label bubble clusters. However, the cluster labels change with the cluster distribution in the network. To keep track of cluster properties (V_g, P_g, n_g, etc.) in each simulation step, the cluster evolving from a nucleation site is labeled sequentially according to the order of site activation. The cluster labels change only in situations of coalescence and fragmentation. When two clusters coalesce, the label of the expanding cluster is assigned to the new cluster. During fragmentation, a new label is assigned to the daughter cluster by adding a sufficiently large number (500 for simulations with 250 nucleation sites; 100 for simulations with 50 nucleation sites) to the original label.

Another critical algorithm involves node coordination. With reference to Figure 5.6 b, each gas-occupied pore is represented by four nodes, meaning that the total number of nodes depends on both the network size and the number of pores containing gas,

$$n_{total} = n_x n_y + 3n_p \tag{5.19}$$

where n_x and n_y are the network dimensions and n_p is the number of gas occupied pores. Figure 5.10 graphically depicts the coordination system of a 3 by 4 network. The node identification number depends on the location and the gas distribution in the network:

$$n = (i-1)n_y + j + n_{corner} + 3n'_p \tag{5.20}$$

where i, j denote the location of the pore, n_{corner} is the corner number (n_{corner} = 0, 1, 2, 3 for top, left, right and bottom corner nodes and n_{corner} = 0 for pore nodes), n'_p is the

167

number of the gas-occupied pores before a certain node in the node sequence, for example, $n'_p = 2$ for node 14 in Figure 5.10 a.

For each simulation step, solute concentrations at the nodes are obtained before bubble nucleation, expansion and mobilization, after which the node coordination changes (see Figure 5.10 b). Because mass balance in the next step requires the concentration data of the current step to calculate the mass accumulation, a new concentration array has to be constructed corresponding to the new node coordination. This is detailed below.

For a node without a phase displacement event in its host pore (e.g., pore 14 in Fig 5.10 a, i.e. pore 20 in Fig 5.10 b),

$$C^0[n + 3(n'_{drainage} - n'_{imbibition})] = C[n] \qquad (5.21)$$

where C is the concentration for the current step, C^0 is the new concentration array to be used in the next step, $n'_{drainage}$ and $n'_{imbibition}$ are the numbers of newly drained and imbibed pores before the host pore in the sequence. For a newly drained pore due to nucleation (pore E in Fig 5.10 b), expansion (pore D in Fig 5.10 b) or mobilization (pore B in Fig 5.10 b),

$$C^0[n + 3(n'_{drainage} - n'_{imbibition}) + n_{corner}] = C[n] \qquad (5.22)$$

For a newly imbibed pore (pore 22 in Fig 5.10 b),

$$C^0[n + 3(n'_{drainage} - n'_{imbibition})] = \overline{C} \qquad (5.23)$$

where $\overline{C}$ is the volumetric average concentration of the four corner nodes before the imbibition.
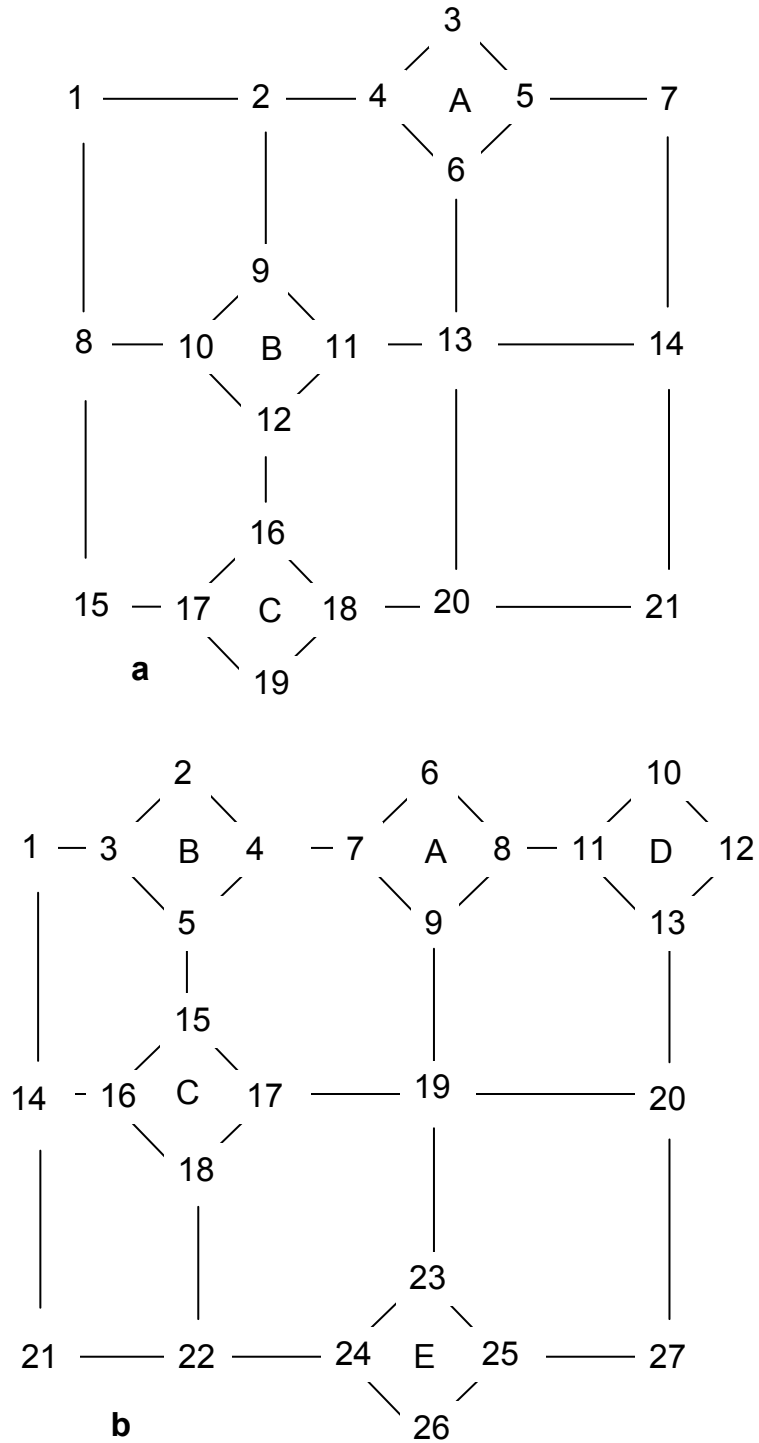
Figure 5.10 Schematic of node coordination system. (a) A, B, C are gas occupied pores (b) A expands to D, cluster B-C is mobilized upwards to a new location and E is a new nucleated bubble.

5.5   Summary of simulation steps

FORTRAN programs were developed to simulate the bubble evolution process and provided in Appendices. Boundary pressures are set to make supersaturated water flow through the network that is initially saturated with pure water. Using the method described in Section 5.3.1, the pressure and concentration fields of the liquid phase are obtained. Bubbles are nucleated at the pre-assigned nucleation sites when local solute concentrations reach the nucleation thresholds. Gas pressures, volumes and masses are calculated from the pore geometry and ideal gas law. The amounts of solute masses diffusing into the bubbles by convective mass transfer are computed and bubbles are pressurized. Gas distribution in the network is updated when any process of nucleation, invasion percolation, coalescence, mobilization and fragmentation of gas clusters takes place. Additional iterations are conducted to determine the configurations of local gas-water interfaces and pressures and volumes of gas clusters are calculated accordingly. The HK algorithm is used to label the gas clusters and the liquid pressure and concentration fields are then computed anew. When gas clusters reach the boundaries, the amount of gas transferred into the clusters is considered to escape from the network. A flow chart of the program is given in Figure 5.11.
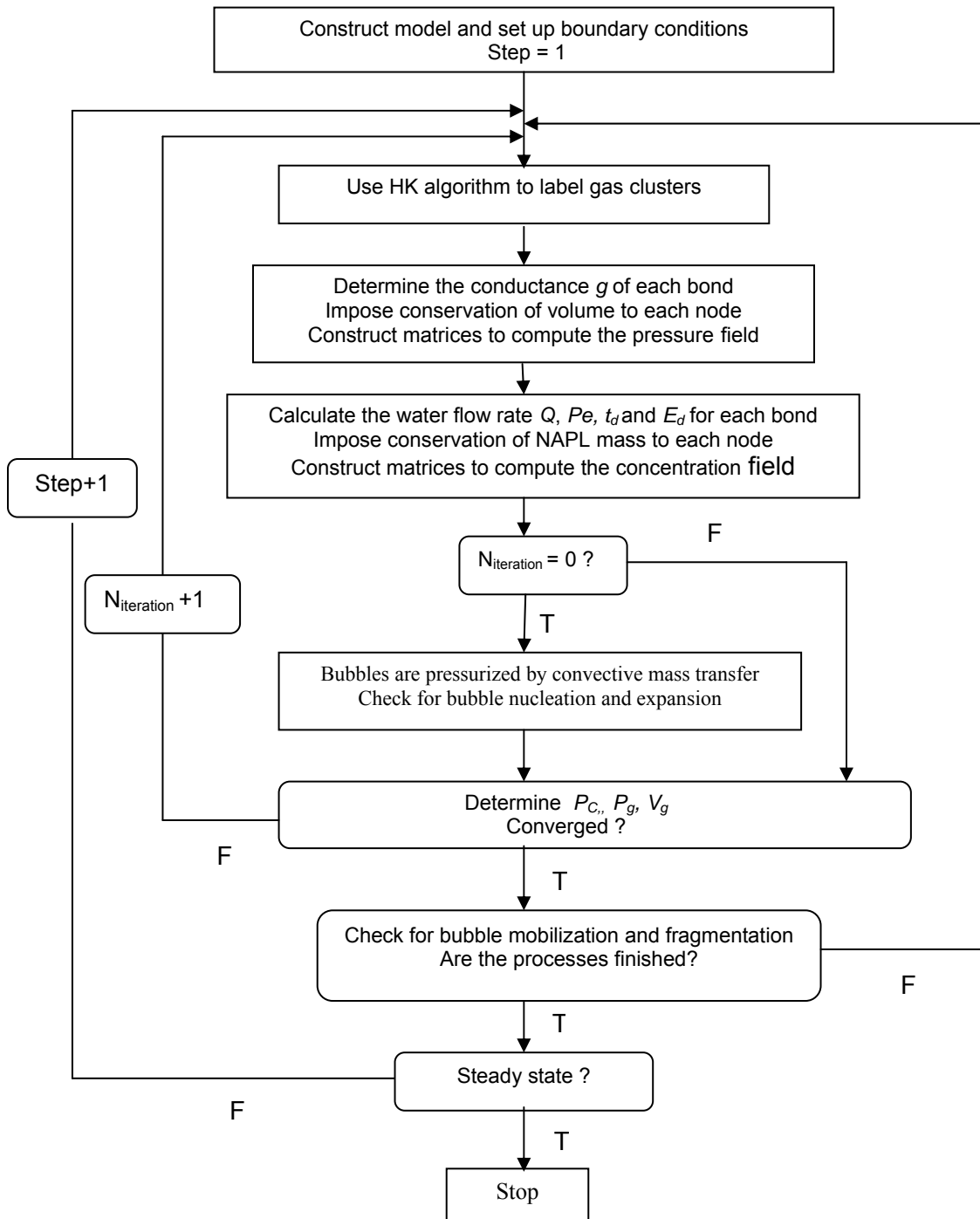
Figure 5.11 Flow chart of simulation gas evolution in pore-network model.

5.6   Results and Discussions

Pore sizes are generated following a lognormal distribution to idealize a homogeneous porous medium. Carbon dioxide is chosen as the representative gas phase and parameter values corresponding to the system CO_2 – water are listed in Table 5.1.

The equilibrium solute concentration, C_s, is determined by Henry's law

$$C_s = \frac{P_l}{H} \tag{5.24}$$

where P_l is the hydrostatic liquid pressure and H is Henry's constant. A coefficient, S_f, is used to indicate the supersaturation of the injected solution above the equilibrium concentration:

$$C_{in} = S_f C_s \tag{5.25}$$

where C_{in} is the inlet concentration of the injected supersaturated water. The solute concentration at the gas-water interface is also given by Henry's law:

$$C_{int} = \frac{P_g}{H} \tag{5.26}$$

where P_g is the gas pressure.

Table 5.1 Physical parameters used in simulations.

Parameter	Value
Interfacial tension, σ	7.2×10^{-2} [N/m]
Contact angle, θ	$0°$
CO_2 diffusion coefficient, D_m	2.97×10^{-9} [m^2/s]
CO_2 molecular weight, M	44
Water density, ρ	1000 [kg/m^3]
Water viscosity, μ	8.9×10^{-4} [kg/ms]
Temperature, T	298 [K]
Gravitational constant, g	9.81 [m/s^2]
Henry's coefficient, H	2.59×10^3 [Pa*m^{3}water/(molCO$_2$)]
Ideal gas constant, R	8.314 [Pa*m^3/(molK)]
saturated CO_2 concentration, C_s	43.04 [mol CO$_2$/ m^3 water]
Average pore radius, $\langle R_p \rangle$	400 [μm]
Standard deviation	365 [μm]

5.6.1 Visualizations of bubble growth and concentration field

Simulation is conducted to visualize CO_2 bubble growth from a single nucleation site in a 100 by 50 network. Because the tendency of bubble mobilization increases with the Bond number ($Bo = \dfrac{\Delta \rho g k}{\sigma}$), a large Bond number condition ($Bo = 8.54 \times 10^{-4}$) is imposed to emphasize the process of mobilization and fragmentation. The bubble growth pattern is shown in Figure 5.12 (see also the animation single_bubble.wmv in Appendix). Supersaturated water is injected from the left boundary and the nucleation site is activated as the local concentration exceeds the nucleation threshold. The bubble subsequently grows by convective mass transfer, it is pressurized and a ramified cluster evolves during a process of invasion percolation. When the cluster is large enough so that buoyancy overcomes the pinning capillary forces, it is mobilized upwards and fragmentation is observed. Fragmented clusters migrate upwards independently until they are trapped again by capillary forces. The simulated bubble growth pattern is in agreement with the experimental observations of Birovljev et al. [1995]. Experimental studies on buoyancy-affected two-phase flow in porous media [Auradou et al., 1999; Stohr and Khalili, 2006] also show that gas flow through a channel is unstable and it is more likely that gas migrates upwards intermittently in the form of isolated clusters. The identification of critical gas saturation for continuous gas flow by Tsimpanogiannis and Yortsos [2004], as the gas saturation at the onset of mobilization, is not confirmed by the simulations presented here.
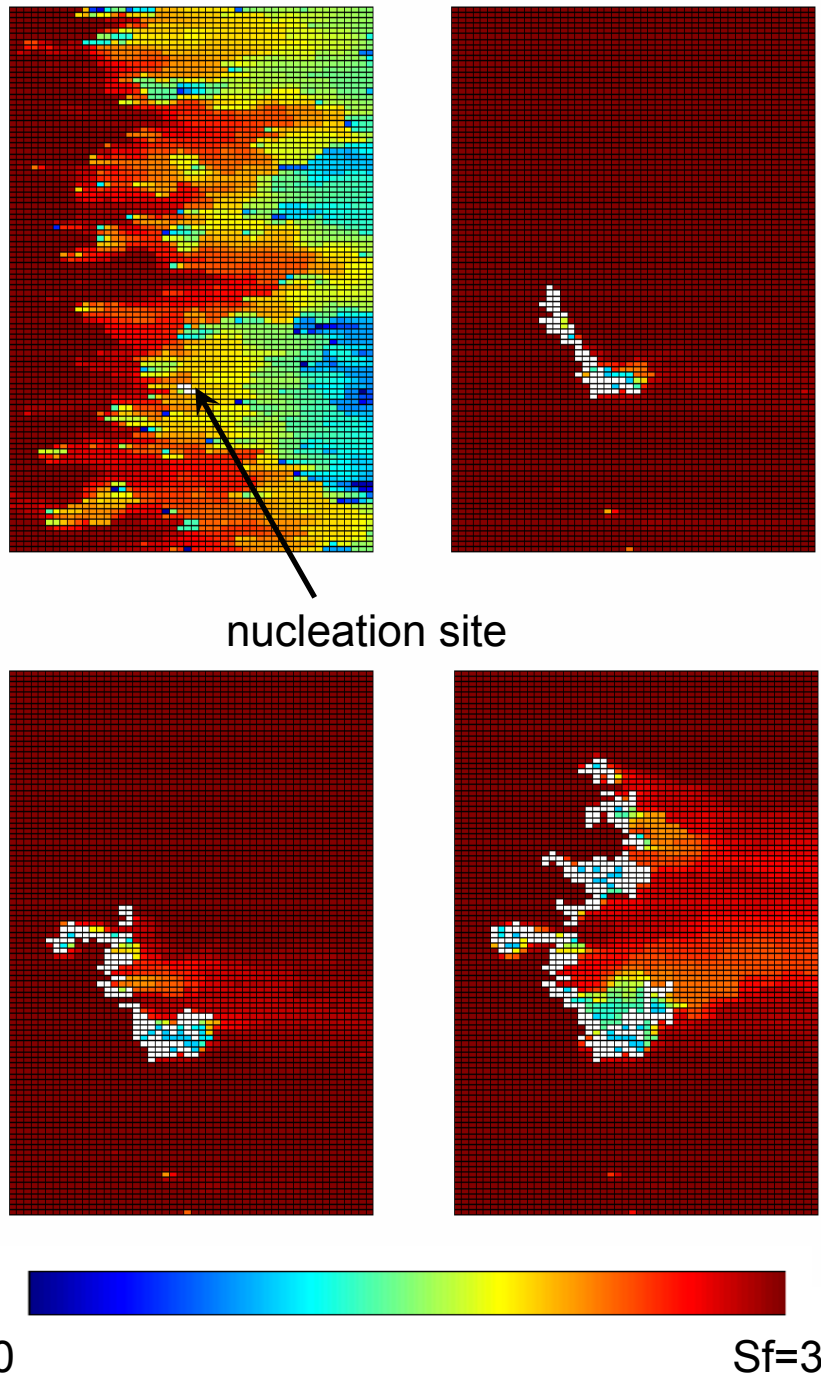
Figure 5.12 Bubble growth from a single nucleation site. 100x50 network, white represents gas, color represents solute concentration in aqueous phase, pore throats are not shown, Bo = 8.54e-4, $\langle R_p \rangle$ = 400 μm, ΔP = 1000Pa. (see also the animation single_bubble.wmv in Appendix)

To visualize the multiple bubble growth pattern, multiple nucleation sites are assigned in a 100 by 100 network, as shown in Figure 5.13. The nucleation sites are randomly distributed in the center of the network (a 60 by 60 square region) to minimize boundary effects. The growth pattern and solute concentration fields are shown in Figure 5.14 (see also the animation multiple_bubble.wmv in Appendix). The advancement of solute concentration is visualized during the miscible displacement of non-carbonated water by the injected supersaturated water. Bubbles are gradually nucleated as the supersaturated water reaches the nucleation sites. Gas saturation increases when more bubbles are nucleated and gas clusters subsequently evolve from the nucleation sites due to convective mass transfer.
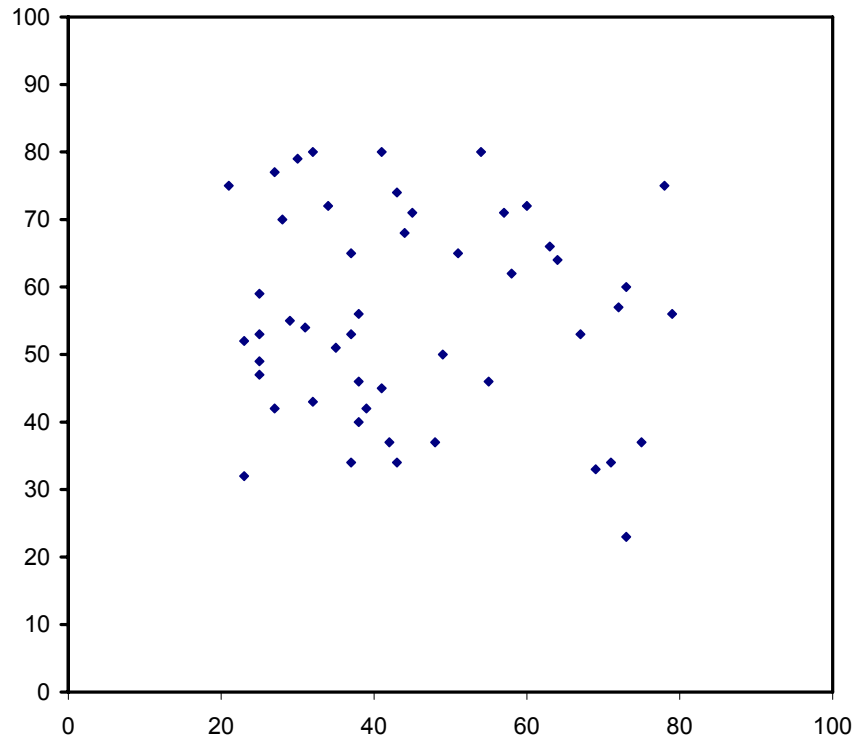
Figure 5.13 Nucleation sites in a 100 by 100 network. Black dots represent 50 randomly assigned nucleation sites.
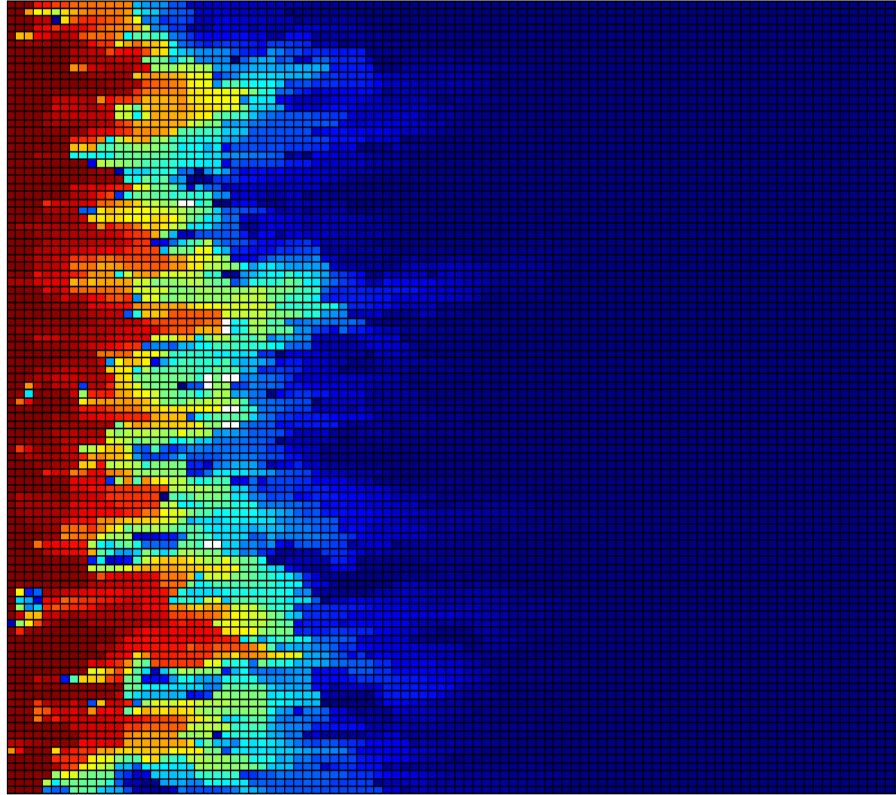
(a) PV = 0.09, Sg = 0.07%

Figure 5.14 (a) visualization of bubble growth pattern and concentration field. 100x100 network with 50 nucleation sites, same colormap as in Figure 5.12, pore throats are not shown, Bo = 8.54e-5, $<R_p>$ = 400 μm, ΔP = 1000Pa. (see also the animation multiple_bubble.wmv in Appendix).
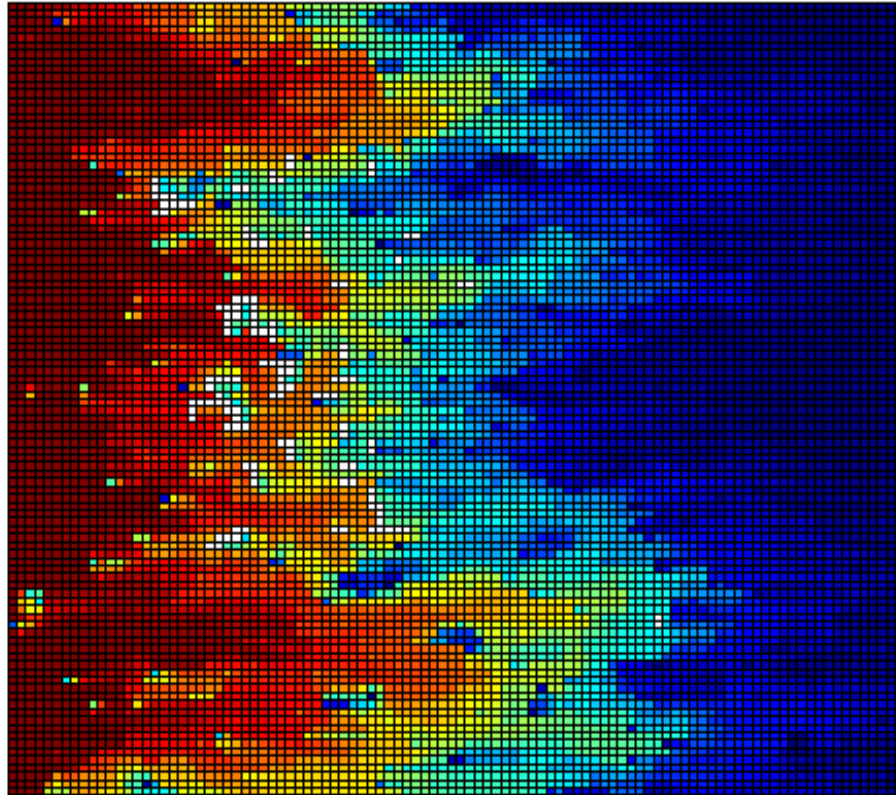
(b) PV = 0.17, Sg = 2.4%

Figure 5.14 (b) visualization of bubble growth pattern and concentration field. 100x100 network with 50 nucleation sites, same colormap as in Figure 5.12, pore throats are not shown, Bo = 8.54e-5, $<R_p>$ = 400 μm, ΔP = 1000Pa. (see also the animation multiple_bubble.wmv in Appendix).
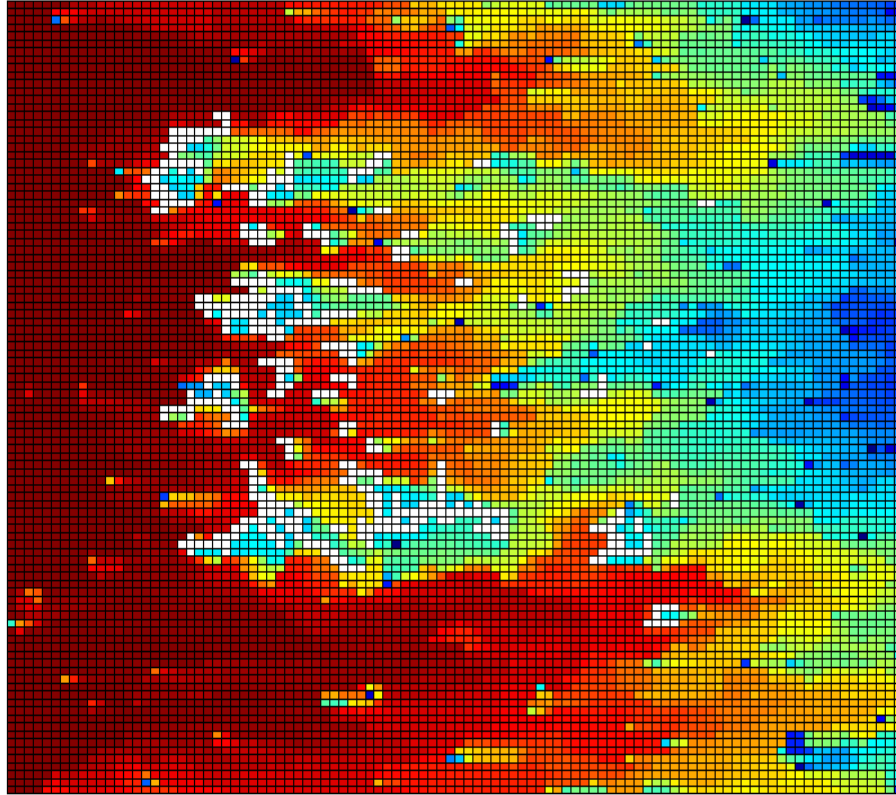
(c) PV = 0.32, Sg = 7.4%

Figure 5.14 (c) visualization of bubble growth pattern and concentration field. 100x100 network with 50 nucleation sites, same colormap as in Figure 5.12, pore throats are not shown, Bo = 8.54e-5, $<R_p>$ = 400 μm, ΔP = 1000Pa. (see also the animation multiple_bubble.wmv in Appendix).
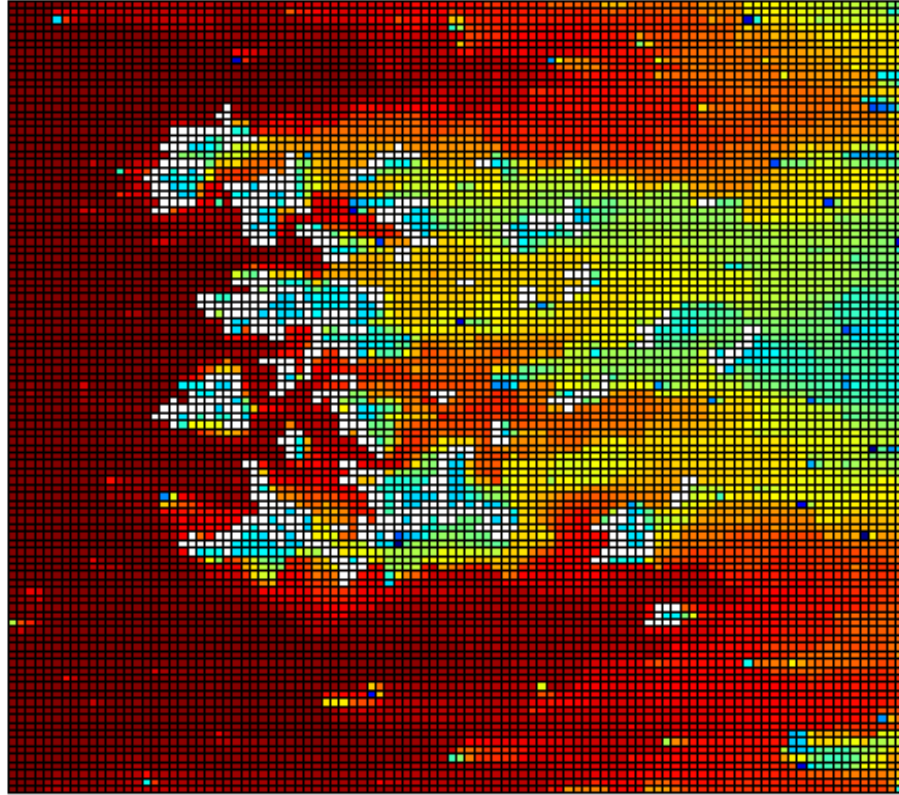
(d) PV = 0.45, Sg = 10.0%

Figure 5.14 (d) visualization of bubble growth pattern and concentration field. 100x100 network with 50 nucleation sites, same colormap as in Figure 5.12, pore throats are not shown, Bo = 8.54e-5, $\langle R_p \rangle$ = 400 μm, ΔP = 1000Pa. (see also the animation multiple_bubble.wmv in Appendix).
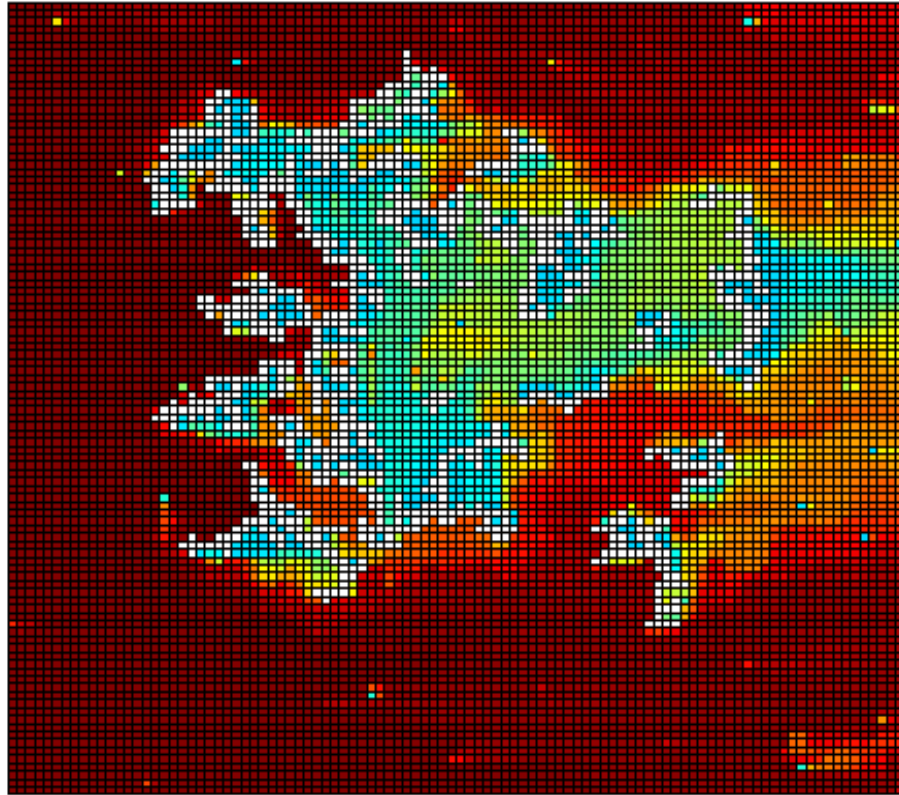
(e) PV = 0.96, Sg = 20.3%

Figure 5.14 (e) visualization of bubble growth pattern and concentration field. 100x100 network with 50 nucleation sites, same colormap as in Figure 5.12, pore throats are not shown, Bo = 8.54e-5, $<R_p>$ = 400 μm, ΔP = 1000Pa. (see also the animation multiple_bubble.wmv in Appendix).
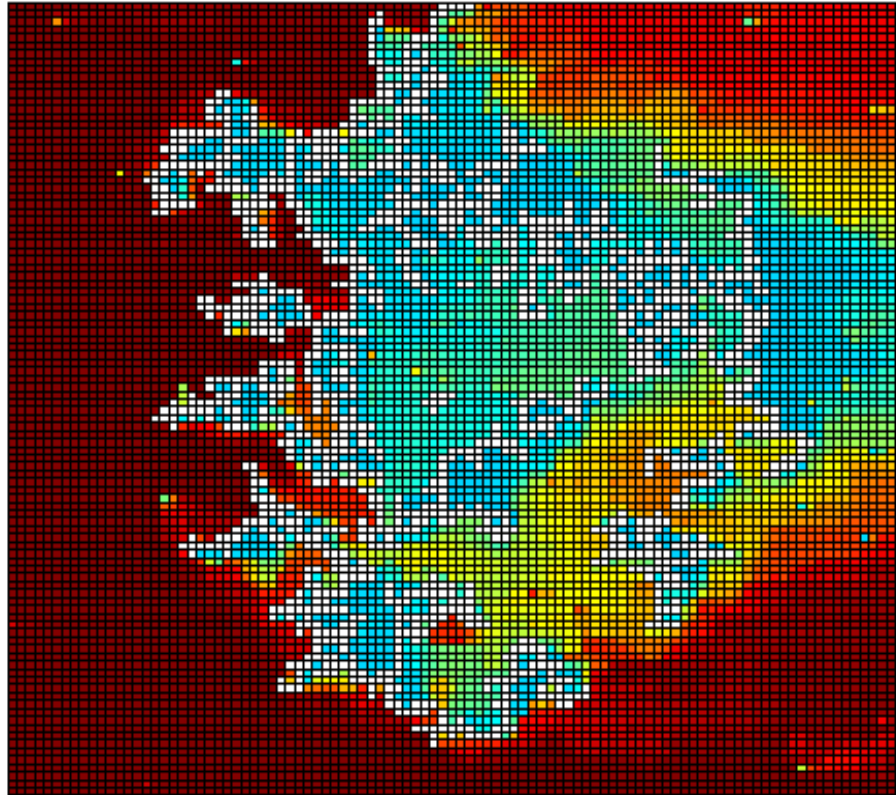
(f) PV = 1.26, Sg = 29.6%

Figure 5.14 (f) visualization of bubble growth pattern and concentration field. 100x100 network with 50 nucleation sites, same colormap as in Figure 5.12, pore throats are not shown, Bo = 8.54e-5, $<R_p>$ = 400 μm, ΔP = 1000Pa. (see also the animation multiple_bubble.wmv in Appendix).

At high gas saturations, large clusters are formed in the network and the liquid flow rate decreases dramatically. The regions behind the clusters in the direction of liquid flow have solute concentrations close to the equilibrium value (see Figure 5.14 f). This could be attributed to the lack of solute supply by liquid flow and the gas stripping process when the solute concentration decreases after supersaturated water flows through the corner filaments around gas-occupied pores. Figure 5.15 depicts the flow potential profiles at different gas saturations in the network corresponding to the concentration fields in Figure 5.14. At low gas saturation (Figure 5.14 b and Figure 5.15 a), the flow potentials are well-distributed across the network. At high gas saturation (Figure 5.14 f and Figure 5.15 b), the potential in regions behind large clusters are almost uniform, resulting in very small liquid flow therein. Growth of the clusters in those regions is slowed unless a pathway of liquid flow is available again by migration of blocking clusters. This phenomenon could be used to explain the observations in SWI experiments (see Figure 5.5) by Li [2004]. Free gas flow can be detected only at a certain distance from the injection point and the gas production distance is independent on the injection flow rate and pressure of supersaturated water. Increasing injection pressure and flow rate can only increase the gas production rate in the vicinity of the injection well [Li, 2004]. The simulations show that although low mass transfer zones exist, gas saturation still increases in the whole medium, a phenomenon also observed in Li's experiments. This is because gas saturation in the whole network is already established before the large blocking clusters are formed.
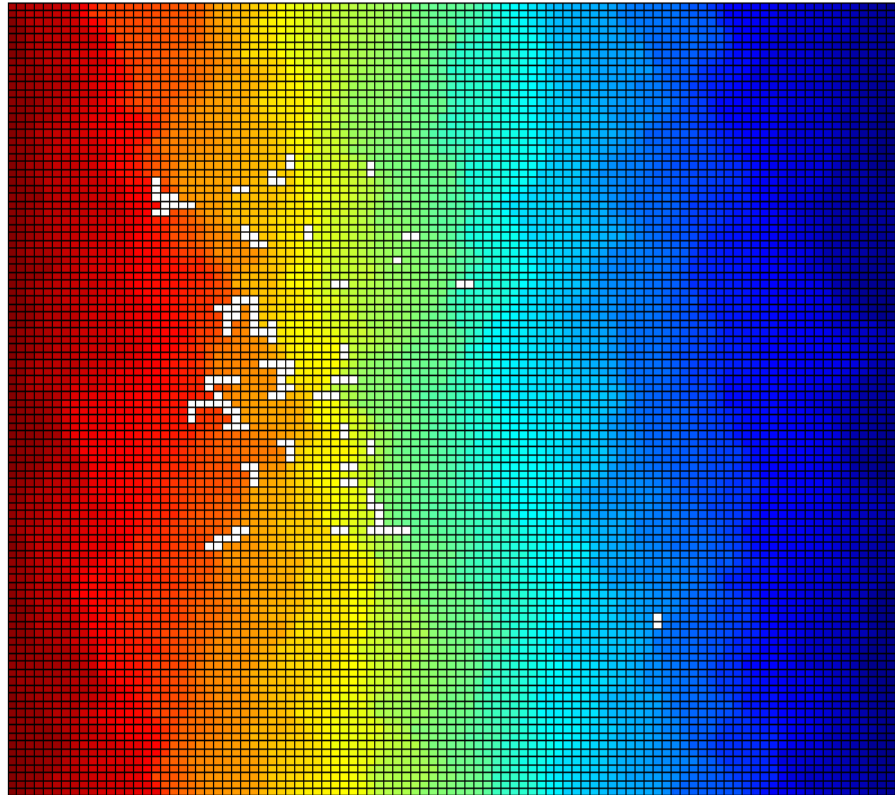
ΔP = 0   ΔP = 1000 Pa

(a) PV = 0.17, Sg = 2.4%

Figure 5.15 (a) Visualization of water potential field corresponding to Figure 5.14 b.
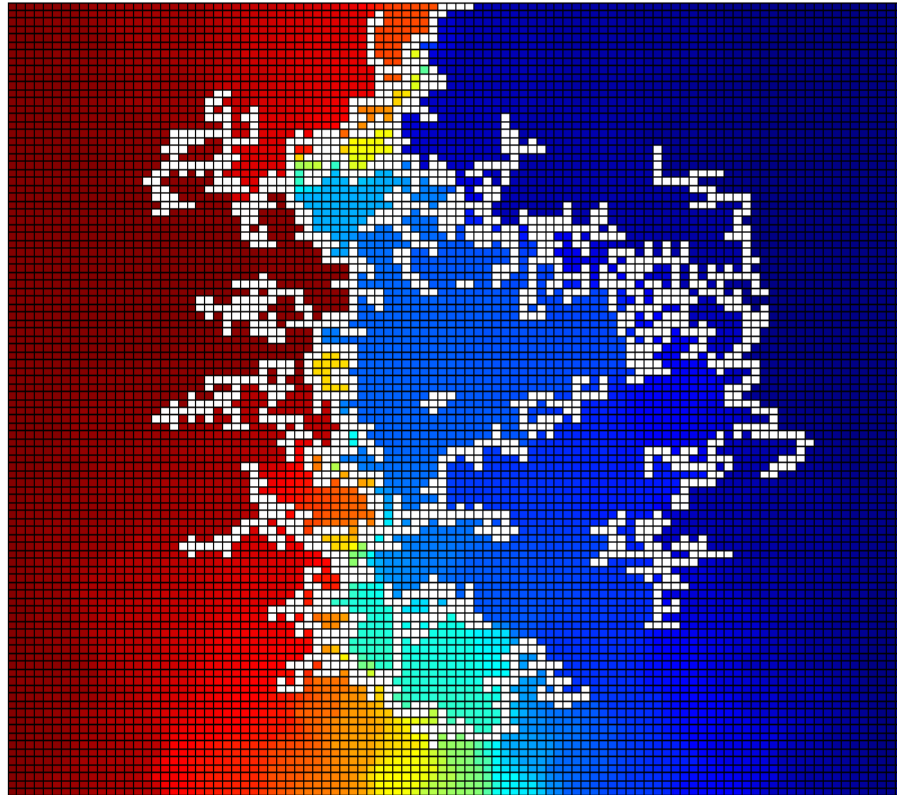
ΔP = 0   **ΔP = 1000 Pa**

(b) PV = 1.26, Sg = 29.6%

Figure 5.15 (b) Visualization of water potential field corresponding to Figure 5.14 f.

5.6.2 Effect of nucleation fraction

To study the effect of nucleation fraction, simulations are conducted with more nucleation sites in the network, as shown in Figure 5.16 (250 nucleation sites compared to 50 in Figure 5.13). The bubble growth and concentration fields with high nucleation fraction are shown in Figure 5.17. The bubble growth pattern is similar to the pattern with lower nucleation fraction. Larger clusters tend to form close to the injection boundary, while smaller ones are trapped at farther downstream. For different nucleation fractions, no significant effect is observed on the highest gas saturation that can be obtained before gas can escape from the network. The highest gas saturations for multiple realizations are in the range of 27 to 31%.
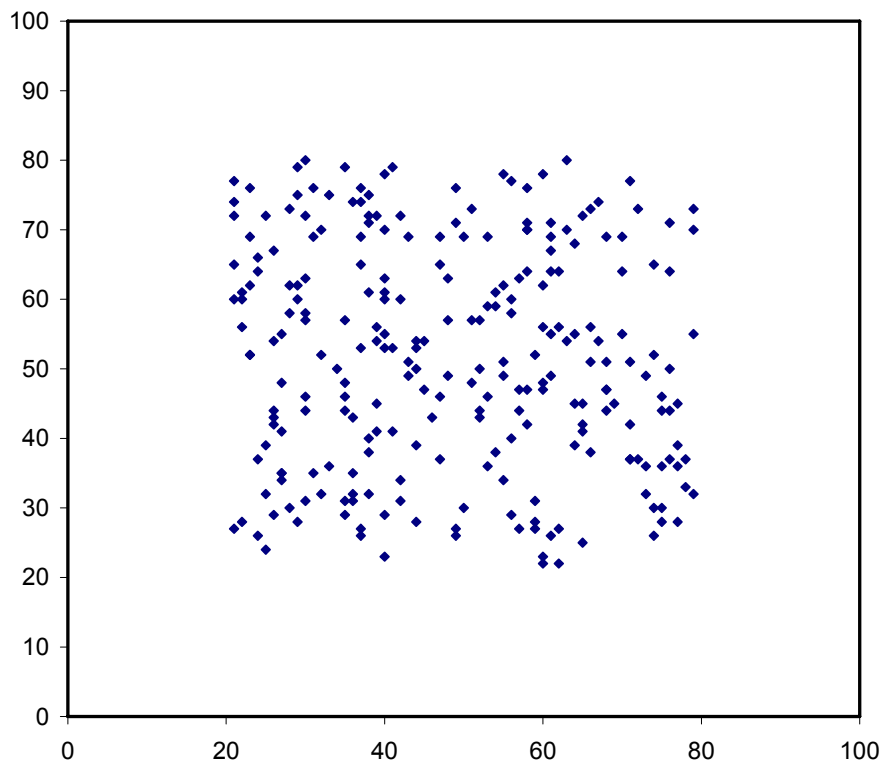
Figure 5.16 Nucleation sites in a 100 by 100 network. Black dots represent 250 randomly assigned nucleation sites.
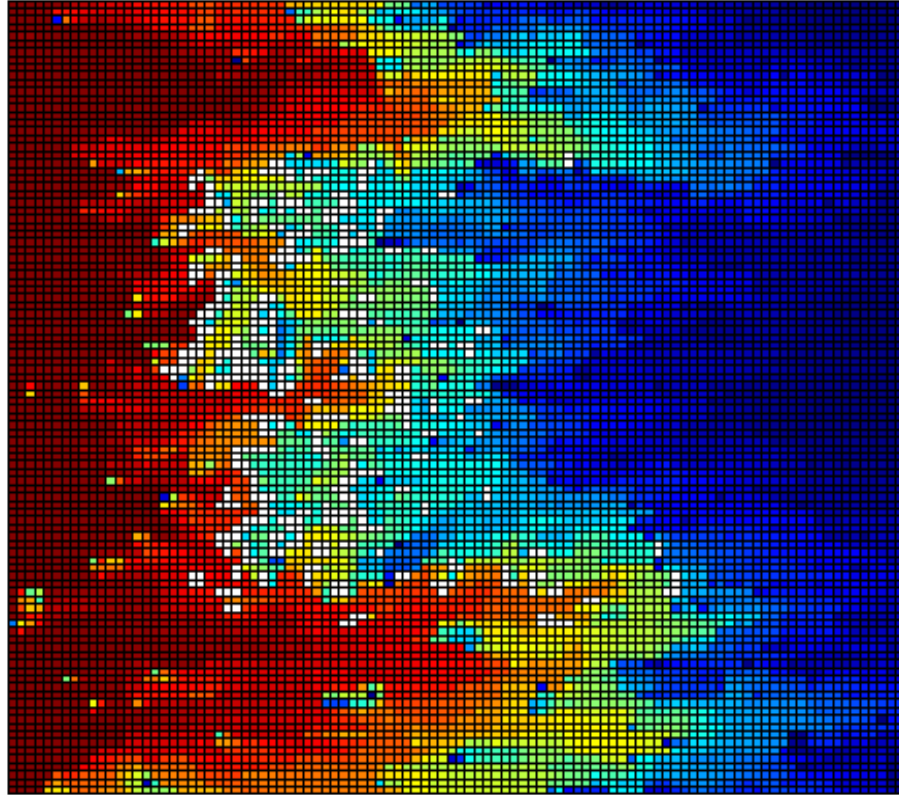
(a) PV = 0.16, Sg = 7.9%

Figure 5.17 (a) visualization of bubble growth pattern and concentration field. 100x100 network with 250 nucleation sites, same colormap as in Figure 5.12, pore throats are not shown, Bo = 8.54e-5, $<R_p>$ = 400 μm, ΔP = 1000Pa.
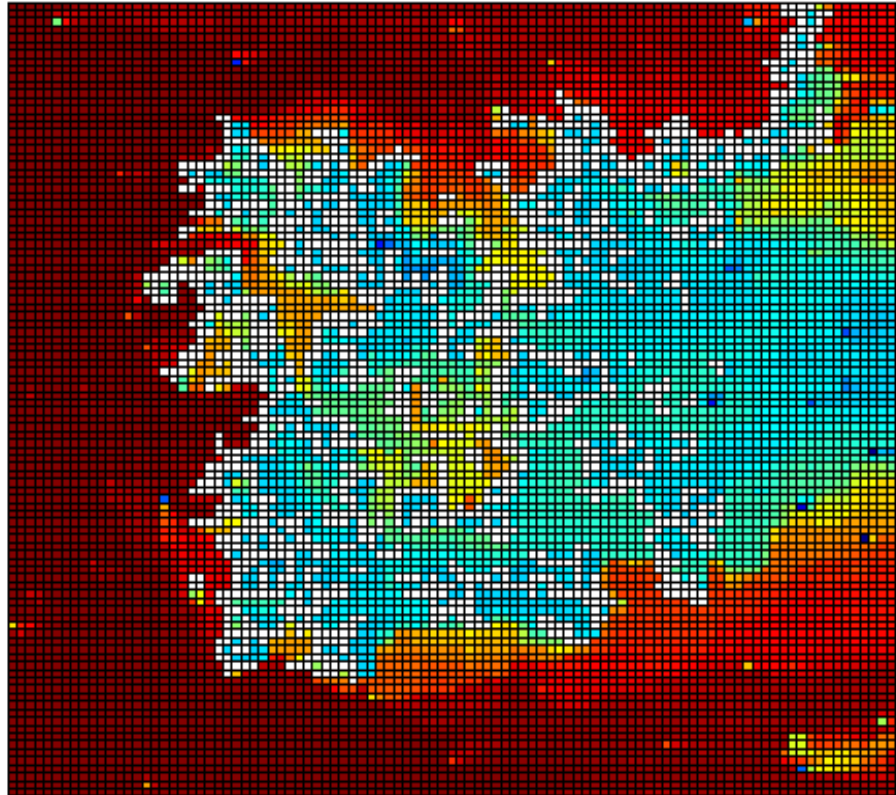
(b) PV = 0.44, Sg = 29.9%

5.17 (b) visualization of bubble growth pattern and concentration field. 100x100 network with 250 nucleation sites, same colormap as in Figure 5.12, pore throats are not shown, Bo = 8.54e-5, $<R_p>$ = 400 μm, ΔP = 1000Pa.

5.6.3　Water relative permeability

Water permeability is calculated by Darcy's Law, $K = U\mu L / \Delta P$, where U is Darcy velocity ($U = Q/A$, where Q is the water flow rate and $A = 2W\langle R_p \rangle$ is the cross-sectional area of the network, W is the width of the network and $\langle R_p \rangle$ is the average pore radius), μ is water viscosity, L is the length of the network and ΔP is the pressure drop. Water relative permeability is the ratio of water permeability to the absolute permeability of the medium, corresponding to the permeability at a water-saturated condition. Water relative permeability curves for the networks with 50 and 250 nucleation sites are shown in Figure 5.18 and Figure 5.19, respectively. A linear relationship between water relative permeability and water saturation is observed within the limited range of water saturation explored by the simulations. As gas saturation increases in the network, liquid flow rate decreases dramatically due to the reduced water conductivity.
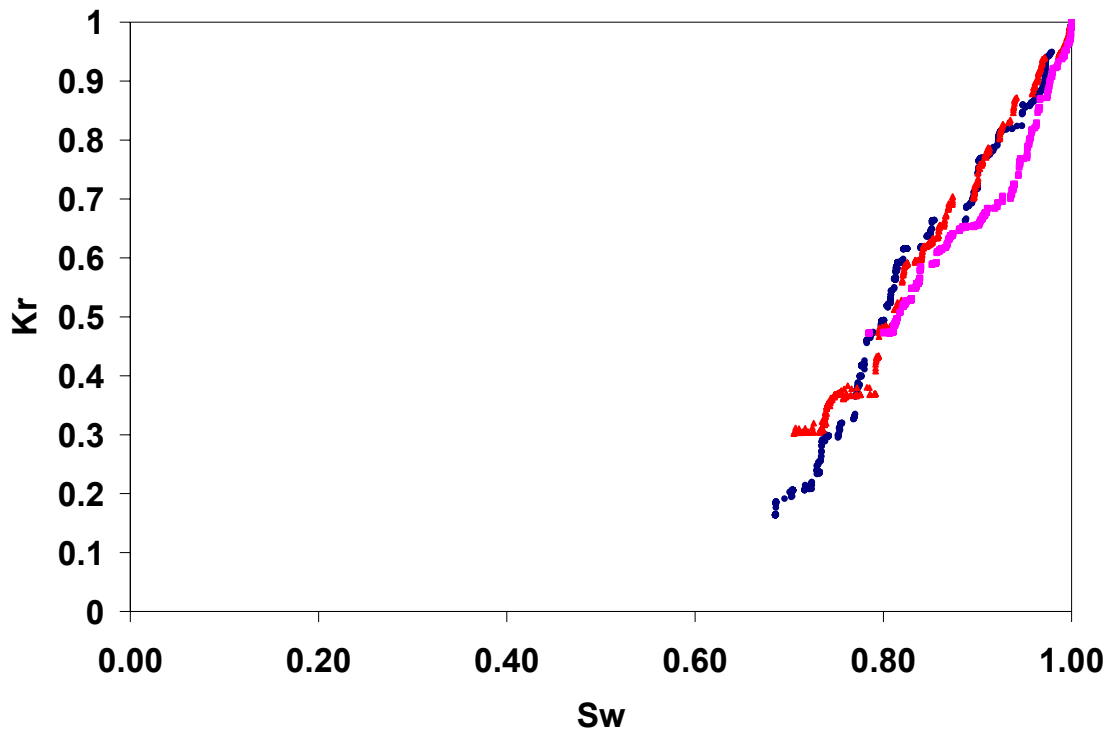
Figure 5.18 Water relative permeability vs. water saturation from three realizations of a 100x100 network with 50 nucleation sites, $<R_p> = 400$ μm, $\Delta P = 1000$Pa.
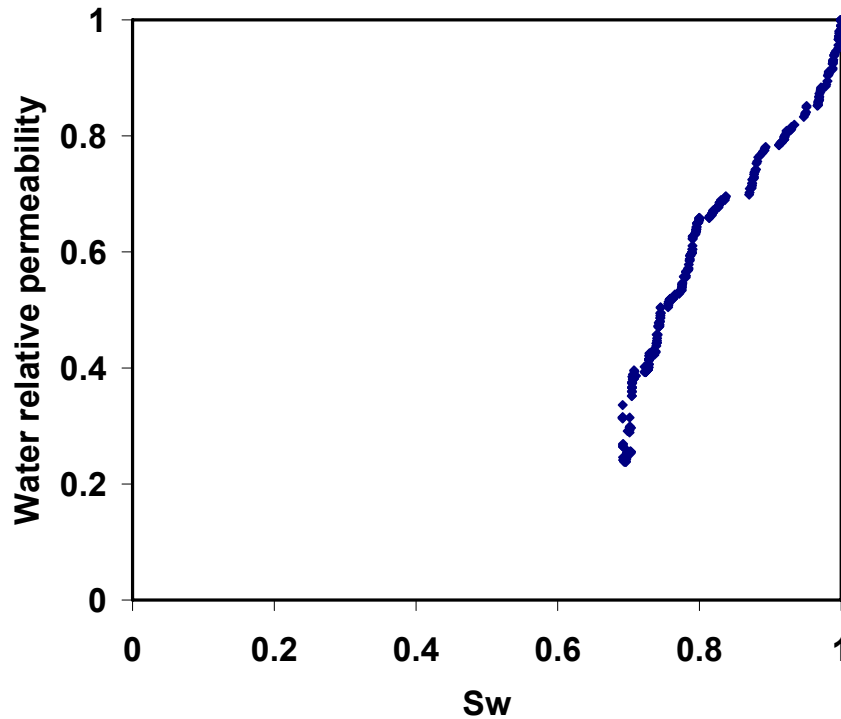
Figure 5.19 Water relative permeability vs. water saturation. 100x100 network with 250 nucleation sites, $<R_p> = 400$ μm, $\Delta P = 1000$Pa.

5.6.4 Effects of heterogeneity

To investigate the effects of heterogeneity, a lower permeability zone is embedded in the network, which is achieved by decreasing the sizes of the pore throats in a 20 by 30 block in the network by 2.5 times. Figure 5.18 shows the gas evolution and concentration profile in the heterogeneous medium. As expected, the solute concentration within the heterogeneity increases slowly compared to the rest of the network due to the lower permeability ($K \propto R_t^2$). However, nucleation sites can still be activated and bubbles appear in the zone, a behaviour that is unlikely to take place during air sparging.
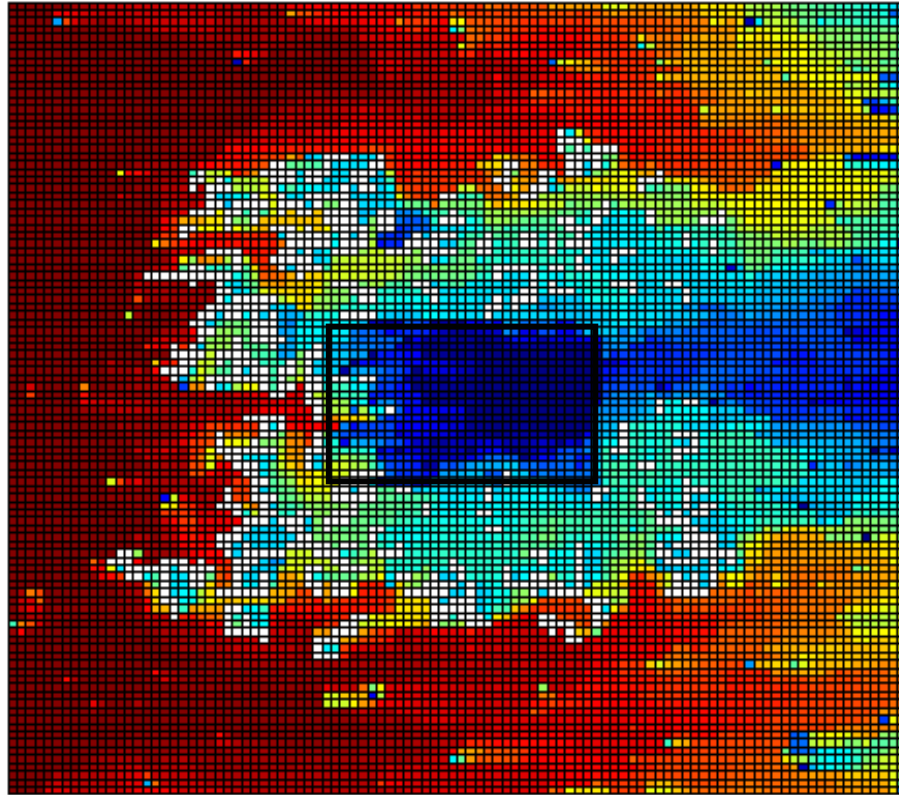
(a) PV = 0.44, Sg = 29.9%

Figure 5.20 (a) visualization of bubble growth pattern and concentration field. A 20x30 heterogeneity is embedded in the 100x100 network with 250 nucleation sites, same colormap as in Figure 5.12, pore throats are not shown, Bo = 8.54e-5, $<R_p>$ = 400 µm, ΔP = 1000Pa.
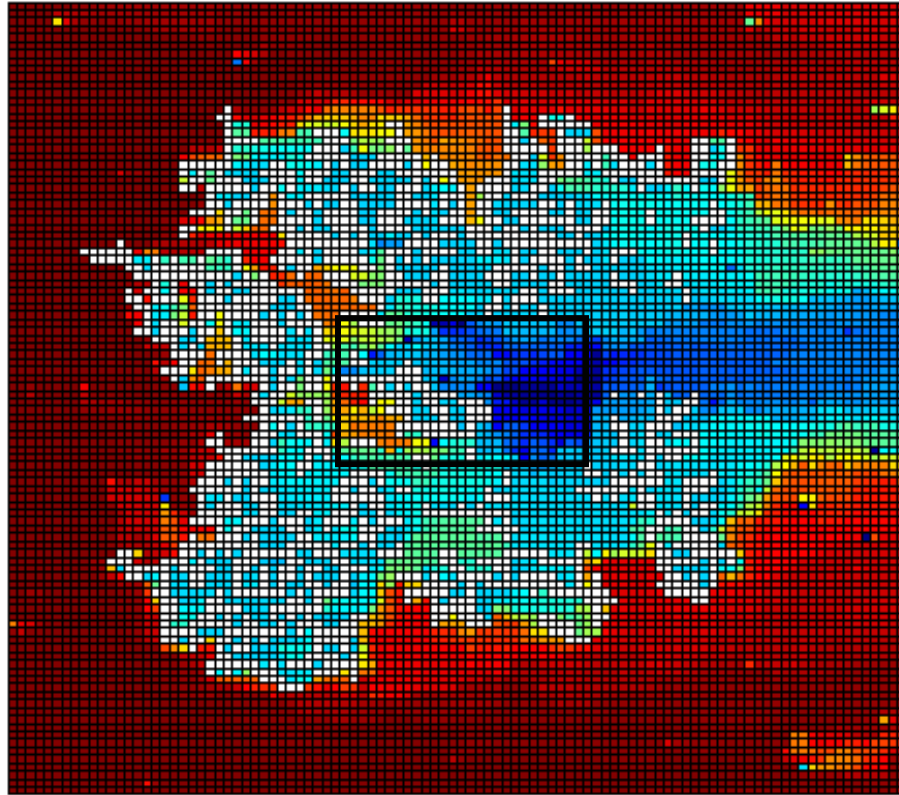
(b) PV = 0.44, Sg = 29.9%

Figure 5.20 (b) visualization of bubble growth pattern and concentration field. A 20x30 heterogeneity is embedded in the 100x100 network with 250 nucleation sites, same colormap as in Figure 5.12, pore throats are not shown, Bo = 8.54e-5, $<R_p>$ = 400 μm, ΔP = 1000Pa.

5.6.5 Macroscopic mass transfer rates

The macroscopic rate of CO_2 mass transfer from the liquid to the gas phase is expressed as:

$$N = K(C - C_{int}) \qquad (5.27)$$

where K [$1/s$] is the mass transfer rate coefficient, C_{int} is the concentration at the interface and C is the volumetric average concentration in the liquid phase:

$$C = \frac{\sum_i V_i C_i}{\sum_i V_i} \qquad (5.28)$$

where V_i and C_i are the volume and solute concentration of the ith node.

The mass transfer rate coefficient, K, is a function of gas saturation. Figure 5.21 displays curves of K against gas saturation for two realizations. At low gas saturation (S_g < 15%), K decreases dramatically with increasing S_g. At high gas saturation (S_g > 15%), the curves level off and K approaches a relatively constant value. The mass transfer rate coefficient K also depends on Peclet number, $Pe = \dfrac{u <R_p>}{D_m}$, which decreases as gas saturation increases, because the simulation is carried out using boundaries of constant ΔP across the network. Figure 5.22 shows the effect of supersaturation of the injected solution on the mass transfer rate coefficient for different gas saturations: K depends on both S_g and S_f at low gas saturations. When gas saturation is close to steady state (S_g > 25%), K becomes independent of S_f. Using a continuum model to fit the SWI experimental results, Li [2004] estimated $K = 3 \times 10^{-4}$ [1/s] at $Pe = 15$, which is in a

good agreement with the value of mass transfer rate coefficient at high gas saturations

calculated in this study (in the range of 1×10^{-4} to 5×10^{-4} [1/s]).
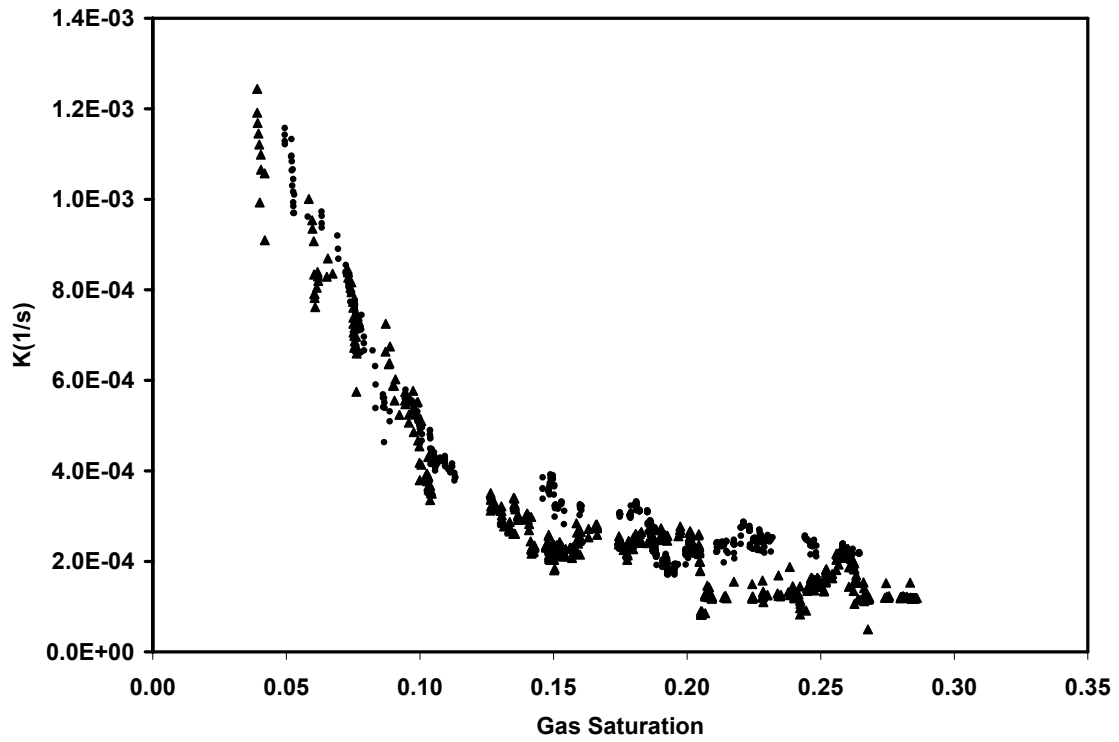
Figure 5.21 Mass transfer rate coefficient vs. gas saturation (two realizations). 100x100

network with 50 nucleation sites. $<R_p> = 400$ μm, $\Delta P = 1000$Pa.
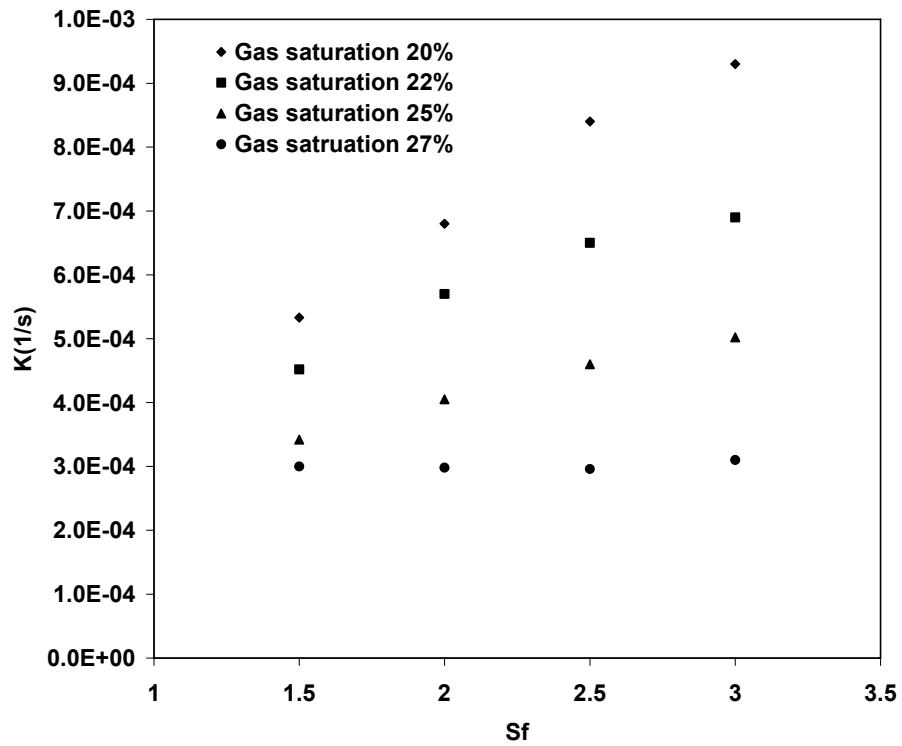
Figure 5.22 Mass transfer rate coefficient vs. supersaturation of injected solution at different gas saturations.

Equation 5.27 describes the macroscopic mass transfer in the network and is often used for continuum models at larger scale. Three assumptions are made:

1) linear driving force for mass transfer, $(C - C_{int})$;

2) uniform liquid concentration in the network;

3) homogeneous gas distribution.

However, gas evolution is a dynamic process. Visualizations show that in the network model, neither the gas distribution is homogeneous, nor is the liquid concentration uniform, especially at low gas saturation conditions. With respect to Figure 5.14 and 5.17, less than one pore volume of the supersaturated water needs to be injected to achieve high gas saturations. Calculations of the volumetric average concentration of the liquid phase, C, actually underestimate the effective driving force of mass transfer, leading to an overestimation of K. This effect is significant, especially at conditions of low gas saturations. For the same Peclet number, higher injection concentration leads to higher mass transfer rate. For simulations shown in Figure 5.22, 0.25 and 0.38 PV of injected solution ($S_f = 3$) are needed to obtain 20% and 27% gas saturation, respectively, compared to 0.66 and 0.98 PV for $S_f = 1.5$.

Correlations between Sherwood number and Peclet number are often used to describe the process of convective mass transfer. The Sherwood number is defined as:

$$Sh = K^* <R_p> \big/ D_m \qquad (5.29)$$

where K^* [m/s] is the mass transfer coefficient. $K^* = K / a_i$, where a_i [1/m] is the specific interfacial area between gas and liquid phases (interfacial area per unit pore

volume of the porous medium). Figure 5.23 shows typical Sh vs. Pe curves from the simulations. These data follow $Sh = 0.065 Pe^{0.42}$ in the range $15 < Pe < 65$.
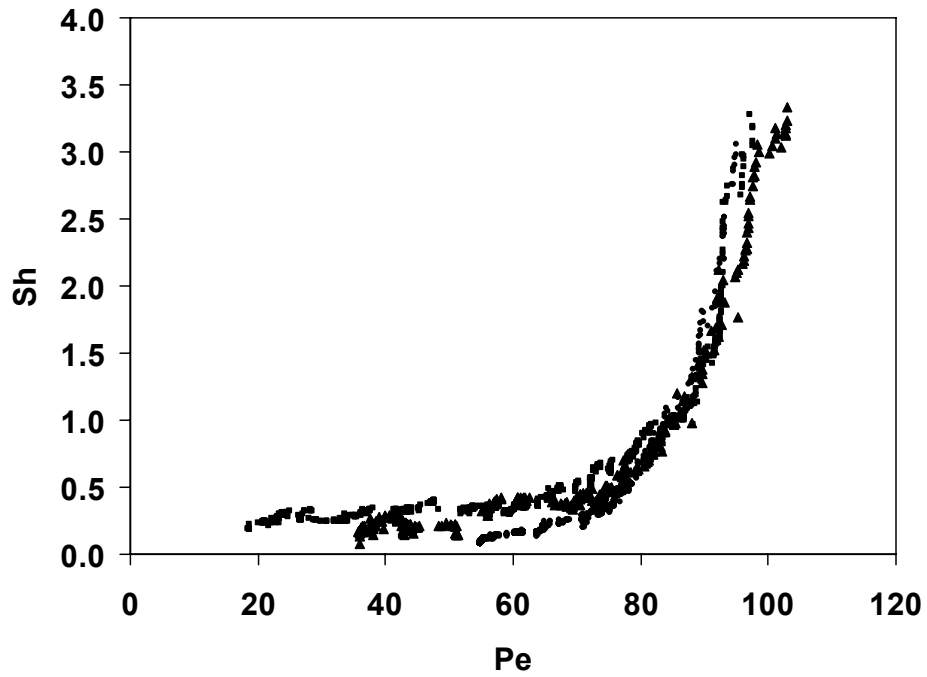
Figure 5.23. Sherwood number vs. Peclet number curves. Three realizations in 100x100 network with 50 nucleation sites. $\langle R_p \rangle = 400$ μm, $\Delta P = 1000$Pa.

5.7 Conclusions

A pore network model is developed to simulate the process of *in situ* gas evolution during supersaturated water injection (SWI). Simulations are carried out under different flow conditions to investigate bubble growth driven by convective mass transfer and bubble migration driven by buoyancy. Ramified clusters evolve from the nucleation sites and migrate upwards intermittently during the miscible displacement of water by supersaturated solution. Processes of cluster coalescence and fragmentation are accounted for. Visualizations of liquid pressure profile show that liquid flow could be significantly affected by gas distribution in the medium. Water relative permeability dramatically decreases as gas saturation increases. The observed pattern of bubbles repeatedly trapped by capillary forces after mobilization implies that the definition of critical gas saturation for continuous gas flow by Tsimpanogiannis and Yortsos [2004] is not applicable to the gas evolution problem in homogeneous porous media. Larger gas clusters tend to form close to the injection boundary and dissolved gas is stripped after the supersaturated water flows through the clusters by corner flow. Although the stripping process could result in the existence of zones with low solute concentration (near the saturated value), relatively homogeneous gas distribution could still be achieved, a phenomenon that is consistent with the experimental observations [Li, 2004]. In this study, the largest gas saturations in a homogeneous medium could be obtained are in the range of 27% to 31%. Effects of heterogeneity of the porous medium are investigated and the simulations show that bubbles could be nucleated and grow inside the zone of low permeability. This behaviour could be favourably exploited in NAPL recovery in order to

overcome the difficulties associated with air sparging (lack of direct contact between gas and contaminants due to the gas bypassing of the less permeable contaminated zones). The developed pore network model reproduces the fundamental physics of two phase flow, convective mass transfer and capillary phenomena and the results obtained, such as water relative permeability, mass transfer rate coefficient and Sherwood number, could be used to inform simulations using continuum models at larger scale.

Chapter 6

Conclusions and Recommendations

6.1   Conclusions

A number of fundamental issues concerning convective mass transfer across fluid-fluid interfaces in porous media are investigated by simulating the processes of mass transfer to/from distributed sinks/sources, which focus on i) slowly dissolving liquid filaments of a wetting non-aqueous phase liquid (NAPL) held in the corners of angular pores or throats and ii) gas bubbles growing during the flow of a supersaturated aqueous phase in porous media. Both of these processes are immediately relevant to groundwater remediation processes.

6.1.1   Effects of the stability of NAPL films on wetting NAPL dissolution

A pore network model is developed to qualitatively explore the dissolution behaviour of wetting NAPL in porous media. Under conditions of preferential NAPL wettability, NAPL is retained within small pores and in the form of thick films (liquid filaments) along the corners and crevices of the pore walls. These NAPL corner filaments are assumed to be responsible for the hydraulic continuity between NAPL-filled pores

and the large interfacial area for mass transfer during NAPL dissolution. A stepwise solution procedure is used to obtain the flow and solute concentration fields in the network. The simulations reproduce the mechanism of mass-transfer-driven drainage observed in experiments using transparent glass micromodels [Sahloul et al., 2002]. Rupture of NAPL films is related to disjoining pressure and film curvature. Distinct clusters of residue NAPL are formed subsequently and a cluster multiple labeling algorithm is developed to simulate the process. The simulation results indicate that the NAPL dissolution behavior is very sensitive to the stability and distribution of thick NAPL films along pore corners. Rupture of NAPL films results in severe loss of NAPL-water interfacial area and a large reduction in the rate of mass transfer. The observed behavior of long-term high effluent NAPL concentrations (near NAPL solubility) is attributed to stable NAPL films. The simulations strongly suggest that factors affecting NAPL film stability may play an important role in residual NAPL dissolution in oil wet systems.

6.1.2 Convective mass transfer across fluid interfaces in straight angular pores

A finite element method is used to study convective mass transfer in wetting fluid filaments along corners of angular pores. The exact geometry of the flow and mass transfer domain within the pore walls and the arc meniscus of the fluid interface is accounted for in terms of the corner half-angle, contact angle and interfacial meniscus curvature. Both perfect-slip and no-slip interfaces were considered. The model is verified by comparing the results of hydraulic resistance factors and hydraulic conductance of the corner filaments to the numerical results reported by Patzek and Kristensen [2001]. Novel

results were obtained for the normalized average exit concentration in corner filaments. These results were correlated with the pore-scale Peclet number and the characteristic dimensions of the corner geometry and compared to the previously published approximations using 2d slit models. The latter solutions are found to be in considerable errors. The results obtained can be used to facilitate the use of pore network simulators in which pores and throats are modeled as straight tubes of rectangular or equilateral triangular cross-sections.

6.1.3 *In situ* gas evolution in porous media during supersaturated water injection

A 2D pore network model is developed to simulate the process of *in situ* gas evolution in porous media during supersaturated water injection (SWI). The model is based on the fundamental physics of miscible flow, capillarity, bubble nucleation, convective mass transfer and buoyancy-driven gas migration and fragmentation. Simulations under different flow conditions show that:

- Bubble growth is driven by convective mass transfer and sufficient large bubbles can be mobilized by buoyancy and migrate upwards intermittently. Bubble coalescence and fragmentation take place repeatedly during the processes. The mobilized bubbles could be trapped by capillary forces again.

- Gas distribution in porous media significantly affects the liquid flow. Liquid relative permeability decreases significantly as gas saturation increases.

- 27-31% gas saturation can be achieved by SWI in homogeneous porous media before gas can escape from the network.

- Relatively homogeneous gas distribution can be obtained by SWI while larger gas clusters tend to form close to the injection boundary.

- Regions of low solute concentration (near the solubility value) and low liquid flow rate exist in the medium when large gas clusters block the liquid flow and dissolved gas is stripped after the supersaturated solution flows through the blocking clusters.

- Gas bubbles can be nucleated and subsequently grow inside low permeability zones, a phenomenon which makes SWI advantageous over air sparging in its potential to contact and volatilize NAPL sources.

6.2   Recommendations

- Since the wettability of porous media plays an import role in multiphase flow and NAPL remediation, experimental data of disjoining pressure for environmentally relevant NAPLs are needed for further investigations of the effects of NAPL film stability on NAPL dissolution. To the best of the author's knowledge, there is no systematic experimental study on the issue in the literature so far.

- The present simulations have neglected viscous NAPL flow in dissolving NAPL filaments, caused by capillary pressure gradients. While this is considered appropriate for a slowly dissolving wetting NAPL, viscous flow in the NAPL phase would have to be accounted for in cases of rapid dissolution (e.g., in the presence of surfactant solutions).

- Convective mass transfer of multiple-component fluids and reactions taking place in corner filaments may be important in modeling some processes of enhanced NAPL remediation.

- In the study of convective mass transfer in angular pores, straight pores or throats are chosen to idealize the pore geometry. However, models with non-constant pore cross sections (*e.g.*, bi-conical pores) are sometimes used in pore scale simulations. The convective mass transfer in such geometries could be studied to facilitate pore network modeling.

- In the study of gas evolution, a single component gas phase is assumed. Models should be developed to simulate the process of gas evolution from multi-component solutions when the partial pressure of each gas component has to be accounted for.

- Further studies on NAPL recovery using SWI method are needed. This is a problem of three phase flow. Upon direct contact with growing bubbles, NAPL spreads on the surfaces of the bubbles and mass transfer issues of diffusion and mobilization of NAPL have to be addressed.

- The reverse process to gas evolution from supersaturated solution is the dissolution of bubbles into an undersaturated aqueous phase. The developed model could be modified to simulate such phenomena.

- Gas evolution in porous media is an important research subject. Two situations of great interest are (i) *in situ* formation of CO_2 bubbles within the porous anode electrode backing layer of direct methanol fuel cells (DMFC) [e.g., Argyropoulos et al., 1999 a, b; Yang et al., 2005] and (ii) the potential loss of seal integrity in reservoirs used for CO_2 sequestration that may accompany the appearance of gas bubbles in cap rock as a result

of reservoir pressure fluctuations [e.g., Patzek et al., 2003, Pruess, 2005]. The developed pore network model could be used (with some modifications) to simulate these processes.

- Most of the computer programs in this research are written in FORTRAN. For models as complicated as the ones developed here, object oriented languages, C++ for instance, are preferable from a programming point of view.

- Upscaling pore network modeling results remains a considerable challenge. How to apply the microscopic results to the macroscopic and field-scale modeling should be the focus of future research on the SWI process.

Bibliography

Adler, P.M. and Thovert, J.F., 1998. Real porous media: Local geometry and macroscopic properties. App. Mech. Rev., 51: 537-585.

Argyropoulos, P., Scott, K. and Taama, W.M., 1999 a. Gas evolution and power performance in direct methanol fuel cells, J. Appl. Electrochem. 29 (6): 661-669.

Argyropoulos, P., Scott, K. and Taama, W.M., 1999 b. Carbon dioxide evolution patterns in direct methanol fuel cells, Electrochem. ACTA. 44 (20): 3575-3584.

Arora, P. and Kovscek, A.R., 2003. A mechanistic modeling and experimental study of solution gas drive. Transp. Porous Media 51 (3): 237-265.

Auradou, H., Maloy, K.J., Schmittbuhl, J., Hansen, A. and Bideau, D., 1999. Competition between correlated buoyancy and uncorrelated capillary effects during drainage, Phys. Rev. E 60 (6): 7224-7234.

Austad, T., Matre, B., Milter, J., Sevareid, A. and Oyno, L., 1998. Chemical flooding of oil reservoirs 8. Spontaneous oil expulsion from oil- and water-wet low permeable chalk material by imbibition of aqueous surfactant solutions, Colloid Surf A: Physicochem Eng Asp, 137: 117-129.

Auzerais, F.M., Dunsmuir, J., Ferreol, B.B., Martys, N., Olson, J., Ramakrishnan, T.S., Rothman, D.H. and Schwartz, L.M., 1996. Transport in sandstone: a study based on three dimensional microtomography, Geophys. Res. Lett., 23: 705-708.

Baldwin, C.A. and Gladden, L.F., 1996. NMR imaging of nonaqueous-phase liquid dissolution in a porous medium. AICHE J. 42 (5): 1341-1349.

Barranco, F.T. and Dawson, H.E., 1999. Influence of aqueous PH on the interfacial properties of coal tar, Environ. Sci. Technol., 33 (10): 1598-1603.

Beckwith, C.W. and Baird, A.J., 2001. Effect of biogenic gas bubbles on water flow through poorly decomposed blanket peat, Water Resour. Res. 37 (3): 551-558.

Berkowitz, B. and Ewing, R.P., 1998. Percolation theory and network modeling applications in soil physics, Surveys in Geophysics, 19, 23-72.

Berg, J.C., 1993. Wettability, M. Dekker, New York.

Birovljev, A., Wagner, G., Meakin, P., Feder, J. and Jossang, T., 1995. Migration and fragmentation of invasion percolation clusters in 2D porous media, Phys. Rev. E, 51 (6): 5911-5915.

Biswal, B., Manwart, C. and Hilfer, R. 1999. Quantitative analysis of experimental and synthetic microstructures for sedimentary rock. Physica A 273 (3-4): 452-475.

Blunt, M.J., 2001. Flow in porous media – pore network models and multiphase flow, Curr. Opinion Colloid Interf. Sci. 6: 197-207.

Blunt, M.J., Jackson, M.D., Piri, M. and Valvatne, P.H., 2002. Detailed physics, predictive capabilities and macroscopic consequences for pore-network models of multiphase flow, Adv. Water Resour. 25 (8-12): 1069-1089.

Bora, R., Maini, B.B. and Chakma, A., 2000. Flow visualization studies of solution gas drive process in heavy oil reservoirs with a glass micromodel, SPE Reservior Evalu. Eng. 3 (3): 224-229.

Borden, R.C., Goin, R.T. and Kao, C.M., 1997. Control of BTEX migration using a biologically enhanced permeable barrier, Ground water Monit. Rem., 17(1): 70-80.

Bradford, S.A. and Leij, F.J., 1997. Estimating interfacial areas for multi-fluid soil systems, J. Contam. Hydrol., 27: 83-105.

Bradford, S.A., Phelan, T.J. and Abriola, L.M., 2000. Dissolution of residual tetrachloroethylene in fractional wettability porous media: correlation development and application, J. Contam. Hydrol., 45: 35-61.

Bradford, S.A., Vendlinski, R.A. and Abriola, L.M., 1999. The entrapment and long-term dissolution of PCE in fractional wettability porous media, Water Resour. Res., 35 (10): 2955-2964.

Brown, R.J.S. and Fatt, I., 1956. Measurements of fractional wettability of oilfield rocks by the nuclear magnetic relaxation method, Trans. AIME, 207, 262-264.

Bryant, S.L., King, P.R., and Mellor, D.W., 1993. Network model evaluation of permeability and spatial correlation in a real random sphere packing, Transp. Porous Media 11: 53–70.

Buckley, J.S., Takamura, K. and Morrow, N.R., 1989. Influence of electrical surface charges on the wetting properties of crude oils, SPE Res Eng, 4: 332-340.

Carmeliet, J., Descamps, F. and Houvenaghel, G., 1999. A multiscale network model for simulating moisture transfer properties of porous media, Transp. Porous Media 35 (1): 67-88.

Chang, D., Ioannidis, M.A., 2002. Magnetization evolution in network models of porous rock under conditions of drainage and imbibition, J. Colloid Interf. Sci. 253 (1): 159-170.

Chatzis, I., 1980. A network approach to analyze and model capillary and transport phenomena in porous media, Ph.D. Thesis, Univ. of Waterloo, ON, Canada.

Chatzis, I. and Dullien, F.A.L., 1977. Modelling pore structures by 2D and 3D networks with application to sandstones, Canadian J. Petro. Technol., 97–108.

Chatzis, I. and Dullien, F.A.L., 1983. Dynamic immiscible displacement mechanisms in pore doublets: theory versus experiment, J. Colloid and Interface Sci., 91, 199-222.

Chatzis, I. and Dullien, F.A.L., 1985. The modeling of mercury porosimetry and the relative permeability of mercury in sandstones using percolation theory. Int. Chem. Eng. 25: 47–66.

Chatzis, I. Kantzas, A. and Dullien, F.A.L., 1988. SPE 18284, SPE 63rd Meeting, Houston, TX.

Cherry, J.A., Feenstra, S. and Mackay, M., 1996. Concepts for the remediation of sites contaminated with DNAPLs. In Pankow, J.F. and Cherry, J.A. (Eds), Dense chlorinated solvents and other DNAPLs in groundwater, Waterloo press. Portland, Oregon: 475-506.

COMSOL AB, 2003. FEMLAB VERS 3 0.

Dean, R.B., 1944. The formation of bubbles. J. Appl. Phys. 15: 446-451.

Deeb, R.A., Scow, K.M., and Alvarez-Cohen, L., 2000. Aerobic MTBE biodegradation: an examination of past studies, current challenges and future research directions, Biodegradation, 11 (2-3): 171-186.

Dillard, L.A. and Blunt, M.J., 2000. Development of a pore network model to study non-aqueous phase liquid dissolution. Water Resour. Res., 36 (2): 439–454.

Dillard, L.A., Essaid, H.I. and Blunt, M.J., 2001. A functional relation for field-scale non-aqueous phase liquid dissolution developed using a pore network model, J. Contam. Hydrol. 48: 89-119.

Dixit, A.B., McDougall, S.R., Sorbie, K.S. and Buckley, J.S., 1999. Pore-scale modeling of wettability effects and their influence on oil recovery, SPE Res Eval Eng, 2 (1): 25-36.

Dobry, R. and Finn, R.K., 1956. Mass transfer in fluid systems, Cambridge Univ. Press, Cambridge.

Dominguez, A., Bories, S. and Prat, M., 2000. Gas cluster growth by solution diffusion in porous media. Experiments and automaton simulation on pore network, Int. J. Multiphase Flow 26: 1951-1979.

Donaldson, J.H., Istok, J.D., Humphrey, M.D., O'Reilly, K.T., Hawelka, C.A. and Mohr, D.H., 1997, Development and testing of a kinetic model for oxygen transport in porous media in the presence of trapped gas, Ground Water, 35, 270-279.

Dong, J., Chowdhry, B. and Leharne, S., 2004., Investigation of the wetting behavior of coal tar in three phase systems and its modification by poloxamine block copolymeric surfactants, Environ Sci Technol, 38 (2): 594-602.

Dong, M. and Chatzis, I., 1995. The imbibition and flow of a wetting liquid along the corners of a square capillary tube. J. Colloid Interf. Sci. 172: 278-288.

Dong, M., Dullien, F.A.L. and Chatzis, I., 1995. Imbibition of oil in film form over water present in edges of capillaries with an angular cross section. J. Colloid Interf. Sci. 172: 21-36.

Drummond, C. and Israelachvili, J., 2002. Surface forces and wettability, J. Petrol. Sci. Eng., 33 (1-3): 123-133.

Du, C. and Yortsos, Y.C., 1999. A numerical study of the critical gas saturation in a porous medium, Transp. Porous Media 35 (2), 205–225.

Dullien, F.A.L., 1992. Porous media: fluid transport and pore structure, Academic Press, SanDiego, CA.

Dwarakanath, V., Jackson, R.E. and Pope, G.A., 2002. Influence of wettability on recovery of NAPLs form alluvium, Environ. Sci. Technol., 36, 227-231.

Dwivedi, P. N. and Updhyay, S. N., 1977, Particle-fluid mass transfer in fixed and fluidized beds, Ind. Eng Chem. Process Design Dev. 16, 157–165.

El Yousfi, A., Zarcone, C. and Bories, S., 1997, Physical mechanisms for bubble growth during solution gas drive, SPE 38921, in: Processings of the SPE Ann. Tech. Conf. and Exhibition, San Antonio, TX.

Elder, C.R. and Benson, C.H., 1999. Air channel formation, size, spacing and tortuosity during air sparging. Ground Water Monit. Rem. 19 (3): 171-181.
Fatt, I., 1956. The network model of porous media. Petroleum Transactions, AIME 207: 144–177.

Fenwick, D.H. and Blunt, M.J., 1998 a. Network modeling of three-phase flow in porous media, SPE J. 3: 86-97.

Fenwick, D.H. and Blunt, M.J., 1998 b. Three dimensional modeling of three phase imbibition and drainage, Adv. Water Resour. 21 (2): 121-143.

Ferrand, L.A. and Celia, M.A., 1990. Computational investigation of the effects of heterogeneity on the capillary pressure-saturation relation, Proceedings of the International Conference on Computational Methods in Water Resources, Venice, Italy, 181.

Firoozabadi, A., 1997, Author's reply to pressure and volume evolution during gas phase formation in solution gas drive processes, SPE J. 2 (2): 228–231.

Firoozabadi, A. and Kashchiev, D., 1996, Pressure and volume evolution during gas phase formation in solution gas drive processes, SPE J. 1 (3): 219–228.

Firoozabadi, A., Ottesen, B. and Mikklesen, M., 1992. Measurement of supersaturation and critical gas saturation, SPE Form. Eval.: 337–344.

Freitas, D.S. and Prat, M., 2000. Pore network simulation of evaporation of a binary liquid from a capillary porous medium, Tansp. Porous Media, 40: 1-25.

Friedlander, S. K., 1957, Mass and heat transfer to single spheres and cylinders at low Reynolds
numbers, AIChE 3, 43–48.

Fry, V.A., Selker, J.S. and Gorelik, S.M., 1997. Experimentl investigations fro trapping oxygen gas in saturated porous media for in situ bioremediation, Water Resour. Res., 33(12):2687-2696.

Geller, J.T. and Hunt, J.R., 1993. Mass transfer from non-aqueous phase organic phase liquids in water saturated porous media. Water Resour. Res., 29: 833-846.

George, D.S., Hayat, O. and Kovscek, A.R., 2005. A microvisual study of solution-gas-drive mechanisms in viscous oils, J Petro. Sci. Eng. 46 (1-2): 101-119.

Grattoni, C.A. and Dawe, R.A., 2003. Gas and oil production from waterflood residual oil: effects of wettability and oil spreading characteristics. J. Petro. Sci. Eng. 39 (3-4): 297-308.

Grattoni, C.A., Hawes, R.I. and Dawe, R.A., 2001. Production of gas from waterflood residual oil–gas saturation build-up and relative permeabilities. Petro. Geosci. 7: 131-136.

Guo, G. and Thompson, K.E., 2001.Experimental analysis of local mass transfer in packed beds. Chem. Eng. Sci., 56 (1): 121-132.

Harrold, G., Gooddy, D.C., Lerner, D.N. and Leharne, S.A., 2001. Wettability changes in trichloroethylene-contaminated sandstone, Environ. Sci. Technol., 35 (7): 1504-1510.

Hawes, R.I., Dawe, R.A. and Evans, R.N., 1996. Theoretical model for the depressurization of waterflooded reservoirs. Trans ICHemE 74 (A): 197-205.

Hawes, R.I., Dawe, R.A. and Evans, R.N., 1997. The release of solution gas from waterflooded residual oil. SPE J. 2: 379-388.

Held, R.J. and Celia, M.A., 2001 a. Pore-scale modeling extension of constitutive relationships in the range of residual saturations. Water Resour. Res. 37 (1): 165-170.

Held, R.J. and Celia, M.A., 2001 b. Pore-scale modeling and upscaling of nonaqueous phase liquid mass transfer. Water Resour. Res. 37 (3): 539-549.

Hinchee, R.E., 1994. Air sparging, state of the art. In Hinchee, R.E. (Ed.), Air sparging for site remediation. Lewis Publishers, Boca Raton, Florida: 1-13.

Hirasaki, G.J., 1991.Wettability: fundamentals and surface forces, SPE Form Eval, 6:: 217-226.

Ho, C.K. and Udell, K.S., 1995. Mass transfer limited drying of porous media containing an immobile binary liquid mixture, Int. J. Heat Mass Transf., 38: 339-350.

Holocher, J., Peeters, F., Aeschbach-Hertig, W., Kinzelbach, W. and Kipfer, R., 2003. Kinetic model of gas bubble dissolution in groundwater and its implications for the dissolved gas composition, Env. Sci. Tech., 37: 1337-1343.

Hoshen, J. and Kopelman, R., 1976. Percolation and cluster distribution. I. cluster multiple labeling technique and critical concentration algorithm. Phys. Rev. B, 14 (8): 3438-3445.

Hui, M.H. and Blunt, M.J., 2000. Effects of wettability on three-phase flow in porous media, J. Phys. Chem. B 104, 3833-3845.

Imdakm, A.O. and Sahimi, M., 1991. Computer simulation of particle transport processes in flow through porous media, Chem. Eng. Sci., 46 (8): 1977-1993

Imhoff, P.T., Arthur, M.H. and Miller, C.T., 1998. Complete dissolution of TCE in saturated porous media. Environ. Sci. Technol., 32 (16): 2417-2424.

Imhoff, P. T., Frizzell, A. and Miller, C. T., 1997. Evaluation of thermal effects on the dissolution of a nonaqueous phase liquid in porous media, Environ. Sci. Technol., 31, 1615–1622.

Imhoff, P.T., Jaffe, P.R. and Pinder, G.F., 1994. An experimental study of complete dissolution of a nonaqueous phase liquid in saturated porous media. Water Resour. Res., 30 (2): 307–320.

Ioannidis, M.A., Chatzis, I. and Payatakes, A.C., 1991. A mercury porosimeter for investigating capillary phenomena and microdisplacement mechanisms in capillary networks, J. Colloid Interf. Sci., 143 (1): 22-36

Ioannidis, M.A. and Chatzis, I., 1993, Network modeling of pore structure and transport properties of porous media, Chem. Eng. Sci., 48, 951-972.

Jackson, R.E. and Dwarakanath, V., 1999. Chlorinated degreasing solvents: physical-chemical properties affecting aquifer contamination and remediation. Ground Water Monit R, 19 (4): 102-110.

Ji, W., Dahmani, A., Ahlfeld, D., Lin, J. and Hill, E., 1993. Laboratory study of air sparging: air flow visualization. Ground Water Monit. Rem., 13(4): 115-126.

Jia, C., Shing, K. and Yortsos, Y.C., 1999. Visualization and simulation of non-aqueous phase liquids solubilization in pore networks. J. Contam. Hydrol., 35 (4): 363-387.

Johns, M.L. and Gladden, L.F., 1999. Magnetic resonance imaging study of the dissolution kinetics of octanol in porous media. J. Colloid Interf. Sci. 210 (2): 261-270.

Jones, S.F., Evans, G.M. and Galvin, K.P., 1999 a. Bubble nucleation from gas cavities – a review, Adv. Colloid Interf. Sci. 80: 27-50.

Jones, S.F., Evans, G.M. and Galvin, K.P., 1999 b. The cycle of bubble production from a gas cavity in a supersaturated solution, Adv. Colloid Interf. Sci. 80: 51-84.

Jones, S.F., Galvin, K.P., Evans, G.M. and Jameson, G.J., 1998. Carbonated water: The physics of the cycle of bubble production, Chem. Eng. Sci. 53 (1): 169-173

Kam, S.I., Gauglitz, P.A. and Rossen, W.R., 2001. Effective compressibility of a bubbly slurry. I. Theory of the behavior of bubbles trapped in porous media, J. Colloid Interf. Sci. 241 (1): 248-259.

Kamath, J. and Boyer, R.E., 1995. Critical gas saturation and supersaturation in low-permeability rocks, SPE Form. Eval. 10 (4): 247-253.

Kashchiev, D. and Firoozabadi, A., 1993. Kinetics of the initial stage of isothermal gas phase formation, J. Chem. Phys. 98 (6): 4690–4699.

Kellner, E., Price, J.S. and Waddington, J.A., 2004. Pressure variations in peat as a result of gas bubble dynamics, Hydrogeo. Processes, 18 (13): 2599-2605.

Khachikian, C.S. and Harmon, T.C., 2000. Nonaqueous phase liquid dissolution in porous media: current state of knowledge and research needs, Transp. Porous Media, 38, 3-28.

Koplik, J., 1982. Creeping flow in two dimensional networks, J. Fluid Mechanics 119: 219–247.

Kortekaas, T.F.M. and van Poelgeest, F., 1991. Liberation of solution gas during pressure depletion of virgin watered-out oil reservoirs, SPE Res. Eng.: 329-335.

Kovscek, A.R., Wong, H. and Radke, C.J., 1993. A pore-level scenario for the development of mixed wettability in oil-reservoirs, AICHE J., 39 (6): 1072-1085.

Legait, B., 1983. Laminar flow of two phases through a capillary tube with variable square cross-section, J. Colloid Interf. Sci., 96 (1): 28-38.

Levich, V.,1962. Physicochemical Hydrodynamics, Prentice-Hall, Englewood Cliffs, N.J.

Li, T., 2004. Recovery of source non-aqueous phase liquids from groundwater using supersaturated water injection, MASc Thesis, Univ. of Waterloo, ON, Canada.

Li, X. and Yortsos, Y.C., 1995 a. Visualization and simulation of bubble growth in pore networks, AICHE. J. 41 (2): 214-222.

Li, X. and Yortsos, Y.C., 1995 b. Theory of multiple bubble growth in porous media by solute diffusion, Chem. Eng. Sci. 50 (8): 1247-1271.

Li, Y. and Wardlaw, N.C., 1986. The influence of wettability and critical pore throat aspect ratio on snap off. J. Colloid Interf. Sci., 109(2): 461.

Liang, Z. Ioannidis, M.A. and Chatzis, I., 2000. Permeability and electrical conductivity of porous media from 3D stochastic replicas of the microstructure. Chem. Eng. Sci., 55: 5247-5262.

Lundegard, P. and LaBrecque, D., 1995. Air sparging in a sandy aquifer (Florence, Oregon, USA): Actual and apparent radius of influence. J. Contam. Hydrol. 19 (1):1-27.

Man, H.N. and Jing, X.D., 2000. Pore network modelling of electrical resistivity and capillary pressure characteristics, Transp. Porous Media, 41: 263-286.

Mani, V. and Mohanty, K.K., 1998. Pore level network modeling of three phase capillary pressure and relative permeability curves, SPE J. 3: 238-248.

Mayer, A.S. and Miller, C.T., 1992. The Influence of porous medium characteristics and measurement scale on pore-scale distributions of residual nonaqueous phase liquids, J. Contam. Hydrol., 11: 189-213.

McDougall, S.R. and Sorbie, K.S., 1999. Estimation of critical gas saturation during pressure depletion in virgin and waterflooded reservoirs, Petro. Geosci. 5: 233-299.

Miller, C.T., Christakos, G., Imhoff, P.T., McBride, J.F., Pedit, J.A. and Trangenstein, J.A., 1998. Multiphase flow and transport modeling in heterogeneous porous media: challenge and approaches, Adv. Water Resour., 21, 77-120.

Miller, C.T., Poirier-McNeill, M.M. and Mayer, A.S., 1990. Dissolution of trapped nonaqueous phase liquids: mass transfer characteristics, Water Resour. Res., 26, 2783-2796.

Mysels, K.J. and Stigter, D., 1953. A new method of measuring diffusion coefficients, J. Phys. Chem. 57 (1): 104-106.

Oren, P.E. and Bakke, S., 2002. Process based reconstruction of sandstones and prediction of transport properties. Trans. Porous Media, 46 (2-3): 311-343.

Oren, P.E. and Bakke, S., 2003. Reconstruction of Berea sandstone and pore scale modelling of wettability effects. J. Petrol. Sci. Eng., 39: 177-199.

Parker, J.C., Katyal, A.K., Kaluarachchi, J.J., Lenhard, R.J., Johnson, T.J., Jayaraman, K., Unlu, K. and Zhu, J.L., 1991. Modeling multiphase organic chemical transport in soils and ground water, Rep. EPA/600/2-91/42, Washington, D.C.

Patzek, T.W. and Kristensen, J.G., 2001, Shape factor correlations of hydraulic conductance in noncircular capillaries, II. two-phase creeping flow, J. Colloid Interf. Sci., 236: 305-317.

Patzek, T.W. and Silin, D.B., 2001. Shape factor and hydraulic conductance in noncircular capillaries: I. one phase creeping flow, J. Colloid Interf. Sci. 236: 295-304.

Pérez-Aguilar, H., Domínguez, A., Rodríguez, C., Rojas, F. and Kornhauser, I., 2002. Virtual study of wettability effects on bubble growth by solute diffusion in correlated porous networks, Inter. J. Multiphase Flow 26: 179-192.

Peyron, M., Pierens, G.K., Lucas, A.J., Hall, L.D. and Stewart, R.C., 1996. The modified stretched-exponential model for characterization of NMR relaxation in porous media, J. Magnetic Resonance A,118 (2): 214-220

Pfeffer, R., 1964. Heat and Mass Transport in Multiparticle Systems, Ind. Engng Chem. Fundamentals, 3, 380–383.

Piri, M. and Blunt, M.J., 2005, Three-dimensional mixed-wet random pore-scale network modeling of two- and three-phase flow in porous media. I. model description, Phys. Rev. E., 71, art. no. 026301.

Powers, S.E., Abriola, L.M. and Weber, W.J., 1992. An experimental investigation of NAPL dissolution in saturated subsurface systems: steady-state mass transfer rates. Water Resour. Res., 28 (10): 2691-2705.

Powers, S.E., Abriola, L.M. and Weber, W.J., 1994. An experimental investigation of NAPL dissolution in saturated subsurface systems: transient mass transfer rates. Water Resour. Res., 30 (2): 321-332.

Powers, S.E., Anckner, W.H. and Seacord, T.F., 1996. Wettability of NAPL-contaminated sands, J Environ Eng-ASCE, 122 (10): 889-896.

Powers, S.E., Loureiro, C.O., Abriola, L.M. and Weber, W.J., 1991 Theoretical study of the significance of non-equilibrium dissolution of nonaqueous phase liquid in subsurface systems. Water Resour. Res. 27 (4): 463-477.

Powers, S.E. and Tamblin, M.E., 1995. Wettability of porous media after exposure to synthetic gasolines, J. Contam. Hydrol., 19 (2): 105-125.

Pruess, K., 2005. Numerical studies of fluid leakage from a geologic disposal reservoir for CO2 show self-limiting feedback between fluid flow and heat transfer, Geophys. Res. Lett., 32 (14): Art. No. L14404.

Quiblier, J. A., 1984. A new three-dimensional modeling technique for studying porous media. J. Colloid Interface Sci, 98: 84-102.
Ransohoff, T.C., Gauglitz, P.A. and Radke, C.J., 1987. Snap-off of gas bubbles in smoothly constricted noncircular capillaries, AICHE J. 33 (5): 753-765.

Ransohoff, T.C. and Radke, C.J., 1988, Laminar flow of a wetting liquid along the corners of a predominantly gas-occupied non-circular pore, J. Colloid Interface Sci., 121, 392-404.

Ranz, W.E. and Marshall, W.R., 1952, Evaporation from drops, Chemical Engineering Progr., 48, 141-146.

Reeves, P.C. and Celia, M.A., 1996. A functional relationship between capillary pressure, saturation, and interfacial area as revealed by a pore-scale network model, Water Resour. Res., 32 (8): 2345-2358

Reynolds, W.D., Brown, D.A., Mathur, S.P. and Overend, R.P., 1992. Effect of in situ gas accumulation on the hydraulic conductivity of peat, Soil Sci., 153: 397-408.

Roof, J.G., 1970. Snap-off of oil droplets in water-wet pores, SPE J., 10 (1): 85.

Sahimi, M., 1993. Flow phenomena in rocks – from continuum models to fractals, percolation, cellular-automata and simulated annealing. Rev. Modern Phys. 65 (4): 1393-1534

Sahloul, N.A., Ioannidis, M.A. and Chatzis, I., 2002. Dissolution of residual nonaqueous phase liquids in porous media: pore scale mechanisms and mass transfer rates. Adv. Water Resour., 25: 33-49.

Salathiel, R.A., 1973. Oil recovery by surface film drainage in mixed wettability rocks, J. Pet. Technol., 1216-1224.

Satik, C., Li, X. and Yortos, Y.C., 1995. Scaling of single-bubble growth in a porous medium, Phys. Rev. E 51(4): 3286–3295.

Sheng J.J., Maini B.B., Hayes R.E. and Tortike W.S., 1999 a. Critical review of foamy oil flow, Transp. Porous Media 35 (2): 157-187.

Sheng J.J., Hayes R.E., Maini B.B. and Tortike W.S., 1999 b. Modelling foamy oil flow in porous media, Transp. Porous Media 35 (2): 227-258.

Sherwood, T. K., Pigford, R. L. and Wilke, C. R., 1975. Mass Transfer, McGraw-Hill, Inc., New York.

Sorensen, J. P. and Stewart, W. E., 1974. Computation of Forced Convection in Slow Flow through Ducts and Packed Beds-IV. Convective Boundary Layers in Cubic Arrays of Spheres, Chem. Engng Sci., 29, 833–837.

Standnes, D.C. and Austad, T., 2000. Wettability alteration in chalk 2. Mechanism for wettability alteration from oil-wet to water-wet using surfactants, J Petrol Sci Eng, 28: 123-143.

Standnes, D.C. and Austad, T., 2003. Wettability alteration in arbonates – Low-cost ammonum surfactants based on bio-derivatives from the conconut palm as active chemicals to change the wettability from oil-wet to water-wet conditions, Colloid Surf A: Physicochem Eng Asp, 218: 161-173.

Standnes, D.C. and Austad, T., 2003. Wettability alteration in arbonates – Interaction between cationic surfactant and carboxylates as a key factor in wettability alteration from oil-wet to water-wet conditions, Colloid Surf A: Physicochem Eng Asp, 216: 243-259.

Stohr, M. and Khalili, A., 2006. Dynamic regimes of buoyancy-affected two-phase flow in unconsolidated porous media, Phys. Rev. E 73 (3): Art. No. 036301.

Stone, H.A., 1989, Heat/mass transfer from surface films to shear flows at arbitrary Peclet numbers, Phys. Fluids A 1, 1112-1122.

Testa, S.M. and Wiengardner, D.L., 1991. Restoration of petroleum contaminated aquifers, Lewis Publishers, Chelsea, MI.

Thompson, K.E. and Fogler, H.S., 1997. Modeling flow in disordered packed beds from pore-scale fluid mechanics, AICHE J., 43 (6): 1377-1389

Toledo, P.G., Scriven, L.E. and Davis, H.T., 1989. Pore-space statistics and capillary pressure curves form volume-controlled porosimetry, SPE, 64th Ann. Tech. Conf. San Antonio, TX. 8-11.

Tomlinson, D.M., Thompson, N.R., Johnson, R.L. and Redman, J.D., 2003. Air distribution in the Borden aquifer during in situ air sparging, J. Contam. Hydrol., 67 (1-4): 113-132.

Tsimpanogiannis, I.N. and Yortsos, Y.C., 2002. Model for the gas evolution in a porous medium driven by solute diffusion, AICHE J. 48 (11): 2690-2710.

Tsimpanogiannis, I.N. and Yortsos, Y.C., 2004. The critical gas saturation in a porous medium in the presence of gravity, J. Colloid Interf. Sci. 270 (2): 388-395.

Van Dijk, M.I.J., Sorbie, K.S. and McDougall, S.R., 2001. Saturation dependencies of three phase relative permeabilities in mixed wet and fractionally wet system, Adv. Water Resour. 24: 365-384.

Van Schijndel A.W.M., 2003. Modeling and solving building physics problems with FemLab, Building Environ., 38 (2): 319-327.

Vizika, O. and Lombard, J.M., 1996. Wettability and spreading: Two key parameters in oil recovery with three-phase gravity drainage, SPE Rerserv. Eng., 11 (1): 54-60

Wagner, G., Meaking, P., Feder, J. and JØssang, T., 1997. Buoyancy-driven invasion percolation with migration and fragmentation, Physica A 245: 217-230.

Wakao, N. and Funazkri, T., 1978, Effect of fluid dispersion coefficients on particle-to-fluid mass transfer coefficients in packed beds: correlation of sherwood numbers, Chem. Eng Sci., 33, 1375–1384.

Wang, F.H.L., 1988. Effect of wettability alteration on water/oil relative permeability, dispersion and flowable saturation in porous media, SPE Reservoir Eng. 4, 617-628.

Wardlaw, N.C., Li, Y. and Forbes, D., 1987. Pore-throat size correlation from capillary pressure curves, Transp. Porous Media, 2: 597–614.

Williams, M.D. and Oostrom, M., 2000, Oxygenation of anoxic water in a fluctuating water table System: an experimental and numerical study, J. Hydrol., 230: 70-85.

Williamson, J. E., Bazaire, K. E. and Geankoplis, C. J., 1963. Liquid-phase mass transfer at low Reynolds numbers, Ind. Eng Chem. Fundamentals 2, 126–129.

Wilson, E. J. and Geankoplis, C. J.: 1966, Liquid mass transfer at very low Reynolds numbers in packed beds, Ind. Eng Chem. Fundamentals 5, 9–14.

Wilson, J.T, Armstrong, J.M. and Rifai, H.S., 1994. A full-scale field demonstration on the use of hydrogen peroxide for in situ bioremediation of an aviation gasoline-contaminated aquifer, In Bioremediation: Field Experience, ed. P.E. Flathman, D.e. Jerger, and J.H. Exner. Ann Arbor, Michigan: Lewis publishers: 333-360.

Yang, H., Zhao, T.S. and Ye, Q., 2005. In situ visualization study of CO_2 gas bubble behavior in DMFC anode flow fields, J. Power Sour., 139: 79–90

Yiotis, A.G., Stubos, A.K., Boudouvis, A.G. and Yortsos, Y.C., 2001. A 2-D pore-network model of the drying of single-component liquids in porous media, Adv. Water Res., 24: 439-460

Yiotis, A.G., Stubos, A.K., Boudouvis, A.G., Tsimpanogiannis, I.N. and Yortsos, Y.C., 2005. Pore-network modeling of isothermal drying in porous media, Transp. Porous Media, 58 (1-2): 63-86

Yortsos, Y.C. and Parlar, M., 1989. Phase change in binary in porous media: application to solution gas drive, SPE 19697. SPE meeting, San Antonio, TX.

Zhao, W. and Ioannidis, M.A., 2003, Pore network simulation of the dissolution of a single-component wetting Nonaqueous phase liquid. Water Resour. Res., 39(10): 1291.

Zheng, J.Z., Behrens, S.H., Borkovec, M. and Powers, S.E., 2001. Predicting the wettability of quartz surfaces exposed to dense nonaqueous phase liquids, Environ. Sci. Techn., 35 (11): 2207-2213.

Zheng, J.Z. and Powers, S.E., 1999. Organic bases in NAPLs and their impact on wettability. J Contam Hydrol, 39 (1-2): 161-181.

Zheng, J.Z., Shao, J.H. and Powers, S.E., 2001. Asphaltenes from coal tar and creosote: Their role in reversing the wettability of aquifer systems, J. Colloid Iterf. Sci. 244 (2): 365-371.

Zhou, D., Dillard, L.A. and Blunt, M.J., 2000. A physically based model of dissolution of nonaqueous phase liquids in the saturated zone. Transp. Porous Media, 39: 227–255.

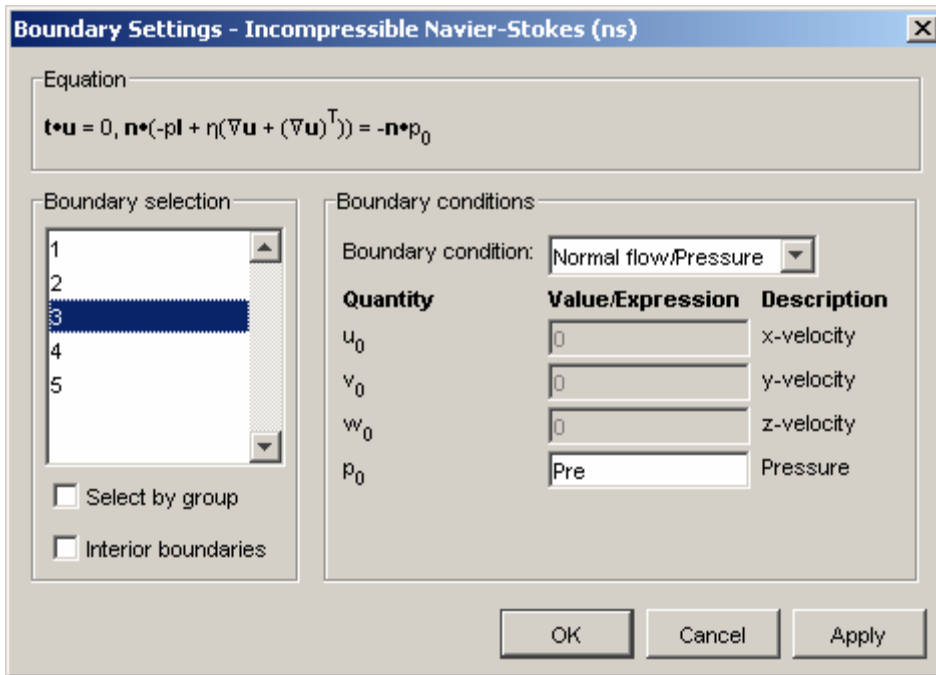# Appendix A

FAMLAB GUI Information in Simulation of Convective

Mass Transfer in Corner Filament
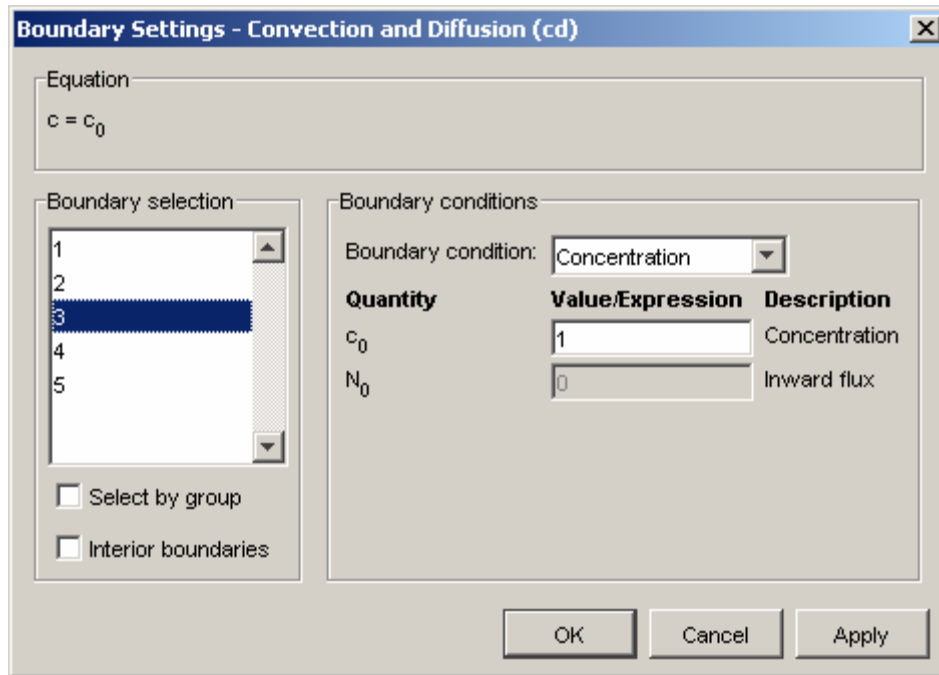
Specified multi-physics equations
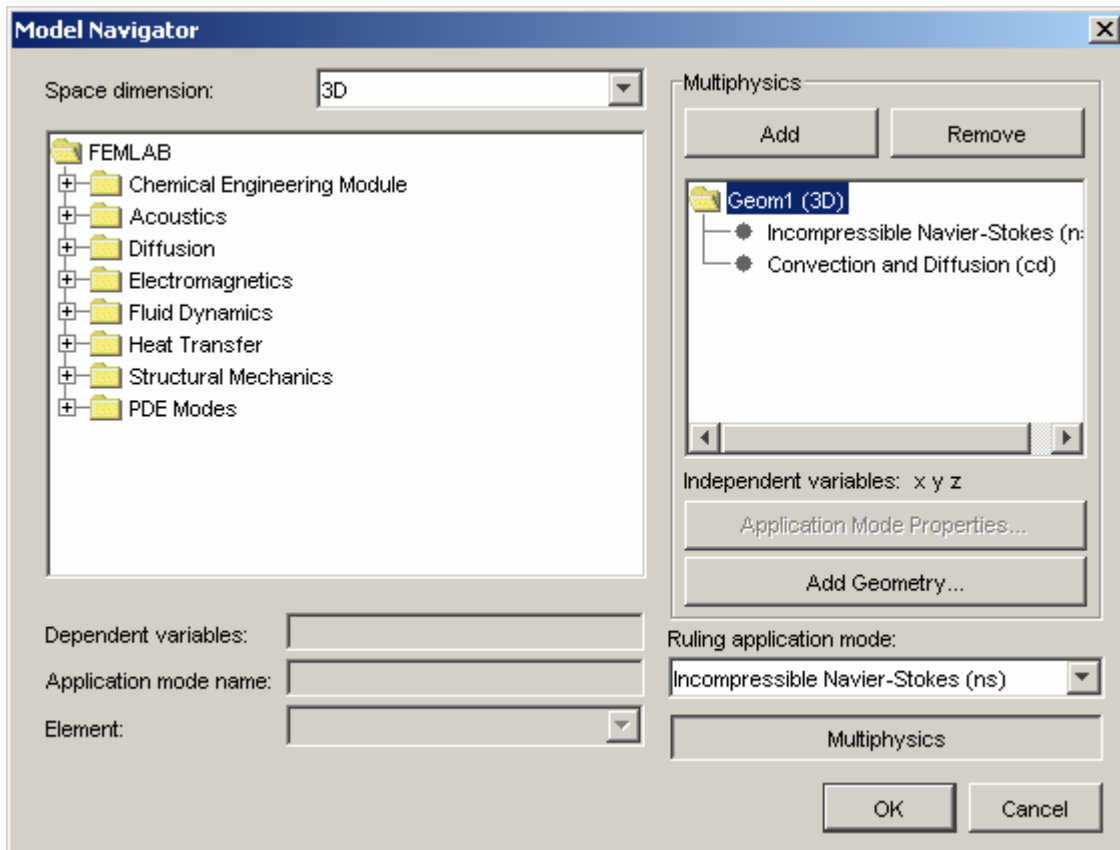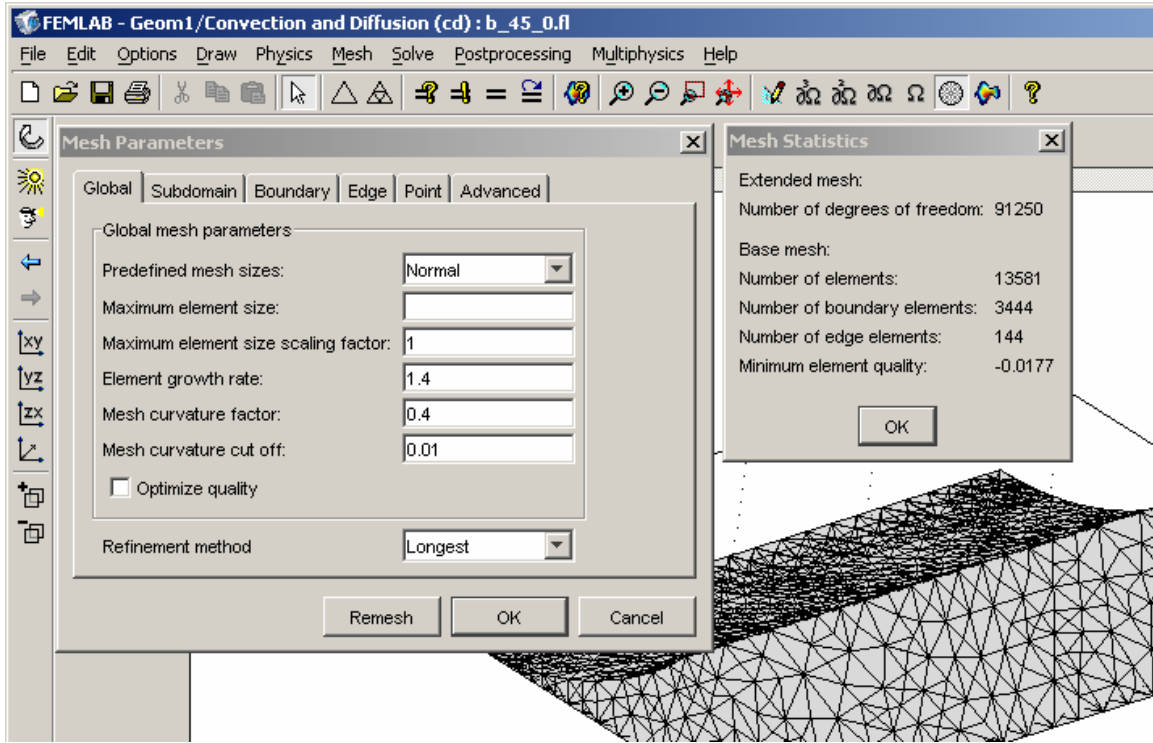
Boundary Settings – Incompressible Navier-Stokes Equation

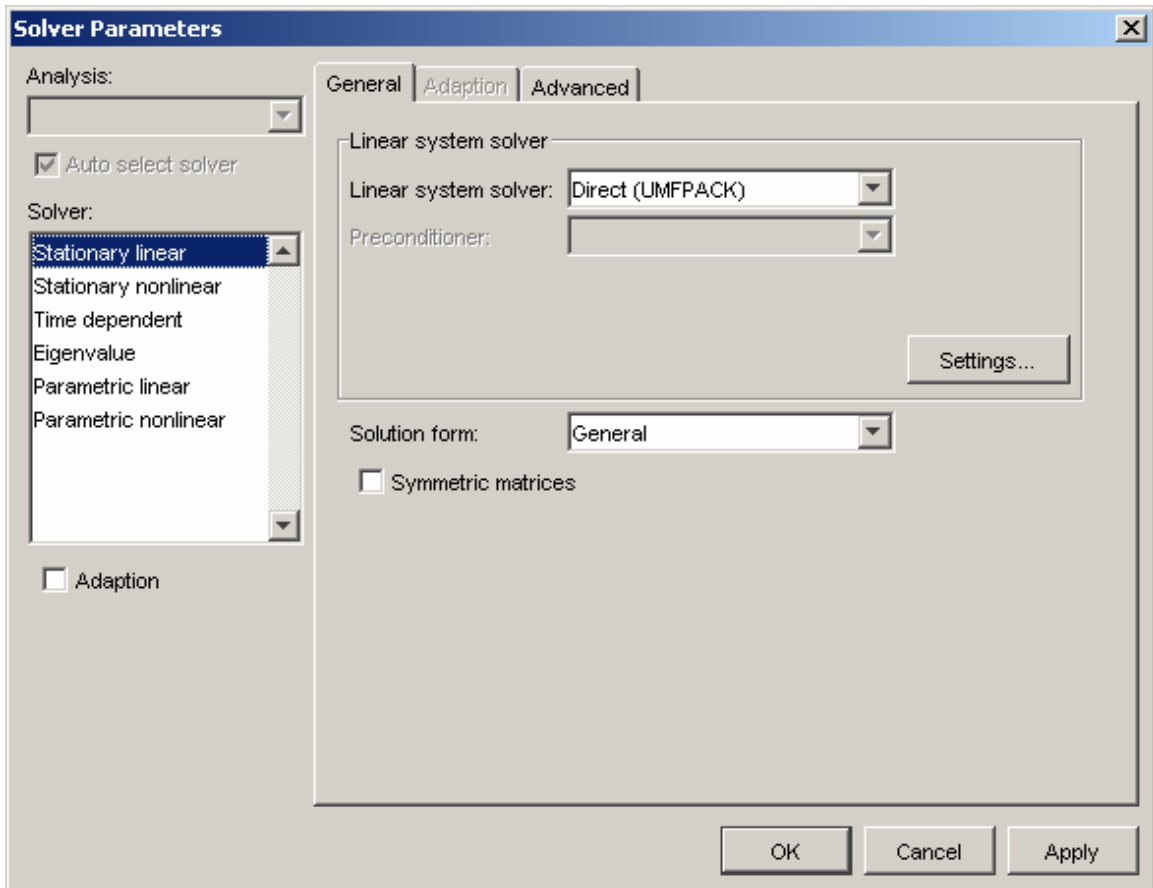| Boundary	Setting	Value
1. pore wall	No slip	
2. plane dividing half domains	Slip/symmetry	
3. inlet	Normal flow/pressure	P_0 = pre
4. outlet	Outflow/pressure	P_0 = 0
5. interface	Slip/symmetry or no slip	

Boundary Settings – Convection and Diffusion

Boundary	Setting	Value
1. pore wall	Insulation/symmetry	
2. plane dividing half domains	Insulation/symmetry	
3. inlet	Concentration	$C_0 = 1$
4. outlet	Convective flux	$P_0 = 0$
5. interface	Concentration	$C_0 = 0$
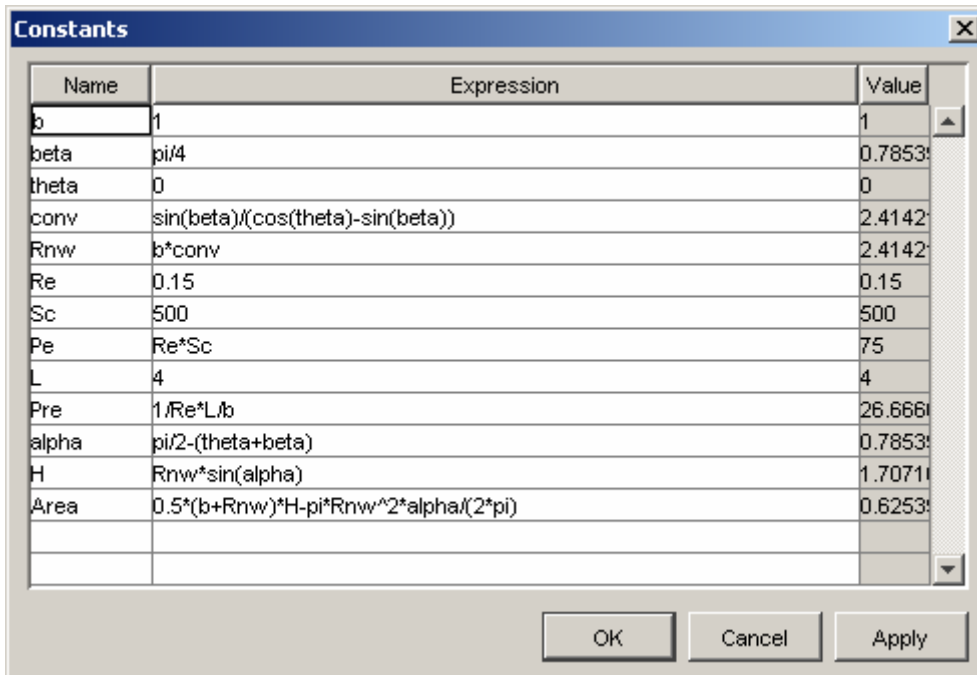
Mesh Parameters

Solver Parameters

Constants

Name	Expression	Value
b	1	1
beta	pi/4	0.7853!
theta	0	0
conv	sin(beta)/(cos(theta)-sin(beta))	2.4142'
Rnw	b*conv	2.4142'
Re	0.15	0.15
Sc	500	500
Pe	Re*Sc	75
L	4	4
Pre	1/Re*L/b	26.6666
alpha	pi/2-(theta+beta)	0.7853!
H	Rnw*sin(alpha)	1.7071
Area	0.5*(b+Rnw)*H-pi*Rnw^2*alpha/(2*pi)	0.6253!

OK   Cancel   Apply

Appendix B

Computer Programs

Computer programs are provided in attached CD (only available in bound copies):

1. FORTRAN program for simulation of wetting NAPL dissolution

   NAPL_film.doc

2. FORTRAN program for simulation of gas evolution

   bubble.doc

3. MATLAB program for visualization of concentration field

   color_plot.m; coord.m; drooc.m; fillex_color.m

4. MATLAB program for visualization of pressure field

   pres_plot.m; fillex_pressure.m

5. MATLAB program for making movie clips for bubble growth

   movietest.m; colorplot_movie.m

6. MATLAB program for visualization of NAPL clusters

   color_cluster.m; fillex_clu.m

Appendix C

Movie Clips

Movie clips for bubble evolution are provided in attached CD (only available in bound copies):

1. Bubble evolution from single nucleation site

   single_bubble.wmv

2. Bubble evolution from multiple nucleation sites

   multiple_bubble.wmv